



universität  
wien

# DISSERTATION / DOCTORAL THESIS

Titel der Dissertation / Title of the Doctoral Thesis

Upper Mantle Anisotropy Under the Eastern Alps and the  
Pannonian basin

verfasst von / submitted by

Ehsan Qorbani Chegeni

angestrebter akademischer Grad / in partial fulfilment of the requirements for the degree of  
Doktor der Naturwissenschaften (Dr. rer. nat.)

Wien, 2015 / Vienna, 2015

Studienkennzahl lt. Studienblatt /  
degree programme code as it appears on the student  
record sheet:

A 796 605 416

Dissertationsgebiet lt. Studienblatt /  
field of study as it appears on the student record sheet:

Geophysik

Betreut von / Supervisor:

Univ.-Prof. Dr. Götz Bokelmann





UNIVERSITY OF VIENNA

# *Abstract*

Faculty of Earth Sciences, Geography and Astronomy  
Department of Meteorology and Geophysics (IMGW)

Doctor of Philosophy

## **Upper Mantle Anisotropy Under the Eastern Alps and the Pannonian Basin**

by Ehsan Qorbani Chegeni

Knowledge of anisotropy within the Earth interiors is crucial; it sheds light into signatures of geodynamic processes and reflects the current strain field and deformation history within and across the continents. This thesis describes investigations on anisotropic properties of the upper mantle under the Eastern Alps and the Pannonian basin, regions that have undergone several deformation processes since Cretaceous. Contrasting hypotheses for subduction systems, diversity of geologic units, and complex tectonic setting still raise many unanswered questions about this area. Here the distribution of deformation and its depth is achieved by measuring anisotropic parameters through the splitting of core shear-waves (SKS) and compared to surface geology and topography.

This thesis presents three main topics. At first the anisotropy pattern along the Alpine chain is presented. The pattern of anisotropy is mountain parallel and shows a progressive rotation along the chain. A breakdown at the longitude of the Eastern Alps is detected; there, individual measurements show a local lateral change in the anisotropy. In addition, by modeling the backazimuthal dependency of the splitting measurements, the vertical variation of anisotropy is assessed. As a result a two-layer model of anisotropy beneath the Eastern Alps is proposed; the deeper layer is related to a detached slab and the upper layer is attributed to asthenospheric flow.

Then, the focus moves to the Tauern Window of the Alps. Coupling between crust and mantle in this area has been assessed by comparison of kinematic data from the lower crustal deformation with the deformation signatures from anisotropy. Measurements suggest a mechanical coupling between the crust and upper mantle, indicating the lithospheric depth extension of the Adriatic indentation on the European plate.

Furthermore, this thesis investigates the deep deformation pattern under the Pannonian region and surrounding areas by means of seismic anisotropy together with constraints from naturally deformed xenolith rock samples. Here a large-scale anisotropy of asthenospheric origin, possibly connected to the upper layer anisotropy under the Eastern Alps, is presented. We present the most plausible model of interaction between asthenospheric mantle with the overlying and surrounding lithosphere. In this model NW-SE flow induced alignments within the asthenosphere is related to NE-ward compressional tectonic regime acting in a region between the Adriatic plate and the East European platform.

The results of this thesis suggest that on the contrary to the complex geology and surface deformation, the upper mantle anisotropy and deformation under the whole Carpathian-Pannonian region and Eastern Alps is rather simple, concluding that this anisotropy depicting NW-SE alignment has to originate from the asthenospheric mantle.



UNIVERSITÄT WIEN

# *Zusammenfassung*

Fakultät für Geowissenschaften, Geographie und Astronomie

Institut für Meteorologie und Geophysik (IMGW)

Doktor der Naturwissenschaften

## **Upper Mantle Anisotropy Under the Eastern Alps and the Pannonian Basin**

von Ehsan Qorbani Chegeni

Seismische Anisotropie im Erdinneren ist von zentraler Bedeutung: Sie liefert Informationen über geodynamische Prozesse, spiegelt das aktuelle Spannungsfeld wieder, und enthält Informationen über die Deformationsgeschichte innerhalb und zwischen Kontinenten. Diese Arbeit beschreibt Untersuchungen von anisotropen Eigenschaften des oberen Mantels unterhalb der Ostalpen und des Pannonischen Beckens, Regionen, die seit der Kreidezeit verschiedenen Deformationsprozessen unterworfen waren. Gegensätzliche Hypothesen zu Subduktionssystemen, die Vielfältigkeit von geologischen Erscheinungen und eine komplexe Tektonik führen dazu, daß viele Fragen über diese Regionen noch unbeantwortet sind. In dieser Arbeit werden Parameter seismischer Anisotropie mittels Scherwellen-Splitting von Kern-Scherwellen-Phasen (SKS) bestimmt, um Deformationen in der Tiefe zu charakterisieren und mit Oberflächengeologie und Topographie zu vergleichen.

Die vorliegende Arbeit umfasst drei Hauptthemen: Zunächst wird das Muster der Anisotropie entlang der Alpen präsentiert. Dieses verläuft parallel zur Topographie und zeigt eine fortlaufende Rotation entlang der Bergkette. Auf Höhe der Ostalpen wird das Muster unterbrochen und zeigt dort lokale laterale Veränderungen der Anisotropie. Durch Modellierung der azimuthalen Abhängigkeit der Splitting-Parameter wird zusätzlich die vertikale Variation der Anisotropie untersucht. Hieraus resultierend wird ein zwei-Schichten Modell für die Anisotropie unter den Ostalpen vorgeschlagen. Die tieferen der beiden Schichten wird mit einer abgetrennten tektonischen Platte in Verbindung gebracht, während die obere Schicht auf Fließbewegungen in der Asthenosphäre zurückzuführen sind.

Der zweite Teil befasst sich mit dem Tauern-Fenster der Alpen und untersucht in dieser Region die Kopplung zwischen Kruste und Mantel mittels Vergleich der Deformation der unteren Kruste mit Informationen aus seismischer Anisotropie. Messungen legen eine mechanische Kopplung von Kruste und oberem Mantel nahe und geben Hinweise auf die Tiefenausdehnung der Lithosphäre der adriatischen Ausbuchtung auf der Europäischen Platte.

Des weiteren wird die Struktur tiefer Verformungen unter dem Pannonischen Becken und benachbarten Gebieten erforscht. Hierfür wird seismische Anisotropie kombiniert mit Untersuchungen an verformten Xenolith-Proben. Hierbei wird eine weiträumige Anisotropie in der Asthenosphäre aufgezeigt, welche möglicherweise mit der oberen anisotropen Schicht unter den Ostalpen verbunden ist. Das plausibelste Modell für die Interaktion des asthenosphärischen Mantels mit der überlagerten und umgebenden Lithosphäre verbindet fluss-induzierte NW-SO Ausrichtung in der Asthenosphäre mit einem NO ausgerichteten, stauchenden Spannungsfeld zwischen der Adriatischen und der Ost-Europäischen Platte.

Im Ergebnis zeigen diese Studien eine vergleichsweise einfache Struktur der seismischen Anisotropie im oberen Mantel, im Gegensatz zur komplexen Geologie und Oberflächendeformation im Gebiet der Ostalpen, der Karpathen und des Pannonischen Beckens. Hieraus folgt, dass diese Anisotropie mit NW-SO Ausrichtung aus dem asthenosphärischen Mantel stammen muss.



*To:*

*Bahar*



# *Acknowledgements*

I would like to express my special appreciation and thanks to my advisor Professor Götz Bokelmann. I appreciate all his contributions of time, ideas, and funding to make my PhD experience productive and stimulating. I would like to thank him for encouraging my research and for allowing me to grow as an independent research scientist. I also gratefully acknowledge the funding received towards my PhD from the Austrian Science Fund (FWF).

I would especially like to thank Dr. Irene Bianchi who has been supportive and has encouraged me to pursue my dissertation without objection. She has provided insightful discussions and advises on my research. Irene was and remains my best role model for a scientist, mentor, and friend.

My sincere thanks also goes to Prof. Walter Kurz (Karl-Franzens-University of Graz), Dr. István Kovács (Geological and Geophysical Institute of Hungary), and Prof. Frank Horváth (Geomega Ltd, Hungary), for sharing their experience and information, which have provided me an opportunity to establish successful collaborative research work. I also gratefully thank my colleges in the Geophysics group, whose support made this thesis an enjoyable experience for me.

I would also like to thank Prof. Mark Handy (Free University of Berlin), Prof Georg Rümpker (Goethe University Frankfurt), and Prof. Bruno Meurers (University of Vienna) for serving as my committee members.

At the end I would like to express appreciation to my beloved wife, Bahar, who was beside me and was always my support at every moment. Her quiet patience and unwavering love, support, and encouragement made this dissertation possible. Words cannot express how grateful I am.





# Contents

<b>Abstract</b>	<b>iii</b>
<b>Acknowledgements</b>	<b>ix</b>
<b>Contents</b>	<b>xi</b>
<b>List of Figures</b>	<b>xiv</b>
<b>List of Tables</b>	<b>xvi</b>
<b>1 Introduction</b>	<b>1</b>
1.1 Background . . . . .	1
1.2 Tectonic setting . . . . .	4
1.3 Upper mantle structure . . . . .	7
1.3.1 The Alps . . . . .	7
1.3.2 The Carpathian-Pannonian region . . . . .	13
1.4 Anisotropy in the Alpine-Carpathian region; Previous studies . . . . .	17
1.5 Outline of thesis . . . . .	21
<b>2 Methodology</b>	<b>23</b>
2.1 Seismic anisotropy . . . . .	23
2.2 Methods of measuring anisotropy . . . . .	25
2.3 Shear-wave splitting . . . . .	26
2.3.1 Transverse component minimization technique . . . . .	29
2.3.2 Eigenvalue technique . . . . .	29
2.3.3 Cross-correlation technique . . . . .	30
<b>3 Large scale anisotropy under the Alpine chain</b>	<b>33</b>
3.1 Introduction . . . . .	34
3.2 Data and method . . . . .	35
3.3 Results and discussion . . . . .	36
3.4 Conclusions . . . . .	42
3.5 Supplementary figures . . . . .	43

<b>4</b>	<b>Eastern Alps</b>	<b>49</b>
4.1	Introduction . . . . .	50
4.2	Tectonic setting . . . . .	51
4.3	Data and method . . . . .	52
4.4	Results . . . . .	54
4.4.1	Splitting parameters; average values . . . . .	54
4.4.2	Individual measurements . . . . .	57
4.5	Discussion . . . . .	59
4.5.1	Lateral change of anisotropy . . . . .	59
4.5.2	Vertical changes; modeling of two anisotropic layers . . . . .	60
4.5.3	Anisotropy versus tomographic images . . . . .	66
4.5.4	Origin of the anisotropy . . . . .	68
4.5.4.1	Upper anisotropic layer: . . . . .	69
4.5.4.2	Deeper anisotropic layer: . . . . .	70
4.5.4.3	Western part, 9°E to 12°E: . . . . .	72
4.6	Conclusions . . . . .	74
4.7	Supplementary figures . . . . .	75
<b>5</b>	<b>Tauern Window</b>	<b>81</b>
5.1	Introduction . . . . .	82
5.2	Geological setting of the Tauern Window . . . . .	84
5.3	Structural evolution and kinematics . . . . .	86
5.4	Methods for constraining upper mantle deformation . . . . .	88
5.5	Results . . . . .	89
5.6	Discussion . . . . .	92
5.6.1	Anisotropy and deformation regimes . . . . .	92
5.6.2	Vertical coherence of deformation and mechanical coupling . . . . .	96
5.7	Conclusion . . . . .	98
5.8	Acknowledgments . . . . .	99
5.9	Supplementary figures . . . . .	100
<b>6</b>	<b>Carpathian-Pannonian region</b>	<b>103</b>
6.1	Introduction . . . . .	104
6.2	Tectonic background . . . . .	105
6.3	Method and data . . . . .	107
6.4	Shear-wave splitting results . . . . .	108
6.5	Petrofabric data . . . . .	111
6.6	Discussion . . . . .	113
6.6.1	Simple upper mantle deformation versus complex tectonic setting . . . . .	113
6.6.1.1	Role of the crust . . . . .	114
6.6.1.2	Role of the lithosphere . . . . .	115
6.6.1.3	Asthenospheric origin of the anisotropy . . . . .	116
6.6.1.4	Lateral extrusion of the Alcapa block . . . . .	117
6.6.2	Models for upper mantle deformation . . . . .	119

6.6.2.1	Mantle upwelling . . . . .	119
6.6.2.2	Subduction roll-back . . . . .	119
6.6.2.3	Gravitational instability . . . . .	120
6.6.2.4	Asthenospheric flow . . . . .	121
6.6.3	Tectonic inversion and compressional regime . . . . .	122
6.6.3.1	Role of the East European Platform in the AEC model . . . . .	124
6.6.3.2	Role of the Dinaric slab . . . . .	125
6.6.4	Local variation of deformation . . . . .	126
6.6.4.1	Fast axis orientation . . . . .	126
6.6.4.2	Splitting delay time . . . . .	129
6.7	Conclusion . . . . .	130
6.8	Acknowledgments . . . . .	132
<b>7</b>	<b>Summary and Conclusion</b>	<b>137</b>
7.1	Large-scale chain-parallel anisotropy along the Alps . . . . .	138
7.2	Slab detachment under the Eastern Alps . . . . .	138
7.3	Tauern Window, indentation depth, crustal-mantle coupling . . . . .	140
7.4	Adria-East European compressional (AEC) deformation model . . . . .	141
<b>A</b>	<b>Null measurements</b>	<b>143</b>
A.1	Eastern Alps . . . . .	143
A.2	Carpathian-Pannonian region . . . . .	145
<b>B</b>	<b>Chi-square and R-square</b>	<b>147</b>
<b>C</b>	<b>Table of individual splitting measurements</b>	<b>149</b>
C.1	Eastern Alps . . . . .	149
C.2	Carpathian-Pannonian region . . . . .	163
	<b>Bibliography</b>	<b>171</b>
	<b>Curriculum Vitae</b>	<b>195</b>

# List of Figures

1.1	Plate tectonic setting of the Alpine-Mediterranean region . . . . .	2
1.2	Map of the study region . . . . .	3
1.3	Alps tectonic map . . . . .	5
1.4	Carpathian-Pannonian region tectonic map . . . . .	6
1.5	Results of receiver function analysis . . . . .	8
1.6	P-wave residual tomography, Eastern Alps . . . . .	9
1.7	Velocity tomographic model under the Alps, 2003 . . . . .	10
1.8	Velocity tomographic model under the Alps, 2011 . . . . .	11
1.9	Comparison of three different velocity models . . . . .	12
1.10	Map of lithospheric depth under the CPR . . . . .	13
1.11	P-wave tomographic model, 2011, CPR . . . . .	15
1.12	Cross-sections of P-wave tomographic model, CPR, 2012 . . . . .	16
1.13	Schematic representation of upper mantle structure, CPR . . . . .	16
1.14	Previous SKS splitting results for the western Alps . . . . .	17
1.15	Surface-wave anisotropy, central Alps . . . . .	18
1.16	SKS splitting results for TRANSALP profile . . . . .	19
1.17	Previous SKS splitting results, CPR . . . . .	20
2.1	Different type of olivine fabrics . . . . .	24
2.2	Schematic diagrams of distribution of different olivine fabrics . . . . .	25
2.3	Splitting of the shear waves . . . . .	27
2.4	Traveling ray path of SKS and SKKS phases . . . . .	28
2.5	Example of measuring SKS splitting parameters . . . . .	31
3.1	Example of shear wave splitting measurements . . . . .	35
3.2	Shear wave splitting results . . . . .	38
3.3	Rotation of fast orientations along the Alps . . . . .	41
3.4	Map of epicentral location of teleseismic events . . . . .	44
3.5	Map of epicentral location of teleseismic events . . . . .	45
3.6	Backazimuth distribution of good splitting measurements . . . . .	46
4.1	Tectonic map of the Alps . . . . .	53
4.2	Map of average SKS splitting parameters . . . . .	56
4.3	Good quality individual splitting parameters . . . . .	58
4.4	Depth projection of measurements; Backazimuthal variation . . . . .	61
4.5	Periodicity of fast orientations as function of event backazimuth . . . . .	63

4.6	Results of two-layer anisotropy modeling . . . . .	65
4.7	Tomographic models . . . . .	67
4.8	Horizontal and vertical cross-sections through velocity model . . . . .	70
4.9	Illustrative of the two-layer anisotropy model under the Eastern Alps . . . . .	71
4.10	Examples of SKS splitting measurements . . . . .	75
4.11	Backazimuthal variation of fast axes; all stations . . . . .	76
4.12	Backazimuthal variation of delay times; all stations . . . . .	77
4.13	Paleogeographic map of the Alps . . . . .	78
5.1	Tectonic map and cross section of the Tauern Window . . . . .	84
5.2	Shear-wave splitting results . . . . .	90
5.3	Correlation between kinematic data and SKS split results . . . . .	93
5.4	Lateral variation of upper mantle strain field and crustal shear direction . . . . .	95
5.5	Demonstration of rheological layering in the Tauern Window region . . . . .	97
5.6	Statistical distribution of the anisotropic parameters . . . . .	101
6.1	Map of tectonic units of the Carpathian-Pannonian region . . . . .	106
6.2	Average shear-wave splitting parameters . . . . .	109
6.3	Individual measurements of SKS splitting parameters . . . . .	114
6.4	Illustrative of Adria-East European compressional (AEC) model . . . . .	123
6.5	Superposition of anisotropy data on the tomographic model . . . . .	128
A.1	Map of null orientation, Eastern Alps . . . . .	144
A.2	Map of null orientation, CPR . . . . .	145

# List of Tables

3.1	Table of average value of splitting parameters, OE stations . . . . .	37
4.1	List of the stations with the average value of splitting parameters . . . .	55
4.2	Two-layer modeling results . . . . .	64
6.1	Average value of fast orientations and splitting delays, Pannonian basin .	133

# Chapter 1

## Introduction

### 1.1 Background

Phenomena in most of the Earth interior, such as geodynamic mechanisms are hidden from direct observation. However, they can be uncovered through the interpretation of seismological observations. One of the greatest challenges facing geoscientists is to find links between dynamics within the deep Earth and processes on the lithospheric/crustal scale, such as plate motion, orogeny, surface topography, faulting, and seismic activity. Interaction between deep earth geodynamics and surface deformation occurs within the upper mantle, where the present-day dynamic activity is taking place (e.g. *Long and Silver, 2009*). Knowledge of stress and strain distribution within the upper mantle thus provides valuable clues as to how deep deformations are aligned, and how they are transferred to the shallower structures.

One of the most promising tools to constrain the strain field through seismological observations is seismic anisotropy (e.g. *Silver, 1996; Savage, 1999; Park and Levin, 2002*). It is thought to be the best approach to image the deformation pattern in the Earth's interior (*Fouch and Rondenay, 2006*). Seismic anisotropy – defined as the dependence of seismic velocity on the direction of wave propagation – is one major characteristic of the upper mantle. Mantle anisotropy is generated by the structural alignment of olivine crystals, which are created in response to deformation (e.g. *Savage, 1999; Mainprice et al., 2000*). Anisotropic properties of the upper mantle material can be explained as a function of strain field due to tectonic stresses. This strain field can reflect both fossil deformations stored in the lithosphere and the geometry of the present-day active flow/alignment within the asthenosphere (i.e. the most ductile and viscous layer in the upper mantle).

Therefore, the observation of anisotropic preferential orientations can be translated into history and trace of the past (e.g. mountain chains) and current (e.g. ongoing orogeny) tectonic episodes, which both yield constraints on the nature of geodynamic processes in the upper mantle. Mountain chains at the Earth's surface are manifestations of deformation processes acting deep within the Earth. It is particularly interesting to study deformation and seismic anisotropy in mountain belts where we know that much internal deformation has occurred. For many mountain belts, fast seismic orientations have been found to be parallel to the mountain ranges, e.g., the Apennines (*Margheriti et al.*, 1996; *Plomerova et al.*, 2006; *Salimbeni et al.*, 2008), the Pyrenees (*Barruol and Souriau*, 1995), the Himalaya/Tibet (*Lave et al.*, 1996; *Flesch et al.*, 2005; *Lev et al.*, 2006), the Appalachians (*Barruol et al.*, 1997; *Levin et al.*, 1999), the Carpathian arc (*Ivan et al.*, 2008), and the Western Alps (*Barruol et al.*, 2011). The same is true for a number of island arcs associated with subduction zones, while chain-perpendicular anisotropy has also been observed (e.g. *Savage*, 1999).

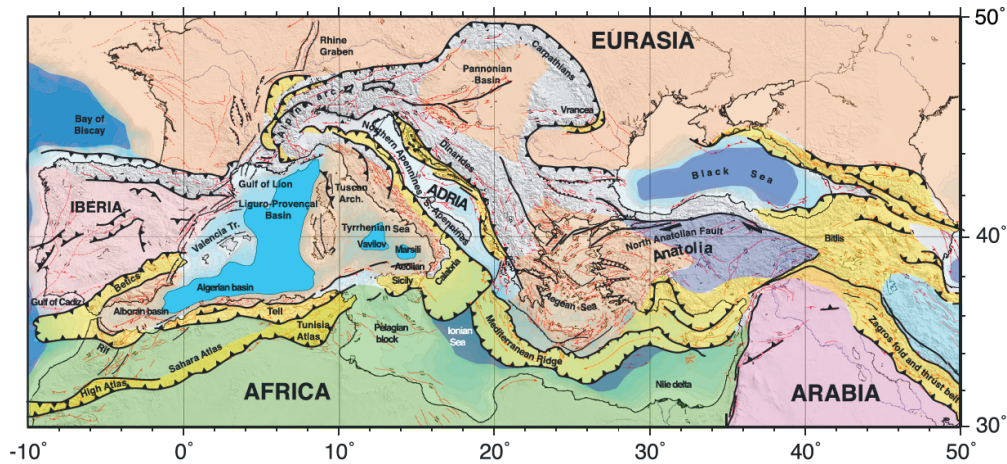


**Figure 1.1:** Plate tectonic setting of the Alpine-Mediterranean region. Figure from *Faccenna et al.* (2014).

The Alps and the Carpathian-Pannonian regions are parts of the greater Alpine-Mediterranean system (Fig. 1.1), which have been squeezed between Africa and Eurasia (*Faccenna et al.*, 2014). The Alpine-Carpathian system (Fig. 1.2), which consists of mountain belts, active tectonic blocks, extensional basins, and convergent regimes, shows complex tectonic features. This provides us with a very particular opportunity to assess the internal deformation under the mountain chains as well as the basins.

Even though the Alpine-Carpathian region has been widely studied, little is known about the tectonic mechanisms and past and present-day deformation processes, particularly in



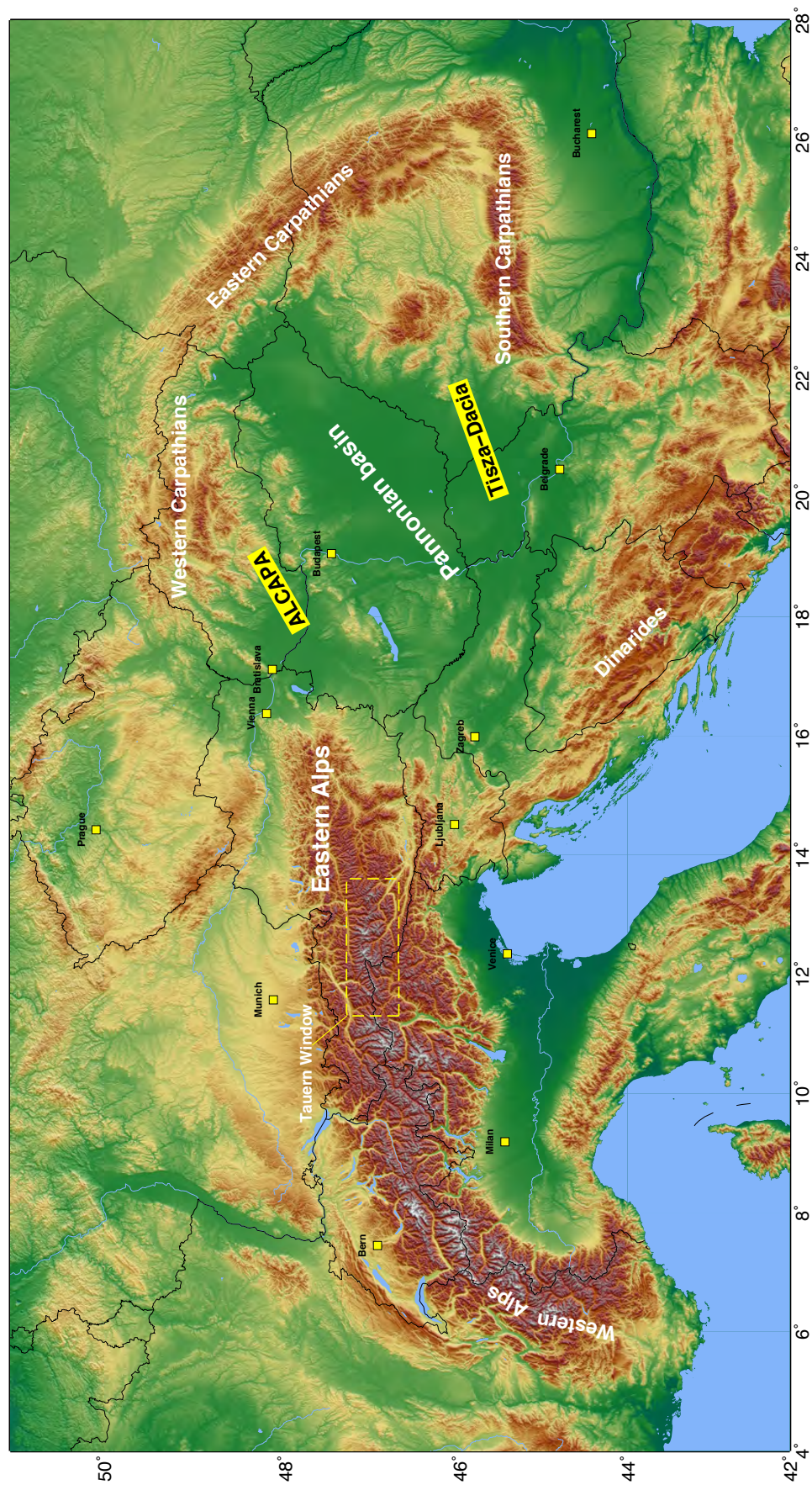


**Figure 1.2:** Topographic map showing the study region of this thesis which focuses on the Eastern Alps and the Carpathian-Pannonian region. The yellow box marks the Tauern Window.

the case of deep lithospheric and upper mantle structures. Especially the Eastern Alps are not well-studied, probably because long-time seismological data (i.e. several years) have been not homogeneously distributed in the past. Analysis of seismic anisotropy can address unanswered questions concerning mantle deformation, yet no anisotropy study was attempted focusing on the Eastern Alps to date. Therefore the aim of this thesis is to achieve more detailed information on deep lithospheric and asthenospheric mantle structures beneath the Alpine chain through seismic anisotropy studies, in particular in the Eastern Alps and the Carpathian-Pannonian region.

## 1.2 Tectonic setting

The Alps are the consequence of convergence between Africa and Eurasia (Fig. 1.1) since late Cretaceous onward. This mountain chain is a small part of Gibraltar-Himalaya orogenic belt (*Piromallo and Faccenna*, 2004), with a complex tectonic history (*Schmid et al.*, 2004, Fig. 1.3). It includes besides the two major plates, namely the European and the Adriatic plate (e.g. *Brückl et al.*, 2010), also several microplates (i.e. Meliata plate and Pannonian fragment), which contribute to the complex evolution of the area. The opening of the Meliata and Vardar oceans in Triassic and late Jurassic time respectively, has been suggested (e.g. *Brückl et al.*, 2010, among the others) to strongly influence the development of the Alps, and its connection with the adjacent mountain belts (Fig. 1.2).

The Alpine belt consists of ophiolites and accreted crust (from the European over the Adriatic plate). These structures (Helvetic and Penninic units in Fig. 1.3) represent the remaining parts of oceanic basins, which are Triassic-Jurassic Neotethys and Jurassic-Early Cretaceous Alpine Tethys (*Schmid et al.*, 2008; *Handy et al.*, 2014). A Flysch belt of Helvetic and Penninic units occupied the northern margin of the Alps as well as parts of the western Arc while the Eastern Alps is mainly composed by Austroalpine units (*Brückl*, 2011). In this area, the Austroalpine units of Adriatic origin (Fig. 1.3) were extended along east-west orientation and decoupled by the South Alpine units (the latter are constituted by continental Adriatic crust) by a sinistral strike-slip fault that was a forerunner of the Periadritic line, called Paleo-insubric-line. The Periadritic lineament has been suggested to separate the Alpine and Adriatic plates along the southern Alps (Fig. 1.3). The Alps are also bounded by Cenozoic sedimentary basins: to the east the Vienna Basin and the Styria basin; to the north the Molasse basin, foreland basin of the north-verging Eastern, Central and Western Alps; to the west the Rhine – Bresse graben, and to the south the Po plain, foreland basin of both the south-verging southern



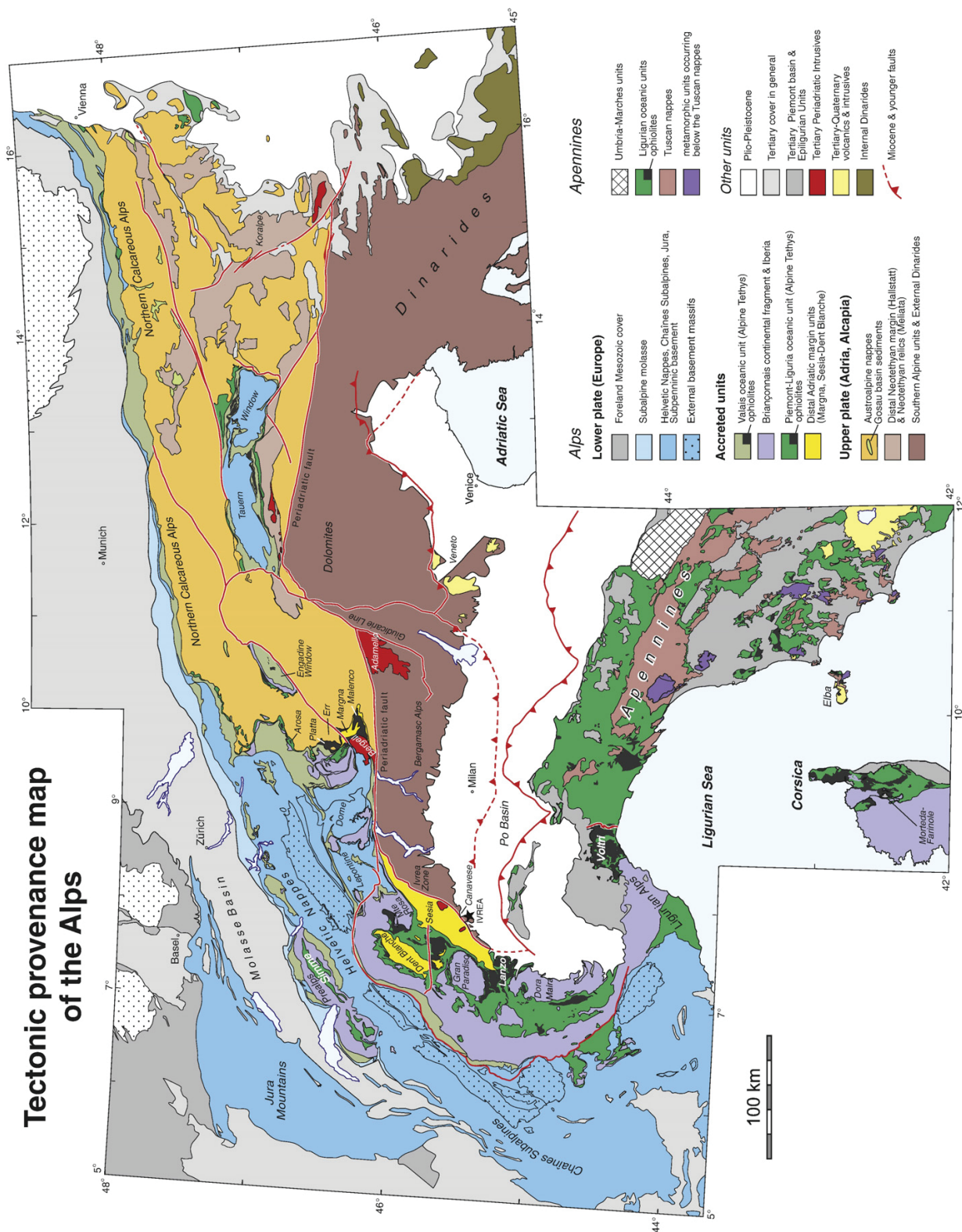


**Figure 1.3:** Map of tectonic units of the Alps. This map is taken from *Handy et al. (2010)* which was modified after *Froitzheim and Manatschal (1996)* and *Schmid et al. (2004)*.

Alps and of the Apennine chain (Fig. 1.3).

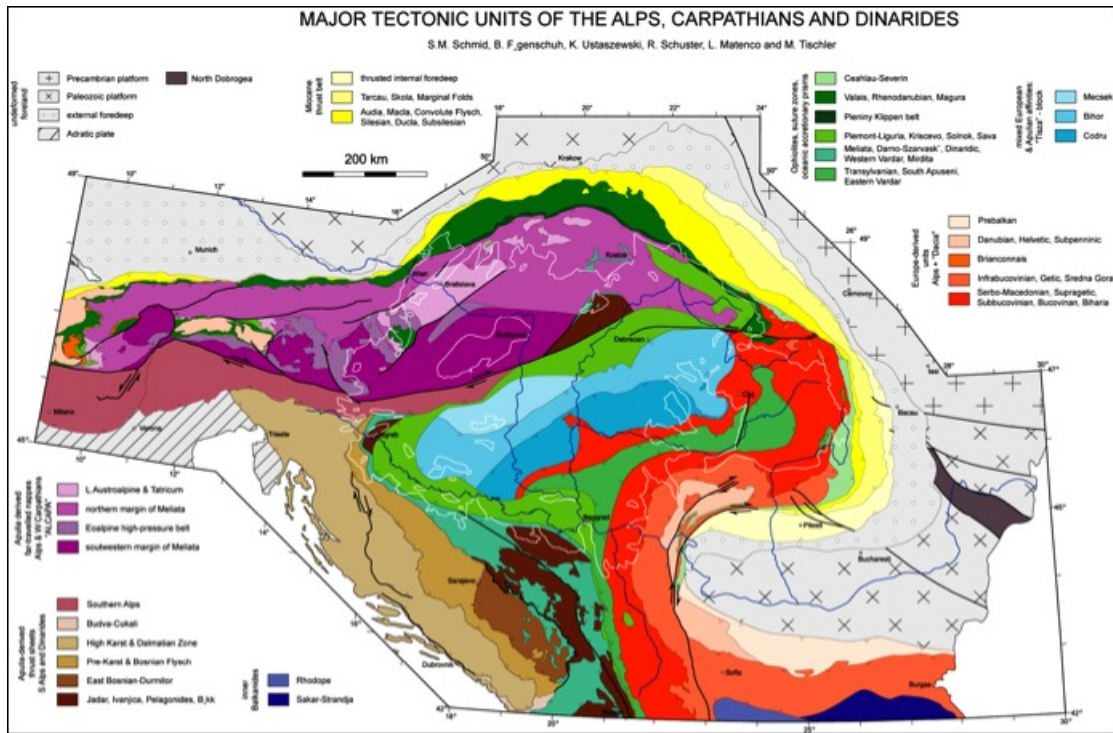


**Figure 1.4:** Major tectonic units of the Carpathian-Pannonian region and its connection with the Eastern Alps. Figure from *Ustaszewski et al.* (2008).

At the eastern end of the Alps, the mountain chains have connected in earlier times with the Carpathians and the Dinarides. Although it has been generally thought that the Alpine tectonic history is deeply linked to that of the adjacent mountain chains, the nature of the transition today has still to be defined. The Carpathian-Pannonian region (CPR) is the northeastern end of the Alpine mountain belt, including Carpathians and Dinarides mountain chain, and the Vienna and Pannonian basins.

The Pannonian basin, which is one of the extensional basins in the Alpine-Mediterranean region (Fig. 1.1) is surrounded by mountain belts: the Alps, Carpathians, and Dinarides (*Horváth et al.*, 2006). Formation of the Carpathians and Pannonian basin occurred at the same setting in the latest Oligocene (Fig. 1.4) in which the evolution and extension of the Pannonian basin has been related to the subduction under the East Carpathians (*Horváth*, 1993; *Horváth et al.*, 2006). In this setting, retreat of the subducting plate under the eastern Carpathians has governed the extension of the Pannonian basin, and also the extrusion of the Alcapa block (*Royden and Baldi*, 1988), where a migration

of slab roll back and slab detachment along the East Carpathians has been proposed (*Wortel and Spakman, 2000; Horváth et al., 2015*).

The Pannonian basin has covered two main tectonic units, the Alcapa to the north and Tisza-Dacia to the south (Fig. 1.2, 1.4), both have experienced strong internal deformation. Tisza-Dacia, the second major megaunit, is extended between Dinarides and the east and south Carpathians. It has been proposed that this unit was rifted apart from the European margin of the Mesozoic Tethys (*Horváth et al., 2006*). Moreover, paleomagnetic data suggested a clockwise rotation for the Tisza-Dacia unit and on the contrary, a counterclockwise rotation for the Alcapa (*Márton, 2001*).

In the Eastern Alps, in an area between Periadriatic line to the south and SEMP (Salzach-Ennstal-Mariazell-Puchberg) fault to the north, the general fault pattern, different crustal shortening, and strike-slip displacement along the Periadriatic line led to suggest a model in which a megaunit (Alcapa) has been extruding eastward (*Gutdeutsch and Aric, 1987; Ratschbacher et al., 1991a; Brückl et al., 2010*). Alcapa consists of the Eastern Alps, western Carpathians, and Pannonian basin (Fig. 1.2). The Periadriatic line defines the southern margin of this mega unit from the Eastern Alps to the Lake Balaton in Hungary and is followed by the Mid-Hungarian fault in the Pannonian basin (Fig. 1.3, 1.4). Both Europe-derived units and Adria-derived nappes have also been observed within the Alcapa block (*Schmid et al., 2008*). Additionally, lateral extrusion of the Alcapa may explain the passage between the Alps and Pannonian basin, however, further investigation on this area is needed to provide more reliable evidence and to prove this hypothesis.

## 1.3 Upper mantle structure

### 1.3.1 The Alps

In the Alpine region, several seismological studies have been performed to constrain the upper mantle structures. *Aric et al. (1989)* characterized the geometry of lithosphere beneath the Eastern Alps using teleseismic P-wave residuals. They observed a lateral change of the average residuals from the east to west which was attributed to the variations of the lithospheric thickness. According to the negative values, usually related to high-velocity anomalies (cold slab), they proposed a triangular shape for the lithospheric

root. A depth of over 200 km was also suggested for the penetrated root into the mantle under the Eastern Alps.

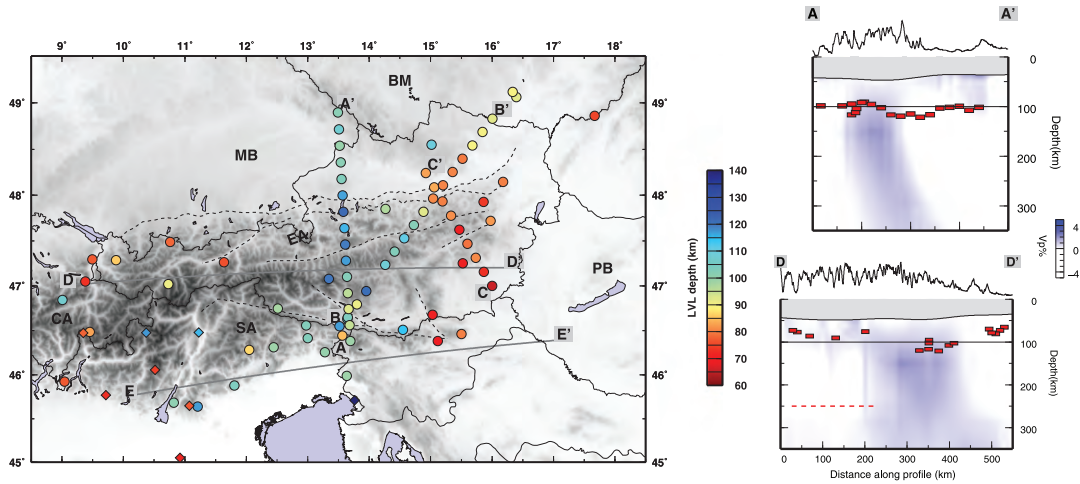


**Figure 1.5:** Depth of the seismic discontinuity inferred from receiver function analysis under the Eastern Alps (left panel). Depth of discontinuities along the two vertical profiles (right panels). Background of the vertical profiles is the P-wave velocity model (Koulakov *et al.*, 2009). Receiver function analysis and figures from Bianchi *et al.* (2014).

The eastern portion of the Alps is still an unexplored territory in terms of upper mantle structure and geometry of the lithosphere roots, and also the way in which it is connected to adjoining regions. Nevertheless, the lithospheric depth under Europe including the Alpine-Carpathian region has been investigated through several studies (Artemieva *et al.*, 2006; Jones *et al.*, 2010; Plomerová and Babuška, 2010). Recently, Bianchi *et al.* (2014) imaged the seismic discontinuities beneath the Eastern Alps by analysis of P- and S-wave receiver function. Receiver function technique characterizes seismic discontinuities under seismic station using the converted S from P-wave (P-to-S) occurred at such discontinuities. In that study, the lithospheric-asthenospheric boundary (LAB) is presented between 78-80 km at the eastern part of the Eastern Alps, while for its western part two discontinuities were detected; 80-90 km, and about 250 km (Fig. 1.5). Concerning the deeper one (Fig. 1.5, Profile DD'), a gradual decline in the LAB depth, from the central Alps to the easternmost part can be traced which is consistent with earlier propositions. Ratschbacher *et al.* (1991a), and Frisch *et al.* (1998) proposed a variation of the lithospheric depth under the Eastern Alps over a distance of 200 km in which it decreases from 170-220 km at the eastern edge of the Tauern Window (Fig. 1.2), to 70 km under the western Pannonian basin. This remarkable thinning is continued to the central Pannonian basin at 60 km depth (Horváth *et al.*, 2006).



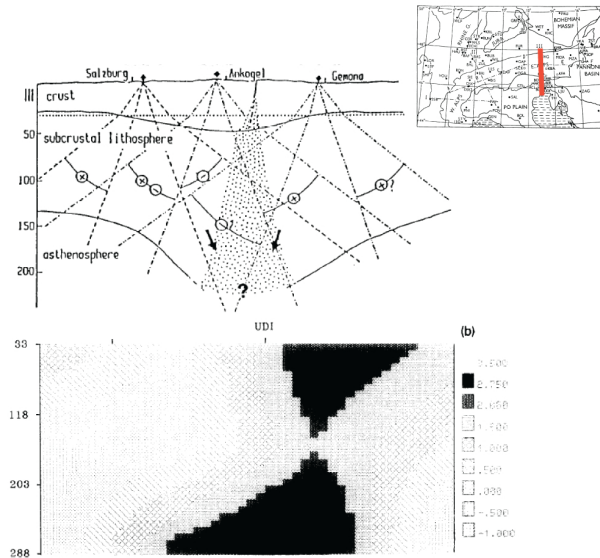


**Figure 1.6:** Results of P-wave residual tomography for the Eastern Alps showing on a cross-section through the lithosphere. Inset shows the location of the profile. Arrows indicate assumed relative movements of both European (to the north) and Adriatic plate (to the south). Figure from *Babuška et al. (1990)*.

Seismic activity in the Alps is relatively low and limited to the crust (*Piromallo and Faccenna, 2004*). It has been reported that the local events are occurred mainly above the Moho level (*Apoloner et al., 2014; Apoloner and Bokelmann, 2015*). Thus the only available observations to investigate the deeper structures, especially the upper mantle, are data from regional and teleseismic earthquakes which can be used in anisotropy, receiver function, and seismic tomography analyses. Seismic tomography utilizes seismic records in order to characterize the seismic velocity perturbation and attenuation. This leads to velocity images of deeper structures. The upper mantle under the Alps is rather widely documented by numerous different tomographic studies (e.g. *Piromallo and Morelli, 2003; Lippitsch et al., 2003; Koulakov et al., 2009; Mitterbauer et al., 2011*). Still, the dynamics of plate collision under the Alps is under debate and different hypotheses on the polarity of the subduction in the Eastern Alps exist and leave open questions.

First attempts to images the deep lithospheric structure under the Alps by assessing seismic velocity perturbations were done by *Aric et al. (1989)* and *Babuška et al. (1990)*. *Babuška et al. (1990)* analyzed the relative P-wave residuals followed by assessing their spatial variations. They showed two different roots of lithosphere beneath the central and Eastern Alps. Figure 1.6 shows their cross-section profile in which a symmetric shape for the lithospheric root was observed. They proposed that this slab-root consists of two sectors; a detached part of the Adria, and the southeastern tip of the European plate in which both sectors penetrate steeply into the mantle.

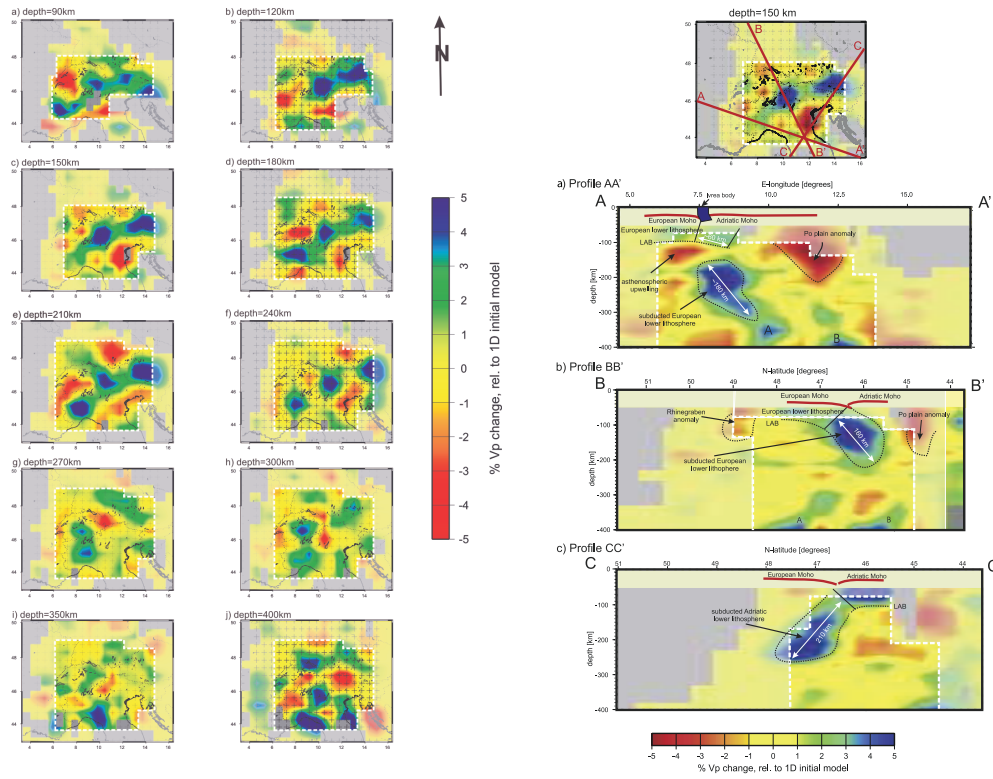


**Figure 1.7:** Left: Horizontal depth sections of P-wave tomographic model between 90 km and 400 km depth. The colors represent the velocity anomaly with respect to a reference model. Right: Three vertical profiles crossing the upper mantle through to the velocity model, AA' at the western, BB' at the central, and CC' at the Eastern Alps. Top panel show the location of the profiles. Note the difference between the results of this study (*Lippitsch et al.*, 2003) with *Mitterbauer et al.* (2011) along the same profile, CC' in Figure 1.9. Velocity model and figures from *Lippitsch et al.* (2003).

In the recent years, tomography studies have shown high-velocity anomaly under the whole Alps which have widely been related to the presence of subducting slabs (*Wortel and Spakman*, 2000; *Piromallo and Morelli*, 2003; *Koulakov et al.*, 2009). At the western and central Alps where these anomalies were observed down to 200-300 km, there is a general interpretation agreement. They are attributed to the southward subduction of the European plate under the Adria (*Wortel and Spakman*, 2000; *Piromallo and Morelli*, 2003; *Lippitsch et al.*, 2003; *Koulakov et al.*, 2009; *Mitterbauer et al.*, 2011). Figure 1.7 and 1.8 show depth slices from P-wave tomographic model proposed by *Lippitsch et al.* (2003) and *Mitterbauer et al.* (2011), in which profiles AA' and BB' in Figure 1.7 evidence the southward dipping subduction of the European plate. At the depth range between 120 km to 180 km (Fig. 1.7 and Fig. 1.8), two high-velocity areas reveal a sharp discontinuity between western and eastern Alpine root which was also observed earlier by *Babuška et al.* (1990). We can consider a separation line at about 12°E in between.



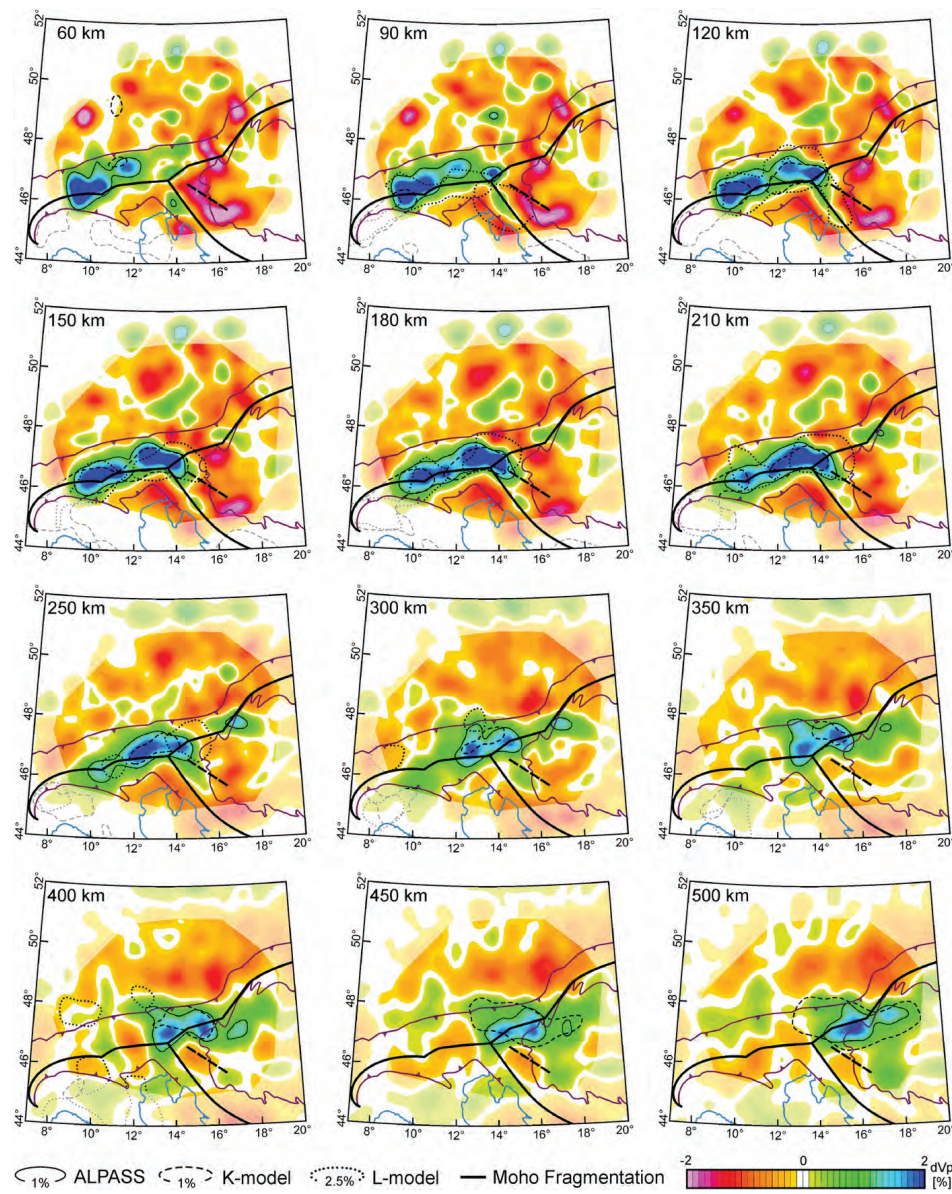


**Figure 1.8:** Velocity tomographic depth slices from ALPASS-model between 60 km to 500 km depth. The velocity anomalies relative to the reference model are illustrated by color. To compare this model (*Mitterbauer et al., 2011*) with the former models, +1% contours of the K-model (*Koulakov et al., 2009*) are shown as medium dashed black lines, and +2.5% contours of the L-model (*Lippitsch et al., 2003*) are shown as medium dotted black lines. Velocity model and figure from *Mitterbauer et al. (2011)*.

To the east of this line, *Lippitsch et al. (2003)* and *Kissling et al. (2006)*, have related the high-velocity anomaly to lithospheric root of the Adria. In a different way than for the Western Alps, they have proposed a northeastward subduction system for the Eastern Alps showing subduction of Adria under Europe. This hypothesis requires assuming a polarity change of subduction along the Alps (Fig. 1.7) in, profile CC').

On the contrary, subduction along the whole Alpine chain has been suggested as a single subduction system which is southward dipping subduction of Europe under Adria (*Mitterbauer et al.*, 2011; *Brückl et al.*, 2010). Through tomographic images (ALPASS project, Fig. 1.8), *Mitterbauer et al.* (2011) observed a nearly vertical slab dipping down to 250 km under the Eastern Alps. They related this to the slab root of the European plate, detached from the crust, as a part of southward subduction system. At depths greater than 300 km, they observed another high-velocity body, dipping nearly eastward under the Pannonian basin. This slab has been interpreted as a detached part of subducted lithosphere of Alpine Tethys origin.

Figure 1.9 (*Mitterbauer et al.*, 2011) shows a comparison between the above-mentioned hypotheses via same vertical profiles (CC') from different studies, *Koulakov et al.* (2009), K-model; *Lippitsch et al.* (2003), L-model; and *Mitterbauer et al.* (2011), M-model. Different angles of dipping slab between L- and M-model, derived through same path are remarkable which can be due to spatial resolution of the tomographic models. Concerning the high-velocity anomaly observed under the Eastern Alps down to 300 km, *Koulakov et al.* (2009) suggested that both European and Adriatic plates likely have a connection with this body, while *Piromallo and Morelli* (2003) proposed a lack of connection neither to Europe nor to the Adria. However, the subduction polarity change remains enigmatic and further studies with higher resolution are required to clarify the contrasting hypotheses.

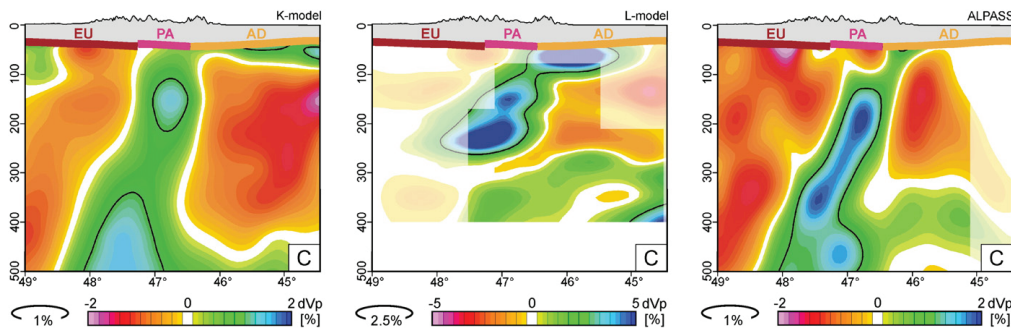


**Figure 1.9:** Comparison of cross-sections from different velocity models, (*Koulakov et al.*, 2009), (*Lippitsch et al.*, 2003), and ALPASS-models (*Mitterbauer et al.*, 2011) along the same profile, CC'. See also Figures 1.7 and 1.8. Figure from *Mitterbauer et al.* (2011).

### 1.3.2 The Carpathian-Pannonian region

The back-arc basins (e.g. Pannonian basin) are generally developed in lithospheric scale (*Horváth et al.*, 2006). Thickness of the lithosphere under the Pannonian basin follows a declining pattern, which starts from the Tauern Window at the Eastern Alps. In the Carpathian-Pannonian region (CPR), under the west, east, and southern Carpathians the LAB depth is imaged in average at about 120, 160, and 180 km respectively (Fig. 1.10, *Horváth*, 1993; *Ádám and Wessergom*, 2001).

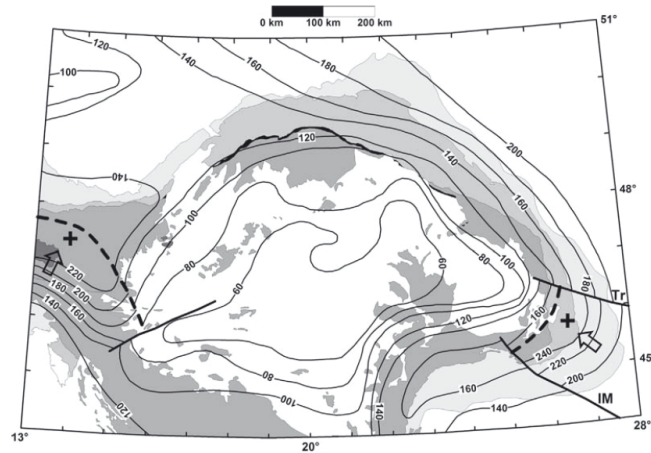


**Figure 1.10:** Map of lithospheric thickness (in kilometers) of the Pannonian Basin and the surrounding area. Figure from *Horváth et al.* (2006).

Upper mantle structure under this area has been studied through several tomography analyses. Data from the recent Carpathian Basin Project (CBP), which aimed to characterize the deep structures under this region, has been used to image the upper mantle as well as the crust. *Dando et al.* (2011) derived P- and S-wave velocity models using CBP data for the whole upper mantle. Figure 1.11 shows the depth slices of P-wave velocity model from 75 km to 600 km. They observed a high-velocity body (cold slab) extending from the Eastern Alps dipping eastward down beneath the Pannonian basin. Additionally they observed a broad high-velocity anomaly at the mantle transition zone (MTZ) extending under the CPR, part of the Alps, and the Bohemian massif (Fig. 1.11). This high-velocity material has been detected not only by that study, but also by *Bijwaard and Spakman* (2000), *Piromallo and Morelli* (2003), *Koulakov et al.* (2009), and *Mitterbauer et al.* (2011).

Moreover, *Ren et al.* (2012) used the CBP data applying P-wave finite-frequency tomography and presented a 3-D velocity model for the entire CPR. Figure 1.12 shows vertical

cross-sections from that study. They imaged a sub-vertical slab under the Eastern Alps, similar to what has been observed by *Mitterbauer et al.* (2011). This slab, which consists of high-velocity material, extends eastward to the Pannonian basin and connects to the slab graveyard at the MTZ (Fig. 1.12, profile 5). They interpreted their observation as a manifestation of mantle downwelling, which happened after continental collision, governed by gravitational instability. We discuss this model in more detail in Chapter 6.

The geometry of the main large-scale tomographic feature at around MTZ (600 km depth) has been considered by receiver function analysis. *Hetényi et al.* (2009) used the CBP data together with the records of permanent stations located in the Eastern Alps, Pannonian basin, and Bohemia and suggested an upper boundary for this high-velocity area (at MTZ) at 410 km. In terms of its lower boundary, they found that this area is 40 km thicker than the global average of MTZ depth. This thickening is caused without an effect on the upper boundary. They related the thickening to cold and dense material accumulated at the MTZ, which could have happened due to delamination of the lithosphere from the subduction systems around the Pannonian basin. Figure 1.13 shows the proposed schematic interpretation based on this model. Since the space which was made by lithospheric delamination has been filled by hot and viscous material from the asthenosphere, seismic anisotropy observation can provide insight into the direction and presents saturation of this replacement (see Chapter 6 for discussion).



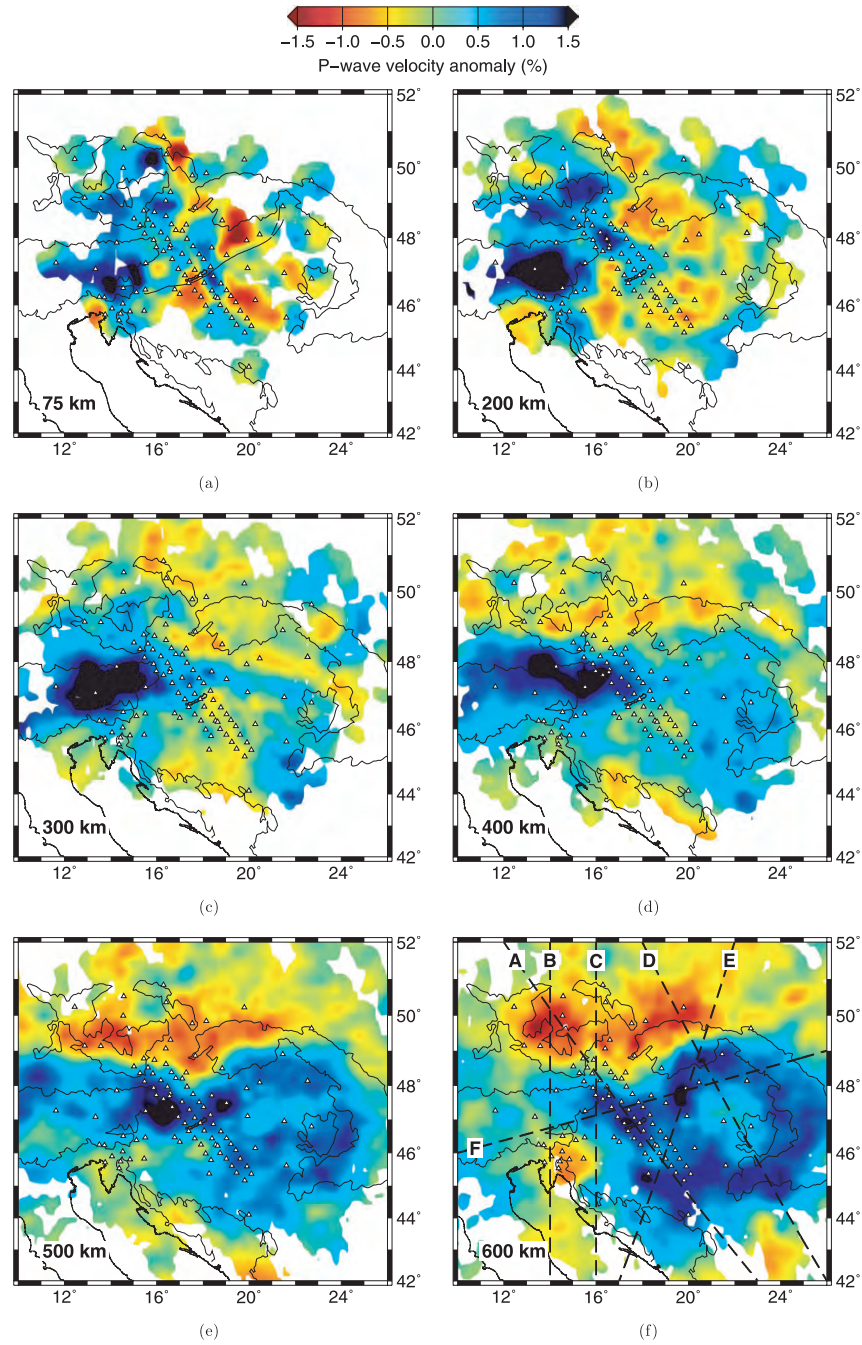


**Figure 1.11:** Horizontal depth sections through the P-wave tomographic model for the Carpathian-Pannonian region. Velocity changes (in percent) are scaled with colors. Last panel shows the locations of vertical sections. Velocity model and figure from *Dando et al. (2011)*.

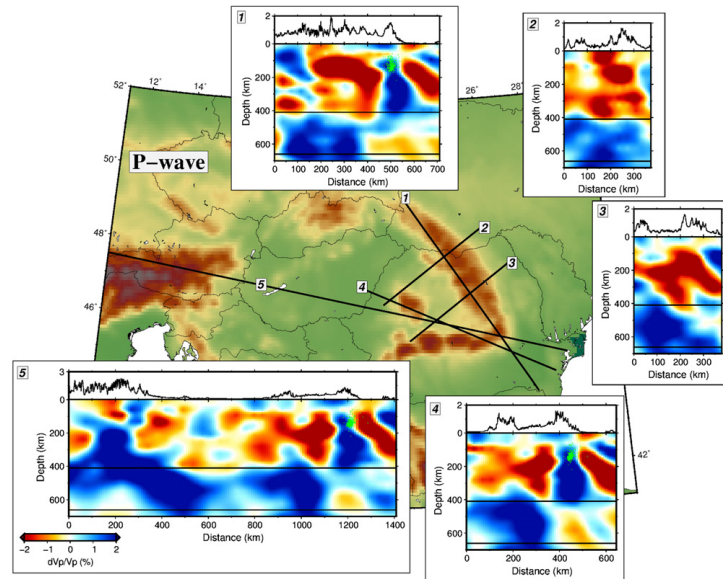


**Figure 1.12:** Vertical profiles through the P-wave tomographic model for the Eastern Carpathians (1, 2 and 3), the Vrancea Zone (4) and the Eastern Alps-Southern Apuseni Mountains (5). Velocity model and figure from *Ren et al. (2012)*.

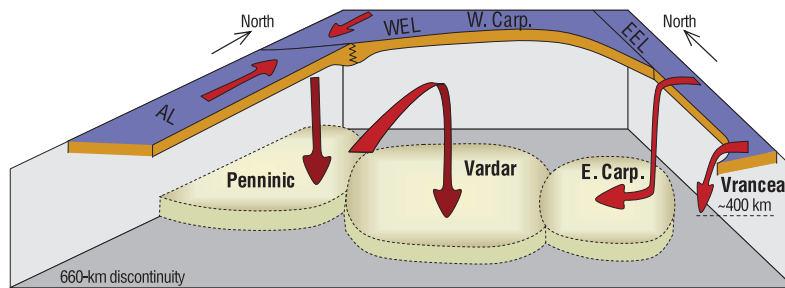


**Figure 1.13:** Schematic model proposed for the Carpathian-Pannonian region to explain the depth anomalies at the MTZ from results of receiver function analysis. This model represents lithospheric relationships and evolution in the Pannonian Basin. Blue-yellow colors mark the Adriatic (AL), the West European (WEL) and the East European (EEL) lithospheres. Red arrows show lithosphere movement paths along which lithospheric material has reached the mantle transition zone. Model and figure from *Hetényi et al. (2009)*.

## 1.4 Anisotropy in the Alpine-Carpathian region; Previous studies

Even though several arguments have been raised regarding the geodynamic processes and subduction models in the Alps, our knowledge of the upper mantle anisotropy and deformation has been limited mainly due to the lack of a dense seismic network in the past. This is particularly the case for the Eastern Alps. In the following, earlier anisotropic studies for the western and central Alps are summarized.

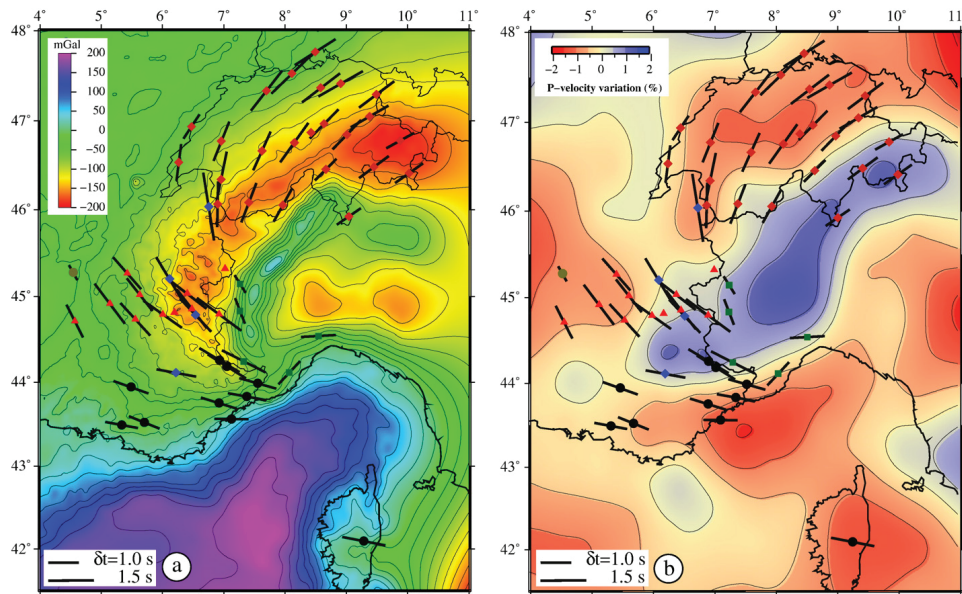


**Figure 1.14:** Map of average value of the SKS splitting parameters, superimposed on the Bouguer gravity anomaly (on the left), and P-wave velocity map (on the right). Orientation of the bars shows fast polarization azimuth with respect to north and the length corresponds to the splitting delay time (s). Anisotropy measurements and figures from *Barruol et al. (2011)*

The Western Alps are represented by an arc shape, which was suggested to be formed during the late Tertiary (e.g. *Schmid and Kissling, 2000*). By utilizing shear-wave splitting for this area of the Alps, *Barruol et al. (2011)* presented a coherent image of the upper mantle anisotropy. They used teleseismic events recorded at permanent seismic networks installed in the western and central Alps (Swiss permanent digital network, Regional seismic network of northern Italy, French RLB) together with the records of temporary experiments (Alpes, RosAlp, TRACK, and Geoscope stations SSB). Figure 1.14 shows the average values of splitting parameters, fast orientations and delay times (see Chapter 2 for details), which are superimposed on the tomographic image and Bouguer anomaly map. A good correlation between the trends of lithospheric root with the anisotropic



pattern can be seen. Their measurements showed a belt-parallel anisotropy pattern, which was attributed to the flow geometry in the upper mantle. Specially, a toroidal flow within the asthenosphere surrounding the slab keel was suggested to explain this chain-parallel anisotropy pattern.

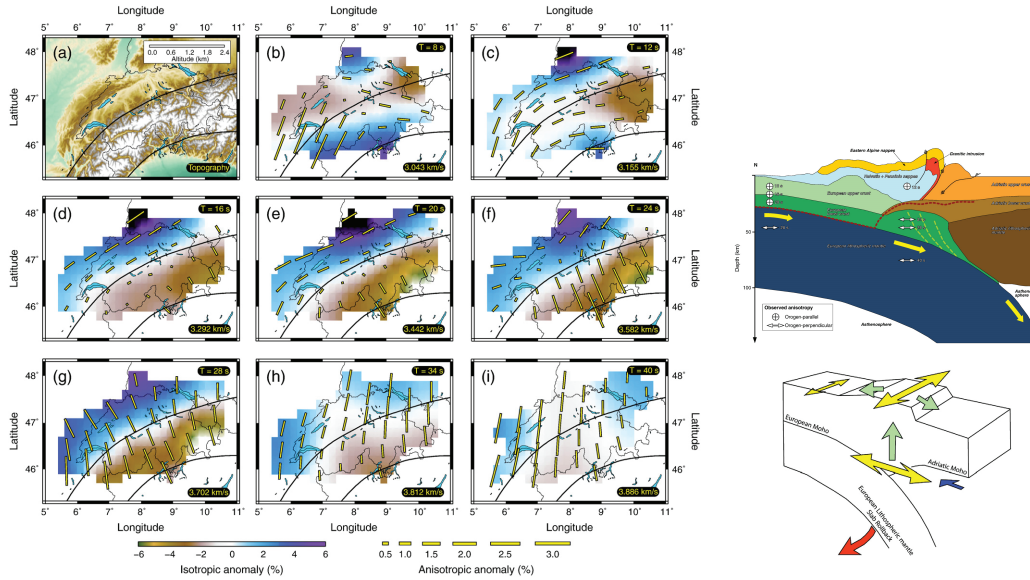


**Figure 1.15:** Left: panels show the isotropic velocity model (background), and anisotropic model (bars) for different depth level. Bars orientation represent the fast  $2\psi$  axis which are scaled according to the anisotropic magnitude. Study area is illustrated in the first panel. Right: schematic interpretation of the depth variation of the anisotropy obtained from the inversion (top), and the suggested tectonic model (bottom). Results and figure from *Fry et al.* (2010).

For a part of the western and central Alps, ambient noise analysis has presented an anisotropic image of the crust and lithosphere. Using noise data and inverting the dispersion curves of Rayleigh phase velocity, *Fry et al.* (2010) mapped anisotropy for different periods which refer to different depths (Fig. 1.15). The results of the inversion showed orogen-parallel anisotropy in the depth range of 20 to 30 km (in the crust), while between 30 to 70 km depth orogen-perpendicular anisotropy was obtained. The regional and vertical variations of the anisotropy were interpreted as a two-layer anisotropic model, illustrated in Figure 1.15. According to this model, origin of the belt-parallel anisotropy was referred to the LPO of crustal minerals, and LPO of olivine aggregates was suggested to be the origin of the belt-perpendicular anisotropy. Southward flow geometry and also bending of the European lithosphere was proposed as the cause of the belt-perpendicular anisotropy (*Fry et al.*, 2010).

In the central Alps, at about 12°E where the TRANSALP profile was located, shear-wave splitting method was applied to measure seismic anisotropy (*Kummerow and Kind*,

2006). TRANSALP seismic network was a N-S profile crossing the Alps which was operated between 1998 and 1999, and also for a month in 2002. Teleseismic records from this temporary network were used to measure SKS splitting parameters. Figure 1.16 shows the anisotropy results derived at stations along the TRANSALP profile. Most of the fast orientations show an azimuth between  $60^\circ$  to  $70^\circ$  with respect to the north parallel to the Alpine belt. According to the amount of delay time, *Kummerow and Kind* (2006) related the anisotropy to the upper mantle.

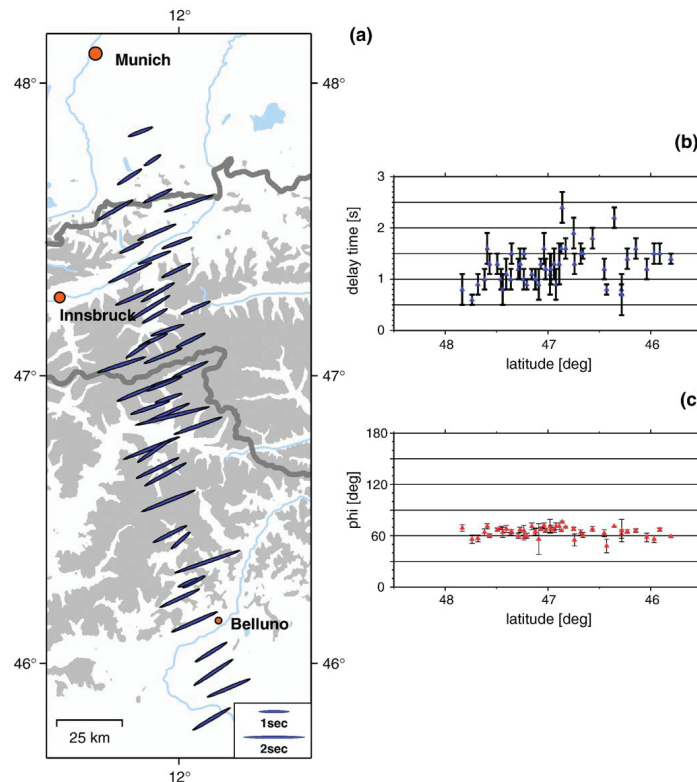


**Figure 1.16:** Left: SKS splitting parameters (fast axis and delay time) obtained by applying the multichannel analysis from the TRANSALP stations. Right: Variation of delay times (top) and fast axis azimuth (bottom) as function of latitude. Anisotropy measurements and figures from *Kummerow and Kind* (2006).

In the Pannonian basin, data from Carpathian Basin Project (CBP) have been used to measure the upper mantle anisotropy. *Stuart et al.* (2007) presented an image of upper mantle (lithospheric) anisotropy using these data by applying the shear-wave splitting method. Figure 1.17 summarizes previous anisotropy results for the Carpathian-Pannonian region which have mainly used shear-wave splitting (*Vinnik et al.*, 1994; *Plomerová et al.*, 2000; *Ivan et al.*, 2008) including the results from the CBP stations (*Stuart et al.*, 2007). The latter has been referred to upper mantle anisotropy, as a lithospheric origin (*Houseman and Stuart*, 2011). Fast anisotropic orientation from the

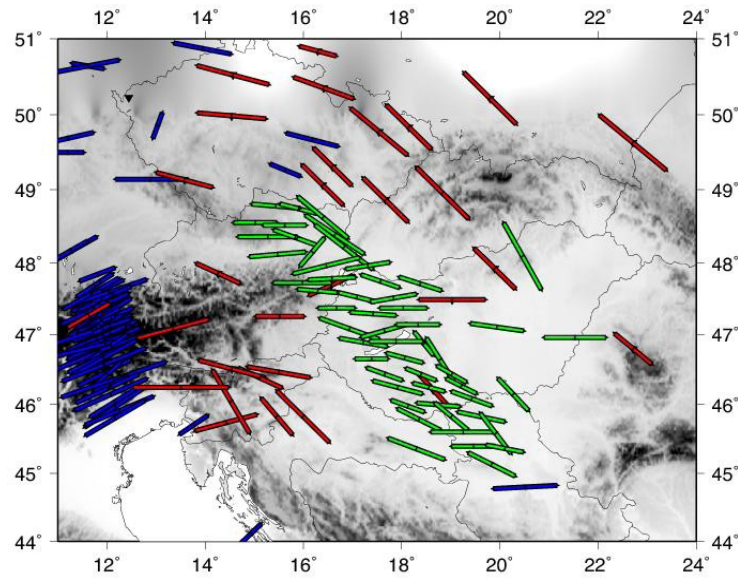


**Figure 1.17:** Results of SKS splitting measurement using the records of the CBP stations in the Pannonian basin illustrated by green lines (*Stuart et al.*, 2007). Red and blue lines are the results from *Vinnik et al.* (1994); *Plomerová et al.* (2000); *Ivan et al.* (2008). Figure from (*Houseman and Stuart*, 2011). See Chapter 6 for details.

CBP stations data has also been attributed to an asthenospheric flow mostly in line with the eastward extrusion of the Alcapa unit (*Kovács et al.*, 2012a). See Chapter 6 for discussion.

## 1.5 Outline of thesis

This thesis aims to investigate upper mantle anisotropy and deep deformation patterns beneath the Eastern Alps and the Pannonian basin by means of shear-wave splitting. It comprises four major themes, summarized as follows:

### Theme 1:

The first theme focuses on the overall anisotropy pattern under the whole Alpine chain (Chapter 3). Seismic anisotropy as indicator of the internal deformation in the mountain chain is measured using data from 12 permanent seismic stations in the Eastern Alps. Together with earlier observations from the western and central Alps, we present the clearest examples yet of mountain chain-parallel anisotropy, with a progressive rotation along the Alpine mountain chain. This section has been published as: G. Bokelmann, E. Qorbani, and I. Bianchi, 2013, *Seismic anisotropy and large-scale deformation of the Eastern Alps*, Earth and Planetary Science Letters, 383, 1-6.

### Theme 2:

We aim for characterization of the upper mantle anisotropy under the Eastern Alps (Chapter 4). We analyze teleseismic SK(K)S phases from over 10 years records of data in order to measure splitting parameters (fast orientation azimuth and splitting delay time). By focusing on the spatial variations of the splitting parameters, the backazimuthal changes of anisotropy are modeled in terms of multi layers of anisotropy. We present a new model of anisotropic structures that includes two layers of anisotropy. Comparison with the tomographic images and the LAB depths from receiver function analysis reveals that the deeper layer is attributed to a detached part of the European slab under the Eastern Alps. This section has been published as: E. Qorbani, I. Bianchi, and G. Bokelmann, 2015, *Slab Detachment under the Eastern Alps seen by seismic anisotropy*, Earth and Planetary Science Letters, 409, 96-108.

### Theme 3:

The Tauern Window is located in the western part of the Eastern Alps and exposes exhumed parts of Europe-derived crust. In Chapter 5 we present the results of a collaborative study with geologists on coupling between crust and upper mantle in the Tauern Window area. Measurements of upper mantle anisotropy (deformation signatures) are compared with the kinematic data as indicators of crustal deformation. We suggest a vertical coherence of deformation between crust and upper mantle which indicates the lithospheric-scale extension of the Adriatic indenter on the European lithosphere. This

section has been published as: E. Qorbani, W. Kurz, I. Bianchi, and G. Bokelmann, 2015, *Correlated Crustal and Mantle Deformation in the Tauern Window*, Eastern Alps, Austrian Journal of Earth Science, 108/1, 161-173.

**Theme 4:**

We present a study of deformation patterns beneath the Pannonian Basin and surrounding areas in eastern central Europe (Chapter 6). The Pannonian basin is an integral part of the Alpine, Carpathians and Dinarides orogen. In collaboration with petrologists we analyze the seismic records of 59 temporary and permanent seismic stations to measure shear-wave (SKS) splitting parameters. Together with petrological indicators of deformation in basalt-hosted upper mantle xenolith we use the seismic measurements to characterize the anisotropy. We show an asthenospheric-related transpressional deformation pattern under the Pannonian basin. We discuss the most plausible origin of this deformation within the asthenosphere with respect to several tectonic models which have been suggested for the extension and the evolution of the Pannonian basin. Results of this section have been submitted to Journal of Geophysical Research as: E. Qorbani, G. Bokelmann, I. Kovacs, F. Horvath, and G. Falus, 2015, *Deep Deformation Pattern for the Carpathian-Pannonian region*.

# Chapter 2

## Methodology

### 2.1 Seismic anisotropy

Directional dependence of physical properties is defined as anisotropy. In an anisotropic medium, seismic velocity varies as a function of seismic wave propagation direction. Seismic anisotropy has been observed in many regions of the Earth including the crust, the upper and the lowermost mantle, and the inner core (*Long and Becker, 2010*). It can be the consequence of fractures and cracks in the vicinity of active faults (in the upper crust) and mineral preferred orientation of rocks, mainly observed in the lower crust and the upper mantle (*Mainprice et al., 2000*, and reference therein).

One of the most important sources of anisotropy in the Earth is the upper mantle. The cause of this anisotropy is lattice preferred orientation (LPO), generated by the structural alignment of olivine crystals, which constitute the upper most part of the mantle. Experiments on plastic deformation of olivine minerals have shown that different physical and chemical conditions result in different lattice preferred orientation. They have thus been categorized into distinctive types of olivine fabrics based on their slip system (e.g. *Karato, 1995; Jung et al., 2006*). The slip system is defined by slip direction (Burgers vector) and slip plane (defined by its normal vector) during the deformation experiment. In A-type fabrics the fast axis of individual crystals is aligned along the direction of shear (*Karato et al., 2008*). In case of a horizontal flow geometry, shear is thought to be aligned with the flow direction in the upper mantle (*Savage, 1999*).



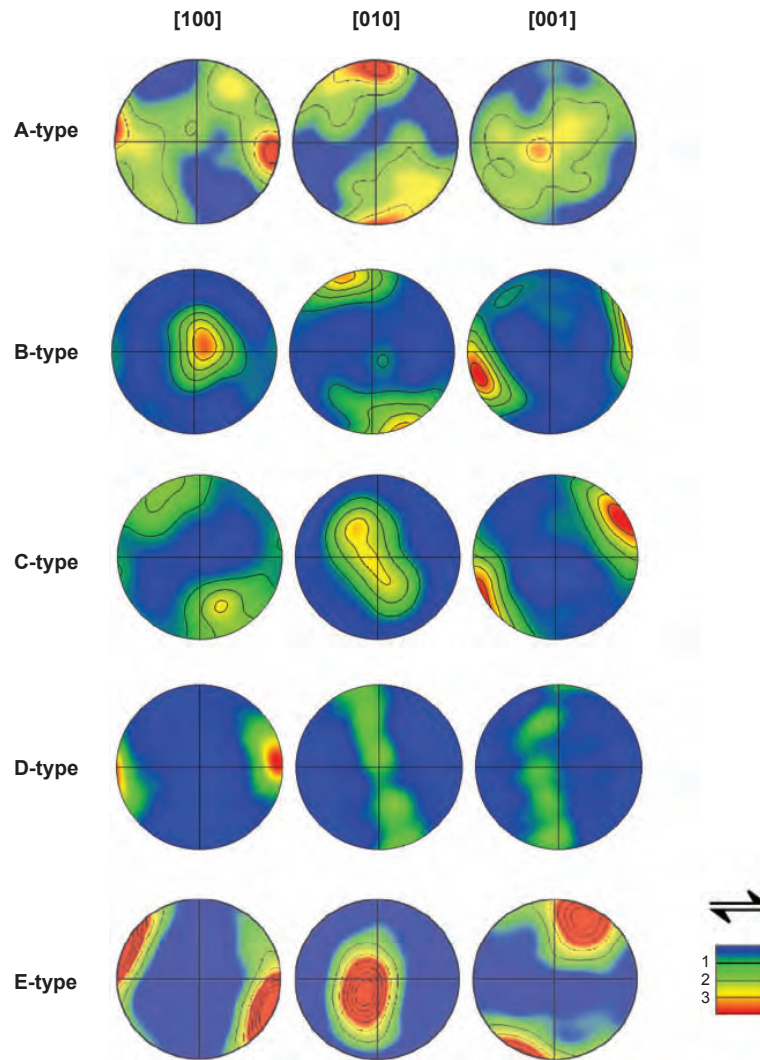


**Figure 2.1:** Pole figures for different type of olivine LPOs found in the simple shear deformation experiments. Arrows show the shear direction and distribution of crystal orientation (density of data points) are given by color. Figure from *Karato et al. (2008)* modified after *Jung et al. (2006)*.

The A-type fabric is likely distributed everywhere in the lithospheric mantle and also within the asthenosphere, except for some regions with specific temperature and pressure conditions. In such cases, the fabric can also be developed as C-, E-, and D-type (Fig. 2.1). In these types of fabric, the fast axis is also parallel to the flow orientation, although they differ in the  $V_{sh}/V_{sv}$  ratio. For B-type fabric the fast axis is normal to the flow direction under horizontal flow geometry. However, this type of fabric only develops under very special conditions: high stresses, low temperatures and most importantly some amount of water (*Karato et al., 2008*). The B-type fabric can explain the trench-parallel seismic anisotropy in the subduction wedge which has been observed



near the trench of Tohoku, Japan (*Nakajima and Hasegawa, 2004*).

Apart from experimental results of olivine LPO (Fig. 2.1), anisotropy can also be inferred from naturally deformed rock samples. Experimental analyses of these samples yield additional information about the spatial distribution of different type of olivine fabrics, particularly, when they are interpreted jointly with seismic anisotropy data. Figure 2.2 shows sketches representing the distribution of olivine fabrics in the upper mantle predicted from laboratory studies, seismological observations and analysis of rock samples.

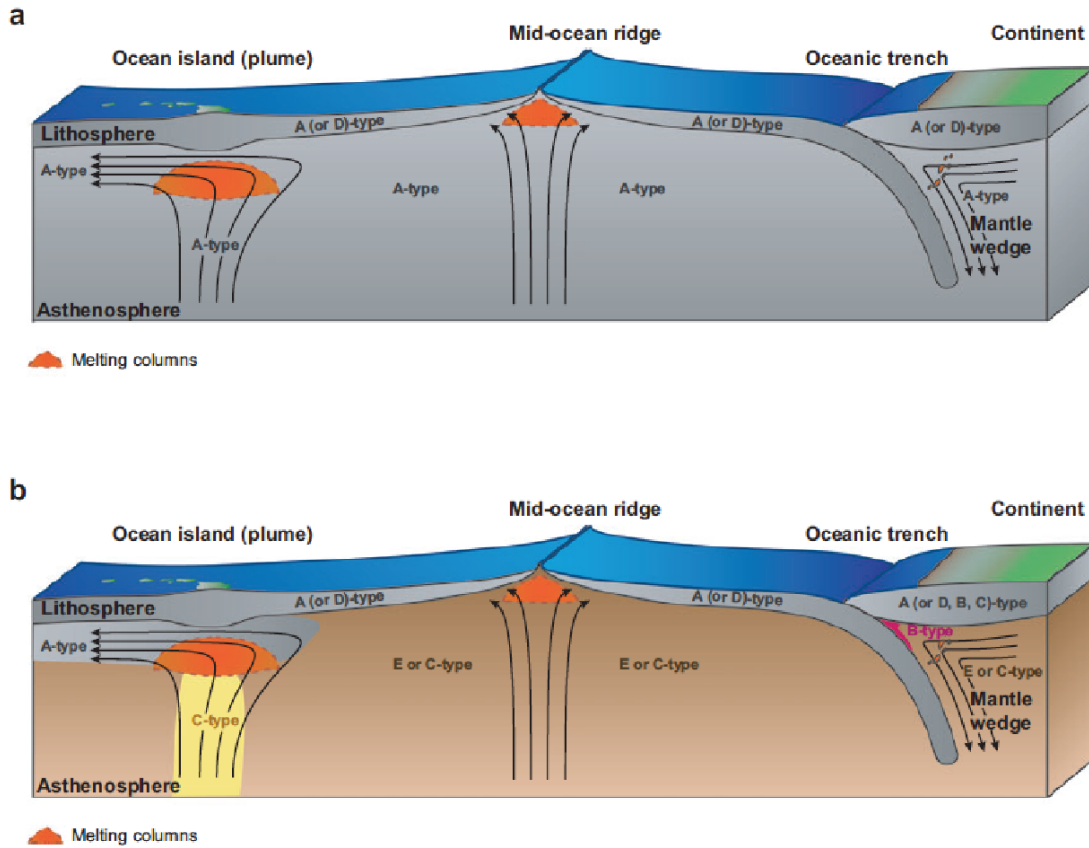


**Figure 2.2:** Schematic diagrams showing the likely distribution of different olivine fabrics. a) Shows the conventional model in which A-type fabric is assumed to be observed everywhere. b) New model of olivine LPOs developed by *Karato et al. (2008)* and reference therein in which the other (new) type of olivine fabric (e.g. B-type) are proposed. Figure from *Karato et al. (2008)*

## 2.2 Methods of measuring anisotropy

The most direct constraints available on anisotropy within the Earth are seismic observations (*Long and Becker, 2010*). These observations can be explained as a function of strain field, and can be translated into signatures of geodynamic processes in the mantle.

In case of upper mantle materials, they provide important clues about the mantle flow pattern and also past deformation within the lithospheric mantle.

Since 1964 when seismic anisotropy was observed in oceanic mantle from Pn-waves (*Hess*, 1964), several methods have been introduced and developed to measure the anisotropic properties of the Earth's interior. They are mainly categorized into body waves (P and S) and surface waves-based methods. *Hess* (1964) used the azimuthal variation of Pn (body wave) velocities of incoming waves to measure anisotropy, in particular to derive the coefficients of the stiffness tensor (relating stress and strain and describing the elastic properties of the medium, see *Davis* (2003) for details). Polarization of long period P-waves is another observation to analyze the upper mantle anisotropy. Polarization or particle motion of the P-wave in an isotropic medium is in line with the ray propagation direction. However, when waves pass through anisotropic structures, the particle motion would show deviation from the wave propagation direction, which among other reasons, can be related to the effect of anisotropy (e.g. *Bokelmann*, 1995; *Fontaine et al.*, 2009).

Anisotropy can also be observed with surface waves, Love and Rayleigh (e.g. *Gaherty*, 2004). Velocity of surface wave varies with wavelength, which is called dispersion curve. Observation of the discrepancy of the dispersion curves of the surface wave can be attributed to anisotropy (both azimuthal and radial). Anisotropy then is inferred by inverting the Rayleigh and Love discrepancy by finding the best fitting anisotropic coefficients which is applied to a reference velocity model (e.g. *Gaherty*, 2004; *Wüstefeld et al.*, 2009).

## 2.3 Shear-wave splitting

Seismometers record seismic energy (as displacement) in a reference geographic coordinate system (N, E, Z) in which displacement of shear-wave have three components ( $u_n, u_e, u_z$ ). These three components in the north-south, east-west, and vertical are often rotated into a reference system based on the ray propagation direction, RTZ. R direction (radial component) is a horizontal projection of the ray propagation direction, T (transverse component) is normal to the R in the horizontal plane, and Z is the vertical component positive to up.

If we rotate the three geographical components (N, E, Z) onto an orthogonal ray system (L, Q, T), the displacement of the shear-wave have only two orthogonal components, namely SV and SH. In this system, L component is along the ray path from earthquake

to receiver, Q component (radial) is perpendicular to L in the ray plane, and T component (transverse) is normal to the radial component and completes the orthogonal system.

The two polarizations of shear-wave (SH and SV) travel at the same speed in isotropic media. However, in anisotropic media shear-wave split and the SH and SV propagate with different velocity in, thus, they arrive at seismic station at different times. The first arrival defines fast polarization, while the slower one represents the plane of slow polarization. This phenomenon caused by anisotropic structures is referred to as shear-wave splitting or birefringence. Shear wave splitting is the most common way for constraining anisotropy in a variety of applications and scales, from very shallow structures (i.e. sedimentary rocks) to the mantle depths (Fig. 2.3).

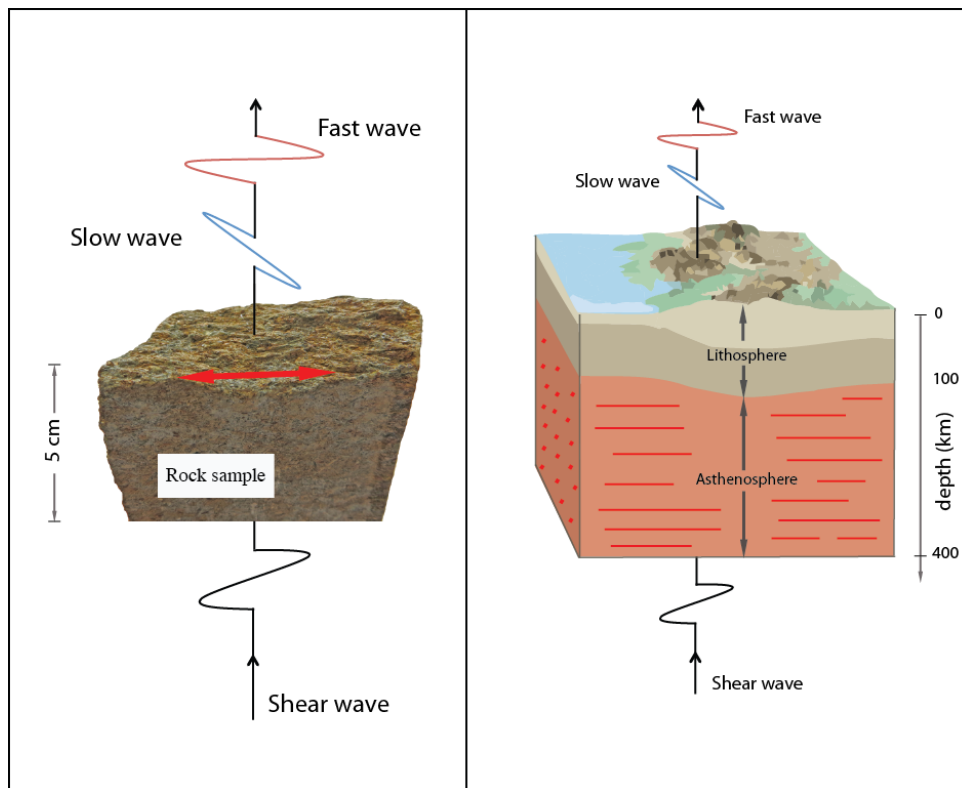


**Figure 2.3:** Left) Rock sample showing mineral alignment (indicated by the red arrow). This alignment would split an incident elastic shear-wave into two waves, with the faster one (in red) polarized parallel to the alignment and slow phase (in blue) which is polarized normal to the fast phase. Right) At mantle scale, similar splitting is observed. It shows the mineral alignment within the Earth's upper mantle.

The most suitable seismic phases to investigate anisotropy at scale length of the upper mantle are core SKS and SKKS phases. No shear energy can pass through the fluid outer core and therefore shear-waves passing from the mantle into the outer core are converted to P-waves and are converted back to shear-waves (called SKS) when entering again into the lower mantle. For this reason, during the conversion of the

inner core P-wave into an S-wave at the core-mantle-boundary (CMB), the resulting SKS wave would not have shear component therefore it is entirely polarized in the radial (ray propagation) direction. Figure 2.4 shows the ray path of the core SKS and SKKS shear-waves through the mantle and outer core. Theoretically SK(K)S does not contain any energy on the transverse component and the amplitudes (energy) of this component should be zero on any seismogram readings. However, the anisotropy of the mantle affects on the polarization of the SKS and we often observe a significant portion of energy on both radial and transverse components. This effect, which we observe as splitting of the shear-wave, is used to infer the anisotropy of the mantle. Two splitting parameters are defined; the fast polarization azimuth ( $\phi$ ), which is the angle between fast axis and radial direction, and arrival delay time ( $\delta t$ ) between the fast and slow polarizations.

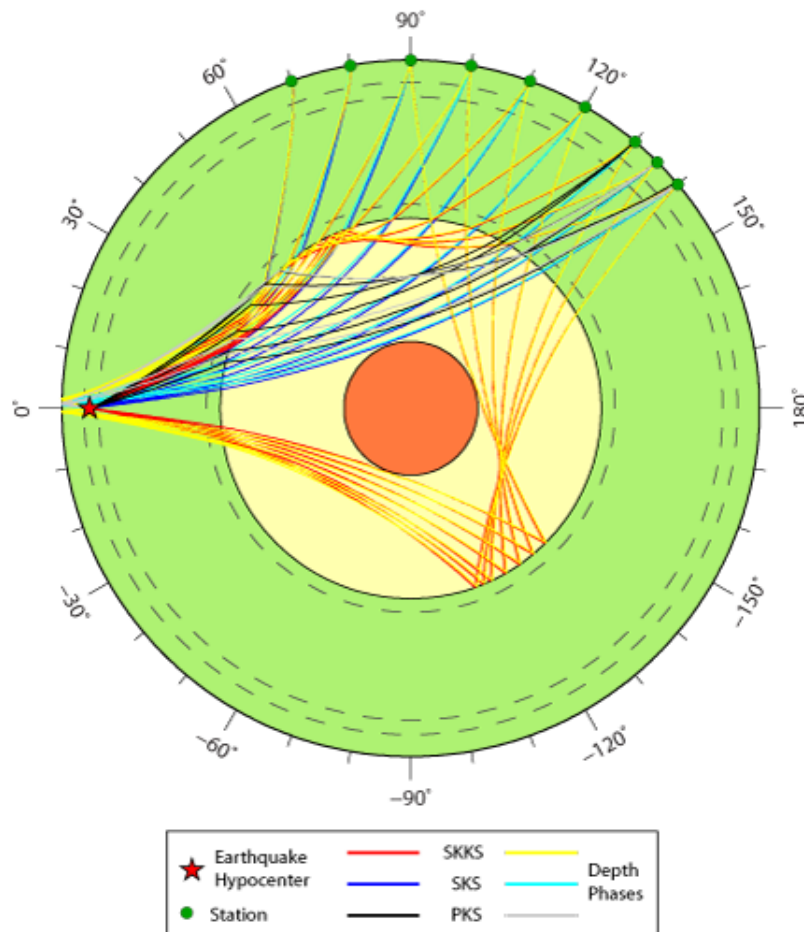


**Figure 2.4:** Ray paths of the core shear-wave phases SKS and SKKS. They enter into the outer core as converted P-waves and convert back to shear-wave upon exit. At the core-mantle boundary they are polarized only on the radial component. Figure from [www.seismology.harvard.edu](http://www.seismology.harvard.edu).

A variety of techniques exist to measure and constrain anisotropy using the splitting of

shear waves such as the multichannel method, cross correlation, eigenvalue technique, and minimization of energy method. They all utilize shear-waves to characterize the upper mantle anisotropy and have similar measuring procedures (*Long and Silver, 2009*). For instance, all techniques assume a single layer of anisotropy in which the symmetry axis is horizontal. All techniques also rely on the assumption that SKS is radially polarized for an isotropic medium. Since we observed energy both radially and transversely, we try to correct the effect of anisotropy and refer the correction parameters to the anisotropic parameters. In the following the three methods, which are used in this thesis (generally known as single event-based techniques), are briefly explained.

### 2.3.1 Transverse component minimization technique

Transverse component minimization technique (SC) was proposed by Silver and Chan (1991). This technique applies a grid search approach over the splitting parameters, attempting to remove the effect of anisotropy that has caused the delay time between fast and slow polarization. This is done by time shifting applied to the radial and transverse components in order to fit these components best. Through rotation of the components, this technique seeks best fitting for minimum amount of energy (amplitude) on the T component to infer anisotropy. Minimizing the amplitude on the transverse component leads to linearize the particle motion on the direction of the wave propagation (radial). The optimum angle of rotation identifies the fast polarization azimuth (e.g. *Wüstefeld et al., 2008; Long and Silver, 2009*).

The grid search is performed over all possible values of fast axis between 0-180° as we infer the fast polarization orientation, which can be in both directions for a given azimuth (e.g. 45°N and 225°N). The possible values for delay time are 0 to 4, s which is based on the maximum reasonable splitting delay time (*Long and Silver, 2009*). The SC technique can be applied on either the R (radial) and T (transverse) in RTZ reference system, or on the Q and T components in the LQT system (*Wüstefeld et al., 2008*).

### 2.3.2 Eigenvalue technique

The eigenvalue method (EV), also discussed first by *Silver and Chan (1991)*, is similar to the transverse minimization technique. This technique is based on particle motion in which the radially polarized shear-wave would result in a linear horizontal particle

motion. Searching for the most linear particle motion yields the best-fit splitting parameters. In particular, this is performed by minimizing the second eigenvalue of the covariance matrix of the horizontal particle motion, since the eigenvalues of this matrix are quantitative tool for measuring the linearity of the particle motion (*Long and van der Hilst*, 2005). This technique may be used more often in the cases that the initial polarization of the SKS phases is not known (e.g. *Savage*, 1999).

### 2.3.3 Cross-correlation technique

The cross-correlation technique (RC) was suggested by *Fukao* (1984) and *Bowman and Ando* (1987). In this method, the radial and transvers components are rotated and time shifted in order to seek for the best fitting rotation angle and time shift to gain the maximum correlation between these components. The optimum rotation angle and time shift are attributed to the fast axis of polarization and splitting delay time respectively. A grid search approach is also utilized to find the splitting parameters ( $\phi$  and  $\delta t$ ), which fit the data best (*Long and Silver*, 2009).

In all these techniques the general measurement procedure is the same. It includes rotating the 3-components seismograms into the LQT or RTZ system, filtering data to gain higher signal-to-noise ratio, selecting the proper time window according to the wavelength of the phase (e.g. 30 s time window based on the 10 s SKS wavelength), performing the grid search approach, correcting the effect of anisotropy on the radial and transverse components, and error estimation (*Wüstefeld et al.*, 2008; *Long and Silver*, 2009).

In this thesis, to measure the splitting parameters of the upper mantle anisotropy we applied the cross-correlation (RC), eigenvalue (EV), and transverse minimization (SC) techniques using the SplitLab package (*Wüstefeld et al.*, 2008). SplitLab is a MATLAB-based graphical user interface to measure the shear-wave splitting and allows utilizing RC, EV, and SC simultaneously. Applying all three techniques at the same time improves the quality of the measurements by comparing the results of different techniques. To qualify the results as "good", "fair", and "poor", several factors have been suggested (*Barruol et al.*, 1997; *Wüstefeld and Bokelmann*, 2007); They include the similarity of results from different techniques (e.g. fast azimuth deviation should be less than 8-10°), high signal-to-noise ratio, the ellipticity of the particle motion before rotating and time shifting (correction), and its the linearity after correction, and determining the confidence area region for the best fitting splitting parameters, which is corresponding

to  $2\sigma$  (Wüstefeld *et al.*, 2008). Figure 2.5 shows example of measuring the splitting parameters using the SplitLab package.

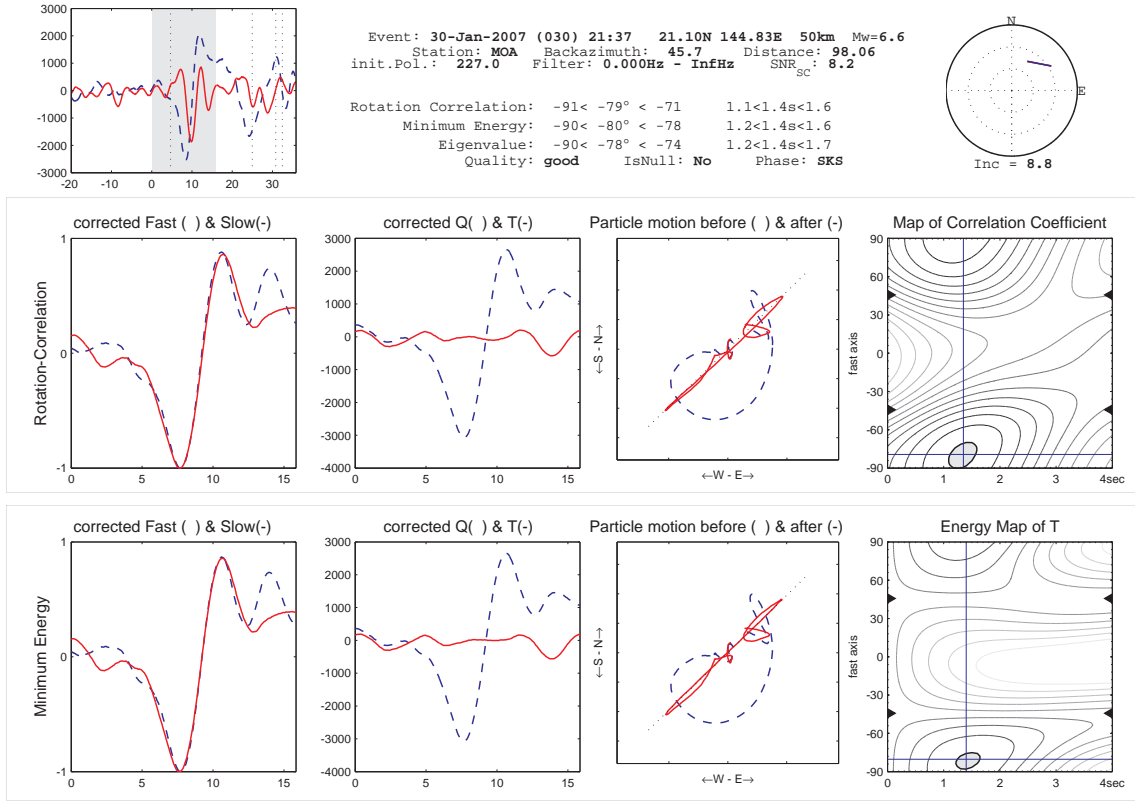


**Figure 2.5:** Example of shear wave splitting measurements using the SplitLab package (Wüstefeld *et al.*, 2008). Three techniques, cross-correlation, eigenvalue, and transverse minimization are utilized simultaneously. Top left panel shows the radial and transverse components (Q, and T) without amplitude scaling. The selected time window around the SKS phase is highlighted. The next two rows represent the outputs of cross-correlation and transverse minimization techniques respectively. First panel (from left) at each row shows the time shifted (Q and T) components to obtain the best-fitting splitting delay time. Second panel displays rotated components in order to find the azimuth (fast polarization) which best removes the amplitude on the transverse component. Third panel shows particle motion on the horizontal plane before and after correction. The contour plot presenting the confidence region of the best-fitting splitting parameters is shown in the fourth panel. Listed at the top are parameters of the teleseismic event used in this measurement, applied filter, signal-to-noise ratio, and also the results of the different techniques. Data from Qorbani *et al.* (2015a).





# Chapter 3

## Large scale anisotropy under the Alpine chain

This section has been published as: G. Bokelmann, E. Qorbani<sup>1</sup>, and I. Bianchi, 2013, *Seismic Anisotropy and Large-Scale Deformation of the Eastern Alps*, Earth and Planetary Science Letters, 383, 1-6.

### Abstract

Mountains chains at the Earth's surface result from deformation processes within the Earth. Such deformation processes can be observed by seismic anisotropy, via the preferred alignment of elastically anisotropic minerals. The Alps show complex deformation at the Earth's surface. In contrast, we show here that observations of seismic anisotropy suggest a relatively simple pattern of internal deformation. Together with earlier observations from the Western Alps, the SKS shear-wave splitting observations presented here show one of the clearest examples yet of mountain-chain parallel fast orientations worldwide, with a simple pattern nearly parallel to the trend of the mountain chain. In the Eastern Alps, the fast orientations do not connect with neighboring mountain chains, neither the present-day Carpathians, nor the present-day Dinarides. In that region, the lithosphere is thin and the observed anisotropy thus resides within the asthenosphere. The deformation is consistent with the eastward extrusion toward the Pannonian basin that was previously suggested based on seismicity and surface geology.

---

<sup>1</sup> Author contribution: E. Qorbani performed the measurements, analysed the data, and prepared figures and tables. The manuscript was written by G. Bokelmann (70%), and E. Qorbani (30%).

### 3.1 Introduction

Surface geology and tectonic evolution of the Alps appear rather complex (*Schmid et al.*, 2004), and it may be enlightening to study mantle structure in the region. Several geophysical studies have been performed, and they have produced 3D tomographic models (*Gebrande et al.*, 2002; *Piromallo and Morelli*, 2003; *Lippitsch et al.*, 2003; *Brückl et al.*, 2010; *Dando et al.*, 2011; *Mitterbauer et al.*, 2011; *Legendre et al.*, 2012). Tomographic images show velocity anomalies that can be interpreted in the context of suture zones and the major subduction events. The above-cited studies did not fully clarify the dynamics of the collision however, since they apparently allow opposing views on the structure and evolution of the Eastern Alpine region. More specifically, two recent studies using P-wave velocity tomography for the Eastern Alps come to different conclusions. *Lippitsch et al.* (2003) interpreted the high velocity anomaly in the Western Alps as dipping southeastward European lower lithosphere beneath the Adriatic microplate while the anomaly in the Eastern Alps is interpreted to represent Adriatic lower lithosphere dipping northeastward beneath the European plate. On the other hand, the more recent ALPASS tomographic model, proposed by *Mitterbauer et al.* (2011), does not suggest a change of subduction polarity between the Western and Eastern Alps.

At the eastern end of the mountain chain, the Alps have been connected in the geological past with the Carpathians and the Dinarides. Nowadays, the Eastern Alps (*Gutdeutsch and Aric*, 1987; *Ratschbacher et al.*, 1991; *Brückl et al.*, 2010) may be extruding towards the Pannonian basin. Further investigation is needed to provide more reliable evidence, and to study the vertical extent of the eastward extrusion. Many parts of the Eastern Alps have never been studied with respect to seismic anisotropy and deep deformation, due to the sparse coverage of seismic stations in the area.

In this study, we investigate upper mantle anisotropy beneath the Eastern Alps by measuring the splitting of teleseismic SKS/SKKS phases for the Alpine region. These shear waves record large-scale anisotropy produced by lattice-preferred orientations (LPO) of rock-forming minerals and particularly of olivine that represents the major upper mantle volume. The LPO of olivine grains develops in response to tectonic strain (*Mainprice et al.*, 2000; *Nicolas and Christensen*, 1987; *Savage*, 1999; *Silver and Chan*, 1991). We present here our first results from permanent seismic stations in the Eastern Alpine region (their location and network are listed in Table 3.1) and discuss them in conjunction with earlier measurements from the Western Alps (*Barruol et al.*, 2011) and from the central Alps along the TRANSALP profile (*Kummerow and Kind*, 2006).

## 3.2 Data and method

In this study we focus on large-scale anisotropy in the upper mantle under the Alps, through the splitting of teleseismic SKS/SKKS wave phases. To characterize the nature of anisotropic structures using the shear wave splitting method, two splitting parameters are defined as the fast orientation azimuth ( $\phi$ , angle between fast axis and radial direction) and arrival delay time between the fast and slow polarizations ( $\delta t$ ). We used the transverse energy minimization technique (SC) (Silver and Chan, 1991) to recover the splitting parameters. In this technique a grid search approach was performed over all possible values of  $\phi$  and  $\delta t$  by rotating the components and correcting the delay time. Thus, the minimum amplitude of the transverse component is achieved corresponding to the best fitting value of splitting parameters. In most cases we applied no filter to include the entire frequency range. To carry out the measurements of anisotropic parameters based on SC techniques, the SplitLab package (Wüstefeld *et al.*, 2008) was used. Figure 3.1 shows an example of splitting measurements by SplitLab for two stations, DAVA and SOKA after the application of the SC technique.

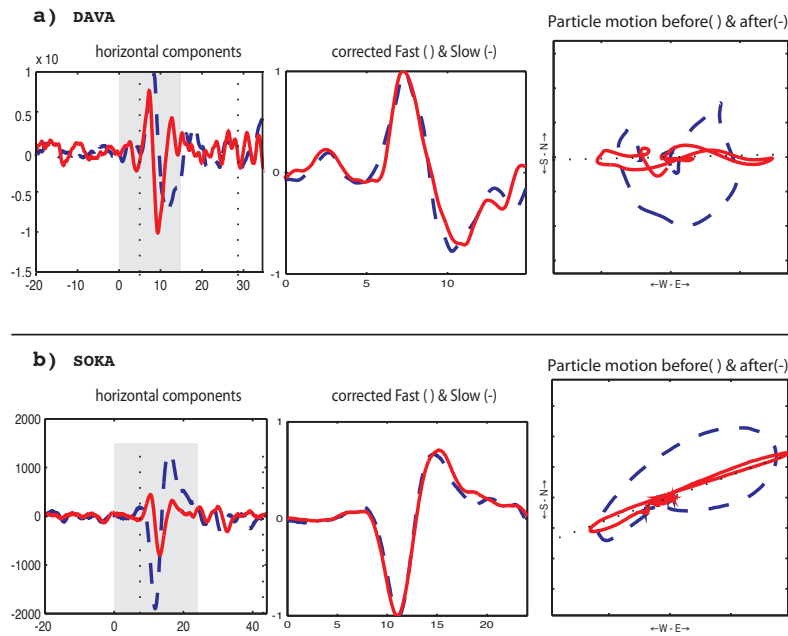


**Figure 3.1:** Two examples of SKS splitting measurements obtained by using the minimum energy (SC) technique at stations (a) DAVA and (b) SOKA from the Eastern Alps. For each event–station pair, the left panel shows the horizontal (radial – dashed, transverse – solid) components, in the middle panel fast and time-matched slow (solid and dashed) components of the SKS wave, and the right panel the horizontal particle motion before (dashed) and after (continuous) anisotropy correction.

The data set comprised the teleseismic events in the epicentral distance range  $90^\circ$  to  $130^\circ$  and magnitudes greater than 6  $M_w$ , recorded by the Austrian broadband seismological network (OE) between 2002 and 2011. The OE network includes 12 permanent stations (see Table 3.1) with three-component broadband STS-2 sensors. We inspected teleseismic events at the stations on average 197 per station. Altogether 2371 SKS/SKKS phases have been investigated for all stations; out of this number of events, we measured the individual splitting parameters for 418 SKS/SKKS phases and obtained between 12 and 76 clear split phases per station. All results were classified as “good”, “fair”, and “poor” quality (*Barruol et al.*, 1997; *Wüstefeld and Bokelmann*, 2007). That way, at least 9 good quality measurements were achieved for most stations, ABTA, ARSA, CONA, DAVA, MOA, MYKA, OBKA, RETA and SOKA (except for FETA with 5, and KBA with 6). A circular mean was calculated only over the good quality fast axis azimuths to obtain an average value of splitting parameters for each station.

### 3.3 Results and discussion

Mean values of the measured splitting parameters are summarized in Figure 3.2. Vectors present the orientations of fast azimuths where their length corresponds to the mean value of delay times ( $\delta t$ ) for each station. Table 3.1 provides the mean values of measured fast axis azimuth, together with 95% confidence intervals (CI). This value is less than  $\pm 8^\circ$  for 8 stations, smaller than  $\pm 12^\circ$  for ABTA and ARSA, and  $\pm 16^\circ$  and  $\pm 33^\circ$  for KBA and FETA, respectively. Since the measured fast orientations for each station show tightly grouped distribution, we will discuss only the calculated mean values of fast azimuth in the following, instead of the individual measurements. Measured splitting delay times ( $\delta t$ ) (*Silver and Chan*, 1991) scatter considerably, with mean values between 0.76 and 1.55 seconds (Table 3.1). These values are generally in line with earlier measurements (*Barruol et al.*, 2011), and would be interpreted as a layer thickness on the order of 85 to 170 kilometers, assuming a velocity difference of 4% between the two shear-wave phases. The larger splitting values would be difficult to accommodate all within the lithosphere. *Kovács et al.* (2012a) have also found values around 4% from mantle xenoliths from the nearby Pannonian basin, with some samples giving 6.4%. The latter samples pertain to the lower part of the lithosphere only. An asthenospheric contribution is apparently required for explaining the anisotropy. This is especially the case for the easternmost stations.

**Table 3.1:** Station location and mean splitting parameters, as calculated by transverse energy minimization technique (SC, *Silver and Chan*, 1991). The value of errors (95% confidence interval) for the measured mean value of splitting parameters is also listed for each station, together with the number of split events (S-e) and good quality measurement (G-m)

Station	Lon(°E)	Lat(°N)	$\phi(^{\circ})$	$\phi$ -error	$\delta t$ (s)	$\delta t$ -error	S-e	G-m
ABTA	12.5123	46.7474	85	12	1.26	0.28	17	9
ARSA	15.5230	47.2505	116	12	1.30	0.21	63	11
CONA	15.8618	47.9282	124	8	1.00	0.19	33	11
DAVA	9.8803	47.2867	56	5	1.35	0.11	36	20
FETA	10.7291	47.0211	63	33	0.76	0.12	12	5
KBA	13.3447	47.0784	107	16	0.98	0.29	14	6
MOA	14.2659	47.8495	109	5	1.08	0.13	55	32
MYKA	13.6416	46.6299	104	5	1.37	0.22	37	23
OBKA	14.5489	46.5092	119	4	1.47	0.13	76	40
RETA	10.7623	47.4871	50	6	0.82	0.10	19	13
SOKA	15.0327	46.6780	124	6	1.14	0.17	22	16
WTTA	11.6363	47.2638	68	8	1.55	0.27	28	11

Measured fast orientations fall into two groups: Stations in the West show SW-NE fast orientations, and stations in the East NW-SE. In between, station ABTA has an intermediate fast orientation azimuth of N85°, nearly E-W. Stations in the western part of this study closely agree with results from Switzerland (*Barruol et al.*, 2011). In the center, the North-South TRANSALP profile (*Kummerow and Kind*, 2006) at longitude  $\sim 12^{\circ}\text{E}$ , has provided fast orientations of  $60^{\circ}$ - $70^{\circ}\text{N}$ , very similar to station WTTA, as well as Western Austria and Switzerland. On the other hand, stations in the easternmost part of the Alps show fast orientations that are rather different, NW-SE, yet they again show a very good spatial consistency among that group. *Barruol et al.* (2011) had found fast axes azimuths that rotate along with the Alpine Arc in the Western Alps. This has raised much interest in how anisotropic fast axes would be oriented in the rest of the Alps. Figure 3.2 shows that the pattern continues, but in Central Austria there is an abrupt change, and fast orientations jump to a NW-SE pattern.

To study this in more detail, we have projected the stations from Figure 3.2 onto the centerline of the Alps that we have determined by connecting the centers of gravity of the mountain chain (assuming constant density in the Alps for simplicity). This projection allows inspecting fast orientation as a function of distance along the Alps, from the Southwest to the Northeast (Figure 3.3). We note that, within the progressive rotation along the Alps, there are two zones in the Alps where fast orientations remain constant. These are **a)** Central Switzerland to about Innsbruck (between points 1 and 2



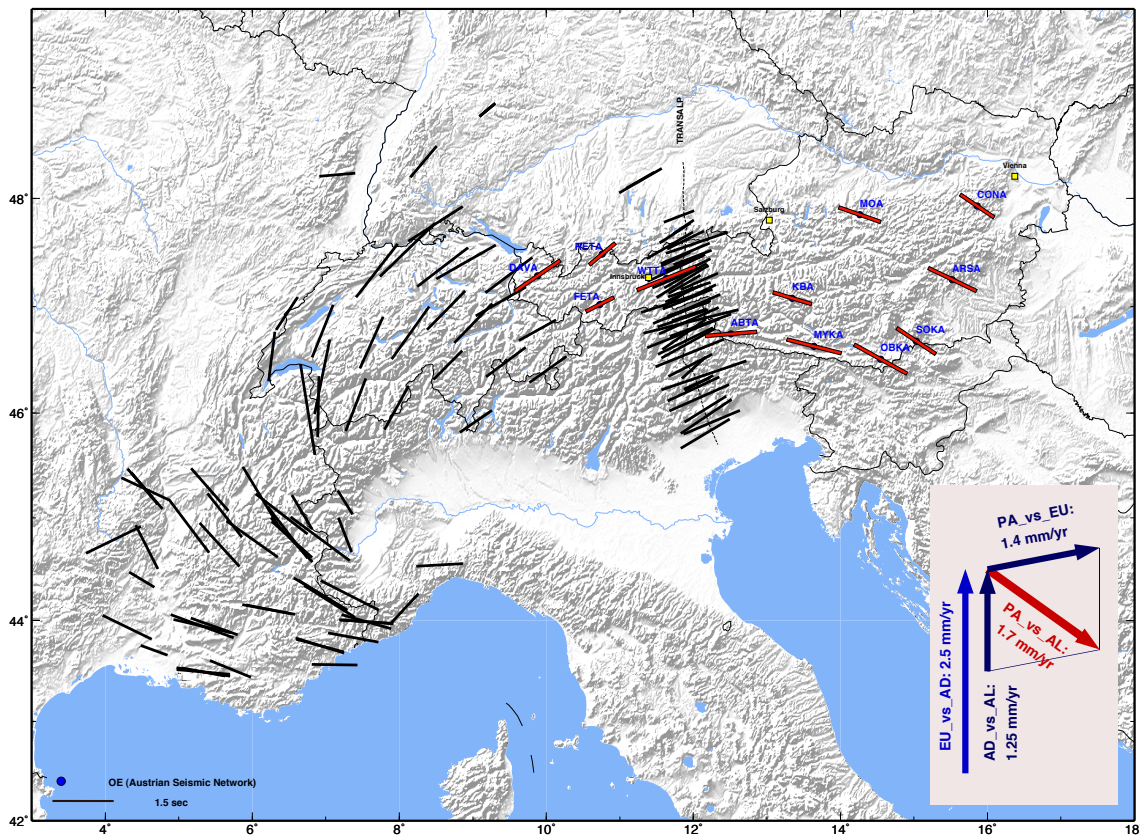


**Figure 3.2:** Shear wave splitting results for stations in the Alps. New results from 12 permanent stations in the Eastern Alps are shown with red bars. Black bars for results from previous studies (*Barruol et al.*, 2011; *Kummerow and Kind*, 2006). The bars show fast orientation ( $\phi$ ) and delay time ( $\delta t$ ), is scaled by length. Note the changing fast axes orientations along the Alps. The insert shows the construction of the relative motion of the Eastern Alps (red arrow) relative to the deeper part of the Alps, from the convergence of the Adriatic plate toward stable Europe, and the extrusion of the Eastern Alps, to explain the fast orientations in the Easternmost Alps (see text).

in Figure 3.3), and **b**) to the East of Salzburg (point 3). No significant spatial change of fast orientation is detected within these two zones. All of the progressive change along the Alps occurs in the Western Alps and at longitudes between Innsbruck and Salzburg. The latter zone agrees well with the Tauern Window in which exhumed deep structural units are exposed. The pattern of fast orientation in these two zones appears to be similar, as far as one can tell with the stations available at the moment. On the other hand, splitting delays do not show clear spatial variations.

The effect of the Alpine orogenic events is manifest in the clear rotation of seismic anisotropy along the Alps, similar to that of the mountain chain. Such mountain chain-parallel fast orientations have been found beneath many other mountain ranges, e.g., the Hercynian (*Bormann et al.*, 1993), Apennines, the Pyrenees, the Himalaya/Tibet (*Lave*



*et al.*, 1996), the Appalachians (*Barruol et al.*, 1997), the Carpathian arc (*Ivan et al.*, 2008), and the Western Alps (*Barruol et al.*, 2011). Except for Tibet, the pattern for the Alps is the clearest example of this phenomenon. Since all of these mountains chains have been associated with subduction, it is interesting to compare this trend in seismic anisotropy with active subduction zones. Several of those show similar behaviour, with fast axes parallel to the trench, e.g., the Calabrian arc (*Baccheschi et al.*, 2007), and the Gibraltar arc (*Buontempo et al.*, 2008; *Diaz et al.*, 2010), but not all; some show different splitting characteristics, usually with trench-parallel orientations close to the trench, but trench-normal toward the back-arc. *Fry et al.* (2010) show orogen-parallel fast orientations for the crust in Switzerland, from ambient noise, while the depth region just below the Moho may be characterized by orogen-normal orientations. The latter may possibly be a thin layer, thinner than resolvable in SKS shear-wave splitting observations. Surface waves (e.g., *Marone et al.*, 2004) suggest layering for the wider region around the Alps with Love waves requiring higher shear velocities than Rayleigh waves. One key suggested recently for explaining the spatial variation of splitting behaviour within the wedge was the effect of water that might cause different slip systems in olivine grains to be activated during large-scale deformation, either in nominally anhydrous minerals (*Karato et al.*, 2008), or through free fluids (*Kovács et al.*, 2012b). In the Alps and similar (older) settings in the last stage of orogeny, most of the water may have left the upper mantle, and the dominant slip system may be the classical A-type (*Nicolas and Christensen*, 1987; *Nicolas*, 1993). This may perhaps be the reason why we have not found any indication of orogen-perpendicular fast orientation in the Alps upper mantle so far. In the following we will therefore only consider A-type fabric. Another guiding model for the internal deformation of mountain ranges is transpression (*Nicolas*, 1993), where part of the material (e.g., layers) undergoes pure shear, and other parts simple shear with a horizontal flow direction, and orogen-parallel flow (*Barruol et al.*, 2011).

We have noted the relatively good agreement between fast directions and the trend of the mountain chain. Given the high quality of the observations, we can go a step beyond, and address this pattern in more detail, and especially the region where the similarity with the topographic trend actually breaks down, e.g., in the Eastern Alps. In this, we need to keep in mind that our shear-wave splitting observations are associated with a finite Fresnel zone, with a width (diameter) of about 100 km at a depth of 150 km. This may smooth the observed spatial variation somewhat, but it does not cause the overall smooth rotation of fast orientation along the Alps.

The abrupt change of fast orientation occurs across the Tauern Window, which is also

the area where the Adriatic indenter acts (*Robl and Stüwe, 2005*). Its effect may be to bend the colliding block around its edge, which may explain the banana-shape of the Tauern window through the effect of a clockwise block rotation of the zone to the East relative to that in the West; such a difference in orientation across the Tauern Window longitude range is also observed in paleomagnetic data (*Mauritsch and Frisch, 1980*). To the east of the Tauern Window, fast azimuths point toward the Southeast, in between the orientations which Carpathians (Ca) and Dinarides (Di) have nowadays. In principle, that orientation is not far from the ancient orientation of the Carpathians, before the opening of the Pannonian basin (*Royden and Baldi, 1988*), which had been around 110 degrees from North, with a relatively large uncertainty from the reconstruction though. If pre-Alpine deformation played an important role, then this would predict that seismic anisotropy in the Dinarides would also follow the trend of the Dinarides. This is to be seen. A difficulty in this view, however, is that the three easternmost stations are located on a thin lithosphere of about 60-80 km thickness (*Artemieva et al., 2006; Bianchi et al., 2014*), and the lithosphere can therefore not explain the major portion of the splitting signal there. The three stations in the East thus may be recording mainly asthenospheric anisotropy that would be younger compared with frozen-in anisotropy within the lithosphere, and probably even related with ongoing deformation. The anisotropy at the easternmost stations is not much different from the four stations further to the west, except that the fast orientation is slightly more southerly.

An important tectonic feature of the area is the extrusion of the central part of the Alps toward the Pannonian basin in the East. There is good evidence that this occurs, at least at the Earth's surface, from seismicity (*Brückl et al., 2010; Gutdeutsch and Aric, 1987*), structural geology (*Frisch et al., 1998; Ratschbacher et al., 1991*), and geodesy (*Bus et al., 2009*). Recent GPS velocities from the European geodetic networks have given motions approximately toward the east for the Eastern Alps (*Bus et al., 2009*), relative to stable Europe, although individual stations scatter somewhat around that direction, and the different studies performed so far do not agree very well.

To relate surface motion to the shear-wave splitting observations, we need to consider that seismic anisotropy records internal deformation rather than displacement. Plate-motion-related deformation with a horizontal flow plane would attain a fast orientation parallel to the relative motion of the deeper mantle relative to the surface. We assume that the mantle is stationary with respect to the central Alps. If the convergence across the Alps is taken up by roughly constant strain, the Central Alps would move toward stable Europe with approximately half the velocity of the Adriatic Indenter. The latter is 2.5 (mm/yr) (*Bus et al., 2009*) relative to stable Europe (AD versus EU in the insert

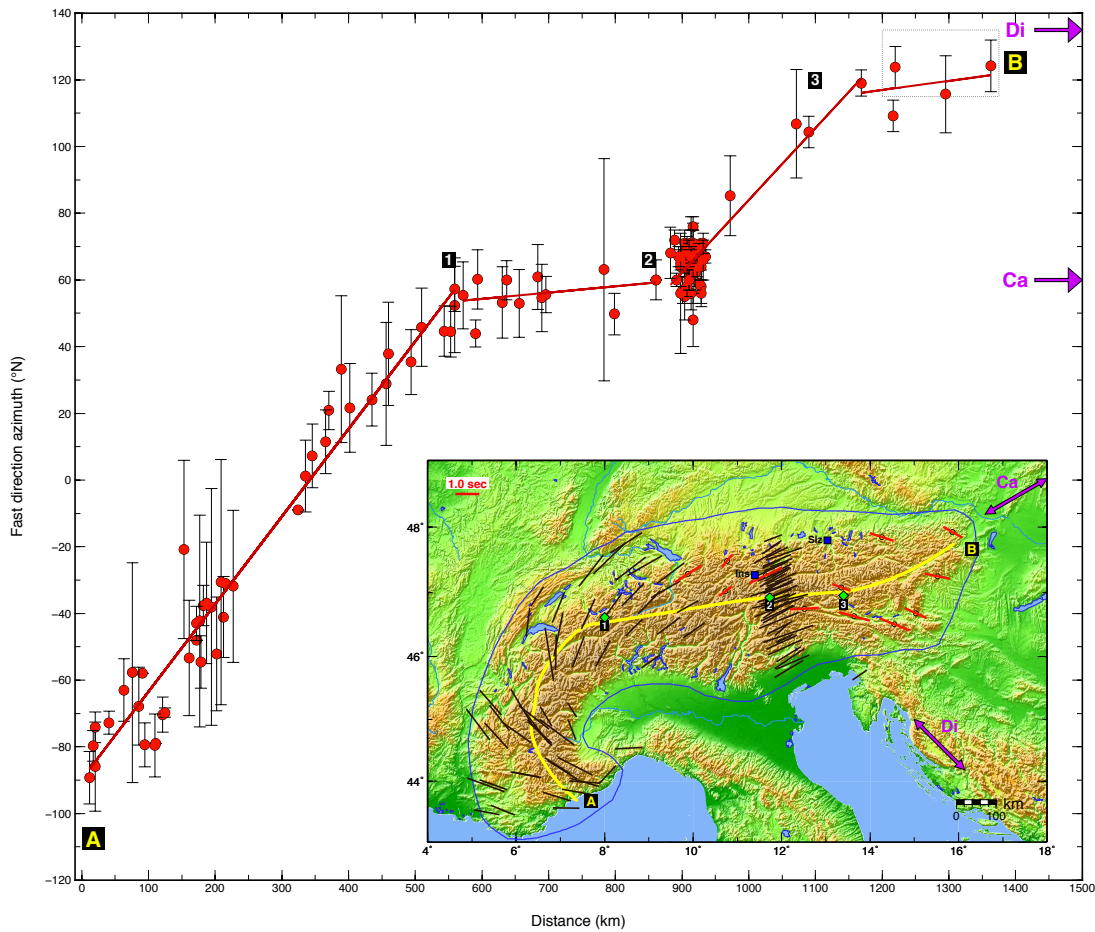


**Figure 3.3:** Rotation of fast orientations with distance along the Alps. Red circles give the fast azimuth for station locations projected onto the central line along the Alps. Note the regions of constant fast azimuths around Switzerland and the Eastern Alps, and the region of fast spatial rotation in between (see text). For the Eastern part of the Alps, starting at point 3, the topographic trend rotates toward the North, while the fast azimuths rotate toward the South. The easternmost stations (box) are located on thin lithosphere (see text).

of Figure 3.2. The direction of motion of the Pannonian unit relative to stable Europe (PA versus EU) is 1.4 (mm/yr) with an azimuth of 79 degrees from North (*Bus et al.*, 2009). The motion of the Pannonian unit with respect to the Central Alps (PA vs AL) is then 1.7 mm/yr with an azimuth of 126 degrees. This is in the range of the fast directions that are between 110 and 125 degrees (Table 3.1), showing that the observed anisotropy for the easternmost stations is consistent with the eastward escape proposed by earlier authors. Our observations for the easternmost stations are thus consistent with deformation associated with the eastward escape. This deformation would occur in the asthenosphere then, which would suggest that not only the crust, but also the entire lithosphere escapes toward the Pannonian basin. The splitting directions generally agree

also with predicted escape motions from thin viscous sheet modeling (*Robl and Stüwe, 2005*) of the effect of the indenter on the lateral escape. Deformation in the asthenosphere does not exclude that some of the deformation is taken up within the lower crust though. Perhaps high-resolution techniques such as anisotropic receiver functions will be able to contribute that component of lithospheric deformation independently. Known faults in the area (Mur-Mürz fault, SEMP fault) do not seem to dominate the deformation in the upper mantle, since they are striking in ENE direction, except the Periadriatic line which strikes ESE. At smaller scale this deformation might become visible.

### 3.4 Conclusions

We constrain upper mantle anisotropy beneath the Eastern Alps by measuring shear wave splitting parameters. Fast orientation measurements indicate the presence of a more-or-less mountain chain parallel seismic anisotropy in the upper mantle under all of the Alps, showing a clear rotation of fast axis azimuths along the Alps, in accordance with the topographic pattern. This indicates a simple pattern of mantle deformation that is all the more remarkable, since geological structure at the surface of the Alps shows a very complicated pattern. In the Eastern Alps, fast orientations jump by about 45 degrees across the Tauern Window area. For the easternmost stations, which are located on thin lithosphere, yet record a shear-wave splitting of similar size, we find that fast directions agree closely with those predicted by the relative motion of the surface (GPS) with respect to the central Alps. This suggests that we may be observing a mantle deformation signal of the eastward extrusion. In that case, the entire lithosphere takes part in the lateral escape toward the Pannonian basin. The measured splitting parameters show a remarkably simple spatial pattern of fast orientations, given the complex surface geology of the Alpine orogen.

### Acknowledgments

We would like to thank Wolfgang Frisch for discussions, and Andreas Wüstefeld for the use of the SplitLab code (*Wüstefeld et al., 2008*). The Zentralanstalt für Meteorologie und Geodynamik (ZAMG)(<http://www.zamg.ac.at>), provided online access to the data recorded by OE network stations. The data was accessed through the database

operated by Observatories and Research Facilities for EUropean Seismology (ORFEUS) (<http://www.orfeus-eu.org>).

### 3.5 Supplementary figures



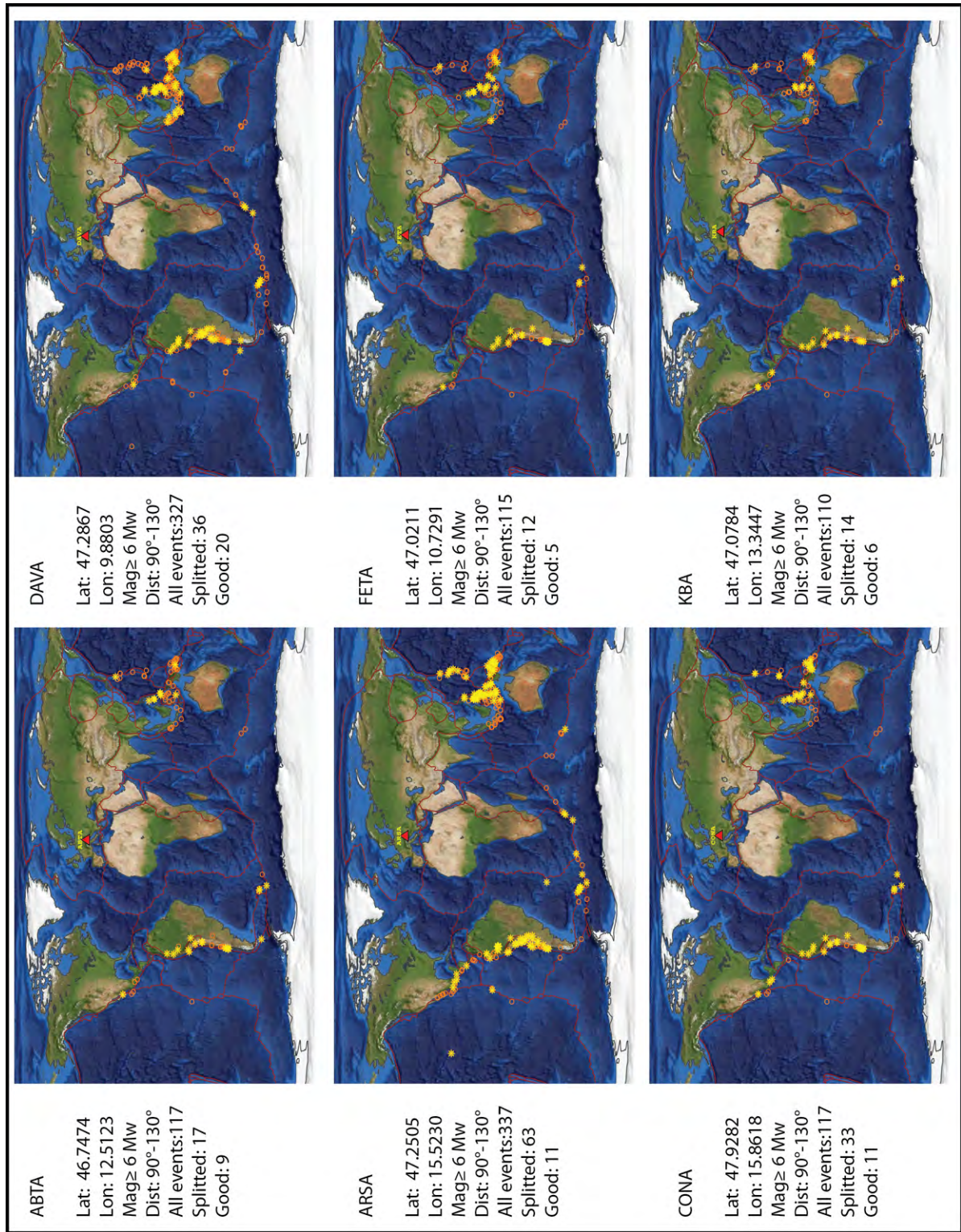


**Figure 3.4:** Map showing the epicentral location of teleseismic events recorded at the stations; ABTA, ARSA, CONA, DAVA, FETA, and KBA. Circles indicate events analyzed at the respective station, at epicentral distances between 90° and 130°, and between the years 2002 and 2011. Stars represent events that display good, fair, and poor splitting. Only good quality measurements were used for our analysis.



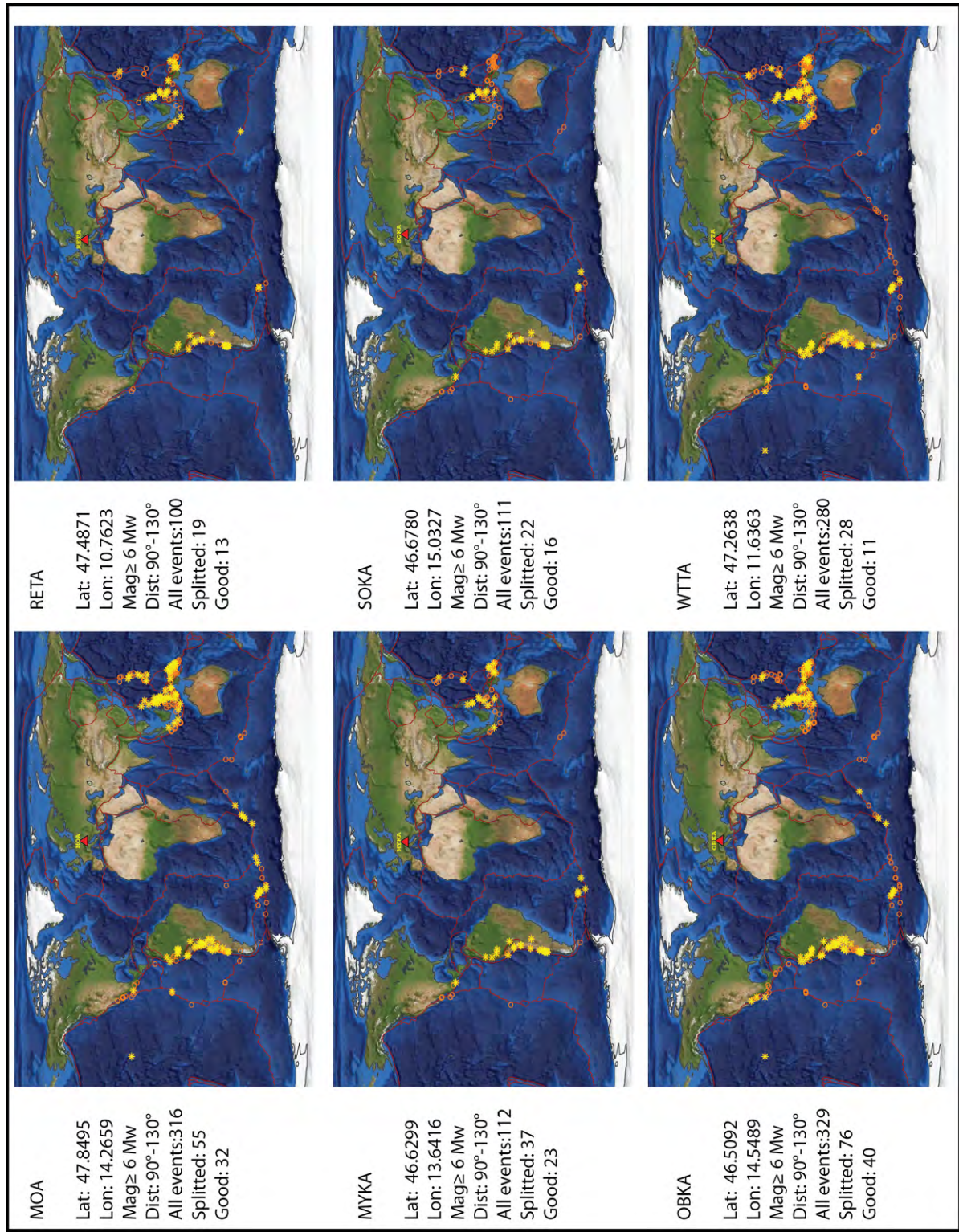


**Figure 3.5:** Map showing the epicentral location of teleseismic events recorded at the stations; MOA, MYKA, OBKA, RETA, SOKA, and WTTA. Circles indicate events analyzed at the respective station, at epicentral distances between 90° and 130°, and between the years 2002 and 2011. Stars represent events that display good, fair, and poor splitting. Only good quality measurements were used for our analysis.

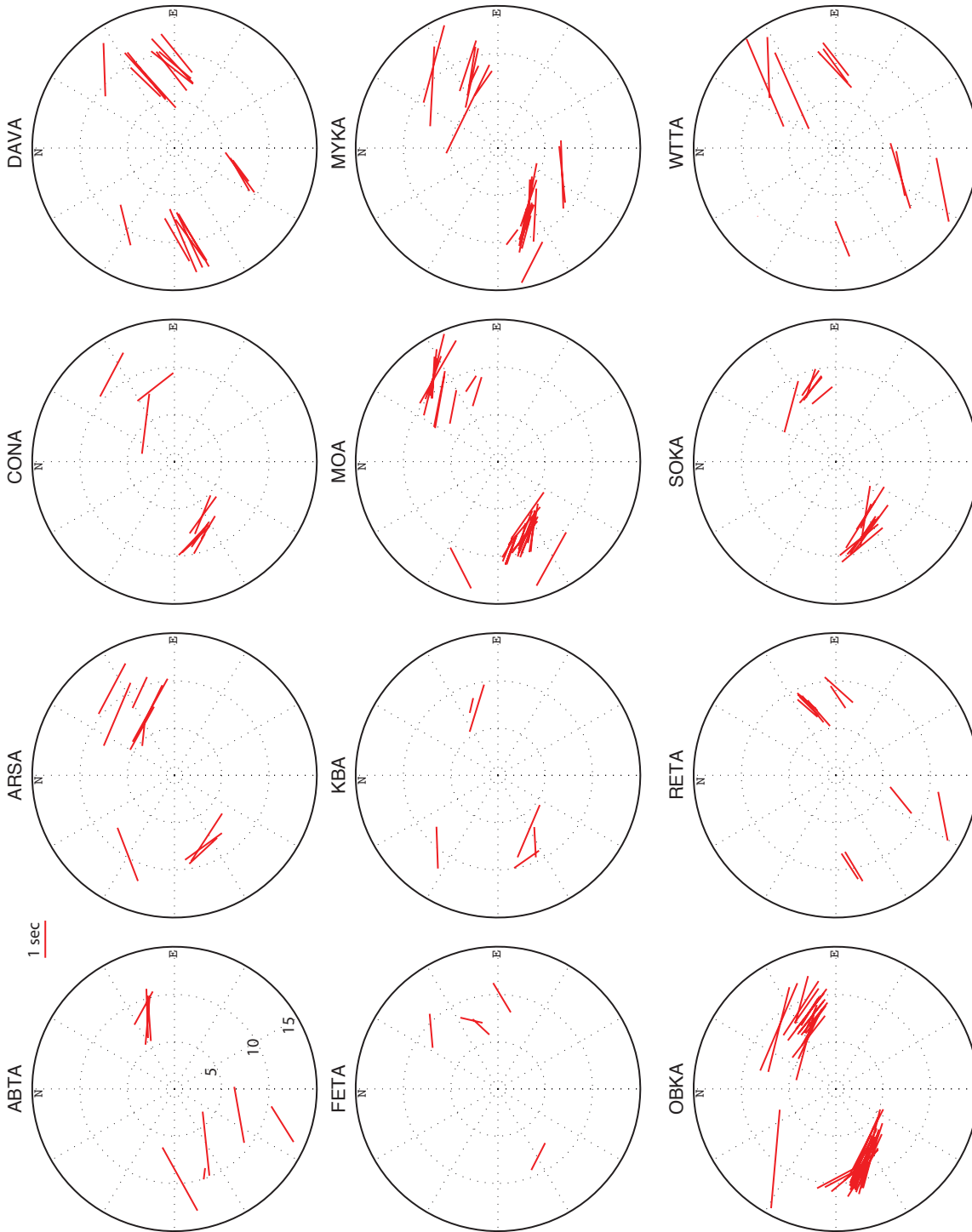


**Figure 3.6:** Backazimuth distribution of good splitting measurements at each station. The position of each individual good measurement indicates its backazimuth with respect to North while the orientation of red bars shows the fast orientation azimuth. Length of bars represents the splitting delay time. Incidence angle of SKS phases is shown in 5 degrees sectors

## Published paper:

Earth and Planetary Science Letters 383 (2013) 1–6



Contents lists available at ScienceDirect

## Earth and Planetary Science Letters

www.elsevier.com/locate/epsl



## Seismic anisotropy and large-scale deformation of the Eastern Alps



Götz Bokelmann, Ehsan Qorbani\*, Irene Bianchi

Department of Meteorology and Geophysics, University of Vienna, Austria

## ARTICLE INFO

## Article history:

Received 24 June 2013

Received in revised form 16 September 2013

Accepted 19 September 2013

Available online 8 October 2013

Editor: P. Shearer

## Keywords:

seismic anisotropy  
shear-wave splitting  
orogeny  
upper mantle  
deformation

## ABSTRACT

Mountain chains at the Earth's surface result from deformation processes within the Earth. Such deformation processes can be observed by seismic anisotropy, via the preferred alignment of elastically anisotropic minerals. The Alps show complex deformation at the Earth's surface. In contrast, we show here that observations of seismic anisotropy suggest a relatively simple pattern of internal deformation. Together with earlier observations from the Western Alps, the SKS shear-wave splitting observations presented here show one of the clearest examples yet of mountain chain-parallel fast orientations worldwide, with a simple pattern nearly parallel to the trend of the mountain chain. In the Eastern Alps, the fast orientations do not connect with neighboring mountain chains, neither the present-day Carpathians, nor the present-day Dinarides. In that region, the lithosphere is thin and the observed anisotropy thus resides within the asthenosphere. The deformation is consistent with the eastward extrusion toward the Pannonian basin that was previously suggested based on seismicity and surface geology.

© 2013 Elsevier B.V. All rights reserved.

## 1. Introduction

Surface geology and tectonic evolution of the Alps appear rather complex (Schmid et al., 2004), and it may be enlightening to study mantle structure in the region. Several geophysical studies have been performed, and they have produced 3D tomographic models (Gebrande et al., 2002; Piromallo and Morelli, 2003; Lippitsch et al., 2003; Brückl et al., 2010; Dando et al., 2011; Mitterbauer et al., 2011; Legendre et al., 2012). Tomographic images show velocity anomalies that can be interpreted in the context of suture zones and the major subduction events. The above-cited studies did not fully clarify the dynamics of the collision however, since they apparently allow opposing views on the structure and evolution of the Eastern Alpine region. More specifically, two recent studies using P-wave velocity tomography for the Eastern Alps come to different conclusions. Lippitsch et al. (2003) interpreted the high velocity anomaly in the Western Alps as dipping southeastward European lower lithosphere beneath the Adriatic microplate while the anomaly in the Eastern Alps is interpreted to represent Adriatic lower lithosphere dipping northeastward beneath the European plate. On the other hand, the more recent ALPASS tomographic model, proposed by Mitterbauer et al. (2011), does not suggest a change of subduction polarity between the Western and Eastern Alps. At the eastern end of the mountain chain, the Alps have been connected in the geological past with the Carpathians and the Di-

narides. Nowadays, the Eastern Alps (Gutdeutsch and Aric, 1987; Ratschbacher et al., 1991; Brückl et al., 2010) may be extruding towards the Pannonian basin. Further investigation is needed to provide more reliable evidence, and to study the vertical extent of the eastward extrusion. Many parts of the Eastern Alps have never been studied with respect to seismic anisotropy and deep deformation, due to the sparse coverage of seismic stations in the area.

In this study, we investigate upper mantle anisotropy beneath the Eastern Alps by measuring the splitting of teleseismic SKS/SKKS phases for the Alpine region. These shear waves record large-scale anisotropy produced by lattice-preferred orientation (LPO) of rock-forming minerals and particularly of olivine that represents the major upper mantle volume. The LPO of olivine grains develops in response to tectonic strain (Mainprice et al., 2000; Nicolas and Christensen, 1987; Savage, 1999; Silver and Chan, 1991). We present here our first results from permanent seismic stations in the Eastern Alpine region (their location and network are listed in Table 1) and discuss them in conjunction with earlier measurements from the Western Alps (Barruol et al., 2011) and from the central Alps along the TRANSALP profile (Kummerow and Kind, 2006).

## 2. Data and method

In this study we focus on large-scale anisotropy in the upper mantle under the Alps, through the splitting of teleseismic SKS/SKKS wave phases. To characterize the nature of anisotropic structures using the shear-wave splitting method, two splitting parameters are defined as the fast orientation azimuth ( $\phi$ , angle between fast axis and radial direction) and delay time between the

\* Corresponding author. Address for correspondence: 2D506, UZAIL, Althanstrasse 14, 1090 Vienna, Austria. Tel.: +43 1 4277 53727.

E-mail address: ehsan.qorbani@univie.ac.at (E. Qorbani).





# Chapter 4

## Eastern Alps

This chapter has been published as: E. Qorbani, I. Bianchi, and G. Bokelmann, 2015, *Slab Detachment under the Eastern Alps Seen by Seismic Anisotropy*, Earth and Planetary Science Letters, 409, 96-108.

### Abstract

We analyze seismic anisotropy for the Eastern Alpine region by inspecting shear-wave splitting from SKS and SKKS phases. The Eastern Alpine region is characterized by a breakdown of the clear mountain-chain-parallel fast orientation pattern that has been previously documented for the Western Alps and for the western part of the Eastern Alps. The main interest of this paper is a more detailed analysis of the anisotropic character of the Eastern Alps, and the transition to the Carpathian-Pannonian region. SK(K)S splitting measurements reveal a rather remarkable lateral change in the anisotropy pattern from the west to the east of the Eastern Alps with a transition area at about 12°E. We also model the backazimuthal variation of the measurements by a vertical change of anisotropy. We find that the eastern part of the study area is characterized by the presence of two layers of anisotropy, where the deeper layer has characteristics similar to those of the Central Alps, in particular SW-NE fast orientations of anisotropic axes. We attribute the deeper layer to a detached slab from the European plate. Comparison with tomographic studies of the area indicates that the detached slab might possibly connect with the lithosphere that is still in place to the west of our study area, and may also connect with the slab graveyard to the East, at the depth of the upper mantle transition zone. On the other hand, the upper layer has NW-SE fast orientations coinciding with a low-velocity layer which is found above a more-or-less eastward dipping high-velocity body. The anisotropy of the upper layer shows large-scale NW-SE fast orientation, which is consistent

with the presence of asthenospheric flow above the detached slab foundering into the deeper mantle.

## 4.1 Introduction

Seismic anisotropy is defined as a directional dependence of seismic velocity. It is assumed that the upper mantle presents significant anisotropy (*Maupin and Park, 2007*). This anisotropy is most probably due to a non-random distribution of crystallographic orientation of minerals in the olivine-rich ultramafic upper mantle rocks. The non-random distribution is known as lattice-preferred-orientation (LPO). The relation between the typical intrinsic anisotropy in the upper mantle and LPO, which is a result of the deformation, has been well-documented (*Babuška and Cara, 1991; Silver and Chan, 1991; Mainprice et al., 2000*). It is generally accepted that the anisotropy is due to deformation that either occurred at earlier times (“fossil deformation”) or due to present tectonic activities (*Savage, 1999*, and references therein). In either case, the anisotropy indicates the geometry of the flow. Therefore mapping seismic anisotropy can resolve the pattern of mantle flow in the asthenosphere as well as the fossil deformation pattern within the lithosphere, which has great importance for understanding the upper mantle geodynamics.

The simplest measure of upper mantle anisotropy is the shear-wave splitting, particularly using SKS core phases (e.g. *Vinnik et al., 1984; Silver and Chan, 1988; Long and Silver, 2009*) which have been studied extensively in recent years. Near-vertical incidence angles of SKS phases give good lateral resolution (i.e. 50 km, the radius of Fresnel zone at 150 km depth), since anisotropy is to be attributed to a steep ray path. However, the depth where the splitting occurs is less well-determined. Although the measuring procedure of shear-wave splitting is straightforward, the practical interpretation of measurements can be quite challenging.

In this study we first present the overall pattern of anisotropy, based on the average values of SKS splitting parameters, then we focus on the spatial changes of the individual measurements and we show striking lateral variations of anisotropy within the region. Later the backazimuthal variation of fast orientations is modeled by means of two anisotropic layers. Finally, using the results of two anisotropic layers modeling, together with some constraints from velocity tomography studies and the analysis of lithospheric thickness,



we present a possible lithospheric and asthenospheric upper mantle structure for the Eastern Alps.

## 4.2 Tectonic setting

The Alps are an arc-shaped double-verging mountain chain developed at the boundary between the Eurasian plate (to the North) and the Adriatic microplate (to the South). They are geographically divided into Southern, Eastern, Central, and Western Alps. Alpine tectonic history is deeply linked to that of the adjacent mountain chains as the Dinarides, the Carpathians and the Apennines. Paleogeographic reconstructions suggest that in the area where the Alps are located today there was the Meliata Ocean in Triassic time, a marginal ocean basin of the neo-Thetis. In Late Triassic-Early Jurassic this ocean initiated subduction towards SE (*Kozur, 1991*); in the late Jurassic the opening of the Vardar Ocean took place in its backarc, and at the same time occurred the opening of the Piemonte-Ligurian Ocean. During Cretaceous time, another ocean, the Valais, opened on top of the Piemonte-Ligurian Ocean, in association with the opening of the Atlantic further to the West (*Frisch, 1979; Stampfli, 1994*). About 80 Ma ago the Piemonte-Ligurian Ocean started subducting below the Adriatic continental margin following the SE directed subduction initiated by Meliata. The contact between the Adriatic continental crust and the Piemonte-Ligurian oceanic crust coincide with the geological boundary observed today between the Austroalpine units (in the Eastern Alps) and Penninic Units (see Supplementary Fig. 4.13).

The continental collision between Europe and Adria started  $\sim 35$  Ma ago (*Froitzheim et al., 2008; Handy et al., 2010*). The image we have today of the deep structure of the Alps is derived by the interpretation of tomographic images. The different regional models (i.e. *Lippitsch et al., 2003; Koulakov et al., 2009; Mitterbauer et al., 2011*) agree in identifying two lithospheric roots, one located below the Eastern Alps, and one located below the Central-Western Alps, separated between  $12^\circ$  and  $13^\circ\text{E}$ .

On the surface, geodetic data generally agree with a counterclockwise rotation of the Adriatic plate with respect to stable Europe around a pole in the western Alps (e.g. *Calais et al., 2002; Nocquet and Calais, 2004*). The CCW rotation of Adria leads to different deformation regimes along the Alpine arc, such as: compression in the Eastern Alps, dextral shear in the Central Alps and transtension or very slow deformation in the western Alps. This suggests that active deformation in the Alps (and in the neighboring

Apennines and Dinarides) is controlled, and possibly dynamically driven, by the motion of the Adriatic microplate rather than by the convergence between Africa and Eurasia (*Nocquet and Calais, 2003*). Vertical GPS ground motions show that the most elevated areas are uplifting while the adjacent sedimentary basins undergo subsidence (*Serpelloni et al., 2013*). Similar evidence is given by measured erosion rates along the Alpine arc. First of all there is a crucial difference between the European plate (undergoing erosion) and the Adriatic plate (undergoing deposition), suggesting a decoupling between the two plates (*Baran et al., 2014*). Concerning the European side, the western Alps are characterized by high levels of erosion ( $>0.6$  km/My), while the Eastern Alps show lower erosion rates ( $\sim 0.06$  km/My), with the exception of the Tauern Window area, where a rate of 0.3 km/My is reached (*Baran et al., 2014*). The difference in erosion rate supports the hypothesis of slab brake-off below the western part of the Alps (*von Blanckenburg and Davies, 1995*).

### 4.3 Data and method

The most frequently used method for constraining the anisotropy within the upper mantle is the shear-wave splitting method, which is based on birefringence, or splitting of the core shear-waves (SKS) into two orthogonally polarized quasi-phases. The splitting of teleseismic SKS phases has been largely used in order to constrain upper mantle anisotropy (e.g. *Vinnik et al., 1984*; *Silver and Chan, 1991*; *Margheriti et al., 2003*; *Buontempo et al., 2008*; *Barruol et al., 2011*). Two fundamental parameters can be measured through this method: the fast orientation azimuth ( $\phi$ , angle between fast axis and radial direction) and the splitting delay between fast and slow polarizations ( $\delta t$ ). Assuming that the upper mantle anisotropy is confined in one laterally uniform layer, the horizontal components of SKS phases can be analyzed in order to estimate the amount and symmetry orientations of the azimuthal anisotropy (*Vecsey et al., 2008*). Several techniques are used to measure splitting parameters. The one used in this study is the transverse component minimization technique (SC) illustrated by *Silver and Chan (1991)*. The application of this technique was performed by the use of the SplitLab package (*Wüstefeld et al., 2008*).

The splitting parameters are retrieved by applying a grid-search over all possible values of  $\phi$  and  $\delta t$ . The azimuth and delay that better remove the effect of splitting on the T component are those that describe the anisotropic parameters of the mantle beneath the recording station (*Wüstefeld et al., 2008*). One example of splitting parameters

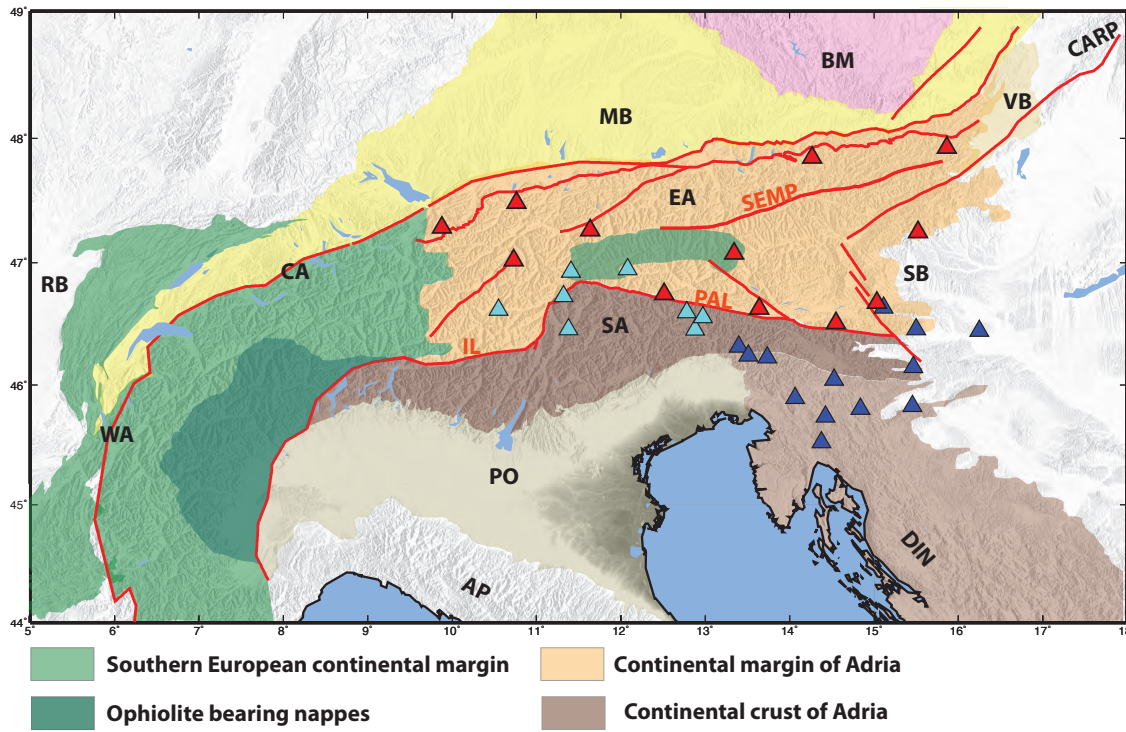


**Figure 4.1:** Map of the study area. Tectonic superunits, as described in the legend, are shown according to their presumed paleogeographic origin (after *Schmid et al.*, 2004, N. Froitzheim, *Geology of the Alps*, <http://www.steinmann.uni-bonn.de>). Labels are as in the following: Western Alps (WA), Central Alps (CA), Eastern Alps (EA), Southern Alps (SA), Dinarides (DIN), Apennines (AP), Carpathians (CARP), Bohemian Massif (BM), Vienna Basin (VB), Styria Basin (SB), Molasse Basin (MB), Po Plain (PO), Paleoadriatic Line (PAL), Insubric Line (IL), Salzach-Ennstal-Mariazell-Puchberg fault (SEMP). Locations of broadband stations used for SKS splitting analysis are shown. Red triangles for the Austrian broadband seismological network (OE); blue triangles for the Slovenian seismic network (SL); cyan for the Italian seismic networks: Istituto Nazionale di Geofisica e Vulcanologia (IV), NE-Italian broadband network (NI), and South-Tyrolian network (SI).

measurement by the SC technique is illustrated in supplementary Figure 4.10(a,b). In most measurements we applied no filter to keep the complete frequency range in order to not lose part of the waveform energy and to prevent the dependence of measured splitting parameters on filtering.

Data collection for this study consisted of the teleseismic events with magnitude  $M_w$  greater than 6 occurring in epicentral distance range of  $90^\circ$  to  $130^\circ$  recorded by 33 stations of 5 permanent networks (see Table 4.1 and Fig. 4.1). We used data recorded by the Austrian broadband seismological network (OE) between 2002 and 2013. This network includes 12 permanent stations maintained by the Zentralanstalt für Meteorologie und Geodynamik (ZAMG, <http://www.zamg.ac.at>). Data from 13 broadband stations of the

Slovenian seismic network (SL) recorded between 2005 and 2013 were included in this study, and accessed through the Observatories and Research Facilities for European Seismology (ORFEUS) database (<http://www.orfeus-eu.org>). Data recorded between 2008 and 2012 were retrieved from one station of the Italian seismic network (IV) maintained by INGV (Istituto Nazionale di Geofisica e Vulcanologia). From the NE-Italian broadband network (NI, operated by OGS, Istituto Nazionale di Oceanografia e di Geofisica Sperimentale), events occurred between 2010 and 2011 recorded by at least two stations have been included. Events occurring between 2006 and 2011 and recorded by 5 stations of the South-Tyrol network (SI) have been included. Altogether 5845 SKS/SKKS phases recorded at all stations have been visually selected. Among these phases, we observed and measured the individual splitting parameters for 868 SKS/SKKS phases. All measurements were classified as "good", "fair", and "poor" splitting quality (*Barruol et al.*, 1997; *Wüstefeld and Bokelmann*, 2007). When no significant energy on transverse components was recorded, the event was considered as displaying a "Null" orientation. 642 Null measurements were observed; out of this number of Nulls, we labeled 372 Null measurements as "good Null". Supplementary Figure 4.10(c) shows an example of good Null measures.

## 4.4 Results

### 4.4.1 Splitting parameters; average values

Among 868 measured splitting parameter pairs (fast orientation and splitting delay) showing clear splitting of SKS phases, we selected 470 individual good quality pairs (Appendix C.1). The calculated average value for each station over the good measurements is listed in Table 4.1 as well as the number of total splitting measurements and the number of good splitting measurements. In order to have an estimate of dispersion of individual measurements around the obtained averages, the value of 95% confidence intervals (CI) were calculated. Table 4.1 shows these values, where  $\phi$ -error corresponds to the circular average fast azimuths, and  $\delta t$ -error to the average splitting delays.  $\phi$ -error is  $\leq 13^\circ$  for 29 stations; the largest error value ( $\pm 18^\circ$ ) was obtained for station JAVS. With the exception of KNDS, VISS, and GROS that show 0.32, 0.31, and 0.52 seconds respectively, the  $\delta t$ -errors are smaller than 0.30 s for all stations. The magnitude of errors indicates that there is a low spread of the individual measurements, so that the average of splitting

**Table 4.1:** List of stations and networks used in the study as well as average fast orientations and splitting delays including their corresponding error. Number of splitting measurements (SM) and good quality splitting (GS) are listed together with the number of Null measurements (NM) and good quality Nulls (GN). See Appendix A for Nulls

Station	Net	Lon(°E)	Lat(°N)	$\phi(^{\circ})$	$\phi$ -error	$\delta t(s)$	$\delta t$ -error	SM	GS	NM	GN
ABTA	OE	12.5123	46.7474	85	11	1.26	0.28	17	9	12	7
ARSA	OE	15.5230	47.2505	110	14	1.27	0.19	66	13	87	49
CONA	OE	15.8618	47.9282	118	10	1.01	0.14	42	15	34	15
DAVA	OE	09.8803	47.2867	56	5	1.35	0.11	36	20	33	25
FETA	OE	10.7291	47.0211	63	12	0.97	0.15	26	10	47	21
KBA	OE	13.3447	47.0784	92	10	1.11	0.15	27	16	22	14
MOA	OE	14.2659	47.8495	108	4	1.12	0.13	59	35	56	29
MYKA	OE	13.6416	46.6299	98	6	1.38	0.17	47	31	9	6
OBKA	OE	14.5489	46.5092	118	4	1.47	0.12	85	47	16	11
RETA	OE	10.7623	47.4871	50	6	0.82	0.10	19	13	25	13
SOKA	OE	15.0327	46.6780	122	5	1.16	0.14	33	23	15	7
WTTA	OE	11.6363	47.2638	68	7	1.55	0.27	28	11	61	25
CADS	SL	13.7370	46.2280	74	-	1.20	-	12	1	12	10
CEY	SL	14.4267	45.7388	90	5	1.10	0.13	11	6	22	13
CRES	SL	15.4578	45.8260	125	6	1.05	0.18	32	26	20	14
DOBS	SL	15.4691	46.1495	110	7	1.24	0.16	27	24	3	2
GORS	SL	13.3999	46.3170	108	10	1.38	0.52	12	5	1	1
GROS	SL	15.5017	46.4608	117	6	1.26	0.19	14	10	7	4
JAVS	SL	14.0643	45.8934	92	18	1.09	0.25	22	12	15	13
KNDS	SL	14.3775	45.5276	71	16	0.70	0.32	11	5	17	13
KOGS	SL	16.2503	46.4481	98	4	1.35	0.11	29	22	12	7
LJU	SL	14.5278	46.0438	112	13	1.13	0.21	26	14	20	19
PERS	SL	15.1139	46.6365	124	4	1.05	0.08	28	17	4	3
ROBS	SL	13.5103	46.2450	115	17	1.37	0.29	17	9	4	3
VISS	SL	14.8383	45.8029	112	11	1.65	0.33	9	4	19	13
FVI	IV	12.7804	46.5966	72	7	1.62	0.11	19	11	8	5
CLUD	NI	12.8814	46.4569	82	-	1.90	-	5	1	4	4
ZOU2	NI	12.9729	46.5584	86	10	1.53	0.14	21	11	8	4
ABSI	SI	11.3200	46.7300	52	7	1.59	0.18	14	7	9	4
RISI	SI	12.0800	46.9500	78	12	1.70	0.26	18	16	17	9
ROSI	SI	11.4100	46.9300	63	10	1.75	0.24	26	6	7	1
MOSI	SI	10.5500	46.6200	50	9	0.82	0.12	14	6	11	6
KOSI	SI	11.3800	46.4600	44	4	1.29	0.08	17	14	6	3



parameters is a good approximation of overall azimuthal anisotropy beneath the stations and it can be considered and discussed as well for individual splitting measurements.

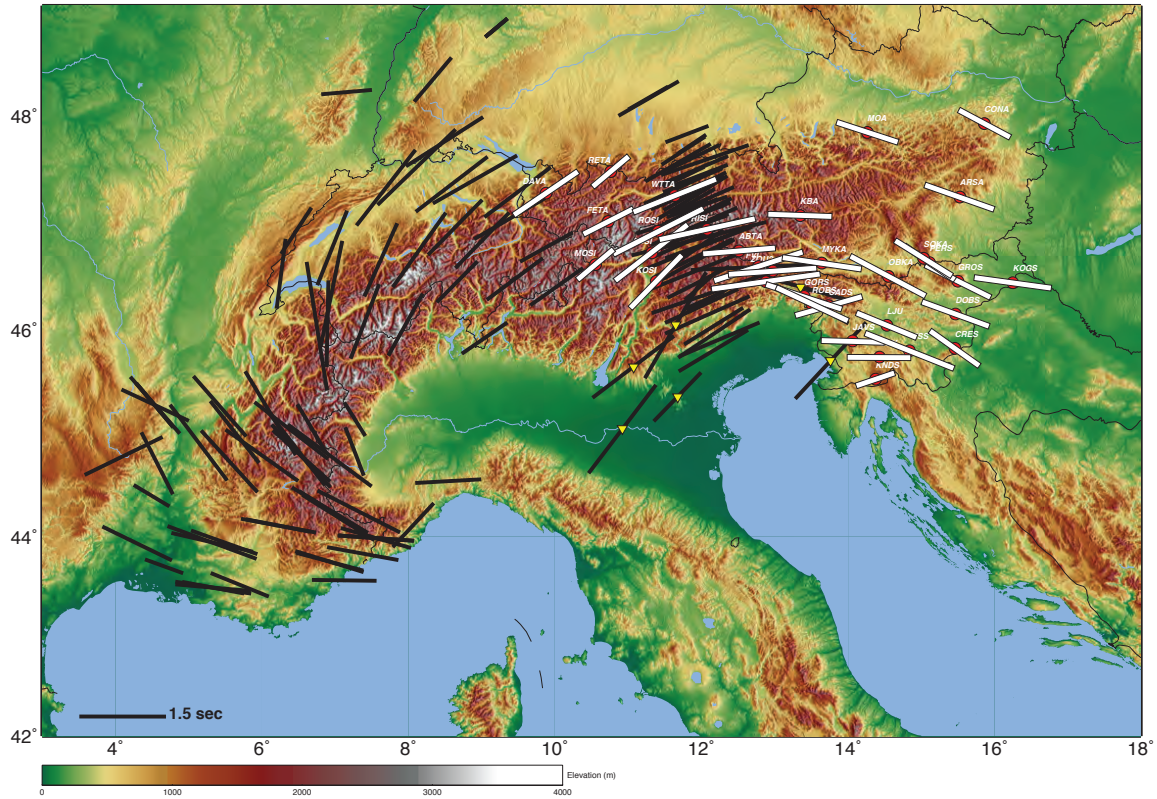


**Figure 4.2:** Map of average SKS splitting parameters calculated over the good quality measurements. Thick white lines represent average fast orientation ( $\phi$ ) at each station from this study and *Bokelmann et al.* (2013). Splitting delays ( $\delta t$ ) are shown by the length of the line (see scale on lower left). Black lines display measurements from previous studies (*Barruol et al.*, 2011; *Kummerow and Kind*, 2006), and station located in the Southern Alps and Po-plain, marked by triangles, (*Salimbeni et al.*, 2013). For discussion see the text.

The average values of splitting pairs are displayed in Figure 4.2. The line's orientation presents the average fast orientation azimuth for each station and the line's length indicates the average splitting delay. The stations DAVA, FETA, RETA, WTTA, ABSI, ROSI, MOSI, and KOSI which are located in longitude range between 9°E and 12°E show fast azimuths at about N60° (azimuth from North). These azimuths are in good agreement with the results of previous studies for the Western Alps presented by *Barruol et al.* (2011) and the Central Alps by *Kummerow and Kind* (2006) (black lines in Fig. 4.2). The NE-SW fast orientation detected for the western stations turns gradually to nearly East-West at the stations RISI, ABTA, CLUD, and ZOU2 (located at longitudes between 12°E and 13°E). The station FVI is an exception, with a fast azimuth



oriented  $N72^\circ$ . East-West fast orientation are detected for station KBA, JAVS and CEY as well (Fig. 4.2). Further to the East, the fast orientations turn from E-W to NW-SE, where the fast azimuth are predominantly  $N115^\circ$  oriented. This is observed for the stations located at longitudes greater than  $13^\circ\text{E}$ .

In a previous study (*Bokermann et al.*, 2013), we described the mountain chain-parallel anisotropy pattern in the upper mantle and discussed the rotation of fast orientation along the Alpine chain. The results of 21 further stations are added to the 12 stations used in that study. They clearly show the rotating pattern of fast orientation along the Alps previously described (seen in Fig. 4.2). The amounts of average splitting delays are in the reported range by former studies (*Barruol et al.*, 2011; *Kummerow and Kind*, 2006). The largest splitting delays (larger than 1.0 sec) with maximum value of 1.90 s at station CLUD, are observed for the stations located between  $13^\circ\text{E}$  and  $14^\circ\text{E}$ , southeast of the stations displaying the E-W oriented anisotropic fast azimuth.

#### 4.4.2 Individual measurements

Assuming that the mantle anisotropy is confined in a single uniform layer with a horizontal symmetry axis, splitting parameters can be averaged among individual measurements retrieved at a single station (*Silver and Savage*, 1994). Although the average values of fast orientation in this study have provided a reliable estimation for the overall anisotropic structures, the individual splitting parameters should be taken into account, allowing to inspect their variation in more detail. Among all measurements showing clear splitting, 470 were qualified as good in addition to 338 fair and 60 poor qualities.

Figure 4.3 shows the good quality individual measurements. Individual fast azimuths at single stations, particularly for those stations located in the eastern part of the region (east of  $12^\circ$ ), are grouped into two categories; therefore they are represented in different color. Fast azimuths displaying an angle smaller than  $90^\circ$  with respect to the North are shown in blue. Measurements obtained from stations situated in the western part of the study area show fast azimuth smaller than  $90^\circ$  from the North. The second category (shown by red lines) displays fast azimuth oriented at an angle greater than  $90^\circ$  from North; these orientations are observed east of  $12^\circ\text{E}$  (Fig. 4.3). Few fast azimuth orientation greater than  $N90^\circ$  (from North) are observed at stations located between  $12^\circ$  and  $13^\circ\text{E}$ , and by moving to the East the number of such oriented fast azimuths gets noticeably larger. According to the fast azimuth categories, we divide the region East and West of longitude  $12^\circ\text{E}$  (dashed line in Fig. 4.3).

The spatial distribution of individual splitting delays is illustrated in Figure 4.4,a. Different values are shown in three different colors. The largest values which are greater than 2.2 s, are localized around 12°E, 47°N and further to the southeast direction (orange lines in Fig. 4.4a). A significant decline in splitting delay values is observed about 11°E longitude, in particular stations RETA, FETA, and MOSI (Fig. 4.4a) show small values mostly less than 1 s.

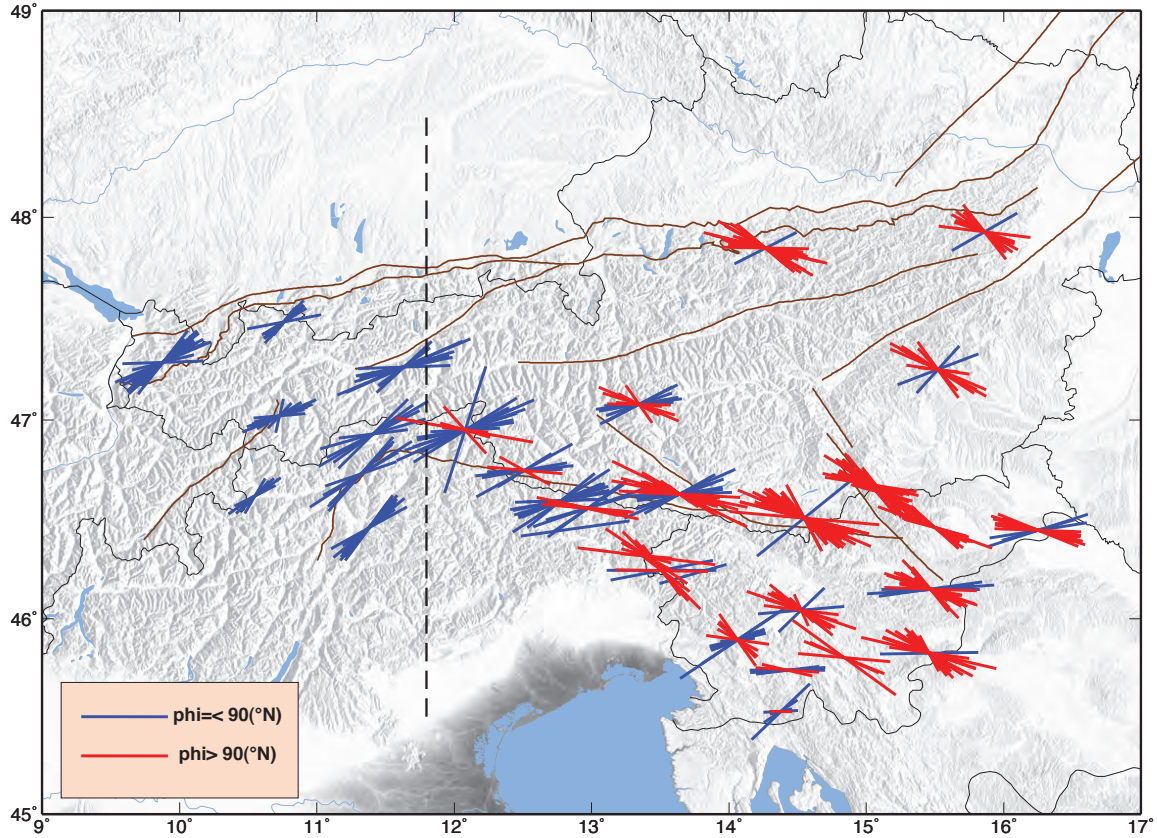


**Figure 4.3:** Good quality individual splitting parameters obtained in this study. The stations show two fast orientation categories (in different colors). Fast axes with azimuths smaller than 90° with respect to North are shown in blue, red for azimuth larger than N90° (mostly obtained for stations located in the eastern part of the study area). The dashed line (at about 12°E) separates the region according to the fast azimuth categories. Brown lines show main tectonic faults (Geological Map of Austria, edited by the Geological Survey of Austria (GBA), 1999, Vienna).

## 4.5 Discussion

### 4.5.1 Lateral change of anisotropy

Since every individual measure is obtained from a single event, the variation of splitting parameters can be evaluated as: i) variation in measured values from one teleseismic event recorded at nearby stations which refers to lateral change of anisotropy in the scale of distance between the stations, ii) variation in measurements derived from events of different backazimuth at a single station (*Margheriti et al.*, 2003).

In our results, the individual splitting parameters from a single event, recorded at nearby stations, do not show systematic differences. Instead, the single events that show NE-SW fast orientation at the stations in the West, present NW-SE orientation at the stations in the east. Figure 4.4,b shows examples of different fast azimuth obtained from same events. For instance, a single event (2002.285) recorded at MOA (in the East) exposes a fast azimuth of N111° which is different from fast azimuth N58°, recorded at DAVA (in the West). Although, stations do not show local variations, observing two categories of anisotropy pattern (in the eastern and western part (Fig. 4.3), and also considering the variation of anisotropy from singular events (Fig. 4.4b) indicates a lateral variation of anisotropy, which is remarkable in a larger scale, extending from the Central to the Eastern Alps. Regarding this lateral change, we can consider a transition area in between (at about longitude of 12°E), where the dominant fast orientation changes. Along the Alpine belt, the average fast azimuths follow the mountain belt trend (*Barruol et al.* (2011) for the western arc; *Kummerow and Kind* (2006) along the TRANSALP profile in the Central Alps) and show a clear rotating pattern (*Bokelmann et al.*, 2013) for the Central and Eastern Alps (Fig. 4.2). The mentioned area of transition from individual measurements coincides with the location of the pattern change in average fast azimuth.

The good coverage of event backazimuths from N38° to N312° provides the possibility of assessing the variation of measurements with respect to event backazimuth. We projected all good measurements from their station locations down to 150 km depth, following the ray paths of the SK(K)S phases. Figure 4.4b shows the projection of fast orientations. There is no evidence of backazimuthal dependence in the western part of the study area, meaning that events coming from different backazimuth show the same anisotropic fast azimuth. On the other hand, in the eastern part of the region, fast orientation azimuth varies with event backazimuth. In this area, NE-SW fast orientations (shown in blue in Fig. 4.4b), are mostly obtained from events with backazimuth of around N300°; events

arriving from backazimuth about  $N60^\circ$  and the opposite direction, give NW-SE fast orientation (e.g. station MOA in Fig. 4.4b). This backazimuthal variation shows that there is clearly a lateral change of anisotropy.

However, the backazimuthal change can sometimes be related to vertical changes of anisotropy, e.g., multi-layer anisotropy or non-horizontal anisotropic layers.

### 4.5.2 Vertical changes; modeling of two anisotropic layers

The shear-wave splitting method is performed by assuming the ray passing through an anisotropic medium with a hexagonal and horizontal symmetry axis. Splitting parameters, found under this simplified anisotropic single layer assumption and called apparent measurements, are supposed to be independent of initial polarization orientation, events' backazimuth for the SKS phases, (*Silver and Savage*, 1994). Observing any backazimuthal dependence in splitting parameters indicates that this single horizontal (hexagonal symmetry) is a simplistic assumption to characterize the anisotropy.

backazimuthal variations might reveal the depth-dependence of anisotropy (*Silver and Savage*, 1994; *Faccenna et al.*, 2014). This can be due to the effect of dipping symmetry axis on incoming rays thus showing  $2\pi$  periodicity of splitting parameters as function of events' backazimuth (*Silver and Savage*, 1994). In another circumstance, the backazimuthal dependence can be an indicator that incoming shear-waves have been split more than once, which happens in the presence of multiple anisotropic layers. In such case, exposing  $\pi/2$  periodicity of measurements in backazimuth suggests the presence of two anisotropic layers (*Silver and Savage*, 1994; *Rümpker et al.*, 1999).

With this intention, the periodicity of measurements was checked at the eastern and western stations separately, as shown in Figure 4.5. Single stations located in the eastern part (Fig. 4.5) present  $\pi/2$  periodicity as a function of backazimuth (Supplementary Figs. S3, S4). An example (MYKA) in Figure 4.5 clearly displays the  $\pi/2$  periodicity at a single station. On the other hand, measurements obtained in the West (e.g. WTTA, Fig. 4.5) do not show this periodicity. The same  $\pi/2$  periodicity is recognized for all measurements obtained in eastern part the region (Fig. 4.5) whereas this is not the case for the stations in the West (Fig. 4.5).

Observed  $\pi/2$  backazimuthal periodicity suggests the presence of two anisotropic layers in the eastern part of the study region. In order to model the two layers, we used the expression between splitting parameters of two anisotropic layers and measurements (apparent parameters), proposed by *Silver and Savage* (1994):



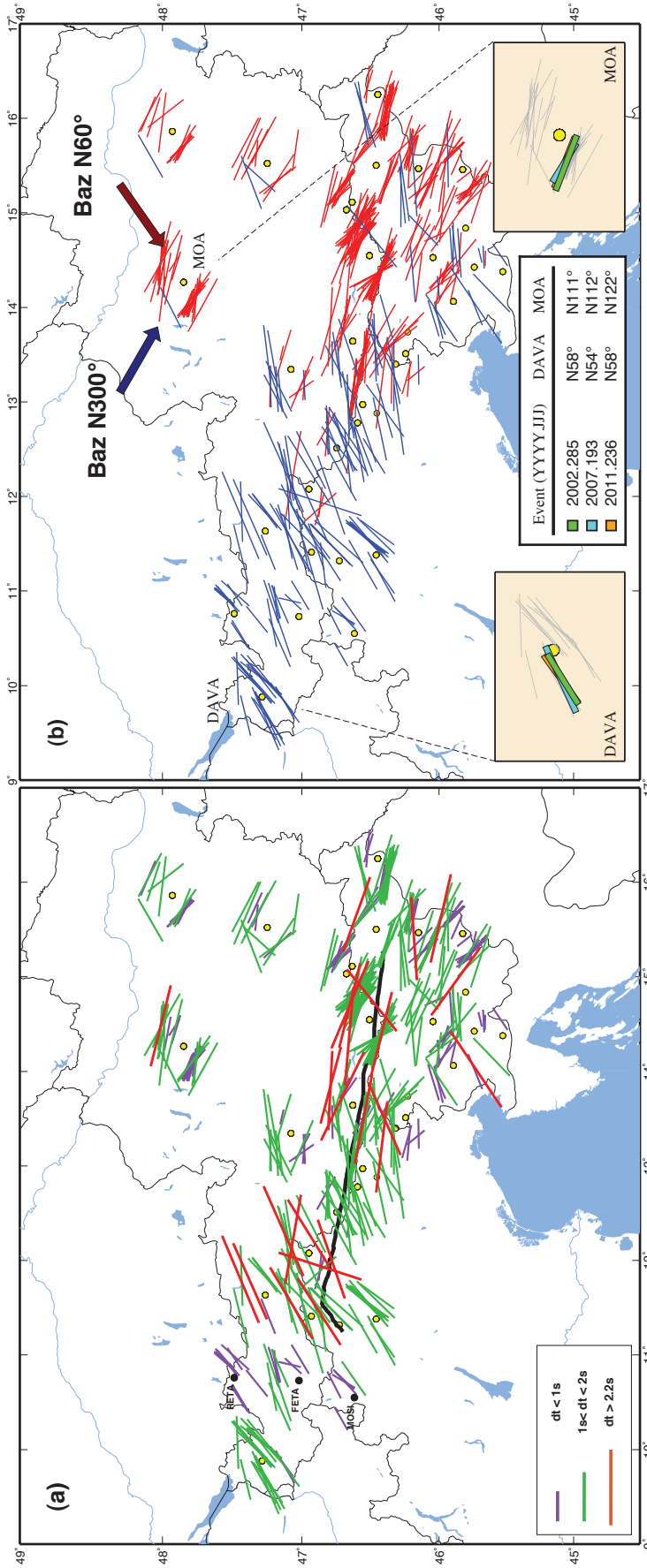


**Figure 4.4:** a) Individual fast orientations projected along the ray paths down to 150 km depth, colored according to the splitting delay. Largest values (greater than 2.2 s) are observed in the general area along the Periadriatic lineament (black line) and to the south of it. Black circles indicate the three stations that give the smallest splitting delays. b) Map of backazimuthal variation of measurements. Individual measurements are projected back to 150 km depth. In the eastern part, events from backazimuths around N60° and the opposite direction (~N240°) show NW-SE fast orientations (red lines). Events from backazimuths around N300° show NE-SW orientations (blue lines). No backazimuthal variation is observed in the western part. Insets represent a zoom of measurements at MOA and DAVA, showing in several examples how the same event can give rise to different fast orientations at different stations. Fast azimuths measured from three events recorded at MOA (in the East) show N111°, N122°, and N112° while measurements from the same events recorded at DAVA (in the West) show fast azimuths at N58°, N65°, and N54° (small table).

$$\begin{aligned}
\tan(\alpha_a) &= \frac{a_{p\perp}^2 + C_s^2}{a_{p\perp} a_p + C_s C_c} \\
\tan(\theta_a) &= \frac{a_{p\perp}}{C_s \cos(\alpha_a) - C_c \sin(\alpha_a)} = \frac{C_s}{a_p \sin(\alpha_a) - a_{p\perp} \cos(\alpha_a)} \\
a_p &= \cos \theta_1 \cos \theta_2 - \sin \theta_1 \sin \theta_2 \cos(\alpha_2 - \alpha_1), \\
a_{p\perp} &= -\sin \theta_1 \sin \theta_2 \sin(\alpha_2 - \alpha_1), \\
C_c &= \cos \theta_1 \sin \theta_2 \cos \alpha_2 + \cos \theta_2 \sin \theta_1 \cos \alpha_1, \\
C_s &= \cos \theta_1 \sin \theta_2 \sin \alpha_2 + \cos \theta_2 \sin \theta_1 \sin \alpha_1
\end{aligned}$$

where,  $\alpha_1$  and  $\alpha_2$  are obtained from the difference between fast azimuth of upper/deeper layer and initial polarization (events backazimuth), and multiplied by 2.  $\theta_1$  and  $\theta_2$  are splitting delays of the two layers multiplied by the angular frequency (0.628 Rad/s) and divided by 2.

All possible models with fast orientations between 0 and N180° (at 10° interval) and splitting delay of 0-4 s (at 0.1 s interval) were created, which gave a total of 518400 models for each station. We also tested the presence of two anisotropic layers by multi-station modeling. In this approach, all good-quality measurements of the stations showing  $\pi/2$  periodicity were used in that modeling. However, we observed a poor model fit which was unacceptable in comparison with the results of the single-station approach. This can be due to the effect of the strong lateral change of anisotropy in the eastern Alps since multi-station modeling requires an assumption of no lateral variation. Therefore, the modeling process was individually performed for single stations. Minimization of the Chi-Square value has been used to calculate the fit to the model. The best fitting splitting parameters ( $\phi$ -top,  $\delta t$ -top,  $\phi$ -bot, and  $\delta t$ -bot) for upper and deeper anisotropic layers were chosen according to the minimum Chi-Sq. Coefficient of determination (adjusted R-square) was calculated at each station in order to quantify the quality of the best-fit models (*Walker et al., 2005a; Fontaine et al., 2007*)(Walker et al., 2005a; Fontaine et al., 2007). Adjusted R-square takes the values between  $-\infty$  and 1. A two-layer model fits better than a one-layer model, giving values closer to 1 (see Appendix B). The two layers modeling results including the adjusted R-square values are summarized in Table 4.2. Anisotropic parameters of the upper layer ( $\phi$ -top,  $\delta$ -top) and deeper layer ( $\phi$ -bot, and  $\delta t$ -bot) are presented for the stations involved in the modeling process.



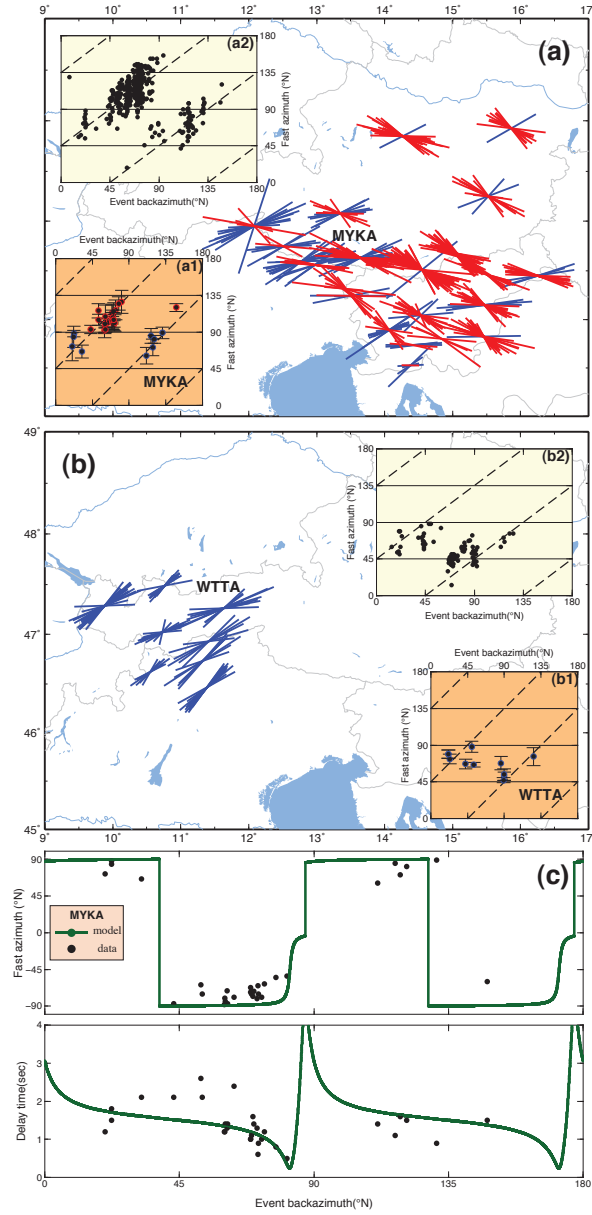


**Figure 4.5:** Periodicity of fast orientations as function of event backazimuth. a) Measurements shown at the stations in the eastern part. a1) A single station as example, MYKA, of  $\pi/2$  periodicity. a2) All measurements obtained at stations in the eastern part of the study area, showing  $\pi/2$  periodicity. b) Measurements obtained from the stations in the West do not show  $\pi/2$  periodicity neither at the single station (b1, WTTA) nor for all measurements in this area (b2). c) Theoretical distribution of apparent splitting parameters from the best-fit two layers model for MYKA. Black circles are the good quality measurements used in the modeling process. Top and bottom panel show fast axis orientation and delay time respectively.

As shown in Figure 4.6a, for the upper layer, most of the stations yield fast axes in NW-SE orientation. They are in agreement with the average fast azimuth of stations in the eastern part (Fig. 4.2). The results indicate fast azimuth between N110° and N140°

**Table 4.2:** Two-layer modeling results. Fast axis azimuth ( $\phi$ -top) and splitting delay ( $\delta t$ -top) of the upper anisotropic layer.  $\phi$ -bot, and  $\delta t$ -bot are the parameters of the deeper anisotropic layer. Adjusted coefficient of determination (R-square) values are also listed together with the number of data used in the modeling process at each station. For the procedure yielding them, see the text and Appendix B.

Station	Lon(°E)	Lat(°N)	$\phi$ -top(°N)	$\delta t$ -top(s)	$\phi$ -bot	$\delta t$ -bot	$R^2$ -adj	N
ABTA	12.5123	46.7474	110	0.5	60	0.8	0.44064	9
ARSA	15.5230	47.2505	130	1.3	60	0.4	0.87185	13
CONA	15.8618	47.9282	130	1.0	50	0.4	0.97441	15
CRES	15.4578	45.8260	140	1.3	60	0.8	0.96365	26
DOBS	15.4691	46.1495	140	1.0	80	0.6	0.91705	24
GROS	15.5017	46.4608	110	1.8	40	0.8	0.99871	10
KBA	13.3447	47.0784	90	1.0	60	0.4	0.66214	16
KOGS	16.2503	46.4481	100	0.5	80	1.1	0.87627	22
LJU	14.5278	46.0438	140	1.2	60	0.5	0.87236	14
MOA	14.2659	47.8495	120	0.9	90	0.4	0.98031	35
MYKA	13.6416	46.6299	100	0.5	80	1.1	0.90708	31
OBKA	14.5489	46.5092	120	1.4	70	1.2	0.99165	47
PERS	15.1139	46.6365	110	1.5	50	0.9	0.99735	17
RISI	12.0800	46.9500	160	0.4	60	2.1	0.63477	16
ROBS	13.5103	46.2450	140	1.1	160	0.8	0.81959	9
SOKA	15.0327	46.6780	110	1.7	50	1.0	0.99616	23

with the exception of KBA (90°) and RISI (160°). Moving to the East, the splitting delays for the upper anisotropic layer increase, reaching maximum values (1.7, 1.8 s) at SOKA and GROS respectively (KOGS marks an exception to this trend). The minimum splitting delay (0.4 s) is obtained for RISI which is situated at about 12°E.

Although the fast orientations for the deeper layer are not as tightly grouped as those for the upper layer, the overall pattern of modeled fast azimuth is in good agreement with the average measured values at the westernmost stations (black lines in Fig. 4.6b). Stations located North of the Periadriatic lineament generally show similar fast azimuth (exception for MOA). On the other hand, stations in the Southern Alps (south of Periadriatic line) show a complicated pattern. This might indicate complex anisotropic structure in the southern part of the area. Splitting delays show a slight decrease towards the North and towards the South with respect to the Periadriatic lineament, we anyway do not consider meaningful the splitting delays variation for this deeper layer. Figure 4.6 (right panel) shows the three-dimensional spatial distribution of splitting delays of the two layers. The location of the stations involved in the modeling process is displayed in the upper horizontal plane. The vertical axes represent the amount of

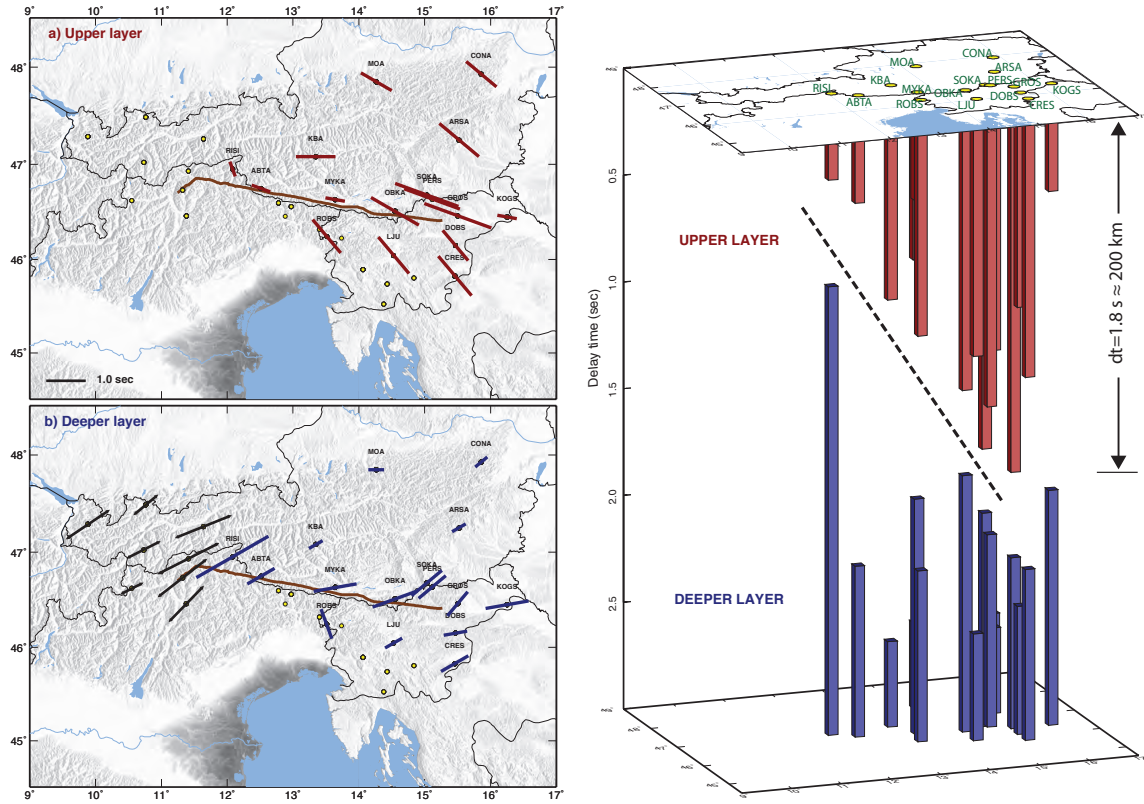


**Figure 4.6:** Left panels: Maps of splitting parameters for the two anisotropic layers. a) Fast axis azimuths of the upper layer are shown by the orientation of the red lines, with lengths of lines showing the relevant splitting delays. b) Deeper layer (blue lines). Right panel; Three-dimensional spatial distribution of splitting delays for the upper layer (red bars) and the deeper layer (blue bars). Station location is shown in the horizontal plane. Vertical axes display the amount of splitting delays. Dashed line marks the possibility of an inclined interface between the upper and deeper anisotropic layers. Considering anisotropy magnitude of 3-5% and 1.8 s splitting delay, result in an anisotropic path (layer thickness) of about 200 km at stations GROS and SOKA (right panel, and Figure 4.2). The anisotropic path can be estimated using  $D = \frac{v_s^2 dt}{dv} = \frac{v_s dt}{\delta v}$ , where  $v_s$  is shear-wave velocity,  $\delta v = \frac{dv}{v}$  represents the magnitude of anisotropy, and  $dt$  is the amount of delay time.

splitting delays for the anisotropic layers. The splitting delay gradient (from West to East) in the upper layer is clearly visible in the 3D spatial distribution. The maximum splitting delay in the deeper layer (2.1 s) is observed at station RISI, this station also displays the minimum splitting delay for the upper layer. In this situation, the strong effect of anisotropy due to the deeper layer might indicate the larger thickness of deeper structure in comparison with the smaller thickness and weak effect of the upper structure. According to the splitting delay distribution in the upper and deeper layer, we can draw an inclined boundary between these two layers as it is displayed by the dashed line in Figure 4.6 (right panel), which would mark a wedge-shaped upper anisotropic layer on the top.

### 4.5.3 Anisotropy versus tomographic images

Tomographic images of the eastern Alpine mantle highlight the presence of high-velocity bodies interpreted as the cold lithospheric slab (*Piromallo and Morelli*, 2003; *Lippitsch et al.*, 2003; *Koulakov et al.*, 2009; *Mitterbauer et al.*, 2011). Along the Alps, the high-velocity anomaly nearly follows the trend of the mountain chain and is placed almost vertically. Figure 4.7 shows horizontal depth slices of P-wave velocity anomalies at 150, 300, 510 km after *Mitterbauer et al.* (2011), and at 150, 240, 350 km after *Lippitsch et al.* (2003). The high-velocity bodies (blue areas in Figure 4.7, at 150 km) have been interpreted as southeastward-subduction of European slab in the West, and as northeastward subducting Adriatic slab in the East (*Lippitsch et al.*, 2003; *Kissling et al.*, 2006). In another hypothesis, the two high-velocity bodies in the West and in the East (Fig. 4.7, at 150 km) have been interpreted and related to nearly vertical southward-subducting European slab (*Mitterbauer et al.*, 2011; *Brückl*, 2011). In addition to these two regional-scale models, the upper mantle structure of the European-Mediterranean area has also been imaged by tomography from *Piromallo and Morelli* (2003) and *Koulakov et al.* (2009). Depth slices through the velocity models of these studies at 150, 300, 500 km are also shown in Figure 4.7.

To compare velocity anomalies and the anisotropy pattern retrieved in this study, the depth projections of individual measurements are superimposed on the tomography sections at 150 km for all models as shown in Figure 4.7. The NE-SW fast orientation at longitudes less than  $\sim 12^\circ\text{E}$  cannot be related to the high-velocity anomaly alone (cold lithospheric slab) since we observed the same fast orientation outside of the high-velocity body. For the measurements in the eastern part, there is no considerable match of fast orientation neither with the high-velocity nor to the low-velocity anomalies.

Although we cannot directly attribute the anisotropy pattern to the high/low-velocity anomalies, we instead focus on the trend of high-velocity body in comparison to the results of the two anisotropic layers modeling (Fig. 4.6). In both *Lippitsch et al.* (2003) and *Mitterbauer et al.* (2011) models, further at depth, the high-velocity anomalies move ENE-ward to Eastward, revealing a steeply down-going cold slab, with tendency to follow the Alps-Carpathian trend. This down-going body is observed in *Lippitsch et al.* (2003) velocity model only down to about 250 km depth while in *Mitterbauer et al.* (2011) model it reaches 510 km depth.

*Piromallo and Morelli* (2003) and *Koulakov et al.* (2009) show similar velocity structures for the upper mantle (Fig. 4.7) in which the positive velocity anomalies in the Eastern



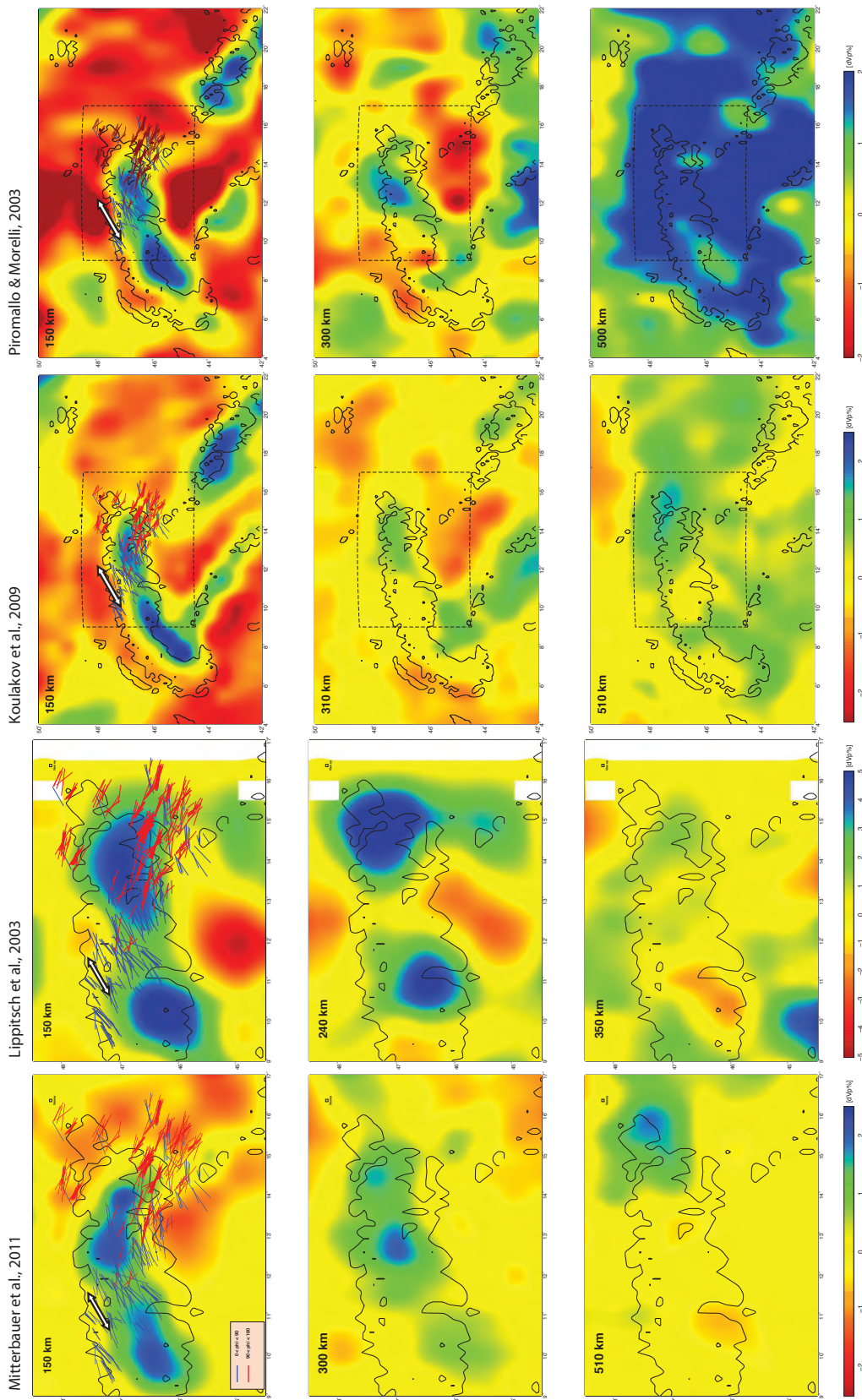


**Figure 4.7:** Tomographic depth slices after *Mitterbauer et al.* (2011), at 150, 300, and 510 km depth, *Lippitsch et al.* (2003) at 150, 240, and 350 km, after *Koulakov et al.* (2009), at 150, 310, and 510 km, and *Piromallo and Morelli* (2003) at 150, 300, and 500 km depth. Projections at 150 km depth of individual splitting measurements are superimposed on the tomography depth slices for all models. EU plate motion (N240°) with respect to hotspot reference frame (HS3-NUVEL-1A plate model, *Gripp and Gordon* (2002)), is shown by black-white double arrow. Black contours are topography in 700 m elevation anomalies showing the trend of orogenic belts. Coincidence of the trend of Alpine and Dinaride mountain chains with the high-velocity anomalies can be seen at 150 km depth slices. For comparison, the box used in the two models on the left is reproduced on the right panels.

Alps have been observed at 150 km depth and steeply extend down to the East reaching the depth of 500 km. A slab graveyard is suggested at a depth  $\geq 500$  km almost covering the whole area beneath the Alpine-Mediterranean region.

#### 4.5.4 Origin of the anisotropy

The spatial variation of velocity anomalies from tomographic models together with geophysical and petrofabric findings are employed here in order to constrain depth and origin of the two anisotropic layers.

Figure 4.8 displays an East-West cross-section through the velocity anomalies from the tomography model of *Mitterbauer et al.* (2011), together with the location of this profile on the 150 km depth slice (Fig. 4.8, top). On the E-W cross-section, the steeply eastward-dipping lithosphere, and the area consisting of low-velocity anomaly on the right-hand side of the dipping slab can be seen. The tapered low-velocity zone is reminiscent of the wedge-shaped distribution of splitting delays of the upper layer (Fig. 4.6). The correspondence of this low-velocity zone with the geometry of the upper layer can be evaluated by tracing the rays, which reach the stations located on the selected E-W profile. Figure 4.8 shows the ray paths, plotted according to the relevant events backazimuth and incidence angles. The events recorded at the station located above the low-velocity zone (SOKA) should mostly sample this area of low velocity. On the other side, the events collected at ABTA should mostly sample the high-velocity zone (Fig. 4.8). Measurements from these two stations are in good agreement with what we expect from the geometry of velocity anomalies. Dominant fast azimuth are NW-SE oriented for SOKA and mostly NE-SW orientation at ABTA (Fig. 4.8, top), indicating a noticeable difference in anisotropy structure between down-going lithosphere and the low-velocity zone.

In addition, we can also compare with lithospheric thickness estimates in the region to address the origin of anisotropic structure. It has been shown that crustal (lithospheric) thickness decreases from 50 (170-200) km at the eastern end of Tauern Window to 25 (60) km at the easternmost part of the Alps (*Ratschbacher et al.*, 1991; *Frisch et al.*, 1998, and reference therein) along the mountain chain, over a distance of 200 km. This is in agreement with the lithosphere-asthenosphere boundary (LAB) depth derived by receiver function analysis, which is mostly less than 100 km with an average of 70 km for the Eastern Alps (*Bianchi et al.*, 2014; *Jones et al.*, 2010, and reference therein). For instance, the LAB depth is estimated 98 km at ABTA and 70 km at SOKA (*Bianchi*



*et al.*, 2014). Therefore, the negative gradient of lithospheric thickness toward the East displays an opposite trend with respect to the positive gradient of splitting delays of the upper anisotropic layer (Fig. 4.6).

Moreover, experimental mineral physics findings derived from upper mantle rock samples suggest an anisotropy of 3-5% in the mantle (*Ben Ismail and Mainprice*, 1998; *Mainprice et al.*, 2000; *Barruol et al.*, 2011). Taking this magnitude into consideration and the amount of splitting delays of the upper layer, an anisotropic structure  $\sim 50$  km thick (at RISI) and  $\sim 200$  km (at GROS, Fig. 4.6) is required for the western and eastern end of the upper layer respectively. Consequently, based on crustal and LAB depths under the Eastern Alps, the lithospheric mantle is not thick enough to represent the observed upper anisotropic layer.

Beside that argument, the results of recent shear-wave-splitting analyses (*Stuart et al.*, 2007; *Qorbani et al.*, 2014) showed that the NW-SE fast anisotropic orientation is not restricted to beneath the Eastern Alps only, but is also widely observed within the Carpathian-Pannonian region. This anisotropy pattern spreads in a wide area from the western margin of the Eastern Alps ( $\sim 12^\circ\text{E}$ ) to the easternmost part of the Pannonian basin ( $\sim 23^\circ\text{E}$ ). Over these areas, the rigid lithosphere might have suffered different tectonic events, which has led to changes in the fossil anisotropy within the lithosphere. It is thus unlikely that the anisotropy has the same lithospheric-origin over a distance of 1300 km. Hence, an asthenospheric origin is most probable.

#### 4.5.4.1 Upper anisotropic layer:

The upper layer exposes an anisotropic pattern that is NW-SE oriented, with a mean fast azimuth of  $\text{N}118^\circ$ . This orientation does not follow the trend of the Alpine mountain chain, which is in contrast to the belt-parallel anisotropy that we expect in such a subduction-associated mountain chain, e.g. the Western Alps. Since also the splitting delay is too large to be explained by the lithosphere alone, as described above, sublithospheric materials beneath the thin lithosphere likely cause this anisotropy pattern. Therefore we attribute the upper anisotropic layer to an asthenospheric flow, which is oriented NW-SE (Fig. 4.9).

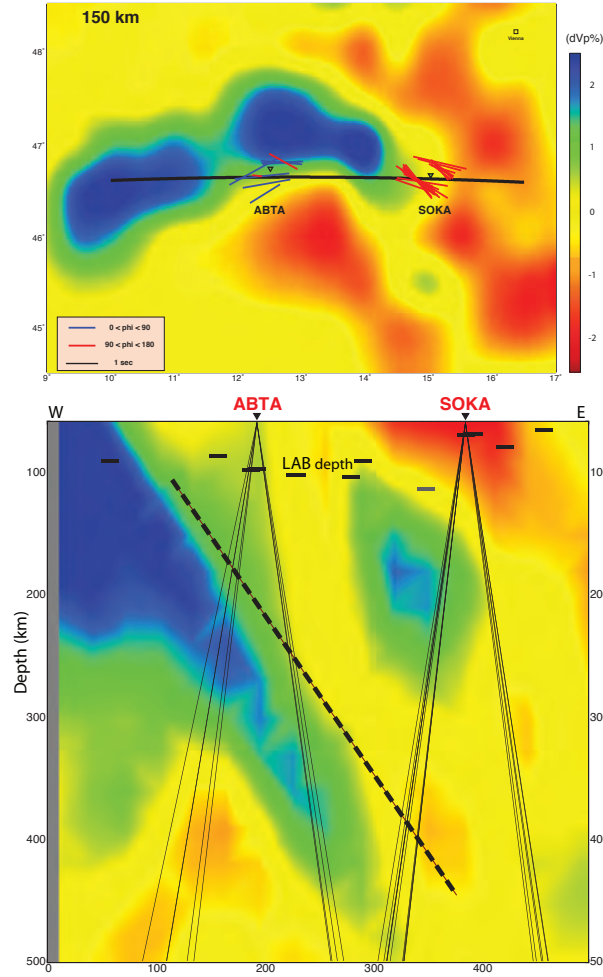


**Figure 4.8:** Horizontal and vertical cross-sections through the velocity anomalies *Mitterbauer et al.* (2011). Top) Depth slice (horizontal) at 150 km depth. Projected measurements at ABTA and SOKA together with the station locations are illustrated on the depth slice. Fast axis azimuths measured at ABTA mostly are smaller than N90° (blue lines) while the measurements from SOKA dominantly display NW-SE orientation (red lines). Bottom) E-W cross-section (vertical) through the velocity anomalies. Two stations located above the high-velocity (ABTA) and low-velocity body (SOKA) are shown. Rays coming to these stations are plotted according to their relevant backazimuths and incidence angles. Lithosphere-asthenosphere boundary (LAB) from receiver function analysis (*Bianchi et al.*, 2014) is shown by thick dashed lines. An inclined interface (dashed line) can be considered between the eastward down-going high-velocity body and low-velocity zone, likewise between the deeper and upper anisotropic layers (Fig. 4.6).

#### 4.5.4.2 Deeper anisotropic layer:

The deeper layer with anisotropic fast orientation of SW-NE (overall azimuth N75°) is in good agreement with the anisotropy detected under the Central Alps (Figs. 2 and 6). We relate the deeper anisotropic layer to a lithospheric origin as a detached slab beneath the Eastern Alps (Fig. 4.9). This anisotropy is remarkably similar to the anisotropy

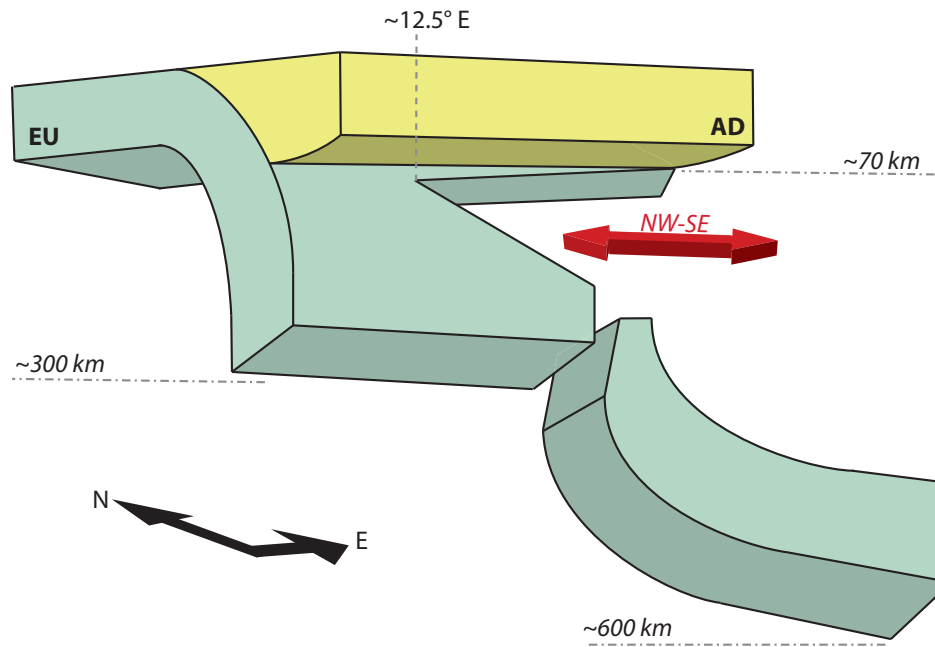


**Figure 4.9:** Schematic figure of the upper mantle structures of the Eastern Alps based on the presence of two layers of anisotropy. The deeper layer with NE-SW fast orientations of anisotropic axes is interpreted as a detached slab of European origin which may connect with the lithosphere under the western part of the Eastern Alps and possibly to the large-scale slab graveyard beneath the Carpathian-Pannonian region. The upper layer, located between the detached slab at the bottom of the thin lithosphere, with NW-SE fast orientations shows similar geometry with the low-velocity area under the Eastern Alps (Fig. 4.8). The layer is attributed to the asthenospheric flow above the detached slab with NW-SE orientation.

pattern of the Central Alps, which follows the Alpine chain. The deeper anisotropic layer may thus represent the same lithospheric layer found in the West and Central Alps therefore we suggest a detached slab is originated from the European (EU) slab. This can be part of the Alpine-Tethys lithosphere (Penninic ocean) (Mitterbauer *et al.*, 2011; Brückl, 2011).

By considering about 200 km thickness for the upper layer at GROS in addition to 70 km lithospheric thickness, the deeper layer would begin at a depth of about 270 km which is comparable to already proposed detached slab models that place it at more than 300 km depths (Piromallo and Faccenna, 2004). The detached slab may have started to break-off at about 29 Ma (Schmid *et al.*, 2013) and it might still be connected to the EU slab at about 300 km depth. It also may connect to the slab graveyard under the Eastern Alps and the Carpathian-Pannonian region, which has already been observed (Bijwaard *et al.*, 1998; Piromallo and Morelli, 2003; Koulakov *et al.*, 2009).

#### 4.5.4.3 Western part, 9°E to 12°E:

The western portion of the Eastern Alps shows a simpler anisotropy pattern, which was not included in the process of two layers modeling. Further to the West, at the western arc of the Alps there is a good correlation (at large scale) between anisotropy, the high-velocity zones (tomographic images), Bouguer gravity anomalies, and the topographic feature of the mountains. These might reflect the lithospheric origin of anisotropy (*Barruol et al.*, 2011). However, to explain the large splitting delays in that area, it has been suggested that anisotropy in the Western and Central Alps may be due to asthenospheric flow that turns around the subducting EU lithosphere (*Barruol et al.*, 2011; *Salimbeni et al.*, 2013). Such upper mantle flow around the subducting slab was also suggested in the subduction rollback model (e.g. *Funiciello et al.*, 2006; *Piromallo and Faccenna*, 2004).

Similarly, in the western portion of the Eastern Alps, a deep EU slab can be associated with anisotropy due to stored deformation from past episodes of the tectonic evolution. Mountain-chain-parallel anisotropy in this region is also a signature for a strong contribution of lithospheric fabric. In the area between 9-12°E in which  $\sim$ N60° average fast azimuth is measured, comparison with tomographic images shows that the stations located inside and outside of the high-velocity regions (cold slab) (see Fig. 4.7) present similar fast orientations. This indicates that SKS rays have sampled both cold lithosphere and the warmer materials around (low-velocity anomalies), suggesting a correlation between frozen-in anisotropy in the lithosphere and asthenospheric flow, which have similar orientation. There is a coherence of upper mantle flow and lithospheric alignments until longitude of 12°E, in which fast azimuths are in the range of N60°-N70° (Fig. 4.2).

To test the possibility of plate-motion-related flow, we consider the direction of plate motion. For the European plate it is in a direction of N240° with respect to the hotspot reference frame (HS3-NUVEL-1A plate model, *Gripp and Gordon* (2002)). This motion may be associated very well to upper mantle flow (e.g. *Barruol et al.*, 2011). Since the fast axis azimuth in the Central Alps is NE-SW oriented, there is a good fit with the plate motion direction and orientation of the anisotropy.

Therefore, in addition to a lithospheric origin for the western portion of the Eastern Alps, we attribute the anisotropy also to the asthenospheric lineation. This argument is stronger for the northern margin of the mountain chain in which most measurements are located to the North of the high-velocity body (Fig. 4.7). In the southern margin, although we do not have any measurements to the South of the EU lithospheric slab

(high-velocity regions, Fig. 4.7), the station averages of fast axis azimuth (*Salimbeni et al.*, 2013), show the azimuth of N30° to N53° (Fig. 4.2) that are close to our results and to the movement direction of EU plate as well. This suggests that part of the observed anisotropy in this region is due to upper mantle flow surrounding the down-going lithospheric slab. However, in this area, is unclear how much of this anisotropy was caused by past lithospheric deformation and how much by present-day dynamic processes in the asthenosphere.

The schematic Figure 4.9 illustrates the suggested interpretation for the Eastern Alps. The attached sub-vertical subduction of the European slab is suggested until about 12°E, in the center of the Tauern Window region. The subducting EU slab starts to detach at about 12°E. This asthenosphere material flows into the wedge-shaped space under the Eastern Alps which extends to the East. The deep detached slab, which might be still connected to the subducting slab, is steeply down-going to reach the slab graveyard under the Eastern Alps and the Carpathian-Pannonian region. The detachment may be caused by the difference in the sinking rates along the subducting plate between deep and shallow part of the slab. This can be due to differences in densities showing different origin of the slabs (e.g. oceanic and continental lithosphere).

The asthenospheric flow above the detached slab is NW-SE oriented. This upper mantle flow might be explained by a corner flow above a subducting slab, with flow direction normal to the strike of the slab (e.g. *Fischer et al.*, 2000), which gives trench-perpendicular anisotropy. However, fluid dynamic modeling has shown that the curvature of the slab can impose trench-parallel mantle wedge flow in the arc and trench-perpendicular flow on the flat slab, which is controlled by three-dimensional changes in the slab geometry (*Kneller and van Keken*, 2007; *Hoernle et al.*, 2008). Such changes from trench-parallel to trench-perpendicular anisotropy also have been suggested by the shear-wave splitting observations (*Anderson et al.*, 2004; *Kneller and van Keken*, 2007).

Although the SKS measurements in the western arc of the Alps show parallelism between anisotropy and the curvature of the slab (*Barruol et al.*, 2011; *Bokelmann et al.*, 2013), the measurements of anisotropy in the Eastern Alps (which is analogous to the flat slab) are oriented at an angle of 30°-50° with respect to the strike of the EU subducting slab (the North Alpine thrust). The deviation of anisotropy from trench-perpendicular direction might be due to the geometry of the slab detachment in this area where there is a gap between lithosphere on the top and the detached slab on the bottom. The flow may be induced by compensation of the mass lack due to slab detachment in order to fill the gap in between.

## 4.6 Conclusions

Upper mantle anisotropic structure under the Eastern Alps has been investigated using SK(K)S splitting measurements. We have shown that while the average values of fast orientations show clear mountain-parallel anisotropy pattern for the Western Alps, this pattern clearly breaks down in the Eastern Alps. Individual measurements at single stations provided an image of lateral changes of anisotropy with a transition area occurring at the same location as the overall pattern is broken.

The backazimuthal variations of fast orientations have been modeled as vertical changes in order to assess the depth sources of anisotropy. The results suggest the presence of two anisotropic layers under the Eastern Alps. By analogy between these results and the tomographic images, a possible origin of upper mantle anisotropy is presented as:

- (1) beneath the Eastern Alps, the deeper layer with NE-SW fast orientation, is characterized by a detached slab of European origin.
- (2) We attribute the upper layer to the asthenospheric flow with NW-SE orientation which is above the detached slab and below thin lithosphere. The flow can be induced by corner flow at the subduction wedge resulting trench-perpendicular fast orientation pattern. However the deviation of the NW-SE flow orientation from trench-normal direction may possibly be due to variation in the slab geometry which causes the slab detachment.
- (3) The measurements at the western part of the Eastern Alps show a simple pattern of anisotropy with NE-SW fast orientation, similar to the pattern of the deeper layer. In this area, the lithospheric alignments and sub-lithospheric material flow are aligned in the same direction.

## Acknowledgments

We thank Ewald Brückl, Stefan Schmid, Peter Molnar, Walter Kurz, and Wolfgang Frisch for the discussion. We also thank Regina Lippitsch, Ulrike Mitterbauer, Ivan Koulakov, Claudia Piromallo and Andrea Morelli for their regional velocity models. The data in this study are from the permanent Austrian network run by the Zentralanstalt für Meteorologie und Geodynamik (ZAMG)(<http://www.zamg.ac.at>), the Slovenian seismic network (SL), the Italian seismic network (IV), the NE-Italian broadband network (NI), and the South-Tyrolian network (SI). We acknowledge funding by the Austrian Science Fund (FWF) through projects 26391 and 24218.



## 4.7 Supplementary figures

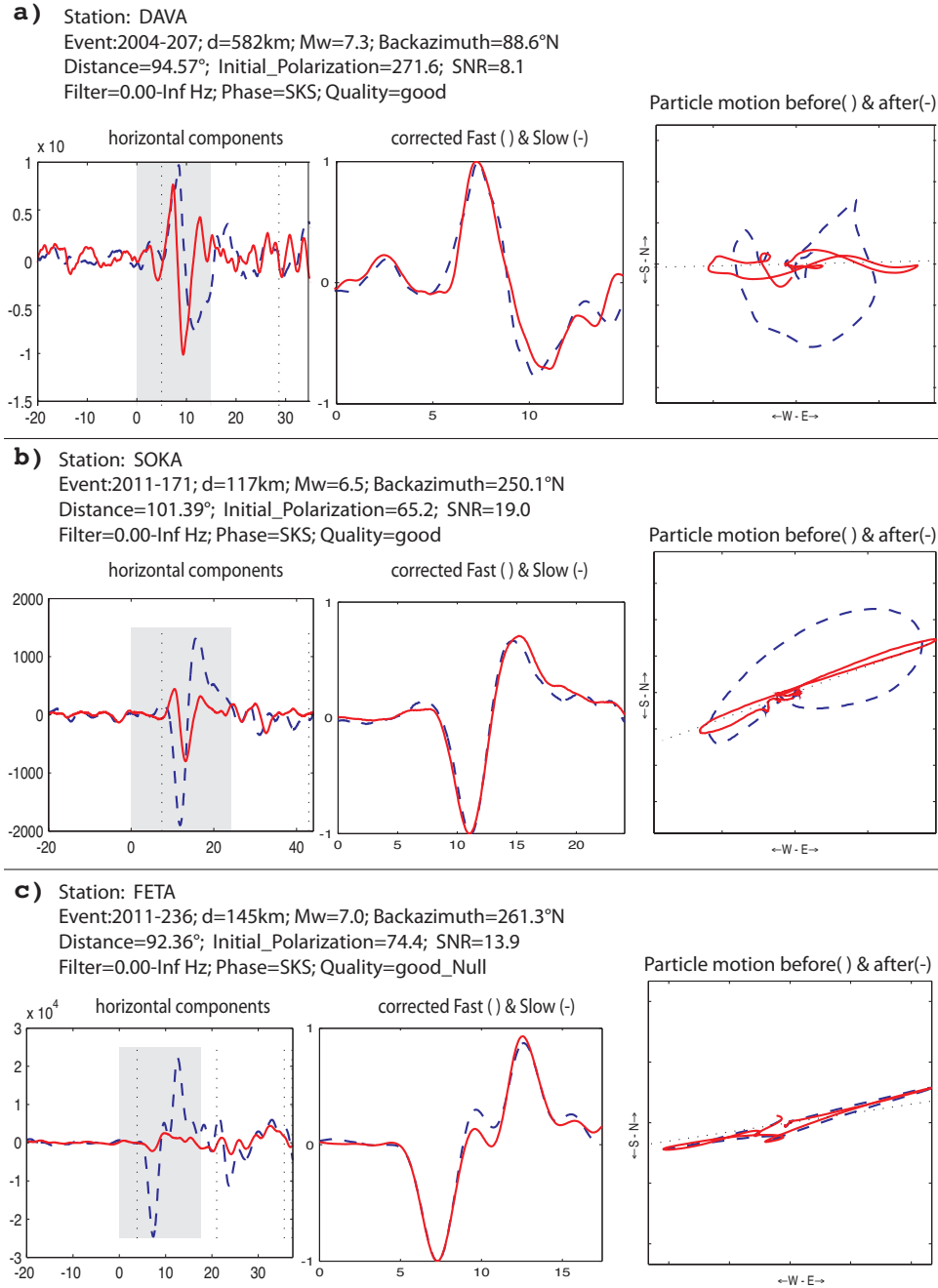


**Figure 4.10: (S1):** Examples of SKS splitting measurements obtained by the minimum energy (SC) technique using SplitLab package at stations a) DAVA and b) SOKA. c) example of Null measurements for FETA. No filter was applied on the waveforms. In a, b, c, the left panels show the horizontal (radial-dashed, transverse-solid) components, in the middle panel fast and corrected time-matched slow (solid and dashed) components of the SKS wave, and the right panel the horizontal particle motion before (dashed) and after (continuous) anisotropy correction. In the case of Null, the initial and corrected particle motions are linear.

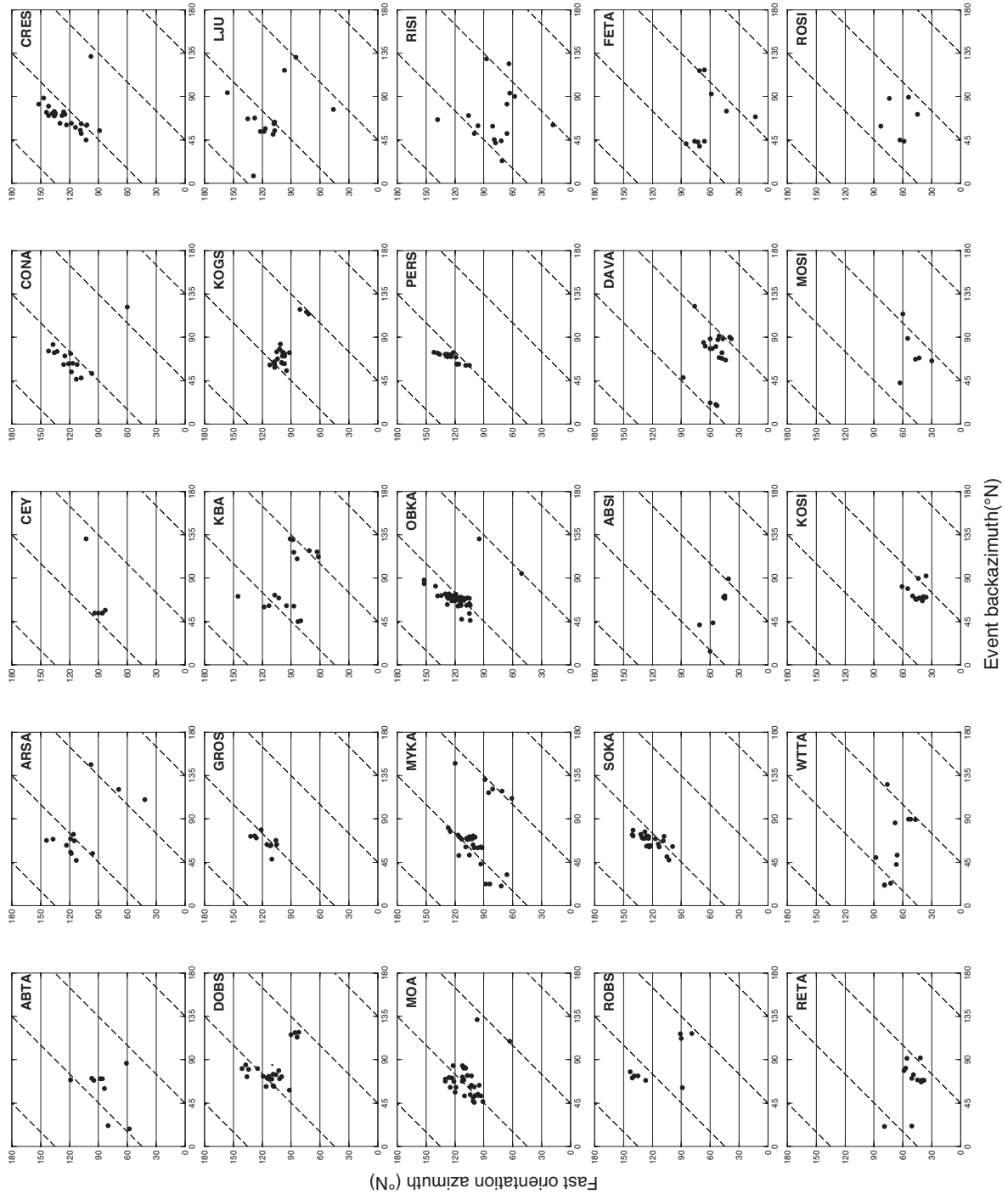


**Figure 4.11: (S3):** Variation of anisotropic fast orientation as function of event backazimuth. Black circles show the azimuth of the fast axes orientations.  $\pi/2$  periodicity can be observed for the measurements at the most of the stations located at the east of the region (KBA, MOA, CONA, ARSA, SOKA, OBKA, MYKA, PERS, KOGS, GROS, DOBS, LJU, ROBS, CRES, RISI, ABTA, CEY). Dashed lines represent theoretical  $\pi/2$  periodicity based on the horizontal (backazimuth) and vertical (fast orientation) axes which are in range of 0-180°. Stations situated at the west mostly do not show this periodicity (DAVA, RETA, FETA, MOSI, WTTA, ROSI, ABSI, KOSI). Fast orientation (vertical axis) and backazimuth (horizontal axis) are plotted in the scale of 0-180°. Connected lines between the angles with  $\pi/2$  difference on the vertical and horizontal axes, represent  $\pi/2$  periodicity (dashed lines). We used this approach as a pre-assessment of  $\pi/2$  periodicity before trying to find the best-fit two layers model for each station.

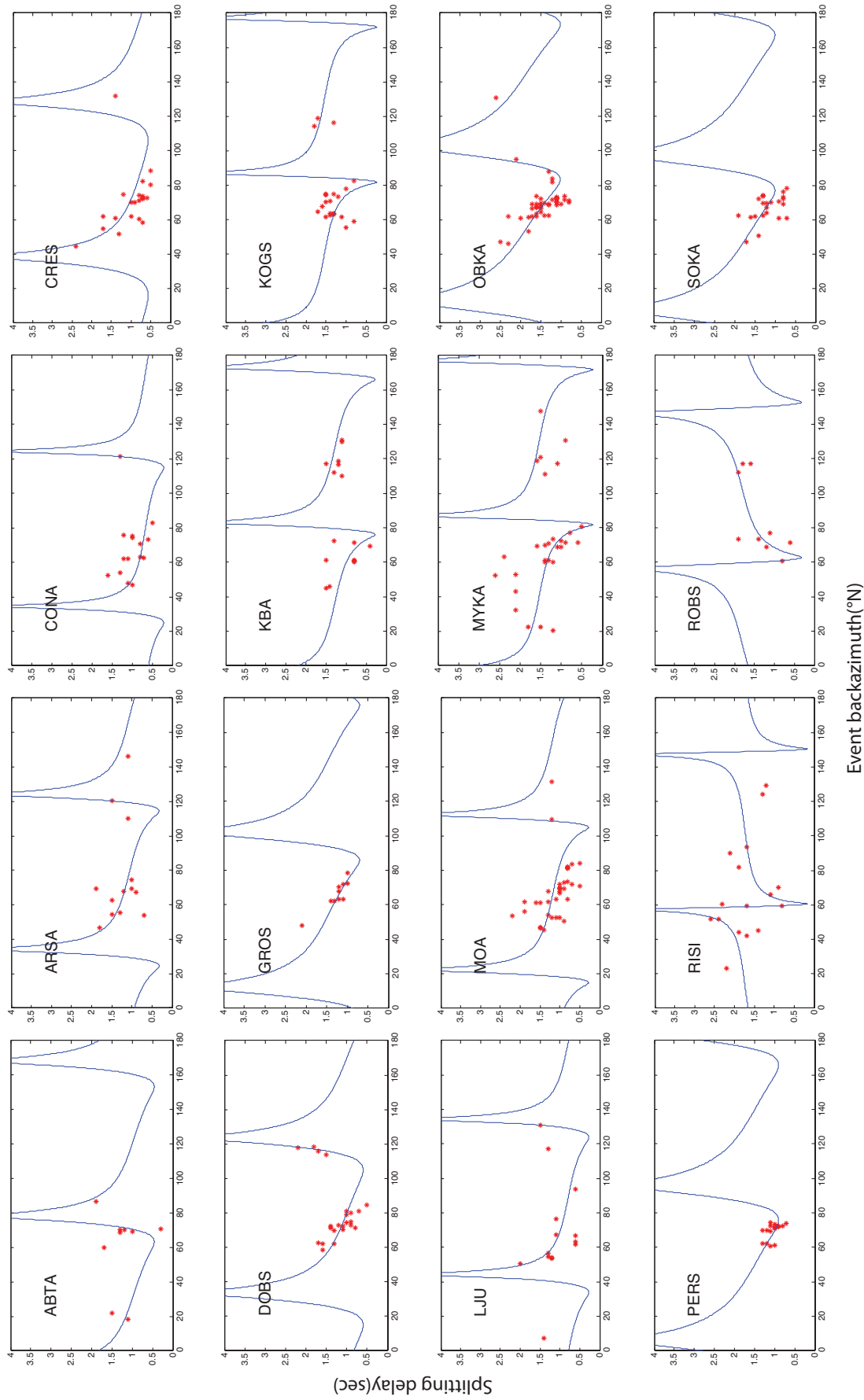


**Figure 4.12: (S4):** Variation of splitting delay times as function of event backazimuth for 16 stations which were involved into the single station modeling. Red stars show the splitting delay time (sec) and blue curves represent  $\pi/2$  periodicity from best-fit splitting parameters of two layers at the respective station.

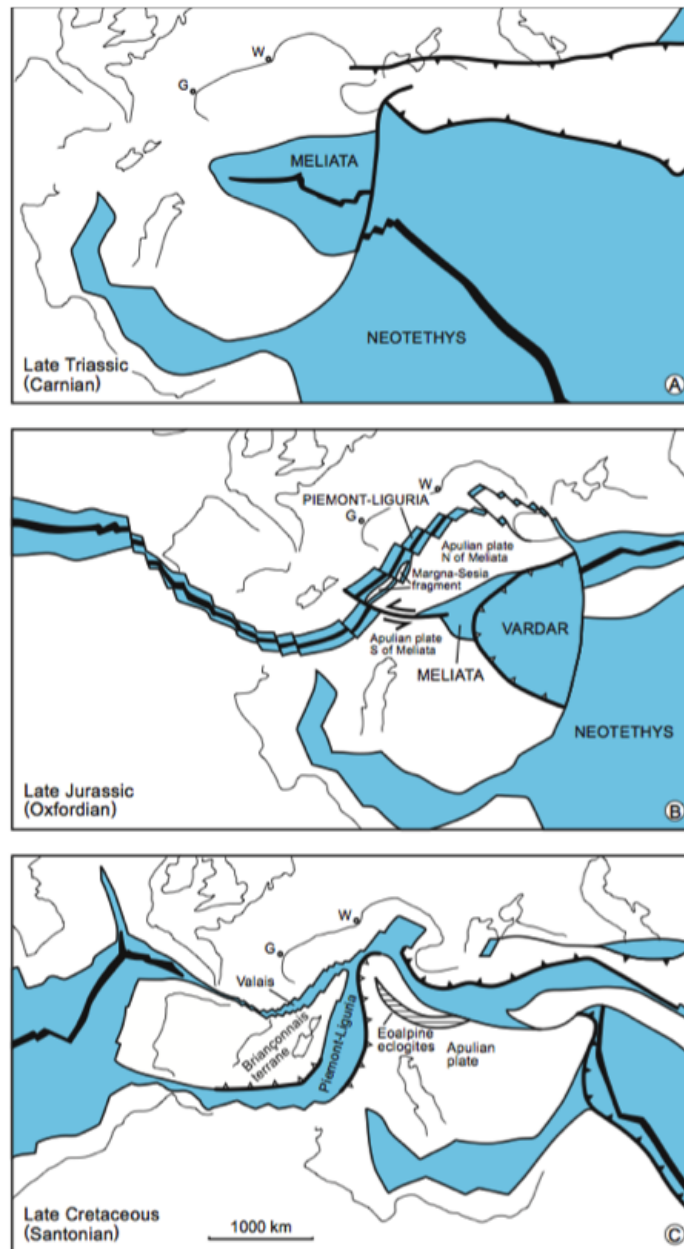


**Figure 4.13: (S5):** Paleogeographic map (*Schmid et al.*, 2004). This figure is a supplementary item to the thesis which is not included in the published paper

## Published paper:

Earth and Planetary Science Letters 409 (2015) 96–108



Contents lists available at ScienceDirect

## Earth and Planetary Science Letters

[www.elsevier.com/locate/epsl](http://www.elsevier.com/locate/epsl)

## Slab detachment under the Eastern Alps seen by seismic anisotropy



Ehsan Qorbani\*, Irene Bianchi, Götz Bokelmann

Department of Meteorology and Geophysics, University of Vienna, Austria

## ARTICLE INFO

## Article history:

Received 23 July 2014

Received in revised form 17 October 2014

Accepted 21 October 2014

Available online 17 November 2014

Editor: P. Shearer

## Keywords:

shear-wave splitting

upper mantle dynamics

deformation

lithosphere

asthenospheric flow

## ABSTRACT

We analyze seismic anisotropy for the Eastern Alpine region by inspecting shear-wave splitting from SKS and SKKS phases. The Eastern Alpine region is characterized by a breakdown of the clear mountain-chain-parallel fast orientation pattern that has been previously documented for the Western Alps and for the western part of the Eastern Alps. The main interest of this paper is a more detailed analysis of the anisotropic character of the Eastern Alps, and the transition to the Carpathian–Pannonian region. SK(K)S splitting measurements reveal a rather remarkable lateral change in the anisotropy pattern from the west to the east of the Eastern Alps with a transition area at about 12°E. We also model the backazimuthal variation of the measurements by a vertical change of anisotropy. We find that the eastern part of the study area is characterized by the presence of two layers of anisotropy, where the deeper layer has characteristics similar to those of the Central Alps, in particular SW–NE fast orientations of anisotropic axes. We attribute the deeper layer to a detached slab from the European plate. Comparison with tomographic studies of the area indicates that the detached slab might possibly connect with the lithosphere that is still in place to the west of our study area, and may also connect with the slab graveyard to the East, at the depth of the upper mantle transition zone. On the other hand, the upper layer has NW–SE fast orientations coinciding with a low-velocity layer which is found above a more-or-less eastward dipping high-velocity body. The anisotropy of the upper layer shows large-scale NW–SE fast orientation, which is consistent with the presence of asthenospheric flow above the detached slab foundering into the deeper mantle.

© 2014 The Authors. Published by Elsevier B.V. This is an open access article under the CC BY-NC-ND license (<http://creativecommons.org/licenses/by-nc-nd/3.0/>).

## 1. Introduction

Seismic anisotropy is defined as a directional dependence of seismic velocity. It is assumed that the upper mantle presents significant anisotropy (Maupin and Park, 2007). This anisotropy is most probably due to a non-random distribution of crystallographic orientation of minerals in the olivine-rich ultramafic upper mantle rocks. The non-random distribution is known as lattice-preferred-orientation (LPO). The relation between the typical intrinsic anisotropy in the upper mantle and LPO, which is a result of the deformation, has been well-documented (Babuška and Cara, 1991; Silver and Chan, 1991; Mainprice et al., 2000). It is generally accepted that the anisotropy is due to deformation that either occurred at earlier times (“fossil deformation”) or due to present tectonic activities (Savage, 1999, and references therein). In either case, the anisotropy can indicate the geometry of the flow. Therefore mapping seismic anisotropy can resolve the pattern of

mantle flow in the asthenosphere as well as the fossil deformation pattern within the lithosphere, which has great importance for understanding the upper mantle geodynamics.

The simplest measure of upper mantle anisotropy is the shear-wave splitting, particularly using SKS core phases (e.g. Vinnik et al., 1984; Silver and Chan, 1988; Long and Silver, 2009) which have been studied extensively in recent years. Near-vertical incidence angles of SKS phases give good lateral resolution (i.e. 50 km, the radius of Fresnel zone at 150 km depth), since anisotropy is to be attributed to a steep ray path. However, the depth where the splitting occurs is less well-determined. Although the measuring procedure of shear-wave splitting is straightforward, the practical interpretation of measurements can be quite challenging.

In this study we first present the overall pattern of anisotropy, based on the average values of SKS splitting parameters, then we focus on the spatial changes of the individual measurements and we show striking lateral variations of anisotropy within the region. Later the backazimuthal variation of fast orientations is modeled by means of two anisotropic layers. Finally, using the results of two anisotropic layers modeling, together with some constraints from velocity tomography studies and the analysis of lithospheric

\* Correspondence to: 2D506, UZAll, Althanstrasse 14, 1090 Vienna, Austria. Tel.: +43 1 4277 53727.

E-mail address: [ehsan.qorbani@univie.ac.at](mailto:ehsan.qorbani@univie.ac.at) (E. Qorbani).

<http://dx.doi.org/10.1016/j.epsl.2014.10.049>

0012-821X/© 2014 The Authors. Published by Elsevier B.V. This is an open access article under the CC BY-NC-ND license (<http://creativecommons.org/licenses/by-nc-nd/3.0/>).





# Chapter 5

## Tauern Window

This chapter has been published as: E. Qorbani, W. Kurz, I. Bianchi, and G. Bokelmann, 2015, *Correlated Crustal and Mantle Deformation in the Tauern Window, Eastern Alps*, Austrian Journal of Earth Science, 108/1, 161-173.

### Abstract

We study the coupling between crust and mantle in a convergent regime, by comparing measures of upper mantle deformation with indicators of crustal deformation. We use shear-wave splitting parameters, in particular the orientation of fast axes in the upper mantle measured from data recorded at 8 broadband stations located within the Tauern Window. These are compared with kinematic indicators in the Tauern Window region of the eastern Alps at the outcrop scale. Our results show a striking parallelism between the upper mantle and crustal patterns, indicating vertical coherence of deformation all the way between the crust and the mantle lithosphere. The new findings suggest a vertical coherence of deformation of crust and upper mantle, particularly in the western part of the Tauern Window. Similar pattern in our results and indentation models indicate that the effect of the Adriatic indentation acts on the European lithosphere, not only at crustal but also at lithospheric mantle depths. We discuss the implication of this vertical coherence for the question of mechanical coupling.

## Zusammenfassung

Wir untersuchen die Kopplung zwischen Erdkruste und Mantel in einem tektonisch konvergenten Regime, indem wir die Deformation des oberen Mantels mit Indikatoren der Krustendeformation vergleichen. Dazu verwenden wir Daten von 8 Breitbandstationen innerhalb des Tauernfensters, um seismische Anisotropie aus der Aufspaltung von teleseismischen Scherwellenphasen zu bestimmen, insbesondere die Orientierung der schnellen seismischen Achsen im oberen Erdmantel. Diese werden mit kinematischen Indikatoren im Tauernfenster (Ostalpen) verglichen. Unsere Ergebnisse zeigen eine auffallende Parallelität zwischen den Deformationsindikatoren des oberen Erdmantels und der Erdkruste. Dieses Muster läßt auf eine vertikale Kohärenz der Verformung schließen, zwischen der oberen Kruste bis in die tiefere Mantellithosphäre. Die neuen Erkenntnisse deuten darauf hin, dass die Wirkung des Adriatischen Indenters auf die gesamte (europäische) Lithosphäre wirkt, d.h. nicht nur in der Kruste, sondern auch im lithosphärischen Mantel. Wir diskutieren die Implikationen der vertikalen Kohärenz für die Frage der mechanischen Kopplung.

## 5.1 Introduction

”The extent to which upper crustal deformation is coupled to deformation within the lower crust and mantle ... remains one of the most important and least understood aspects of continental deformation”. This was the case, when Leigh *Royden* (1996) wrote this sentence, and it is still the case today. However, between now and then new observational constraints, especially seismic anisotropy, have become available. In this study we will use these constraints to address the question of coherence of deformation in crust and mantle. The question has a relation with several other important questions that are open, e.g., is crustal and mantle deformation related? Are they of the same age? To which degree do plate-tectonic driving forces that act in the mantle also act on the crust? Are crust and mantle moving together? Is that case at all times, and are they coupled in that sense? We approach these questions in this paper by comparing the pattern of deformation in crust and mantle. For this, it seems best to consider a region where rocks from deeper levels within the crust are exposed at the surface. This is the case in the Tauern Window, which is a key area for understanding late Alpine deformation (e.g. *Lippitsch et al.*, 2003; *Bokelmann et al.*, 2013).

The Tauern Window of the Eastern Alps exposes exhumed parts of Europe-derived crust. The southern European margin was accreted to the base of an Adria-derived upper plate,

represented today by the Austroalpine nappes (e.g. *Schmid et al.*, 2004, 2013). The Tauern Window is characterized by a complex three-dimensional geometry of tectonic units, including important along-strike changes in its structure (*Schmid et al.*, 2013). This geometry, as described by *Schmid et al.* (2013) by combining surface geology with the results of deep seismic reflection measurements (*Gebrande et al.*, 2002; *Lüschen et al.*, 2006), basically resulted from crustal-scale collisional accretion in the Alps followed by late-Alpine indentation, crustal-scale folding, orogen-parallel extension and lateral extrusion (*Ratschbacher et al.*, 1991a).

While the surface geological structure of the Tauern Window is well-understood, the structure of the deeper parts of the lithosphere and the mantle below still remains an open problem in the lithosphere-scale geometry of the Alps-Carpathians-Dinarides system (e.g. *Brückl et al.*, 2007, 2010). This also concerns the quantification of kinematic and dynamic interactions between crustal and mantle structures. Anisotropy measurements (shear-wave splitting) around the Tauern Window have been performed along the TRANSALP profile (*Kummerow and Kind*, 2006), and for the eastern Alps (*Bokermann et al.*, 2013; *Qorbani et al.*, 2015a). They indicate the geometry of "deep deformation" under the area. For quite a while we have noticed the general similarity of those orientations with structures exposed at the surface, as observed in deformational structures in exhumed crustal rocks within the Tauern Window, and we want to study that relation in detail here. A synthetic view of SKS splitting data and structural observations, as presented in this study, should provide an approach to reveal sub-lithospheric deformation beneath the central Eastern Alps. The relation between crustal and mantle deformation has been addressed before, e.g. by comparing mantle anisotropy with orientations of crustal magnetic anomalies for the North American craton (*Bokermann and Wüstefeld*, 2009), where a very good agreement has been found, in the central Asia (*Flesch et al.*, 2005), and in the north and central Aegean (*Brun and Sokoutis*, 2010). In comparison, the agreement over different actively-deforming tectonic regions/regimes in Western North America is less clear.

We start this paper by presenting the geological structure of the area, and later present evidence for deformation at mantle depth – eventually overlaying the two, and discussing their relation.

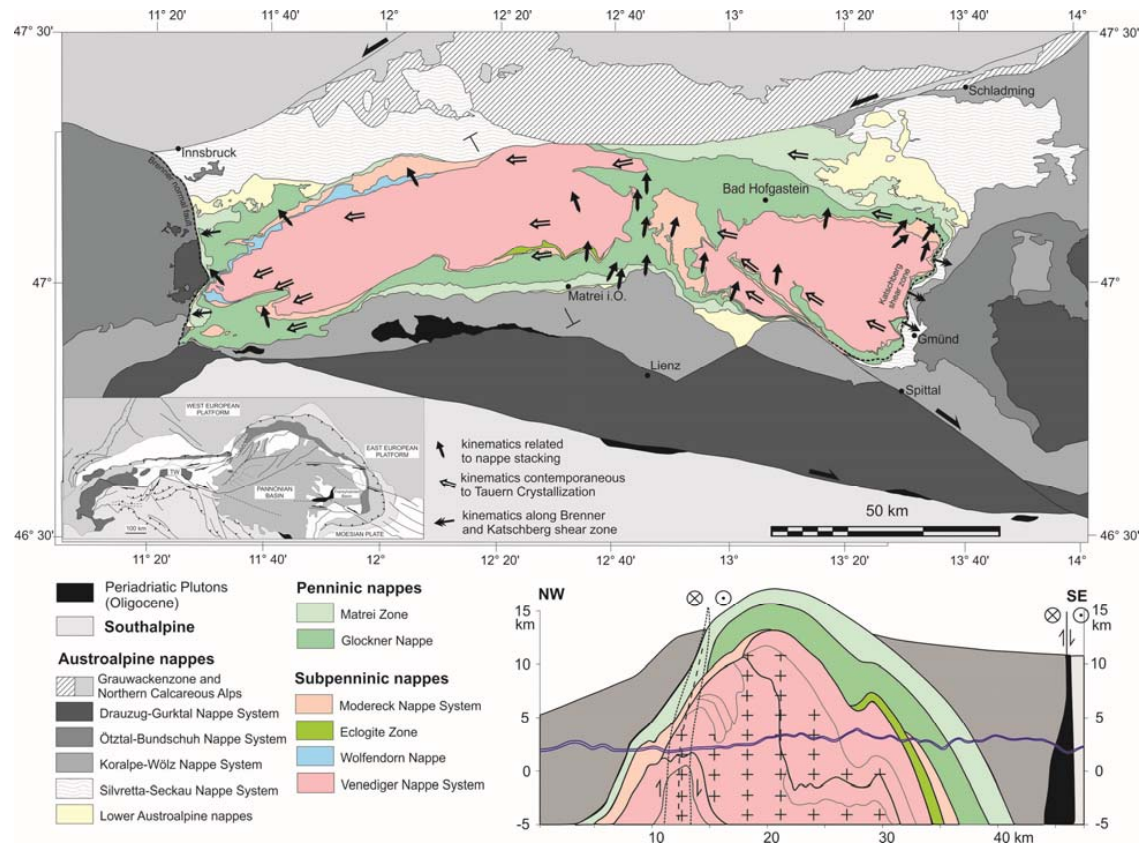


**Figure 5.1:** Tectonic map and cross section of the Tauern Window and adjacent Austroalpine units (after *Kurz et al.*, 1998; *Schmid et al.*, 2013), with a general overview of kinematics of nappe stacking and shearing contemporaneous to amphibolite to greenschist facies metamorphism (Tauern crystallization) with kinematic data (after *Kurz et al.*, 1996; *Neubauer et al.*, 1999). Nappe-stacking-related kinematics was reconstructed from maps and field data (for summary, see *Kurz et al.*, 1996, and references therein). Kinematics along the Katschberg shear zone and the Brenner fault refer to *Genser and Neubauer* (1989), *Scharf et al.* (2013), and *Behrmann* (1988), *Selverstone* (1988), respectively. Stretching directions are derived from *Behrmann* (1990), *Behrmann and Frisch* (1990), *Kurz et al.* (1996), *Lammerer and Weger* (1998), and *Scharf et al.* (2013). Extensional directions of gold-bearing quartz veins are based on *Kurz et al.* (1994), *Genser and Neubauer* (1989), and unpublished data. Inset (after *Hausegger et al.*, 2010) shows tectonic position of Tauern Window (TW) within the Alps-Carpathian-Pannonian system.

## 5.2 Geological setting of the Tauern Window

The Tauern Window exposes a Cenozoic-age nappe pile consisting of crustal slices derived from the distal continental margin of Europe (Subpenninic Units) and a part of the Penninic (or Piemonte Ligurian) ocean (Glockner Nappe System), accreted to an upper plate that consists of the Austroalpine Nappe pile that was structured during Cretaceous times. This general structure of the nappe system within the Tauern Window was

previously described by *Kurz et al.* (1996, 1998), and re-compiled by *Schmid et al.* (2013). The present-day architecture of the Tauern Window is primarily characterized by a crustal-scale late Alpine duplex, the Venediger Duplex (or Venediger Nappe System) that formed during the Oligocene. This duplex structure was severely overprinted by doming and lateral extrusion, which was most probably triggered by the indentation of the Southalpine Units east of the Giudicarie Belt. Indentation initiated at around 20 Ma ago and was linked to a lithosphere-scale reorganization of the geometry of the mantle slabs beneath the central Eastern Alps (*Schmid et al.*, 2004, 2013).

The European continent consists of a deeply eroded Variscan (Late Devonian to Carboniferous) metamorphic continental crust, rich in plutonic rocks (north of the Alpine front), covered by Carboniferous to Eocene sedimentary sequences. This crust is still in contact with its lithospheric mantle and dips southwards beneath the Alps (e.g. *Kummerow et al.*, 2004). The Sub-Penninic Nappes within the Tauern Window (Fig. 5.1) represent the distal European margin, forming ductilely deformed basement and cover nappes, which lost contact with their lithospheric mantle. These form the Venediger Nappe System. This interpretation is based on the conclusion that the crustal material of the Venediger Nappe System was not separated from the European margin by an Oceanic basin (e.g. *Froitzheim et al.*, 1996; *Kurz et al.*, 2001). The eclogitic Sub-Penninic basement units (Eclogite Zone) contain material derived from the Alpine Tethys Ocean and developed in a subduction and accretion channel (*Engi et al.*, 2001; *Kurz and Froitzheim*, 2002).

The Wolfendorn Nappe is restricted to the northwestern Tauern Window where it structurally overlies two imbricates of the Venediger Duplex. The Eclogite Zone occupies a tectonic position above the Venediger Nappe System but just below the Modereck Nappe System. Eclogite facies conditions of 1.9-2.2 GPa and 600- 630° C (*Hoschek*, 2001) were reached about 33-32 Ma (*Nagel et al.*, 2013). Subsequent decompression and reheating to amphibolite facies conditions ("Tauernkristallisation") affected the entire nappe stack including the Venediger Nappe System (*Glodny et al.*, 2008). The onset of subduction is poorly constrained, but available radiometric data suggest an age between 55 and 45 Ma ago (*Berger and Bousquet*, 2008).

The Modereck Nappe System comprises the units in a similar structural position immediately below the Glockner Nappe. The Seidlwinkl Nappe, an isoclinal fold nappe, is exposed in the central Tauern Window (*Frank*, 1969) and makes up most of the Modereck Nappe System. *Kurz et al.* (2008) report that parts of the Modereck Nappe System

located in the Grossglockner area are, together with the adjacent Eclogite Zone, affected by eclogite facies metamorphism.

The Penninic Nappes comprise three paleogeographic elements: the Penninic (Piedmont-Ligurian) Ocean, the Briançonnais microcontinent and the Valais Ocean. The Piedmont-Ligurian Ocean opened in Late Jurassic times. Its initial sea-floor formed by exhumation of the sub-continental mantle of the Apulian microplate (*Froitzheim and Manatschal, 1996*). The Briançonnais microcontinent was a part of the European distal margin until it was cut off by the opening of the Valais Ocean in Cretaceous times. The Valais Oceanic crust comprises Cretaceous ophiolites overlain by Cretaceous to Eocene calcareous turbiditic metasediments. Towards the east the Valais Ocean merged into the Piedmont-Ligurian Ocean, thus forming a single oceanic basin towards the east (e.g. *Stampfli, 1994; Froitzheim et al., 1996*). This situation therefore makes any subdivision of the Piedmont-Ligurian from the Valais basin somewhat artificial in the area east of the Engadine Window (*Kurz, 2005, 2006*).

### 5.3 Structural evolution and kinematics

A structural and kinematic reconstruction of deformation events within the Tauern Window is provided by *Kurz et al. (1996)* and was refined by *Scharf et al. (2013)*. Structures related to internal nappe stacking along distinct thrusts (D0 after *Kurz et al., 1996*) are not developed in mesoscale, but can be derived from the WNW-ESE orientation of branch lines within the Venediger Nappe System. These indicate NNE-to NNW- directed kinematics during nappe detachment (Fig. 5.1), being related to the formation of the Venediger Duplex (*Schmid et al., 2013*).

The oldest clearly distinguishable structures resulted from N-directed ductile shearing (D1 after *Kurz et al., 1996*) (Fig. 5.1). This deformation is only developed penetratively in the upper structural level of the Venediger Nappe System, parts of the Seidlwinkl-Rote Wand Nappe in the central part of the Tauern Window, and within high-pressure mylonites of the Eclogite Zone (*Kurz et al., 1998, 2004*). During D1 a first penetrative foliation (s1) parallel to the thrust surfaces and a S- to SSE- dipping apparent stretching lineation (l1) were developed. Deformation conditions within the Venediger Nappe System were close to 500°C and 6 kbar, and reached eclogite facies metamorphic conditions within the Eclogite Zone and the southern parts of the Seidlwinkl-Rote Wand Nappe. This phase of deformation can therefore be related to the exhumation of units affected by



high-pressure metamorphic conditions within a subduction channel (*Kurz, 2005; Kurz et al., 2008*).

The nappe edifice that formed during D0,1 was overprinted by general west-directed shearing (WNW in the eastern, WSW in the western part of the Tauern Window) (Fig. 5.1). D0,1 structures were obliterated by a penetrative foliation (s2) and a sub-horizontal, NW- to WSW- trending stretching lineation l2 (*Kurz et al., 1996*). Several units within the Tauern Window were affected by this shearing, that occurred at amphibolite facies metamorphic conditions at about 27 to 29 Ma within the central parts of the Tauern Window (*Reddy et al., 1993; Inger and Cliff, 1994*) with a continuous decrease to greenschist facies metamorphic conditions towards the margins of the Tauern Window. During this deformational phase the Penninic units are deformed homogeneously within a constrictional strain geometry. The main deformational zone is transferred continuously to deeper structural levels (*Kurz et al., 1996*). Strain indicators revealed mainly coaxial deformation with subordinate west- directed simple shear (*Kurz et al., 1996, Fig. 5.1*).

Generally l2 stretching lineations trend parallel to large-scale folds (*Scharf et al., 2013*). Accordingly, this deformation phase might be related to crustal scale folding due to north-directed shortening during exhumation of the Tauern Window units and contemporaneous orogen-parallel west-directed stretch within a transpressional regime (*Kurz et al., 1996*). Strain data from the eastern Tauern Window (*Norris et al., 1971; Behrmann, 1990; Kurz et al., 1996*) revealed NW-SE sub-horizontal elongation of approximately 250% and between 50 and 75% NE-SW- directed shortening. Strain generally increases from NE towards SW (*Norris et al., 1971; Behrmann, 1990*).

In the western part of the Tauern Window deformation is more homogenous along a N-S cross section. Data from strain analyses within the Venediger Nappe System revealed subhorizontal WSW-ENE- directed stretch and NNW-SSE- directed shortening (*Lammerer and Weger, 1998*). Shortening varies between 0.4 and 0.24. D3 as described by *Kurz et al. (1996)* is related to the formation of the dome structure within the Tauern Window, orogen-parallel extension and lateral extrusion. This led to the final exhumation of the nappe stack beneath the Austroalpine orogenic lid by a combination of tectonic and erosional unroofing (e.g. *Ratschbacher et al., 1991a; Frisch et al., 1998; Rosenberg et al., 2007*). This phase of deformation is characterized by the interference of multiply developed structures, and by deformation partitioning and shear localization along the dome margins (*Behrmann and Frisch, 1990; Kurz and Neubauer, 1996*). Especially along shear zones bordering the Tauern Window, a new penetrative foliation s3, associated with a stretching lineation l3, was developed. Interior parts of the Tauern Window

have been affected by multiple folding, too. Structural and kinematic data documenting this evolution have recently been published by *Kurz et al.* (1994, 1996, 1998), *Kurz and Neubauer* (1996) and *Scharf et al.* (2013).

## 5.4 Methods for constraining upper mantle deformation

Seismological studies show that the upper mantle presents significant anisotropic characteristics (e.g. *Long and Silver*, 2009). Anisotropy is often caused by plastic deformation of rock forming minerals (*Karato et al.*, 2008), which leads to dependence of physical properties according to different trajectories within the rock mass. Seismic anisotropy is observed by differential arrival times of the seismic waves that travel faster in one orientation and slower in another orientation inside the crossed media; this characteristics of the anisotropic media is termed birefringence. This phenomenon allows us to recognize anisotropy in the upper mantle and consequently to examine the deformation pattern, which refers to tectonic processes. Anisotropy in the upper mantle can be due to the strain field in the lithosphere and/or asthenospheric flow (*Savage*, 1999). Laboratory experiments have shown that the upper mantle is dominated by strongly anisotropic minerals (*Maupin and Park*, 2007). The origin of seismic anisotropy in the upper mantle is assumed to be related to the lattice-preferred orientation (LPO) of olivine due to dislocation creep (*Mainprice et al.*, 2000; *Karato et al.*, 2008).

One of the most useful geophysical methods for constraining upper mantle anisotropy is shear-wave splitting that uses the birefringence or splitting of the shear waves when they pass through an anisotropic medium. Shear-wave splitting is capable to examine the deformation in the upper mantle. As an effect of anisotropy, shear waves are split into two orthogonal phases that arrive at the surface at different time, defining the fast and slow polarization orientations. In the shear-wave splitting method, two splitting parameters are measured: the azimuth of fast axis polarization ( $\phi$ ), and delay time ( $\delta t$ ) between the arrival of fast and slow polarizations. Fast axis azimuth gives useful clues about strain and shear directions (e.g. in the A-type olivine,  $\phi$  tends to be aligned in the direction of shear, *Savage*, 1999; *Karato et al.*, 2008).

Several techniques are developed to derive the splitting parameters. To constrain the upper mantle anisotropy, the frequently used method is the minimum energy technique

(SC, *Silver and Chan*, 1991), in which splitting parameters are derived by single teleseismic events measured at each seismic station. The best choice to apply the shear wave splitting method is to use teleseismic core phases SKS/SKKS. These phases are the converted shear waves from P waves at the core mantle boundary (CBM) and arrive at the surface almost vertically. The converted S-wave at the CBM is radially polarized; therefore the retrieved anisotropy must lie in the mantle below the seismic station.

Here, we show results of individual SKS splitting measurements (*Qorbani et al.*, 2015a) by the SC technique from 8 broadband permanent stations located in the Tauern Window region. Four stations belong to the Austrian broadband seismological network (OE), three stations to the Southern Tyrolia network (SI) operated by ZAMG (Zentralanstalt für Meteorologie und Geodynamik), and one station of the Italian seismic network (IV) operated by INGV (Istituto Nazionale di Geofisica e Vulcanologia). Teleseismic events with magnitude MW greater than 6 within the epicentral distance range of 90° to 130° were used to derive the splitting parameters by means of the SplitLab package (*Wüstefeld et al.*, 2008).

## 5.5 Results

Anisotropic fast axis azimuth ( $\phi$ ), and delay time ( $\delta t$ ) measured at the seismic stations are summarized in Figure 5.2. In the main figure we show the average values of fast axis azimuth and delay times for 12 stations located in the eastern Alps (*Bokelmann et al.*, 2013) as well as 13 stations of the Slovenian network (SL) and 8 stations of Italian networks (IV, NI, SI) (*Qorbani et al.*, 2015a) together with previous results for the western Alps (*Barruol et al.*, 2011) and the central Alps along the TRANSALP profile (*Kummerow and Kind*, 2006). A clear progressive rotation of average fast azimuth orientations was already described by *Bokelmann et al.* (2013) and is visible in Figure 5.2. The change of lines orientation occurs between about 12°E and 13°E longitude. This change is located inside the Tauern Window region.

Nearly vertical incidence angle of SKS phases (8°-12°), when they hit the surface, gives a good lateral resolution in the splitting results. Projecting the measurements from their surface location (station position) to depth allows us to assess the regions sampled by the rays. For this purpose, individual measures in the Tauern Window are projected at 120 km depth by using the incidence angle and events back-azimuth. 120 km is the maximum estimated lithospheric thickness in the Tauern Window region (*Bianchi et al.*,

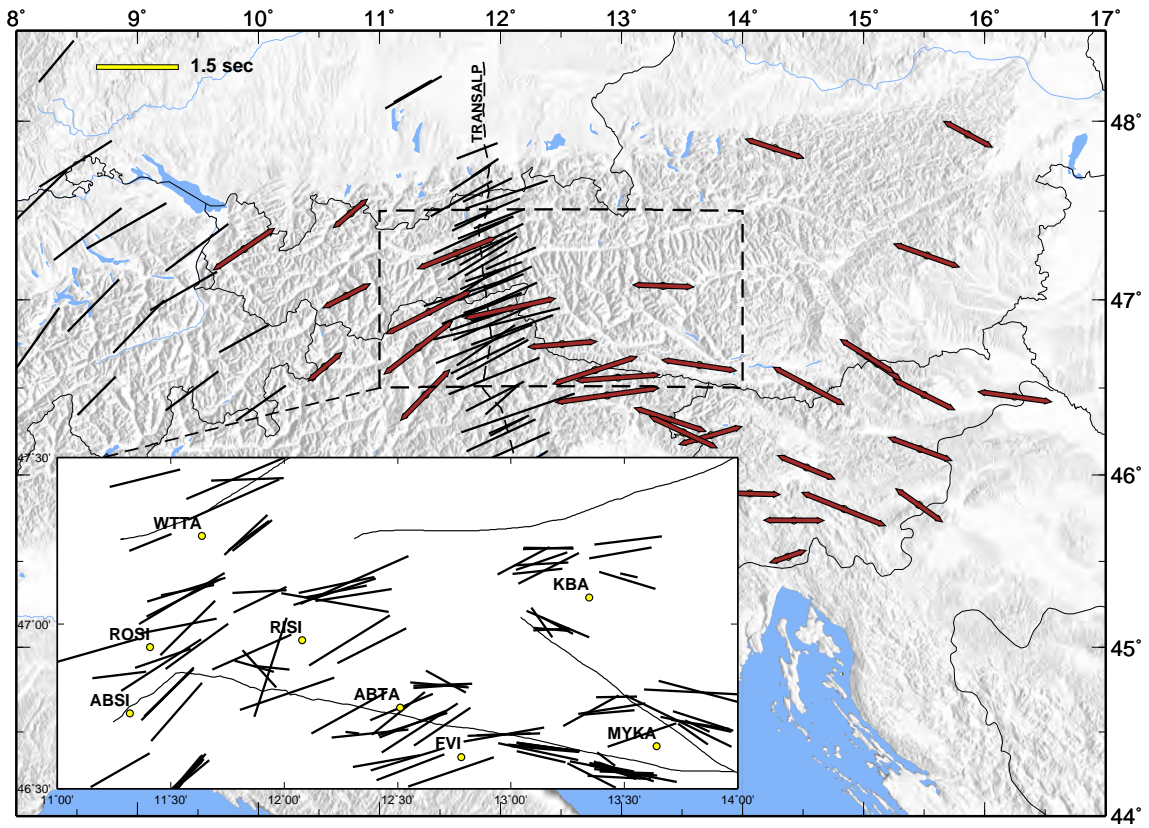


**Figure 5.2:** Background, average shear-wave splitting results (arrows) at broadband stations in the eastern Alps (*Bokelmann et al.*, 2013; *Qorbani et al.*, 2015a). The orientation of the lines represents fast axis azimuth ( $^{\circ}$ N) and the length indicates the amount of delay time in seconds. SKS splitting measures from former studies (*Barruol et al.*, 2011; *Kummerow and Kind*, 2006) are shown in black thin lines. The progressively rotating pattern of average anisotropic fast axes is noticeable. The inset is a zoom of the area included in the dashed perimeter, showing the projection at 120 km depth of individual splitting measurements (*Qorbani et al.*, 2015a), which were obtained from different teleseismic events at each station in the Tauern Window area. Black thin lines in the insert indicate the main strike slip faults.

2014; *Jones et al.*, 2010, and references therein). Inserted in Figure 5.2 is a zoom of the Tauern Window, which shows the individual measurements (*Qorbani et al.*, 2015a) projected at 120 km depth. The lines show orientation of fast axis and delay times are scaled by length. Fast axis azimuths are in the range of  $N45^{\circ}$  to  $N145^{\circ}$  (with one exception  $N18^{\circ}$ ).

By projecting the measurements on the N-S profiles at the west and the east of the Tauern Window region (Fig. 5.6), two groups of fast orientations can be observed. In the west, almost all measures show NE-SW orientation while in the eastern part most of measurements are aligned NW-SE, displaying about  $45^{\circ}$  difference in orientation (Fig. 5.6). We

can therefore consider a separation line at the azimuth of  $N90^\circ$  between them, and for an immediate graphical distinction they have been differently colored according to their orientation. Those displaying azimuths less than  $N90^\circ$  are shown in blue, and those with azimuth greater than  $N90^\circ$  are in red (Fig. 5.3). Stations WTTA, ROSI, ABSI (Fig. 5.2, inset) display a similar pattern of all individual measures, in which fast axes are oriented about  $N60^\circ$ . This similarity can be seen in the average values as well (Fig. 5.2). On the other hand, anisotropy measurements at the stations located in the eastern part of the region display two fast orientation patterns. In the eastern part, depth projection based on the events backazimuth shows that measurements obtained from events coming from  $\sim N50^\circ$  and  $\sim N230^\circ$  back-azimuth show NW-SE orientation of the fast axis ( $> N90^\circ$ , red lines) and rays coming from  $\sim N300^\circ$  back-azimuth result in NE-SW orientation ( $< N90^\circ$ , blue lines). The latter is similar to what we observed in the western part where there is no back-azimuthal variation.

Back-azimuthal dependence of SKS splitting measurements is a signature of depth variation of anisotropy, which can be the presence of multiple layers of anisotropy in the upper mantle (*Silver and Savage*, 1994, and references therein). Modeling vertical changes of anisotropy based on the back-azimuthal dependence (*Qorbani et al.*, 2015a) has presented two anisotropic layers for the upper mantle under the Eastern Alps in which a deeper layer with NE-SW fast orientation and a shallower layer with NW-SE anisotropy on the top are suggested. At the wider scale the latter can be traced to the Carpathian-Pannonian region. In the central part of the TW area, measures obtained for station ABTA mostly display E-W fast orientation, and measurements obtained from RISI are scattered in a wider range of azimuth and delay times.

Kinematic data deduced from exhumed lower crustal rocks, and anisotropic measurements obtained from seismological observations are two independent data sets that provide deformation patterns in the crust and in the upper mantle respectively. A principal difference is though that for the mantle, we have only constraints on the shear orientations (not the sense of direction), while for the crust, we also know the sense of shear. We have plotted these two data sets together for the Tauern Window region (Fig. 5.3). The anisotropy measurements located north of the Periadriatic line have been selected. As seen in Figure 5.3, the D2,3 stretching directions appear to correlate with the orientation of the anisotropic fast axes in the western and the eastern Tauern Window (TW). As mentioned before, the dominant anisotropic fast orientation NE-SW in the western part of the TW gradually changes to E-W orientation in the longitudes of the middle part of the study area (Fig. 5.3). In the same fashion, shear orientations (kinematic data) show

an ENE-WSW trend in the west and turn to E-W in the center of the TW region (green lines in Fig. 5.3). In the eastern part of the TW, anisotropic measurements present two main patterns. In this part, NW-SE oriented fast axis (red lines) coincide with the kinematic data. This suggests that this group of fast orientations, which correlate with the surface deformation geometry, is related to the shallower anisotropic structures (as suggested by two-layer modeling, *Qorbani et al.*, 2015a) rather than the second group of orientations (blue lines) in this part of TW.

## 5.6 Discussion

### 5.6.1 Anisotropy and deformation regimes

Anisotropic structures observed in the mantle below orogens related to continental subduction and subsequent collision (e.g. the Variscan, Apennines, Pyrenees, Himalaya/Tibet, etc.), are commonly aligned perpendicular to the convergence direction (*Bormann et al.*, 1993; *Lave et al.*, 1996; *Barruol et al.*, 1997). This anisotropy can be originating from subduction-related fossil alignment or upper mantle flow that is currently active.

Along the Alpine chain, mountain belt-parallel anisotropy has been already observed (*Vinnik et al.*, 1994; *Smith and Ekström*, 1999; *Barruol et al.*, 2011; *Bokelmann et al.*, 2013; *Bianchi and Bokelmann*, 2014). However, the average fast axis of SKS splitting showed  $\sim 10^\circ$  (counterclockwise) deviation from the Alps trend in the eastern Alps, along the TRANSALP (*Kummerow and Kind*, 2006). This difference is about  $\sim 20^\circ$  in the Central Alps (see *Barruol et al.*, 2011) and further to the east from the TRANSALP profile ( $\sim 12^\circ\text{E}$ , in the middle of TW region), this deviation reaches up to  $\sim 45^\circ$  (see *Bokelmann et al.*, 2013; *Qorbani et al.*, 2015a).

In the TW area, beside the average fast axes, we observe orientations both at the upper mantle level (individual SKS measurements) and crustal tectonic kinematics that are oblique to the general trend of the Alpine mountain chain. Both the crustal and upper mantle deformation patterns (Fig. 5.3) expose a change of orientation in the middle of the TW. To evaluate the location of this change of orientation (or bending), we have compared anisotropic and kinematic data together as a function of longitude (Fig. 5.4). In Figure 5.4, the overall trend of the anisotropic pattern is shown by spatial averages, computed at longitude intervals of 20 min along the TW. The point of change in the orientation of upper mantle deformation patterns occurs at the same longitude as the



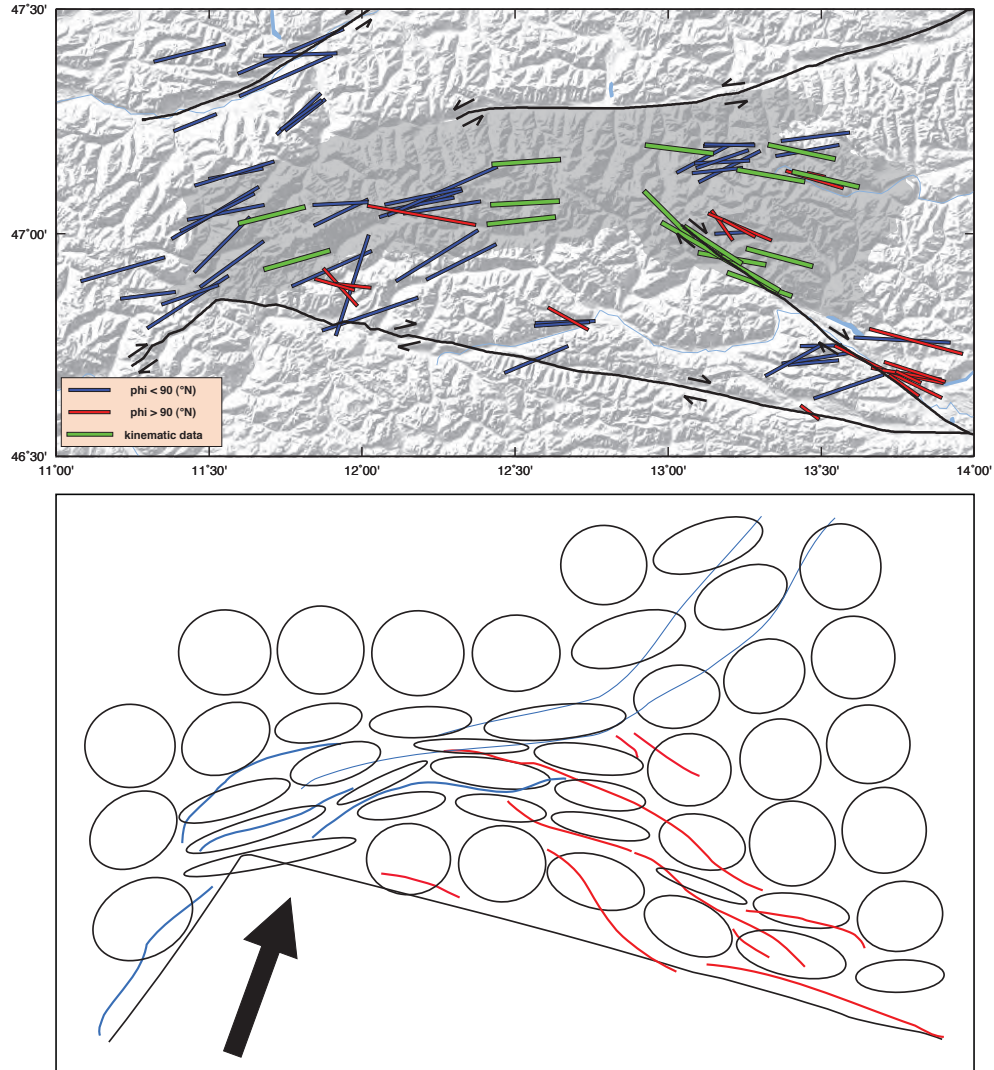


**Figure 5.3:** Top: Map showing correlation between crustal (kinematic data) and upper mantle deformation (the anisotropic fast orientations). Fast azimuths displaying an angle smaller than  $90^\circ$  with respect to the North are shown in blue and those at azimuth greater than  $N90^\circ$  are shown in red (see Fig. 5.6). Green lines show the stretching directions related to D2,3 within the Tauern Window. Bottom: The distribution of deformation resulting from the experimental indentation model of *Rosenberg et al.* (2007). Ellipses represent the strain orientation at the surface of the model. In the west there is good correlation between the strain orientations and the deformation pattern in the upper mantle detected by SKS splitting measurements. In the east, the NW-SE fast orientation (red lines in the top panel) is in the same orientation as the strain pattern (ellipses). Lines show the major faults after the experiment. They are colored based on the similarity to the upper mantle anisotropy. Straight lines are the indenter edges and the black arrow shows the best fitting indentation direction (NNE) in the experiments.

change of stretching directions in the crust ( $12.50^{\circ}\text{E}$ , indicated by the arrow in Fig. 5.4). This bending therefore appears to indicate a correlation between the crust and upper mantle, probably related to a common cause of deformation at the crustal depth and in the deeper lithosphere/asthenosphere.

The average anisotropic delay times in the TW (brown circles in the bottom panel, Fig. 5.4) are greater than 1.0 sec. These values cannot be created by the anisotropic structures in the crust. It has been described delay times of 0.1 second per 10 km thickness and have suggested that the observed splitting signal can not be explained by shear-wave splitting in the crust alone (*Barruol and Mainprice, 1993; Barruol and Kern, 1996*), on kinematic grounds. Moreover, SKS phases used in this study are associated with a dominant period of 10 seconds, and it should also for that reason be not very sensitive with respect to relatively small features such as the crust (*Barruol et al., 2011*). The major part of splitting delay time is therefore due to the anisotropy in the upper mantle under the TW as has been widely suggested before (*Silver and Chan, 1991; Vinnik et al., 1992*).

Considering SKS splitting measures together with the D2,3-related crustal kinematics data shows that crustal and upper mantle deformation is coherent in the TW region. The question that arises is at which time was the deformation (in crust and mantle) created? For the crust, age information is given by D2-related shearing that was widely contemporaneous to amphibolite to upper greenschist facies metamorphism ("Tauern Crystallization"). It affected the entire nappe pile within the Tauern Window. This metamorphic event is dated around 23 to 29 Ma (for summary, see *Kurz et al., 1996; Scharf et al., 2013*). A deformation acting over 20-30 Ma is indeed enough to create the observed anisotropy assuming typical strain rates (*Vinnik et al., 1994; Savage, 1999*). Thus, the SKS splitting results may be associated with these relatively recent tectonic events. Under the circumstances, in which the parallelism of crustal and upper mantle deformation is observed, crustal deformation may be a direct response to the motion in the upper mantle (e.g. *Flesch et al., 2005*). Therefore it is reasonable to infer that what caused the arcuate shape of TW is still active in the upper mantle.

Bending and exhumation of the TW area, which started from late Oligocene to early Miocene (28 – 20 Ma, e.g. *Prosser, 1998; Schmid et al., 2004*) is suggested to be the main consequence of nearly northward movement of the South Alpine block, acting as a rigid indenter (*Ratschbacher et al., 1991; Rosenberg et al., 2004*). Experimental results focusing on the indentation effect in the Eastern Alps (*Rosenberg et al., 2004, 2007*) have

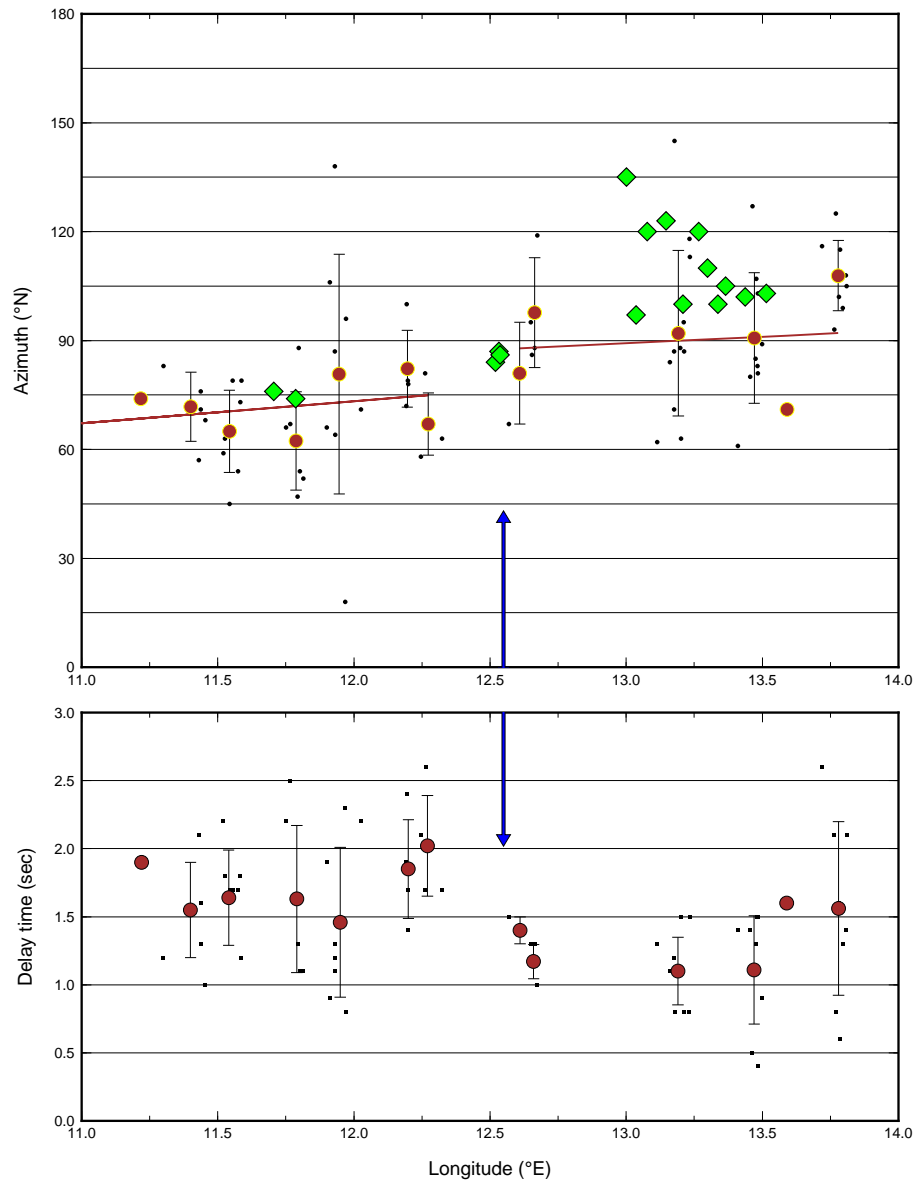


**Figure 5.4:** Lateral variation of upper mantle strain field (anisotropic fast orientation) together with the D2,3- related crustal shear direction as a function of longitude in the Tauern window region (top panel). Small points are individual measurements projected at 120 km depth. Circles present the average value of fast axis azimuth at longitude intervals of 20 min and diamonds show (crustal) shear orientation. Upper mantle and crustal deformation pattern change at the longitude of 12.5°E. Lines fit anisotropy data on the right and left of 12.5°E and indicate the change in deformation geometry of the upper mantle (as well as the crust). Bottom panel shows the variation of splitting delay times as function of longitude. Small points are individual measurements projected at 120 km depth, while Circles are the average value at longitude intervals of 20 min.

suggested that the oblique indentation N20°E shows the most similarity to the deformation pattern in this region.

To evaluate the degree of crustal-upper mantle parallelism as a response to deformation regimes within the upper mantle, we compare our dataset with the distribution of deformation pattern resulted from an indentation experiment (Fig. 5.3, bottom). In this figure, ellipses illustrate the strain orientation at the surface of the model and curvy lines are the major faults after exerting the oblique indenter in the experiment (*Rosenberg et al.*, 2007). On the left, these lines and anisotropic fast axes are oriented in a similar pattern as the kinematic data which all show N50°-N70° azimuth. These lines (on the left) are colored according to the pattern of upper mantle anisotropy derived from SKS splitting in the west of TW (blue lines). Dominant NW-SE fast anisotropy orientation and kinematic data in the East is comparable with the major faults in this part of the model (lower part of Fig. 5.3) which are shown in the same color as the fast anisotropic orientations (red).

The similarity between upper mantle anisotropy and the experimental deformation pattern can be discussed in the terms of indentation effect. Regardless whatever caused the indenter movement, the indentation has affected not only the crust but also the lithospheric mantle as well as the sub-lithospheric structures, resulting in the vertical coherence of deformation from the upper mantle to the crust. This coherence probably initiated in the same age as the indentation started, and exists as long as the indentation lasts.

### 5.6.2 Vertical coherence of deformation and mechanical coupling

We have seen that the geometry of deformation in crust and mantle is vertically coherent, and it is natural to try to explain this by the depth range in which the indenter acts, coupled with rheology in the different layers in the lithosphere. Results of experimental models (*Rosenberg et al.*, 2007) have tested several rheological models for the area, and have suggested that the fault geometry in the Eastern Alps is best explained by a rheological model that consists of a brittle upper crust, a ductile lower crust, and a ductile lithospheric mantle on the top of viscous asthenosphere (Fig. 5.5). The vertical coherence that we observe, is between lower crust (from crustal kinematics) on one hand, and the deeper lithosphere-asthenosphere system (from the splitting measurements) on the other.

Coherent crustal and upper mantle deformation, as it has been observed in many continental settings, e.g. the Canadian Shield (*Bokermann and Wüstefeld, 2009*), the Sao Francisco Craton (*Vaucher et al., 1994*), and in other settings suggests a lithospheric origin of anisotropy in those areas. Alternatively correlated lithosphere-asthenosphere anisotropy (*Fouch and Rondenay, 2006*) was recently suggested to be the cause of belt-parallel deformation in the western Alps (*Barruol et al., 2011*) meaning frozen-in alignments within the lithospheric mantle are oriented in the direction of upper mantle flow in the asthenosphere. This suggestion can explain well-correlated kinematic data and anisotropy measures in the western TW region (Fig. 5.3). For this region, *Willingshofer and Cloetingh* (2003) presented a lithospheric strength model along the TRANSALP profile in which strong coupling between crust and mantle for the Eastern Alps has been suggested. Our dataset is consistent with this, suggesting that lower crust and lithospheric mantle are mechanically coupled

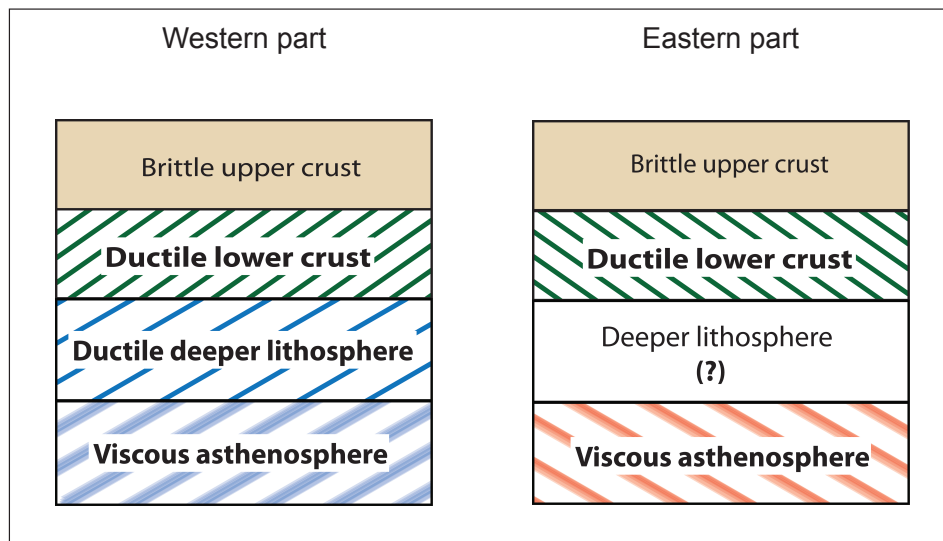


**Figure 5.5:** Demonstration of rheological layering in the Tauern Window region (after *Rosenberg et al., 2007*). Hatchings are colored same as Figure 5.3. Blue hatching represents the depth of observed seismic anisotropy (NE-SW) in the western part of TW that is correlated well with the kinematic data from the lower crust (green hatching) suggesting crust-upper mantle coupling in this area. In the eastern part, red hatching illustrates the depth of NW-SE anisotropy pattern in the asthenosphere that is correlated with the kinematic data. The lithospheric mantle in this area is an invisible layer (see text).

Compared with the western TW, the eastern TW shows a different pattern of upper mantle deformation. The kinematic data correlates with the NW-SE anisotropic orientation. This anisotropy orientation has also been observed much further to the east, in the Carpathian-Pannonian region (*Stuart et al., 2007, Kovacs et al., 2012*). Furthermore, the crustal and lithospheric thickness in the eastern Alps shows an eastward decrease

(*Ratschbacher et al.*, 1991a; *Frisch et al.*, 1998; *Bianchi et al.*, 2014), to on average  $\sim 70$  km lithospheric thickness; that is not thick enough to create the observed SKS splitting (*Qorbani et al.*, 2015a). Therefore, the associated fabric is most probably located in the asthenosphere.

On the other hand, we observed NE-SW anisotropic orientation in the eastern part (blue lines in Fig. 5.3). The back-azimuthal dependence of the SKS measurements can be considered as a signature of vertical change of anisotropic sources. In a separate paper (*Qorbani et al.*, 2015a) we have studied this in detail, and have presented parameters of the seismic anisotropy in the two layers. Hence, the NE-SW anisotropic orientation originates from a structure located deeper than the asthenospheric flow.

Deformation within the ductile lower crust is correlated with the orientation of the flow within the viscous asthenosphere in the eastern TW (Fig. 5.3 and 5.5). By the employed methodology (SKS splitting) we are not able to address the anisotropic structure of the lithospheric mantle in this area, as explained above. This “invisible” lithospheric mantle might very well be aligned in the same orientation as the asthenospheric flow (NW-SE), especially if the deeper lithosphere in the eastern Alps is weak, as has been suggested by *Genser et al.* (1996), *Okaya et al.* (1996), and *Willingshofer and Cloetingh* (2003). In that case, deformation in that layer might very well follow the motion in neighbouring layers. It will be interesting to devise observational strategies for observing deformation in that layer specifically. This is particular interesting since other regions (e.g. *Fry et al.*, 2010) seem to be associated with a different kind of fast orientation. Those authors presented an orogen-parallel anisotropy within the shallow structures (less than 30 km depth), and orogen-perpendicular alignments for the sub-crustal materials (30 km < depth < 70 km), which is the direction of subduction of EU under the AD slab. That study is done for the central Alpine region to the West of the TW area. We cannot rule out that such a fossil-anisotropy layer also exists in the Eastern TW.

## 5.7 Conclusion

SKS splitting measurements and kinematic data deduced from exhumed crustal rocks reveal striking similar deformation patterns in the Tauern Window. Parallelism between crustal shear directions and anisotropic fast orientations exposes vertical coherence of deformation from the upper mantle to the crust. The similar geometry of crustal and upper mantle deformation confirms the earlier notion of *Selverstone* (1988) and *Royden*



(1996) that mantle and crust in the Eastern Alps are (mechanically) coupled. Their inference was based on the shape of the deforming zone at the Earth's surface. This is particularly clear for the western part of the Tauern Window where NE-SW orientations of fast anisotropy axes correlate well with the kinematic data of orogen-parallel stretch. The strong crust-upper mantle coupling had been already suggested using data from the TRANSALP profile (*Willingshofer and Cloetingh, 2003*).

In the eastern part of the Tauern Window, NW-SE oriented anisotropy possibly reveals the orientation of flow in the asthenosphere and is in agreement with the kinematic data. In this area, similar deformation geometry between the ductile lower crust and the viscous asthenosphere is observed. NW-SE fast orientations in the asthenosphere can be seen as a signature of shearing that has been initiated after European plate break off in  $\sim 29$  Ma (*Schmid et al., 2013*) and is still active within the whole lithosphere beneath the Tauern Window area and the Eastern Alps. On the crustal scale, the general structure within the Tauern window indicates that exhumation of the lower crust can be related to crustal scale folding due to north-directed shortening contemporaneous to orogen-parallel west-directed stretch within a transpressional regime, starting in a times range of 29 to 23 Ma which is consisted with the flow regime that initiated within the above mentioned time frame.

The correlation of deformation in crust and mantle indicates that the indentation effect in the area of the Tauern Window is not restricted to the crust, but shows its effect also at deeper levels in the lithosphere-asthenosphere system. In that sense, it constitutes a "crust-mantle coupling". The synchronizing factor in this coupling is the lateral boundary condition imposed by the indenter. The coupling thus exists as long as the indenter acts. This however does not necessarily imply that the crust and mantle portion of the lithosphere move coherently at all times.

## 5.8 Acknowledgments

Online availability of data from Austrian broadband seismological network (OE) and Southern Tyrolia network (SI) was provided by the Zentralanstalt für Meteorologie und Geodynamik (ZAMG) (<http://www.zamg.ac.at>). The data was accessed through the database operated by Observatories and Research Facilities for EUropean Seismology (ORFEUS) (<http://www.orfeus-eu.org>) and INGV (Istituto Nazionale di Geofisica e Vulcanologia) (<http://www.ingv.it>). We thank the editor, Harald Fritz, and three reviewers,

E. Willingshofer, N. Froitzheim, and anonymous for the constructive reviews. Most of the maps are prepared using GMT software (*Wessel and Smith, 1998*).

## 5.9 Supplementary figures

**Figure 5.6 (S1):** Different patterns of upper mantle anisotropy under the Tauern Window (TW) in the Eastern Alps. Top panel shows individual splitting measurements in and around the TW area. Line orientations represent the azimuth of fast anisotropic axis and lines lengths are scaled by splitting delay times. Brown lines are the major faults in the region. Two N-S profiles are shown in the west (blue) and in the east (red). Middle panel illustrates projected anisotropic measurements on the E and on the W profiles. Vertical axis is the azimuth of fast axis and horizontal axis is the distance along the profiles from north. Red circles are average value of fast axis azimuth projected on the East (E) profile at intervals of 20 km. In the same fashion blue circles are corresponding to the west (W) profile. Measurements within a distance of 50 km on each side of each profile, are included. 50 km distance is the Fresnel radius of SKS phases at 120 km depth. Two different pattern of anisotropy can be seen clearly on the projected data. We can consider a separation line at the azimuth of  $90^\circ$  between two groups of anisotropy. Squares are the kinematic data in the west (blue outlines) and in the east (red outlines), which are projected on the western and eastern profile receptively. Bottom panel also shows the projected data on two profiles but without averaging. Dashed lines show the average direction of the orientations for west and east profiles; these orientations clearly show a difference of  $\sim 45^\circ$ . Measurements from the western TW, obtained by SC technique (*Qorbani et al., 2015a*), show an average azimuth of  $N60^\circ$  (blue dashed line) for fast orientation. This is quite similar with the results of the former study along the TRANSALP (*Kummerow and Kind, 2006*), which are measured by a different method (multi-channel analysis). While the measurements in the west show a single pattern of anisotropy (NE-SW), those in the east show two different patterns but dominantly NW-SE orientation.

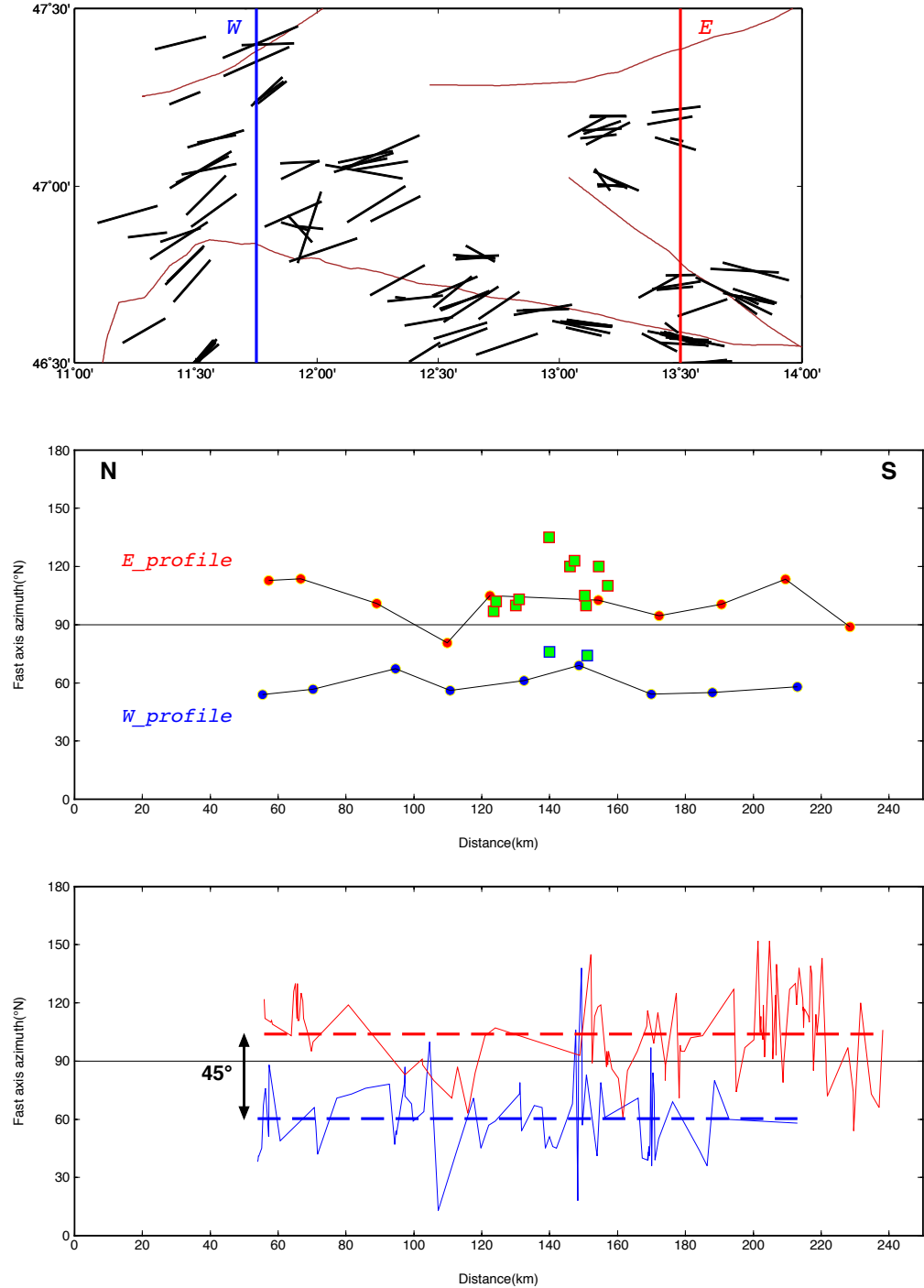


Figure 5.6: (S1)

## Published paper:

AUSTRIAN JOURNAL OF EARTH SCIENCES | VOLUME 108/1 | 161 - 173 | VIENNA | 2015

**CORRELATED CRUSTAL AND MANTLE DEFORMATION IN THE TAUERN WINDOW, EASTERN ALPS**Ehsan QORBANI<sup>1\*)</sup>, Walter KURZ<sup>2)</sup>, Irene BIANCHI<sup>1)</sup> & Götz BOKELMANN<sup>1)</sup>

DOI: 10.17738/ajes.2015.0010

<sup>1)</sup> Department of Meteorology and Geophysics, University of Vienna, Austria;<sup>2)</sup> Department of Geology and Paleontology, Institute of Earth Sciences, Karl-Franzens-University of Graz;

Member of NAWI Graz, an InterUni-versity cooperation between the University of Graz and the Graz

University of Technology, Austria;

<sup>\*)</sup> Corresponding author, ehsan.qorbani@univie.ac.at**KEYWORDS**Tauern Window  
upper mantle  
eastern Alps  
deformation  
anisotropy  
crust**ABSTRACT**

We study the coupling between crust and mantle in a convergent regime, by comparing measures of upper mantle deformation with indicators of crustal deformation. We use shear-wave splitting parameters, in particular the orientation of fast axes in the upper mantle measured from data recorded at 8 broadband stations located within the Tauern Window. These are compared with kinematic indicators in the Tauern Window region of the eastern Alps at the outcrop scale. Our results show a striking parallelism between the upper mantle and crustal patterns, indicating vertical coherence of deformation all the way between the crust and the mantle lithosphere. The new findings suggest a vertical coherence of deformation of crust and upper mantle, particularly in the western part of the Tauern Window. Similar pattern in our results and indentation models indicate that the effect of the Adriatic indentation acts on the European lithosphere, not only at crustal but also at lithospheric mantle depths. We discuss the implication of this vertical coherence for the question of mechanical coupling.

Wir untersuchen die Kopplung zwischen Erdkruste und Mantel in einem tektonisch konvergenten Regime, indem wir die Deformation des oberen Mantels mit Indikatoren der Krustendeformation vergleichen. Dazu verwenden wir Daten von 8 Breitbandstationen innerhalb des Tauernfensters, um seismische Anisotropie aus der Aufspaltung von teleseismischen Scherwellenphasen zu bestimmen, insbesondere die Orientierung der schnellen seismischen Achsen im oberen Erdmantel. Diese werden mit kinematischen Indikatoren im Tauernfenster (Ostalpen) verglichen. Unsere Ergebnisse zeigen eine auffallende Parallelität zwischen den Deformationsindikatoren des oberen Erdmantels und der Erdkruste. Dieses Muster lässt auf eine vertikale Kohärenz der Verformung schließen, zwischen der oberen Kruste bis in die tiefere Mantellithosphäre. Die neuen Erkenntnisse deuten darauf hin, dass die Wirkung des Adriatischen Indenters auf die gesamte (europäische) Lithosphäre wirkt, d.h. nicht nur in der Kruste, sondern auch im lithosphärischen Mantel. Wir diskutieren die Implikationen der vertikalen Kohärenz für die Frage der mechanischen Kopplung.

**1. INTRODUCTION**

"The extent to which upper crustal deformation is coupled to deformation within the lower crust and mantle ... remains one of the most important and least understood aspects of continental deformation". This was the case, when Leigh Royden wrote this sentence (Royden, 1996), and it is still the case today. However, between now and then new observational constraints, especially seismic anisotropy, have become available. In this study we will use these constraints to address the question of coherence of deformation in crust and mantle. The question has a relation with several other important questions that are open, e.g., is crustal and mantle deformation related? Are they of the same age? To which degree do plate-tectonic driving forces that act in the mantle also act on the crust? Are crust and mantle moving together? Is that the case at all times, and are they coupled in that sense? We approach these questions in this paper by comparing the pattern of deformation in crust and mantle. For this, it seems best to consider a region where rocks from deeper levels within the crust are exposed at the surface. This is the case in the Tauern Window, which is a key area for understanding late Alpine deformation (e.g., Lippitsch et al., 2003; Bokelmann et al., 2013).

The Tauern Window of the Eastern Alps exposes exhumed

parts of Europe-derived crust. The southern European margin was accreted to the base of an Adria-derived upper plate, represented today by the Austroalpine nappes (e.g., Schmid et al., 2004, 2013). The Tauern Window is characterized by a complex three-dimensional geometry of tectonic units, including important along-strike changes in its structure (Schmid et al., 2013). This geometry, as described by Schmid et al. (2013) by combining surface geology with the results of deep seismic reflection measurements (Gebbrande et al., 2002; Lüschen et al., 2006), basically resulted from crustal-scale collisional accretion in the Alps followed by late-Alpine indentation, crustal-scale folding, orogen-parallel extension and lateral extrusion (Ratschbacher et al., 1991a).

While the surface geological structure of the Tauern Window is well-understood, the structure of the deeper parts of the lithosphere and the mantle below still remains an open problem in the lithosphere-scale geometry of the Alps-Carpathians-Dinarides system (e.g., Brückl et al. 2007, 2010). This also concerns the quantification of kinematic and dynamic interactions between crustal and mantle structures. Anisotropy measurements (shear-wave splitting) around the Tauern Window have been performed along the TRANSALP profile (Kummerow and

# Chapter 6

## Carpathian-Pannonian region

The section has been submitted to Journal of Geophysical Research as: E. Qorbani, G. Bokelmann, I. Kovács, F. Horváth, and G. Falus, 2015, *Deep Deformation Pattern for the Carpathian-Pannonian region*.

### Abstract

To better understand the evolution and present-day tectonics of the Carpathian-Pannonian region (CPR), we characterize upper mantle anisotropic structures and map deep deformation patterns for this region. SKS splitting parameters measured from teleseismic events recorded by the Carpathian Basin Project (CBP) stations are presented. We investigate these measurements together with petrologic indicator of deformation in basalt-hosted upper mantle xenoliths from the Pannonian basin with regard to anisotropy, deformation geometry, and responsible mechanisms. The results show NW-SE fast orientation under the whole CPR. We contribute this anisotropy to an asthenospheric origin and interpret it as flow induced alignments within the upper mantle that is remarkably inconsistent with the lateral extrusion of the Alcapa block. Several models and scenarios have been suggested so far to explain the evolution and current stage tectonics of the Pannonian basin. These are compared with the deformation pattern observed in the SKS splitting results. We discuss the (in)consistency between these models and our results. We present here the most plausible model responsible for the deformation within the asthenospheric mantle in relation with overlying and surrounding lithosphere. In this model NW-SE deformation is mainly generated in a NE-ward compressional tectonic regime acting in a region between the Adriatic plate and the East European platform.

## 6.1 Introduction

Understanding the mechanisms linking surface deformation with dynamics of the Earth's interior requires constraining upper mantle processes (e.g. *Long and Silver, 2009*). Even though the upper mantle has been extensively studied in terms of seismic velocity discontinuities, thermal conditions, and chemical and physical compositions, interaction between the upper mantle flow and lithosphere requires to be fully elucidated in terms of deformation and strain distribution in the upper mantle.

Seismic anisotropy is manifested by a directional dependence of seismic velocity. Within the upper mantle it is generated mostly by development of the crystallographic orientation of minerals in response to deformation (*Long and Becker, 2010; Mainprice et al., 2000*). Observing seismic anisotropy therefore can be used to describe the strain distribution in the upper mantle, in turn, reflecting the deformation mechanisms, active flow geometry, and also the conditions in which the rock is deformed (*Karato et al., 2008*). These observations allow us to address what happens at depth where stress and strain cannot be measured directly.

The Carpathian-Pannonian region (CPR) is at the northeastern end of the Alpine mountain belt. It consists of a variety of geological structures and tectonic units resulting from subduction, plate collision, basin evolution, and thrust faulting. This region provides a unique opportunity to study mechanisms which govern deep and surface deformation, over a wide range of timescale from the past tectonic episodes until the present-day situation. A large part of the CPR is occupied by the Pannonian basin, which is surrounded by the Alps, Dinarides, and Carpathians (Fig. 6.1).

In order to get insight into the origin of the extensional basins within the CPR, the Carpathian Basin Project (CBP) had been established. It was aimed to provide high 3-D resolution seismic images and numerical modeling using data from seismic instruments deployed mainly in the Pannonian basin. Alongside number of seismological studies including velocity tomography and receiver functions analyses which have been done so far using the CBP data, the upper mantle anisotropy has also been studied through SKS splitting measurements (*Stuart et al., 2007*). While some of the results of that study agree with other recently published anisotropy analysis of the Eastern Alps (*Bokelmann et al., 2013; Qorbani et al., 2015a*), some do not. The present study is planned attempting to address this inconsistency.



In this study, we characterize upper mantle anisotropic structure and deep deformation pattern for the Carpathian-Pannonian region. We reprocess the SKS splitting parameters from the teleseismic events recorded by the CBP stations and reinvestigate them in terms of deformation geometry and its responsible tectonics. The observed anisotropy is referred to an asthenospheric origin and is interpreted as the active flow/alignments within the upper mantle. We consider the models which have been suggested so far to explain the evolution and current stage tectonics of the Pannonian basin according to the deformation pattern observed from the SKS splitting results. This is followed by discussion about the (in)consistency between these models and our results. We present here the most plausible model which may possibly explain the deep deformation pattern in relation with the present-day tectonics of the CPR and its surrounding area.

## 6.2 Tectonic background

The Carpathian-Pannonian region (CPR) was formed in several major steps during the Cenozoic. The "hard collision" between Adria and the stable European platform in the Eocene resulted in the subsequent onset major lateral displacements along main tectonic lines and the consequent lateral escape of Alcapa unit towards the east (*Kázmér and Kovács, 1985; Csontos, 1995; Fodor et al., 1999*). The Pannonian basin comprises two major units, Alcapa and Tisza-Dacia which have experienced different and complex extension processes (*Horváth et al., 2006; Schmid et al., 2008*). The region which separates these two distinct units is the Mid-Hungarian shear-zone (MHZ) where the Balaton fault is located on its northern margin (Fig. 6.1).

Clockwise rotation of the Tisza-Dacia block and counter-clockwise rotation of the Alcapa block have been proposed which took place mainly in the Early Miocene (*Márton, 1987; Csontos et al., 2002*). This was followed by the significant extension and the formation of the Pannonian basin during the rest of the Miocene (*Balla, 1984; Horváth, 1993; Horváth et al., 2006, 2015; Huismans et al., 2001*). The extension affected more substantially the lithospheric mantle than the crust where the lithosphere was thinned four to eight times of its original thickness (*Huismans et al., 2001*). The extension was followed by an episode of tectonic inversion in the past 5-10 Ma which was the consequence of the docking of major tectonic units in the Carpathian embayment (*Bada et al., 2001, 2007*).

There are controversial models as to what was the most important driving force of lithospheric extension and formation of the Pannonian basin during the Miocene. For

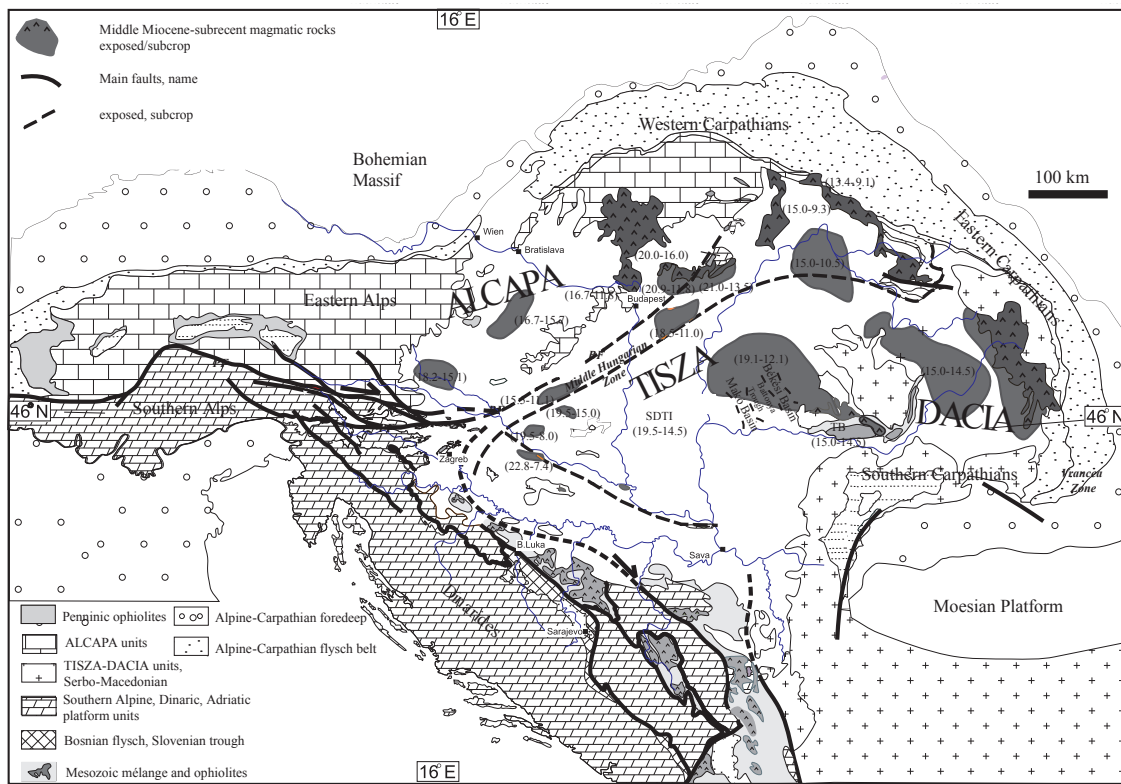


**Figure 6.1:** Spatial distribution of basement rocks and major tectonic units of the Carpathian-Pannonian region. Map is compiled and modified after (Szabó *et al.*, 1992; Tari *et al.*, 1993; Csontos, 1995; Channell and Kozur, 1997; Fodor *et al.*, 1999; Haas *et al.*, 2000; Kovács *et al.*, 2000). Middle Miocene to sub-recent calc-alkaline, alkaline volcanic rocks are highlighted with their respective age (modified after Pecskay *et al.*, 2006; Kovács *et al.*, 2007). Abbreviations for major faults are (with bold italic): PF – Periadriatic fault, BF – Balaton fault.

example, mantle plume(s) (Wilson and Downes, 1992), and diapir(s) (Stegena *et al.*, 1975) were invoked as main driving mechanisms. Geochemical (Harangi *et al.*, 2015) and geophysical data (Hetényi *et al.*, 2009) demonstrated that the potential temperature of the upper mantle is not anomalously high and the subduction "graveyard" beneath the region make the presence of whole-mantle scale, regional upwellings (commonly referred to as plumes) rather unlikely in the CPR. The most commonly accepted model is the slab-rollback model (Horváth, 1993; Horváth *et al.*, 2006) which attributes the extension of the lithosphere to the suction of the rolling back oceanic slab along the Carpathians. More recently Houseman and Gemmer (2007) argued that the extension may be due to the dripping of the overthickened lithosphere along the Carpathians which generated compression along the mountain belt and extension in the adjacent areas.

The most recent scenarios, however, all imply the potential and significant role of sub-lithospheric asthenospheric flow in the formation of the Pannonian basin. While the common point of these models is the asthenospheric flow the authors share contrasting ideas about what is responsible for generation of this flow. *Kovács et al.* (2012a) proposed that the convergence in the Alps is the main driving force, as the asthenospheric material trapped in between the colliding continental lithospheres (Adria and Europe) is squeezed out and escape towards the east parallel to the strike of the Alps. Alternatively, *Horváth and Faccenna* (2011) suggested that the formation of the Pannonian basin may be driven by an asthenospheric flow which is initiated by the roll-back of the oceanic plate beneath the Apennines and this flow enters the CPR through the Dinaric slab window. In addition, *Harangi et al.* (2015) argued that the Pannonian basin acted as a thin spot generating a nearly vertical asthenospheric flow from below the lithospheric roots under the surrounding mountain belts. Each model has its pros and cons and our seismic anisotropy data might potentially have an important contribution to the ongoing controversy about the formation of the CPR.

### 6.3 Method and data

We used the shear-wave splitting method to characterize the anisotropy. This method has become a routine means of characterizing mantle anisotropy by analyzing the splitting of the core shear waves (SKS) phases during their traveling through anisotropic structures particularly within the upper mantle. The splitting parameters, fast orientation azimuth ( $\phi$ ), and splitting delay time ( $\delta t$ ) between the fast and slow phases can be measured by several approaches. Here we measured these parameters simultaneously by applying the following techniques; the waveform cross-correlation (*Bowman and Ando*, 1987), linearizing the particle motion (minimizing the second eigenvalue of covariance matrix, *Silver and Chan* (1991)), and transverse component minimization (*Silver and Chan*, 1991), by utilizing the SplitLab package (*Wüstefeld et al.*, 2008). Applying all those techniques allows us to qualify the measurements as "good", "fair" and "poor" quality. The qualification criteria includes the similarity of results from different techniques as well as the signal-to-noise ratios (SNR), the ellipticity and linearity of particle motion before and after correction, and the region of correlation coefficients (*Barruol et al.*, 1997; *Wüstefeld and Bokermann*, 2007). After qualification, the results of the transverse component minimization approach (SC) were selected and applied to characterize the upper mantle anisotropy.

Data from the records of 59 stations at the Pannonian basin were used to measure the upper mantle anisotropy. Among those, 53 temporary stations were already installed as the Carpathian Basin Project (CBP). The CBP stations were deployed mostly on three parallel NW-SE oriented profiles with the station spacing of about 30 km passing through Austria, Hungary, and Serbia (Fig. 6.2). Records of these stations between 2005 and 2007 were used for our analysis. Data from 6 permanently installed stations of Hungarian Seismological Network (HU) between 2004 and 2014 were also included in the data collection in order to fill the gap of the stations particularly at the central and the eastern Hungary.

The database includes teleseismic events occurring in an epicentral distance range from  $90^\circ$  to  $130^\circ$  with magnitudes greater than 5.75 (Mw). Most of the waveforms were bandpass filtered between 0.01 Hz and 1 Hz and visually inspected to ensure the proper phase window selection and detecting clear splitting of the SKS phases. Altogether 5689 SK(K)S phases were visually examined in which 375 split shear waves were measured. Among those, 230 measures were selected as good quality. In addition, in the absence of significant energy on the transverse component, 109 splitting measurements were selected as good null of total 157 null measurements.

## 6.4 Shear-wave splitting results

To properly characterize upper mantle anisotropy, only good quality measurements have been taken into account. The results are presented in terms of the overall anisotropy pattern by average values of the splitting parameters, and individual measurements to give insight on the local variations of anisotropy.

Overall anisotropy pattern can be generally estimated by averaging over the measurements at each station. Circular and linear average have been calculated here for the fast azimuth and splitting delays respectively. The station average values are listed in Table 6.8, including the error of averaging (95% confidence interval). The error of averaging for the CBP stations (except CBP4J with  $\pm 21^\circ$ ) is between  $\pm 1^\circ$  and  $\pm 12^\circ$ . This error for the Hungarian network (HU) stations is between  $\pm 2^\circ$  and  $\pm 19^\circ$ .

At the number of stations, the measurements are neither tightly distributed, nor randomly scattered. Instead, they can be grouped into two categories. Care should be taken when such case is observed since making an average over all measurements does not represent the dominant fast orientation of the anisotropic structure below a given



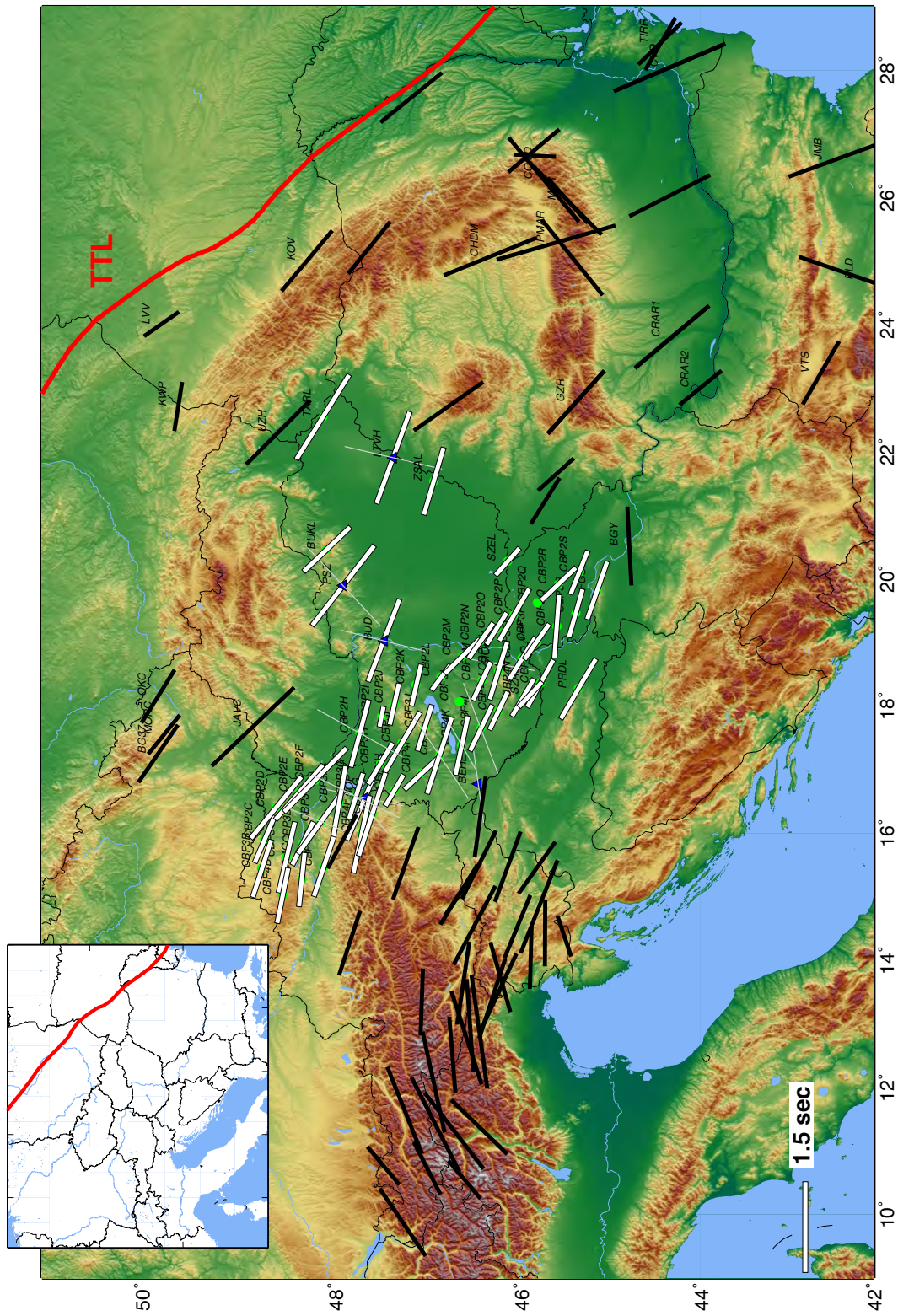


**Figure 6.2:** Average shear-wave splitting parameters, calculated over good quality measures at each station. Orientations of the bars represent the fast axis azimuth ( $^{\circ}\text{N}$ ), and their lengths correspond to the splitting delay time in seconds. White bars are the results of this study, and black bars are from previous studies (Plomerova *et al.*, 2012; Węjacz, 2001; Ivan *et al.*, 2008; Qorbani *et al.*, 2015a). Thin gray bars display the minor average values at some stations (see text). Red line shows the Tornquist-Teisseyre line (TTL). Inset shows the extension of the TTL in a larger view of Europe.

station ("mis-averaging effect"). Regarding this, the measurements at few stations (e.g. CBP2H, LTVH) can be clearly considered as two groups of fast orientations. Therefore, we apply group averaging for such stations and two averages are presented in Table 6.8. In particular, for these stations with two averages, the first one is in good agreement with the dominant fast orientation (NW-SE) from the majority of the stations, and the second (minor) averages show mostly NE-SW for the fast orientation. At three stations CBP2G, CBP3L, and CBP2Q there is no good splitting measurement.

Figure 6.2 shows the splitting parameters (average values) measured at each station. Bars show the fast orientation azimuth (angle with respect to the north) and their lengths are scaled according to the splitting delay. In this figure the thin bars show the second (minor) fast azimuths at the number of station, although the dominant fast azimuth in the whole Pannonian region is NW-SE. The results of this study are shown together with the former SKS splitting measurements in the surrounding regions (*Plomerova et al.*, 2012; *Wiejacz*, 2001; *Ivan et al.*, 2008; *Qorbani et al.*, 2015a). The dominant pattern of anisotropy in the Pannonian basin depicts clearly a coherency with these results. To the north, in the Bohemian Massif (*Plomerova et al.*, 2012) the fast orientation is NW-SE as well as at the Tornquist-Teisseyre zone in Poland (*Wiejacz*, 2001) where both regions are located outside of the Carpathians mountain chain. To the southeast, in the Apuseni area, and south Carpathians in Romania the SKS split results (*Ivan et al.*, 2008) also agree well with ours. This agreement is valid until the eastern part of the Eastern Alps (*Qorbani et al.*, 2015a), where the overall anisotropy eventually changes from NW-SE to NE-SW in the central Alps ( $\sim 12^\circ\text{E}$ , Fig. 6.2).

At the northwestern part of the CBP profiles (e.g. CBP4B station), NW-SE fast orientation slightly rotates to WNW-ESE, tending to follow the large-scale rotating deformation pattern which has been already observed along the Alps (*Bokermann et al.*, 2013). Individual splitting parameters measured at each station are presented in Figure 6.3. Most of the stations depict a robust pattern of the fast orientation (e.g. CBP3I, TARL, CBP2F) that is mainly oriented NW-SE. However, as mentioned before, at a number of stations (i.e. CBP3E, CBP3G, CBP4G, CBP4J, CBP4K, CBP4L, CBP2H, MORH, BUD, PSZ, LTVH, and SOP) the measurements can be grouped into two groups of fast orientation. Inset in the Figure 6.3 shows a histogram of the fast orientations where the values greater than  $80^\circ\text{N}$  display a nearly normal distribution with a mean of  $120^\circ\text{N}$ . The majority of the measurements fall into this distribution in the range  $85^\circ\text{N}$  to  $145^\circ\text{N}$ , while there are a number of good quality measures showing the fast azimuth less than  $80^\circ\text{N}$  which should not be ignored. To evaluate the individual measurements in a clearer way they are colored based on their value (of fast orientation azimuth) in red and blue color (Fig. 6.3).



In the northwest part of the Pannonian basin (e.g. CBP4B), the prevailing fast orientation is  $\sim 105^\circ\text{N}$  while the minor (second) pattern of anisotropy depict  $\sim 25^\circ\text{N}$  (Fig. 6.3, blue bars). At the middle latitudes where the mid-Hungarian fault zone (MHZ) is located the dominant anisotropy pattern changes from  $105^\circ$  to  $120^\circ$ - $130^\circ\text{N}$ . In this area the minor pattern of fast orientation has been measured  $\sim 70^\circ\text{N}$ . The least values of the splitting delay times are observed mostly from the stations located at about the MHZ region. Major faults in the Pannonian Basin are also shown in Figure 6.3. The minor pattern of fast orientation at three stations CBP4J, CBP4K, CBP4L are roughly parallel to the trend of the faults along the MHZ (Fig. 6.3). This is observed at PSZ station in the northern part of the Pannonian basin as well. However, at BUD station, the minor fast azimuth show  $\sim 25^\circ\text{N}$  which is the same at MORH and LTVH.

In the southern part, where the stations CBP3Q, CBP3H, CBP2S, FGSL, and PRDL are located, the dominant NW-SE fast orientation transitions into  $\sim 105^\circ\text{N}$ , similar pattern as the northwestern part. Notably, they follow the trend of the Drava and Sava faults in this area with an exception at CBP2R (Fig. 6.3). Major anisotropy pattern at the eastern Pannonian (i.e. ZSAL, BULK, LTVH, and TARL stations), next to east Carpathians mountain chain, is similar with that observed in the MHZ. Maximum concentration of individual splitting parameters in terms of fast azimuth has been measured at this area at TARL, and BUKL (Fig. 6.3).

## 6.5 Petrofabric data

Tectonic forces cause deformation of rocks within the Earth. On the upper mantle scale, this deformation leads to the arrangement of crystallographic orientation (lattice preferred orientation, LPO) of minerals, mainly olivine, which results in a macroscopic anisotropy at the long scale length of seismic waves. Examination of the anisotropy in the naturally deformed rock samples, thus, provides valuable information about the tectonic processes and mechanisms which develop the deformation within the Earth interior.

In this research we used the petrofabric experimental results from natural xenoliths from the central CPR and then compared the SKS split results to experimental data. Samples are the basalt-hosted upper mantle xenoliths from the Bakony-Balaton Highland (BBH) area and Little Hungarian Plain (LHP, Fig 6.3). The rock samples has been taken from this area which is located in the middle of the CBP profiles, providing beneficial constraints on the deformation fabric at the upper mantle depth. Olivine and pyroxene lattice preferred orientations at these samples were determined using a JEOL

5600 scanning electron microscope (at the Geosciences Montpellier, France) equipped with an EBSD system from HKL technology using Channel 5 software. Accelerating voltage of 17 kV and 25 mm working distance was used and the sample stage was tilted to 70°. Automatic orientation mapping with a step size between 10-100  $\mu\text{m}$  was carried out over areas ranging from 10mm $\times$ 20mm to 25mm $\times$ 35mm depending on grain size. For the representation of stereoplots and the calculation of seismic speed and anisotropy the software package of (*Mainprice*, 1990) was applied (see *Falus et al.*, 2008, for more details). The majority of the data used here have been already published in (*Kovács et al.*, 2012a), here we just give a brief summary of the main points.

From a large set of thoroughly studied xenoliths some representative ones were selected for EBSD measurements. According to prior geochemical and petrological analysis basically two main groups could be distinguished which include;

First group is characterized by higher equilibrium temperatures (1000 - 1150 °C), more fertile major element chemistry, higher "water" contents in nominally anhydrous minerals (NAMs) and coarse grained texture. These xenoliths originate from the depth between  $\sim 40$  and  $\sim 60$  ( $\pm 12$ ) km based on equilibrium temperatures, surface heat flow values and temperature-depth curves (see *Kovács et al.*, 2012a, for more details). Olivine's a-axes from this group plot to a single maximum, with high multiples of uniform distribution parallel to lineation in the plane of foliation in the coarse-grained porphyroclastic lherzolites. The b-axes of olivine crystals plot normal to the foliation and lineation whereas c-axes, with lowest multiples of uniform distribution, plot at relatively high angles. This group is referred to as coarse-grained, porphyroclastic A-type fabric. These xenoliths show higher seismic (5.35 - 7.33%) anisotropy.

The authors interpreted that these xenoliths represent the juvenile lithosphere which was accreted from the uprising asthenosphere during the thermal relaxation stage following the main phase of extension. Note that *Dobosi et al.* (2010) and *Embey-Isztin et al.* (2014) - although with slightly different nomenclature - identified this group as undeformed protogranular series of which geochemical and petrologic characteristics resemble very closely those explained above.

The second - geochemically and petrographically more diverse - group of xenoliths generally show lower equilibrium temperatures ( $\sim 850$  - 1000 °C), depleted major element geochemistry and water content in NAMs and porphyroclastic-equigranular texture. These xenoliths probably represent a thin,  $\sim 10$  km thick uppermost layer of the lithospheric mantle between the MOHO (at  $\sim 30$  km) and  $\sim 40$  km depth. These xenoliths usually show relatively weak seismic anisotropy (3.01 - 5.3%). Note that this group of

xenoliths was also distinguished by *Dobosi et al.* (2010) and *Embey-Isztin et al.* (2014), however, they most probably distinguished several more sub-groups within it such as: enriched poikilitic, enriched mosaic and enriched porphyroclastic and equigranular xenoliths. Since this is a relatively thin layer with only moderate anisotropy we will focus on the former group of xenoliths which presumably can provide additional information on the former asthenosphere (flow).

Note that, *Klébesz et al.* (2015) also examined the anisotropy of the upper mantle under the northern Pannonian basin using the mantle xenolith samples. The rock samples were taken from the Nógrád-Gömör Volcanic field (NGVF) in the vicinity of the BUD station (Fig. 6.3). These results provided us with additional constraints on the LPO of the upper mantle anisotropic minerals. NGVF xenoliths have shown dominantly A-type fabrics in which the fast axes polarization are parallel to the shear, geodynamically in line with the flow orientation. This implies that in the Pannonian basin we can assume the anisotropic fast orientation as an indicator of shear direction.

## 6.6 Discussion

### 6.6.1 Simple upper mantle deformation versus complex tectonic setting

The SKS split results in this study show a dominant anisotropy pattern which is oriented NW-SE (Fig. 6.2). Compared with the complexity of geologic structures (Fig. 6.1), the anisotropy measurements depict a relatively simple pattern of deformation. It is striking that this pattern is the same under different units, such as the Alcapa megaunit to the north, and the Tisza-Dacia unit to the south as well as beneath the mid-Hungarian shear zone in between. Although these two megaunits have undergone strong internal deformation in different manner, the deformation pattern reflected in seismic anisotropy is much simpler. This deformation pattern is not only observed under the Pannonian basin but also extends to the west beneath the Eastern Alps, northern Dinarides, and also the Southern Alps (Fig. 6.2). Moreover, very similar anisotropy pattern has been already measured from the splitting of SKS, at the southern Bohemian massive and the Moesian platform (Fig. 6.2). This significant simple anisotropy, remaining relatively constant in a large region, suggests that this deformation has its origin in a larger scale

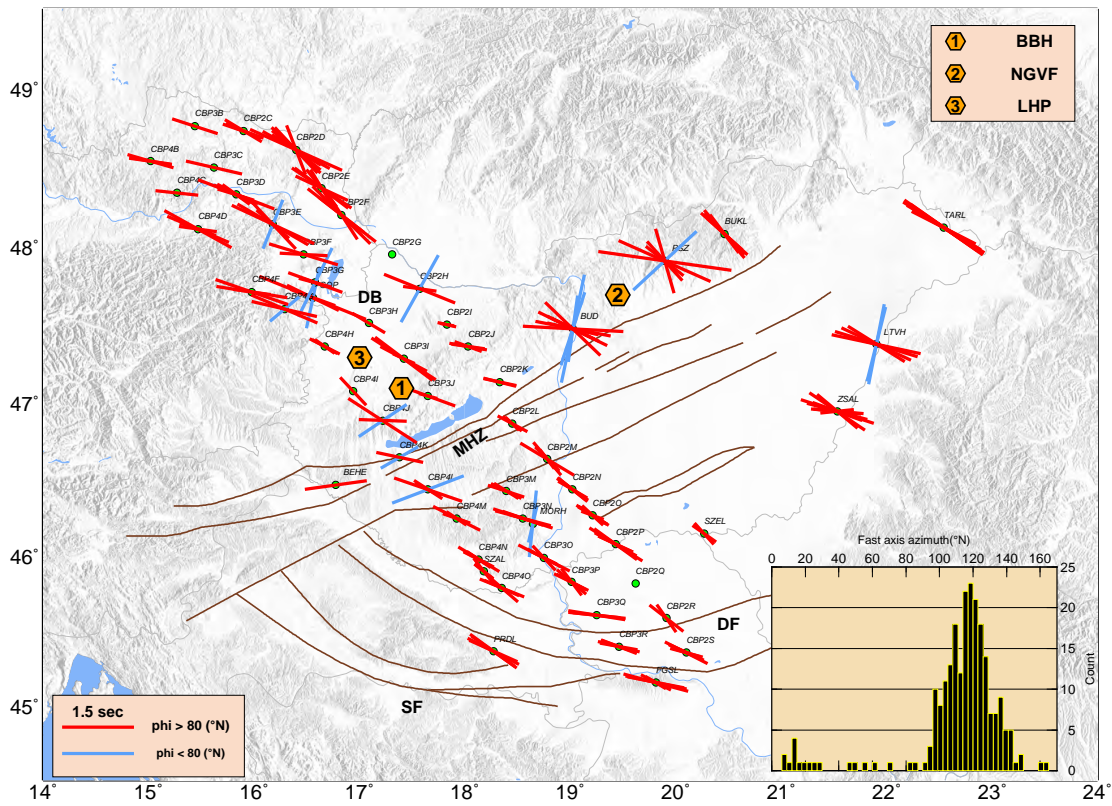


**Figure 6.3:** Individual measurements of SKS splitting parameters at each station. The inset shows a histogram of the fast axis azimuths, normally distributed in the range 80°N to 145°N. Accordingly, fast axes with azimuths larger than N80° are shown in red. There are a few measures mostly sub-perpendicular to the dominant NW-SE fast orientation, shown by light blue. Brown lines display the major faults in the Pannonian basin. DB: Danube basin, MHZ: mid-Hungarian shear zone, DF: Drava fault, and SF: Sava fault. The location of xenoliths sample origin are shown by orange symbols, #1: from Szentbaekkala, in the Bakony-Balaton Highland (BBH), #2: from Nógrád-Gömör Volcanic field (NGVF, Klebesz et al., 2015), and #3: from Little Hungarian Plain (LHP).

process that points beyond the context of the regional geology. We now discuss at which depth the anisotropy is most likely located.

### 6.6.1.1 Role of the crust

On the crustal scale, fractures and cracks in the vicinity of the active faults, and/or intrinsic anisotropy within the rocks can result in anisotropy. These features affect the propagation of seismic waves such as the splitting of the shear-wave. In the Pannonian basin, *Horváth et al.* (2006) compiled a crustal map using the result of reflection and

refraction seismic profiling, structural sections, seismic tomography, gravity and geothermal data. In that work, the crustal depth in the Pannonian basin is presented between 25 and 32 km which reaches to 35 km under the Transylvanian basin. Analysis of receiver function using the records of the CBP stations has also showed a range of 25-30 km depth for the crust which is increasing away from the Pannonian basin to the surrounding mountain chains (*Hetényi et al.*, 2015). In this study we used the core shear phases (SKS) with a dominant period of 10 s (wavelength of 50 km) which are sensitive to structures of much larger (*Barruol et al.*, 2011) than crustal depth in the Pannonian basin. This denotes that the anisotropy within such a thin crust might have not been detected by the SKS phases. On the other hand, crustal anisotropic features generally have an effect on splitting of the shear-waves as 0.1 s of delay times per 10 km (e.g. *Barruol and Mainprice*, 1993). This would lead to a delay time in order of 0.2-0.3 s for the crust in the Pannonian basin, which also consists with the worldwide crustal average value estimated less than 0.3 s (*Silver*, 1996). For this reason, the average SKS splitting delay time measured in the Pannonian basin, which is about 1.00 s, has to be originated from the upper mantle rather than the crust.

#### 6.6.1.2 Role of the lithosphere

At lithospheric depth, deformation can produce significant anisotropy which is thought to be a frozen imprint of tectonic evolution from past episodes. The possible lithospheric contribution to the anisotropy measurements can be evaluated in both terms of the thickness of the lithosphere, and the correlation between the strain field and current tectonic situation.

Lithospheric thickness of the Pannonian basin is about  $\sim 60$  km (*Posgay et al.*, 1995; *Tari et al.*, 1999; *Horváth et al.*, 2006). Comparing this thickness with the amount of delay time points out that the lithosphere might not be thick enough to create this anisotropy. Considering a maximum of 5% of the magnitude of the anisotropy derived from our xenolith samples together with the mean delay time of 1.00 s would correspond to a thickness of 100 km that is noticeably larger than the average 60 km lithospheric depth in the Pannonian basin. Even if we consider that this corresponds to only a  $\sim 30$  km thick lithospheric mantle of which upper 10 km has distinct geochemistry and weaker seismic anisotropy. More specially, the lithospheric-asthenospheric boundary (LAB) under BUD station for example, is characterized by the receiver function analysis at about 70 km depth. The splitting delay time measured at this station is 1.45 s (Table. 1). Considering a maximum of 3.74% of the anisotropy magnitude (*Klébesz et al.*, 2015), and 1.45 s delay

time would result in 194 km thickness for the anisotropic layer. This is more than twice the size of the lithosphere (LAB depth) under this station which suggests that the anisotropy may not be originated from the lithospheric mantle alone. Nonetheless, contribution of the lithosphere to the anisotropy can be assessed through (un)correlation of its deformation with that of the asthenosphere.

### 6.6.1.3 Asthenospheric origin of the anisotropy

It has been extensively suggested that localized anisotropy in correlation with the surface geology and crustal deformation (e.g. *Qorbani et al.*, 2015b) refers to lithospheric origin whereas large-scale anisotropy pattern strongly indicates asthenospheric origin (*Wüsterfeld*, 2007).

The dominant fast axis orientation under the Eastern Alps, Pannonian basin, Carpathians, Dinarides, Moesian platform, and also southern Bohemian is NW-SE (Fig. 6.2). This large-scale anisotropy is uniformly distributed from the Tauern Window (*Qorbani et al.*, 2015b), at the Alps  $\sim 12^\circ\text{E}$ , to the eastern Carpathians. It depicts a very simple pattern under the basins as similar as under and the mountain chains, indicating that the anisotropy is independent of the orogenic processes, variations in geology, and also topography. This independency can also be observed within the Pannonian basin itself namely for the Alcapa and Tisza units. While the past tectonic evolution of these two distinguished units are different, the present-day seismic anisotropy and the upper mantle deformation are very similar for both units. This has also been observed from the relatively uniform crustal thicknesses in the Pannonian basin derived by receiver function analysis which refers to analogous recent deformation phases for the Alcapa and Tisza blocks (*Hetényi et al.*, 2015).

In the previous paragraphs we demonstrated that crust and lithosphere are not thick enough to generate the observed anisotropy. Moreover, large-scale uniform anisotropy pattern under the whole Carpathian-Pannonian region is not correlated with surface geology, topography and orogenic belts (reflecting lithospheric deformation). All together, an asthenospheric deformation (flow/alignment) can be suggested as the source of the anisotropy found beneath the CPR.



#### 6.6.1.4 Lateral extrusion of the Alcapa block

Lateral escape of the Alcapa block is another important aspect that can be investigated regarding deformation mechanism beneath the Pannonian basin and also in terms of lithospheric-asthenospheric interaction. The Alcapa block is extruding laterally with a tendency to ENE direction as a result of continental collision between Adria and Europe (e.g. *Horváth*, 1988; *Fodor et al.*, 1992, 1999). Coincident alignment of the Periadriatic line (at the Eastern Alps), and the Balaton faults at the northern part of the Mid-Hungarian zone, provides suit geometry for this lateral movement (extrusion) of the whole block (*Ustaszewski et al.*, 2008).

It is still a matter of debate whether the extrusion of the Alcapa unit happened at the scale only of the crust or the entire lithosphere. Models invoking the gravitational collapse of the Alps suggest that only the upper part of the crust (where ductile flow restricted in the lower crust below the brittle upper crust and on the top of the mantle) takes part in the lateral escape (*Ratschbacher et al.*, 1991a; *Ranalli*, 1995). Alternatively, some studies (e.g. *Kovács et al.*, 2012a; *Willingshofer et al.*, 2013) proposed that the extrusion occurred at the scale of the entire lithosphere.

There are many "indirect" pieces of evidence that the extrusion most probably involved the entire lithosphere which include: 1) Garnet symplectites were found in mantle peridotites beneath the central CPR confirm that the lithospheric mantle also suffered lateral extrusion and the subsequent extension (*Falus et al.*, 2000); 2) Boninite-related mantle xenoliths from the lithospheric mantle of the central CPR (*Bali et al.*, 2007) along with calc-alkaline magmatites on the surface (i.e. *Kovács et al.*, 2007; *Kovács and Szabó*, 2008) both indicate the close vicinity of a subduction slab. The presence of this signatures both in the upper mantle and the overlying crust may confirm that the lithosphere behaved uniformly during extrusion: in other words the crust and its lithospheric mantle was coupled during the extrusion; 3) Lower crustal granulite xenoliths from the central CPR generally did not reveal anomalously high equilibrium temperatures ( $\sim 1100$  °C) which would suggest that the lowercrust was displaced immediately on the upwelling asthenosphere (*Török*, 1995; *Török et al.*, 2014; *Dégi et al.*, 2010; *Németh et al.*, 2015). Instead, the lower crustal granulite xenoliths generally display general equilibrium temperatures between  $\sim 800$ - $1000$  °C which implies that the lower crust has lower temperatures than the underlying lithospheric mantle therefore the lower crust is not anomalously hot and the temperature decreased gradually towards the surface.

Concerning the extrusion, (*Stuart et al.*, 2007) used the CBP data and found few E-W fast azimuths at the middle Hungarian latitudes. Although they measured a predominant NW-SE fast orientation under the Pannonian basin, they suggested that the E-W anisotropy can be generated by an E-W mantle flow beneath the lithosphere. The E-W fast axis derived from the analysis of *Stuart et al.* (2007) might be because of averaging over non-tightly distributed measurements at the stations situated in the middle Hungarian latitudes. CBP4J, -K, and -L (Fig. 6.3) are good examples of the mis-averaging effect on the fast axis orientation. This is the main reason that we have calculated the group averaging and presented two average values for such stations (Table 1, and Fig. 6.1). The new, and more thorough reprocessing of the SKS splitting indicates that these E-W orientations may only be artifacts and the direction of the asthenospheric flow is dominantly NW-SE (in the middle latitudes), and WNW-ESE at the both ends of the CBP profiles. This, however, does not invalidate current asthenosphere flow models suggesting an asthenospheric flow as the major driving force for the eastward extrusion of the Alcapa block and the subsequent significant extension (e.g. *Horváth and Faccenna*, 2011; *Kovács et al.*, 2012a; *Harangi et al.*, 2015). Our new data contribute to better understand the flow field and find the effects which give rise to the asthenospheric flow in the region.

In fact, similarity between lithospheric deformation and underlying asthenosphere provides us with clues about their interaction and regional plate tectonics. To attribute the driving force of a lithospheric block to the upper mantle flow underneath, coupling of lithosphere and asthenosphere is required, in which the deformation pattern (at least at the base) of the lithosphere would be (sub)parallel to the asthenospheric flow. Analytical modeling showed that (high enough) viscosity contrast between lithosphere and asthenosphere can influence the tectonics (*Doglioni et al.*, 2011; *Jadamec and Billen*, 2010) and consequently can cause relative motions and different deformation patterns.

Here, our signatures (SKS split results) from the asthenospheric flow/alignment are not consistent with the lateral escaping of the Alcapa (lithospheric motion). Therefore, regardless of driving forces whichever way they act, uncorrelation between ENE-ward extrusion of the Alcapa, and NW-SE oriented deformation within the asthenosphere suggests lithospheric-asthenospheric decoupling under this megaunit (Alcapa).

## 6.6.2 Models for upper mantle deformation

In the following we consider the various - sometimes conflicting - models for the formation of the Pannonian basin in terms of anisotropy in relation with deformation mechanisms.

### 6.6.2.1 Mantle upwelling

Mantle upwelling as a plume is one of the earliest models suggested for the formation of the Pannonian basin (*Van Bemmelen*, 1973; *Stegena et al.*, 1975; *Wilson and Downes*, 1992). In this model an active mantle plume would provide the extension driving forces. In this scenario, which is known as active rifting, extension and continental breakup is the consequence of mantle plume action at the base of the lithosphere. We showed that recent geophysical and geochemical results make the existence of a mantle plume beneath the CPR very unlikely. However, it is also worth having a look at this model from the seismic anisotropy's state point of view.

If we assume that we observe the ascent of a plume in the SKS splitting measurements, the pattern of anisotropy should depict a parabolic flow at the base of the lithosphere, as a result of interaction between extension, mantle upwelling and plate motion. Numerical modeling of the shear wave splitting associated with mantle plume-plate interaction have shown that in the lower part of the plume, the fast axis of olivine would be aligned in normal direction to the plume propagation which is radially developed. In the upper part of the plume, close to the base of the lithosphere, the circular pattern of deformation is influenced by horizontal motion (extension) and will be skewed as a parabolic form (*Ito et al.*, 2014). Shear-wave splitting measures at the Eifel hot spot, in Germany, are consistent with this prediction (*Walker et al.*, 2005a).

However, this observation and also the numerical prediction differ from our splitting measurements in the Pannonian basin. NW-SE anisotropy pattern under the whole Carpathian-Pannonian region is inconsistent with the expected anisotropy (parabolic deformation pattern) from a mantle upwelling.

### 6.6.2.2 Subduction roll-back

The subduction roll-back along the Eastern Carpathians may have generated suction of both the lithosphere and the underlying asthenosphere in a direction perpendicular to the trench. Since the former trench may have been roughly NW-SE oriented (i.e.

parallel to the strike of the present-day Eastern Carpathians), the slab suction could generate NE-SW oriented flow, with LPO presumably aligned parallel to the flow direction. This would mean that we should observe NE-SW seismic anisotropy orientation, which is different from what we observed. It was proposed, however, that high water content in NAMs produce trench parallel orientations in subduction zones in the vicinity of the slab (e.g. *Karato et al.*, 2008), which would be compatible with the observed orientations. The water content of NAMs in upper mantle xenoliths from the Persány Mts (in the immediate vicinity of the former subduction along the Eastern Carpathians) is not anomalously high (*Falus et al.*, 2008), in summary, it is unlikely that slab roll-back generated suction alone could give an explanation for the observations of present-day anisotropy and deformation pattern.

### 6.6.2.3 Gravitational instability

*Houseman and Gemmer* (2007) proposed gravitational instability of the lithospheric mantle as a governing force of the extension of the Pannonian basin. Thickened continental crust/lithosphere under the collision-driven orogeny is cold and dense, and has potential to sink. The instability of the thickened lithosphere is developed under some circumstances; consequently it starts to move downward tending to delaminate from the upper lithosphere/crust. Numerical modeling based on the gravitational instability presented a large extension factor between crust and lithosphere. This agrees with the differences in the extension factor of the crust and lithosphere observed in the Pannonian basin (*Houseman and Gemmer*, 2007).

This hypothesis can explain the existence of a high velocity body under the Eastern Alps and western Pannonian (*Dando et al.*, 2011) which has already been interpreted as a detached part of the European slab (*Qorbani et al.*, 2015a). The detachment, however, can have happened, through a preexisting tear on the subducting slab in which the concentration of the slab-pull forces near the tear's tip facilitates the slab detachment (*Wortel and Spakman*, 2000).

According to the gravitational instability, as the unstable lithosphere is downwelling, the developed space is being filled and replaced by the hot and viscous material from the asthenosphere. This implies convergence over the downgoing lithospheric mantle and divergent force field above the upwelling asthenosphere. The direction of replacement may show up in the seismic anisotropy observations, as flow of the material influences the arrangement of crystallographic orientation of minerals. Since we do not know which

direction such a replacement flow would have arrived, we can only state that it would have needed to come from NW and SE to explain the observed shear-wave splitting.

There are other lines of evidence, nevertheless which put the validity of this model into question. This model explicitly implies that downwelling occur under the mountain belts which probably may have developed deep mantle roots and extension takes place in the adjacent areas. It is not outlined under exactly which mountain belt or parts of mountain belts (i.e. Alps, Carpathians, Dinarides) downwelling took place, which would then give the framework for the related flow field. Knowing the rough eastward migration of extension (*Meulenkamp et al.*, 1996) and volcanism (*Pécskay et al.*, 1995; *Pécskay et al.*, 2006) in the Pannonian basin. It is difficult to imagine how such downwellings and consequent extension in the vicinity could reconcile with the spatial and temporal pattern of volcanism and sedimentation. In addition there is no sign of well developed mountain roots under the Western Carpathians (*Grad et al.*, 2006; *Szafián and Horváth*, 2006).

#### 6.6.2.4 Asthenospheric flow

More recently several studies emphasized the potential role of relatively young (i.e. Cenozoic) asthenospheric flow in association with the formation of the Pannonian basin. *Kovács et al.* (2012a) suggested that an active asthenospheric flow was produced as a consequence of collision in the Alps, where the asthenospheric material trapped between the colliding continental blocks (i.e. Adria and Europe) escaped most probably perpendicular to the axis of convergence. This would imply WNW-ESE and W-E orientation which is not that different from the observed subordinate WNW-ESE orientations, but it differs from the dominant NW-SE seismic anisotropy orientation.

*Horváth and Faccenna* (2011) proposed that asthenospheric flow entered the CPR through the Dinaric slab window beneath the Dinarides. This flow was initiated by the roll back of the subducted slab beneath the Apennines which pushed the asthenosphere behind both in north- and southwards. The northward flow may have entered the Pannonian basin from NE direction. This, however, should have developed seismic anisotropy with similar orientation which is almost perpendicular to the observed ones. Consequently it is not likely that this kind of flow may have played a significant role in the production of seismic anisotropy. *Harangi et al.* (2015) also proposed a thin spot induced asthenospheric flow but besides its strong vertical component the authors did not specify the

horizontal direction of the flow. Therefore, it is difficult to assess whether their model is supported or not by our seismic anisotropy observation.

### 6.6.3 Tectonic inversion and compressional regime

It has been suggested that the Pannonian basin is in a Quaternary inversion phase (Horváth, 1993). Folding and thrusting, Quaternary uplift and subsidence, and changes in the regional stress field (Ziegler and Dèzes, 2006) support this distinct transition from extension in Miocene to compression in the Pliocene. The extension of the Pannonian was finalized because the major tectonic units were docked in the Carpathian embayment and active subduction ceased at  $\sim 10$  Ma along the Eastern Carpathians (Horváth *et al.*, 2006). This also coincides with the emerging of the Carpathians towards the end of the Miocene (Krézsek and Bally, 2006). Blocking of a subduction process can be due to consumption of the subductable lithosphere. This can take place when the oceanic slab is completely subducted and the continental lithosphere reaches the subduction trench (Horváth *et al.*, 2006).

We favor the current tectonic inversion phase of the Pannonian basin (Horváth *et al.*, 2015) and apply this expression in the upper mantle scale to elucidate the nature of deformation pattern observed by anisotropy. The inversion phase implies a compressional tectonic regime acting in the NE-SW orientation. Numerical stress field modeling has suggested that the ongoing indentation of the Adria is the essential force of the present-day NE-ward compression in the Pannonian basin (Bada *et al.*, 1998, 2001, 2007). Recent GPS data in the northern part of the Dinarides have also given a motion toward the northeast in a rate of 2 mm/yr (Bus *et al.*, 2009). Convergence in a compressional regime generally leads to large folding within a weakened crust and lithosphere. A NE-SW convergent system can explain well the structural inversion and the late-stage large-scale lithospheric deformation in the Pannonian basin (Dombrádi *et al.*, 2010, their Figure 3).

Within the viscous asthenosphere, the deformation accompanying (oblique) compression is transpression, with part of the system deforming in styles between two end-member deformation models of "pure shear" and "simple shear". It is well-documented that dislocation creep mechanism induced by both styles of shear within the asthenosphere results in the alignments of olivine in which the *a*-axis lies parallel to the shear orientation (A-type fabric), and normal to the compression (e.g. Tommasi *et al.*, 1999). In the Pannonian basin, LPO of the xenolith samples from the upper mantle show dominantly



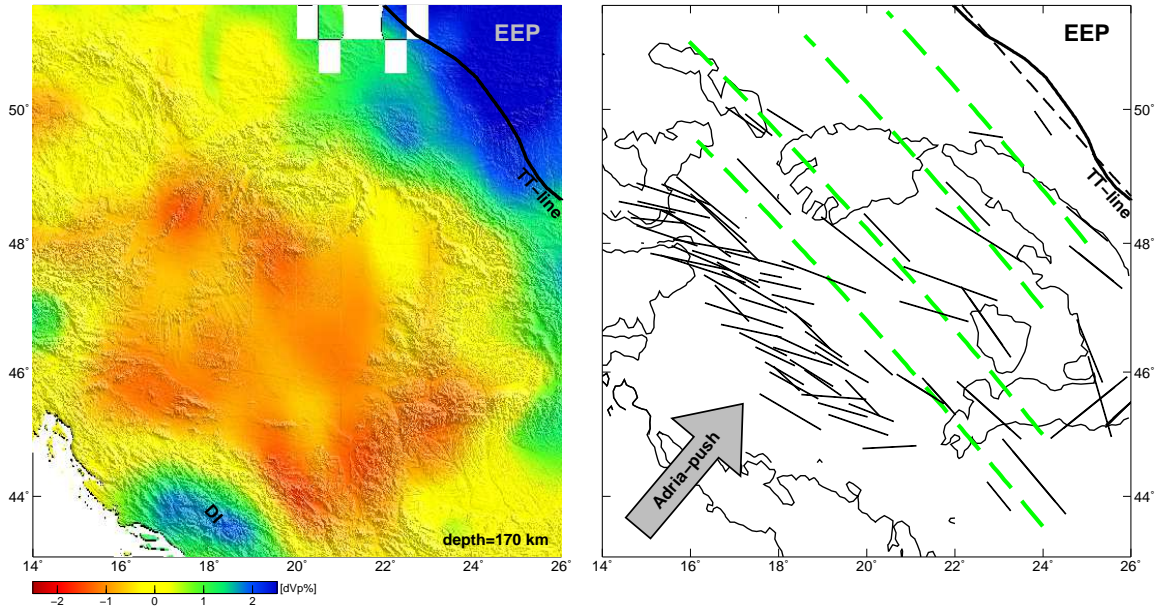


**Figure 6.4:** Left) P-wave velocity anomaly at 170 km depth (Koulakov *et al.*, 2009) which are superimposed on a topographic background. The low velocity zone (red area) at this depth is situated between two high velocity areas, East European Platform (EEP) to the NE, and Dinarides (DI) to the SW, referring to the presence of cold lithosphere at this depth. Right) The model which is suggested in this study for the anisotropy and deformation within the upper mantle under the Pannonian basin. The compressional tectonic regime associated with the Adria-push leads transpression deformation normal to the compression direction and parallel to the shear orientation. Dashed lines are parallel lines to the line best fitting the Tornquist-Teisseyre line (TTL). Our SKS split results are illustrated by black bars which are oriented roughly parallel to these lines. TTL is shown by thick black line. Contour lines are 500 m elevation indicating the orogenic belts.

A-type fabric of olivine in the asthenosphere. This allows us to consider the dominant pattern of anisotropy as the orientation of shear acting within the asthenospheric mantle.

Hence, considering the NW-SE anisotropy pattern together with the current inversion stage of the Pannonian basin suggests that this anisotropy may potentially be the consequence of compression in a convergent system. The compression most possibly is derived by the Adria plate (Adria-push) toward the NE. As the Adria pushes, the asthenospheric materials between the Adria (to the west) and East European platform (to the east) are squeezed, resulting in alignments normal to the compression direction. This compression regime acting normal to the anisotropy pattern therefore is proposed as a possible model for deformation mechanism (Adria-East European compressional model, AEC). However, enough stress and long enough time may be needed to completely rearrange

the orientation of LPO of olivine in mantle mineral.

### 6.6.3.1 Role of the East European Platform in the AEC model

The East European platform (EEP) is an old, large and relatively stable plate. It is situated in the eastern and northern Europe from the Scandinavian mountains to the Urals, and from the Barents Sea to the Black and Caspian seas. The border between EEP and western Europe is identified as the Tornquist-Teisseyre line (TTL, Fig. 6.2). This line separates the tectonically active western Europe from the aseismic and stable Precambrian EEP (*Okay et al.*, 2011). We note that the Adria-push is oriented in a direction nearly perpendicular to the edge of the EEP, and it seems natural to consider the EEP as the backstop of the convergence.

Indeed, lithospheric and crustal structures at the east and west of the TTL show remarkable differences. The low velocity zone (from the tomographic models) between 75 and 300 km in the west of the TTL reveals a relatively thick asthenosphere beneath a thin lithosphere while at the same depth range under the EEP the velocity structures sharply differ from the western part and show a thick lithosphere (Fig. 6.4, 6.5). In this area, tomographic images (*Bijwaard and Spakman*, 2000; *Koulakov et al.*, 2009; *Dando et al.*, 2011) have shown cold slab (as high velocity anomalies) under the East Carpathians which is connected to the sub-vertical slab under the Vrancea zone to the south.

Lithospheric root under the old cratons generally reaches to 200 km depth. Beneath the EEP, according to the tomographic models it extends to about 300 km. This lithospheric root under the EEP, thus, is thick and rigid enough to act against the compression on the upper mantle scale. Hence, in this NE-ward convergent regime toward (fixed) East European platform, the lithospheric root of the EEP may be constrained to act as a barrier. This limits the transpression in the region between the EEP and Adria. Under these conditions, the material within the asthenosphere are deformed and aligned normal to the compression direction and tend to follow the geometry of the barrier (EEP). The NW-SE geometry of the TTL which is nearly parallel to the anisotropy pattern is consistent with this model.

Figure 6.4 shows the AEC model in which the convergence of the Adria with respect to the EEP causes the transpressional shear and develops the compressional deformation as the consequence. To test this, we show in Figure 6.4 parallel lines to (the line best fitting) the TTL suggesting that this orientation explain a fair number of the shear-wave splitting observations. However, the anisotropic pattern shows small deviations from the

general trend of the TTL. This deviation is particularly the case for the observations in the northwest of the CBP profile which are located in a distance from the EEP.

### 6.6.3.2 Role of the Dinaric slab

Tomographic models have imaged a lithospheric root of about 200 km depth under the Dinarides and Hellenides which has been interpreted as the subducted Adriatic plate (e.g. *Koulakov et al.*, 2009). However the velocity models show a slab gap under the northern Dinarides, near to the Eastern Alps (e.g. *Piromallo and Morelli*, 2003), as can be seen in Figure 6.4 between 44°N to 46°N. As a consequent, asthenospheric material can flow NE-wards into this slab window toward the Pannonian basin (*Horváth and Faccenna*, 2011). This flow might have an (minor) effect on the upper mantle anisotropy under the slab window. SKS measurements derived from a number of Slovenian seismic stations (*Qorbani et al.*, 2015a, their Figure 3), and near to the Adriatic coast (*Salimbeni et al.*, 2013) depict slightly complex anisotropy pattern with respect to the other stations located in the eastern Alps. However, it may not be large or thick enough to affect dominantly the splitting of the SKS phases. Most of the SKS measurements in this area (derived from the Slovenian network) show NW-SE fast orientation which are not in line with flow through such a slab gap. Even though in the Pannonian basin there are few measurements depicting NE-SW fast orientation (Fig. 6.2), their origin is not clear. Further anisotropy measurements and analyses particularly in the northern Bosnia and Croatia thus are required to elucidate the existence and to map the geometry of this flow through the slab window to the upper mantle under the Pannonian basin.

On the other hand, a role of NE-ward subduction of the Dinaric slab has been suggested for the extension of the Pannonian basin. (*Matenco and Radivojević*, 2012) retreat of the Dinaric slab and its ongoing delamination as a controlling factor for the extension of the (southeastern) Pannonian basin.

In this circumstance, the observed anisotropy (NW-SE orientation) is more consistent with a trench-parallel flow, which can be associated with the subduction of the Adriatic plate (as Dinaric slab), rather than the NE-ward asthenospheric inflow. Along the Dinarides, the subduction and southeast dipping Dinaric slab toward the Hellenides (*Horváth et al.*, 2006) seem to have notable effect in creation of SE fabric alignment within the uppermost mantle, similar to what we measured. In addition to the AEC model, the Dinaric slab can also be the causing of anisotropy, chiefly for the regions in the vicinity of the Dinarides. Trench-parallel alignment (in turn anisotropy) can be created by either two-dimensional flow in the subduction wedge, or the anisotropic structure within

the down-going slab (*Faccenda et al.*, 2008). In either case, this effect is limited to the forearc region of the subduction and the large-scale NW-SE alignments under the whole Carpathian-Pannonian region has to be created by another mechanism. It is possible to consider that the subduction system under the Dinarides and stretching of the Dinaric slab down to the Aegean, together with the compressional deformation regime under the CPR, are parts or consequences of a larger tectonic system which governs and controls the large-scale NW-SE mantle alignments/flow from the Eastern Alps until the Hellenic subduction zone where NW-SE fast orientation is changed mainly to NE-SW (*Evangelidis et al.*, 2011).

### 6.6.4 Local variation of deformation

Beyond the simple and dominant NW-SE oriented deformation pattern from the SKS split results, fast axis azimuth and splitting delay time show some small-scale spatial variations.

#### 6.6.4.1 Fast axis orientation

Fast orientations depict small fluctuations along the CBP profiles. WNW-ESE orientation at the northwestern of the CBP profiles slightly changes to NW-SE along the most of the profiles and back to WNW-ESE orientation at the end of the profiles. This change is roughly the same for the three CBP profiles. Rotation of the fast axes at the northwest occurs outside the Alpine chain (Fig. 6.3). This pattern (WNW-ESE) alone might be referred to a toroidal flow around the slab keel. However, we observed clear NW-SE orientation right under the chain, which extends even further toward the Eastern Alps, and is in wide angle with the trend of the mountain chain. Presence of a gap under the Eastern Alps, created by slab detachment in which the material can flow through, can explain this anisotropy (*Qorbani et al.*, 2015a). In addition, asthenospheric flow from below the Alps (or/and the Dinarides) could also contribute to this WNW-ESE orientation.

Further to the south along the CBP profiles the NW-SE anisotropy remains rather constant (Fig. 6.3). The noticeable change of the fast axes occurs at the southeast of the CBP profiles where the Drava and Sava faults are located. In this area the anisotropy pattern follows the trend of the faults and is in accordance with the Sava shear zone. Because

of the correlation between the fault pattern and the anisotropy, at the first-order assessment, the anisotropy seems to be associated with the deformation in the crustal/lithospheric scale. This most probably is not the case, since the lithospheric thickness and the amount of splitting delay time into account, indicates that the anisotropy in this particular area is unlikely be generated by the lithosphere alone. For this reason, a correlated lithospheric-asthenospheric deformation can be assumed under this part of the south Pannonian basin.

This would not be in contradiction with the compressional deformation regime within the asthenosphere. Variation in the geometry of the boundary conditions around the Pannonian basin (e.g. TTL, South Carpathians, and NE-ward subduction of the Dinarides) can make local changes in the deformation geometry. In particular, interaction between the Dinarides and South Carpathian in this area can affect the deformation process in the upper mantle and consequently can change the orientation of the anisotropy locally. However, these local changes cannot be related to a variation in the compression regime over on the whole Pannonian basin. For instance, the anisotropy under the Moesian platform (station CRAR1, 2), and also in the southern Carpathians (station GZR) is still NW-SE oriented (Fig. 6.2) which is not consistent with the pattern of the faults. An alternate would be an additional effect of slab roll back along the East Carpathians which might have contributed to the formation of anomalous seismic anisotropy orientations. In this concept, (*Buttles and Olson, 1998*) showed that in a subduction system, during the rollback, a toroidal flow around the subducted slab is generated. Therefore, while the migration of the rollback takes place from the north to the south, the toroidal flow induced by slab retreat is also migrated toward the south. This can provide a SE-ward flow of material in the asthenosphere.

Such a SE-ward flow may influence the transpression deformation, associated with the Adria-push, to be more aligned with the TTL in regions close to the EEP. This toroidal flow might be responsible for the local variations in the fast axis azimuths, and may also explain the small deviations of fast azimuth from the general trend of the TTL (Fig. 6.4). Another alternative that can explain the local variations of the fast azimuths and their small deviations with respect to the NW-SE oriented TTL comes from the effect of strain magnitude on the development of the olivine-rich upper mantle material. Laboratory experiments showed that at large strain ( $>150\%$ ) the LPO of olivine aggregates develops in a case that the a-axis (fast) lies parallel to shear direction, while at low strain and when the dynamic recrystallization is not dominant, the a-axis is oriented oblique to the shear direction (*Zhang and Karato, 1995; Tommasi et al., 2000*). Along with the effect of the



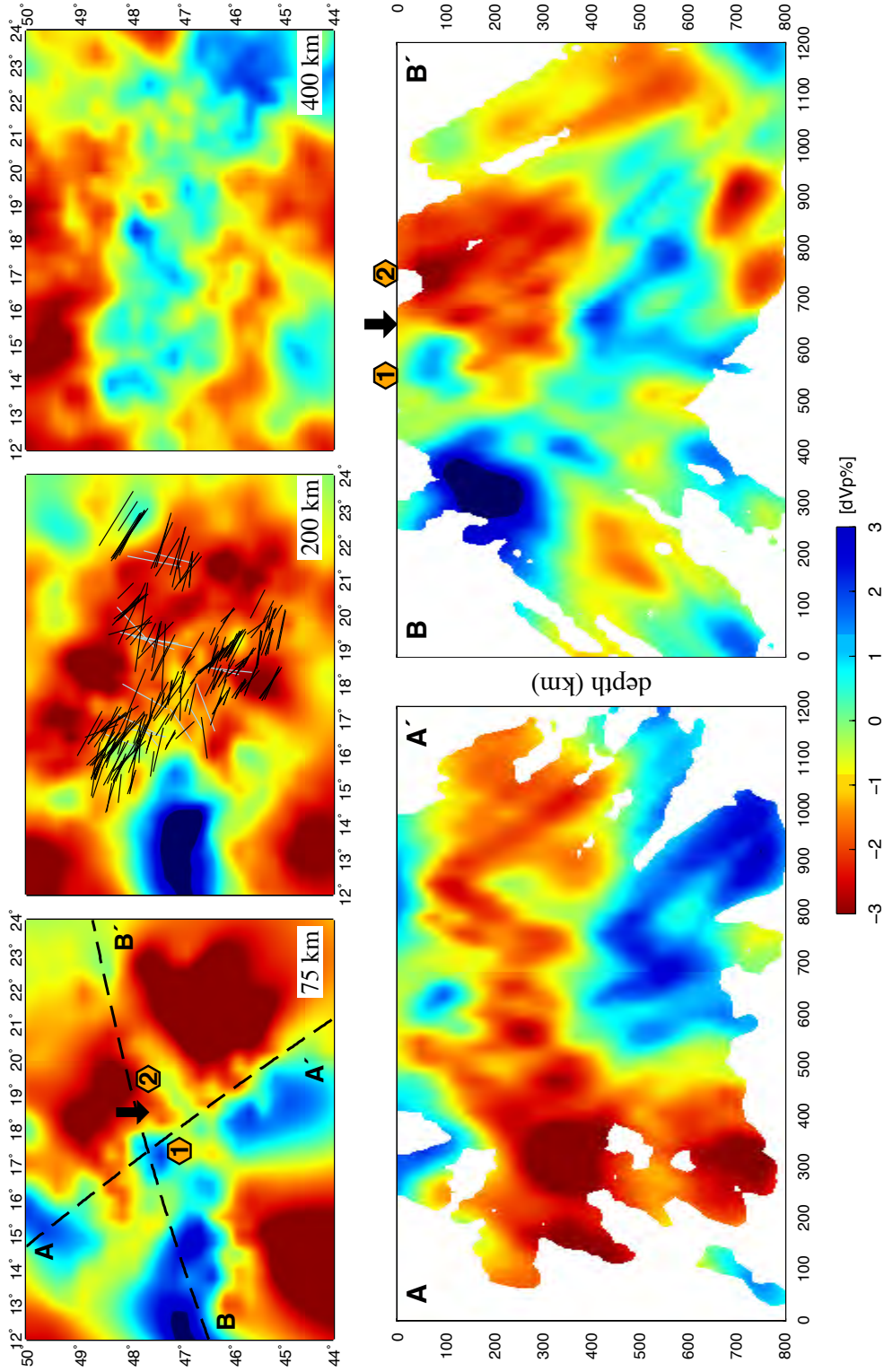


**Figure 6.5:** Top row) Shear-wave velocity anomalies shown at the three depth slices, 75, 200, 400 km. Top left) The location of xenolith sample origins is represented by hexagons, #1 for BBH and #2 for NGVF. The surface positions of two vertical profiles, AA', BB' are also traced. Top middle) Individual measurements (projected at 200 km) are superimposed. Top right) At 400 km depth, large high velocity anomaly is observed extending to the mantle transition zone. Bottom) Two vertical profiles of the velocity model, AA', and BB'. The xenolith samples locations are shown on the BB' profile. Note the changing of thickness of the low velocity zone underneath. NW-SE vertical profile, AA', shows a layer of low velocity zone between 100 and 400 km depth.



dynamic recrystallization, the degree to which the strain field is distributed may depend on the several factors, such as temperature, the geometry of the media (thickness), and the strain history which all are considerable in the Carpathian-Pannonian region.

#### 6.6.4.2 Splitting delay time

Delay times between the fast and slow split phases are generally an expression of the strength of the anisotropy and the thickness of the anisotropic structure. In the Pannonian basin, the delay times show unusual values particularly in a region between the Danube basin and the MHZ (Fig. 6.3). Stations located in this area (e.g. CBP3H, -2I, -2K, Fig. 6.3) are characterized by small values of delay times. In contrast, the nearby stations, which are not located on the CBP profile, show large values where an abrupt change of the delay times is observable (from station CBP2K to BUD, Fig. 6.3). Further to the east from this area the stations mostly yield large delay times. This significant change can be evaluated in terms of the thickness of anisotropic feature. Figure 6.5 shows S-wave velocity variations at the Pannonian basin derived from the CBP data (*Dando et al.*, 2011). Three tomographic images at 75, 200, and 400 km are shown in which the individual anisotropy measurements are superimposed on the 200 km depth slice. The thickness of the low velocity zone (generally interpreted as the hot and viscous asthenospheric material which can flow) can be estimated from two vertical profiles have been made from this tomographic model.

In a similar way as the delay times, the thickness of the low velocity zone is dramatically increased from west to the east (along the BB' profile, marked by arrow in Fig. 6.3). This change occurs at the same area where the transition from small to large delay times appears. The correlation between low velocity zone within the asthenosphere and the splitting delay time is an additional strong support for referring the anisotropy to the alignments/flow in the asthenosphere. In particular, the low velocity (anisotropic) zone under the CBP3H is thin, thus it can cause small value of splitting delay and vice versa for BUD station.

In order to calculate the shear wave anisotropy and to estimate the thickness of the upper mantle anisotropy under this area, *Klébesz et al.* (2015) assessed different foliation and lineation settings for 8 xenolith samples taking from the NGVF area (Fig. 6.3). They also compared their results with those from the BBH xenoliths. This comparison showed that for a similar foliation and lineation geometry, the thickness of anisotropic layer beneath the NGVF area should be about twice as much as the layer thickness

beneath the BBH. Locations of NGVF and BBH regions are shown in Figure 6.5. BBH is situated in the area where small splitting delay times are measured and also with a thin asthenosphere, whereas NGVF is placed among the stations presenting large delay time and with a thick asthenosphere. The SKS split results, velocity anomalies, and petrofabric data are three independent observations from the Pannonian basin, which indicate a correlation between the asthenospheric mantle geometry and the anisotropy. This also strongly points out an asthenospheric origin of the anisotropy.

Consistency between these three groups of observation can be assessed in order to further insight into the deformation mechanism and geometry in terms of foliation plane and lineation direction. Five end-member orientations of foliation and lineation have been evaluated for the xenolith samples taken from NGVF and BBH regions (*Klébesz et al.*, 2015). Among those, in case of horizontal foliation and lineation, for a 1.00 s delay time, the NGVF samples represented 280 km for the thickness of the anisotropic layer, and BBH samples showed 120 km. These values are in range with the thicknesses of the low velocity layer (asthenosphere) underneath (Fig. 6.5, profile BB'). Therefore, the horizontal foliation plane in which the lineation is aligned with the direction of shear seems to be the most plausible model. In these circumstances, the thicknesses of the anisotropic layer also agree with the SKS splitting delay times and are sufficient to cause such anisotropy. Hence, the low velocity zone between 100 and 400 km depth (Fig. 6.5, profile AA') can be considered as a depth range of the anisotropic structure in the upper mantle under the Pannonian basin.

## 6.7 Conclusion

The SKS splitting measurements have provided important insight into the upper mantle deformation pattern under the Carpathian-Pannonian region (CPR). The results depict NW-SE (fast axis) orientation which is dominantly extended under the CPR. In comparison to the complex geology and crustal/lithospheric tectonics, the anisotropy reveals simple deformation pattern at the sub-lithospheric depth. It shows very similar pattern to what has already been observed at the Eastern Alps. We also used experimental results from the naturally deformed upper mantle xenolith rock samples (from the Pannonian basin) to infer the anisotropy. These results mostly show A-type fabrics in which the fast axes are parallel to the shear orientation.

According to the amount of splitting delay time, the Pannonian crust (25-30 km depth) is obviously not thick enough to create this anisotropy. Moreover, comparison of lithospheric depth from receiver function analysis, anisotropic thickness derived from xenolith samples, and splitting delay times indicates that contribution of lithosphere to the observed anisotropy can also be ruled out. Hence, together with the constraints from xenolith samples, we conclude that the anisotropy most likely has an origin from the asthenospheric mantle as flow/alignments in NW-SE orientation. This pattern is remarkably oblique to the lateral (eastward) movement of the Alcapa block. The disparity between lateral extrusion of the Alcapa and asthenospheric flow can be sited as evidence for decoupling of the lithosphere and asthenosphere particularly under the Alcapa meganuit.

Present-day tectonics of the Pannonian basin is mainly governed and controlled by NE-ward pushing of the Adria according as the inversion phases which has already been suggested for the Pannonian basin. We implied this expression to propose a model for the recent and current stage of deformation mechanism at the upper mantle depth. We present Adria-East European compressional (AEC) deformation model as a possibility to explain the deep deformation pattern which is uniformly distributed under the whole Carpathian-Pannonian region. Based on this model, the asthenospheric material is subjected to the oblique compression due to NE-ward pushing of the Adria plate resulting in alignment of the mineral normal to compression. East-European platform (EEP) has an important role in this model. It acts as a backstop in the system and forces the minerals to be aligned with its geometry. The trace of Tornquist-Teisseyre (TT) line which indicates the western margin of the EEP, is parallel to the NW-SE anisotropy. This suggests a strong association of the deep deformation with the geometry of the EEP. In addition, the subduction system beneath the Dinarides and Hellenides can play a role for the NW-SE anisotropy. NE-/E-ward subducted Adriatic plate (has been image as Dinaric slab) is a plausible mechanism in generating trench-parallel (NW-SE) anisotropy. This is particularly the case, and might be restricted for the region under the trench and forearc.

The inference of the upper mantle alignment/flow from seismic anisotropy reveals a large-scale NW-SE orientation not only under the CPR but also beneath the Eastern Alps. It provides an important benchmark and may benefit to address the unanswered questions related to the geodynamics of CPR and surrounding regions.

## 6.8 Acknowledgments

We thank Greg Housman and Graham Stuart for the access to the Carpathian Basin Project (CBP) data used in this study which was provided by IRIS data center. We acknowledge the Hungarian Seismological Network as the source of permanent station data were provided by GFZ webdc data center. We also thank Ben Dando for preparing the tomographic velocity model. This work was supported by Austrian Science Fund (FWF).

**Table 6.1:** List of the stations with the average value of fast orientations and splitting delays including their corresponding error. For the stations showing two patterns of fast orientation, two average values are presented (group-average). Number of splitting measurements (SM) and good quality splitting (GS) are listed together with the number of Null measurements (NM) and good quality Null (GN). "-" symbol for the error indicates only one good measurement at the station. "Na" represents no good quality measurement.

Station	Net	Lon(°E)	Lat(°N)	$\phi(^{\circ})$	$\phi$ -err	$\delta t(s)$	$\delta t$ -err	SM	GS	NM	GN
BEHE	HU	16.77	46.47	82	-	1.30	-	8	1	1	1
BUD	HU	19.02	47.48	111	9	1.46	0.26	23	7	13	8
BUD				14	4	1.45	0.63		4		
LTVH	HU	21.90	47.38	110	6	1.62	0.18	12	5	2	1
LTVH				13	2	1.65	0.07		2		
MORH	HU	18.64	46.21	10	5	1.10	0.42	3	2	3	1
PSZ	HU	19.89	47.92	128	19	1.68	0.59	12	5	2	0
PSZ				47	-	1.80	-		1		
SOP	HU	16.56	47.68	113	3	1.53	0.69	20	3	9	5
SOP				12	-	1.30	-		1		
BUKL	HU	20.46	48.09	136	3	1.07	0.15	9	7	1	1
CBP2C	YG	15.90	48.74	113	5	0.85	0.05	5	4	2	0
CBP2D	YG	16.40	48.62	130	8	1.32	0.22	14	9	0	0
CBP2E	YG	16.64	48.38	131	11	1.20	0.20	8	5	1	1
CBP2F	YG	16.83	48.21	134	8	1.48	0.27	6	4	1	0
CBP2G	YG	17.31	47.96	Na		Na		2	0	2	1
CBP2H	YG	17.57	47.74	105	10	1.15	0.62	4	2	1	0
CBP2H				29	-	1.60	-		1		
CBP2I	YG	17.83	47.51	102	2	0.35	0.07	4	2	0	0
CBP2J	YG	18.03	47.37	103	6	0.70	0.09	4	3	2	1
CBP2K	YG	18.33	47.14	103	1	0.70	0.00	3	2	0	0
CBP2L	YG	18.45	46.87	127	8	0.53	0.14	3	3	0	0
CBP2M	YG	18.78	46.64	135	7	0.82	0.24	9	5	2	1
CBP2N	YG	19.02	46.44	125	3	0.72	0.07	8	5	5	3
CBP2O	YG	19.21	46.27	123	6	0.63	0.09	9	6	3	3
CBP2P	YG	19.43	46.08	120	3	1.00	0.14	8	6	5	1
CBP2Q	YG	19.62	45.82	Na		Na		2	0	0	0
CBP2R	YG	19.91	45.59	136	12	0.80	0.14	7	2	5	4
CBP2S	YG	20.10	45.36	112	4	0.78	0.12	9	5	4	3

CBP3B	YG	15.44	48.77	108	-	1.00	-	1	1	0	0
CBP3C	YG	15.62	48.51	103	-	1.20	-	6	1	3	3
CBP3D	YG	15.83	48.34	116	3	0.80	0.19	15	11	1	1
CBP3E	YG	16.18	48.15	126	7	1.30	0.42	6	5	3	2
CBP3E				22	-	1.10	-		1		
CBP3F	YG	16.47	47.96	100	10	1.25	0.35	5	2	1	1
CBP3G	YG	16.58	47.78	107	2	0.80	0.33	6	3	0	0
CBP3G				26	-	1.60	-		3		
CBP3H	YG	17.09	47.52	121	-	0.80	-	3	1	0	0
CBP3I	YG	17.42	47.29	120	5	1.17	0.42	6	4	2	2
CBP3J	YG	17.65	47.05	108	3	0.80	0.55	2	2	2	2
CBP3L	YG	18.06	46.67	Na		Na		1	0	0	0
CBP3M	YG	18.39	46.43	115	5	0.70	0.07	5	4	6	5
CBP3N	YG	18.55	46.25	107	2	1.00	0.27	8	4	5	4
CBP3O	YG	18.75	45.99	122	9	0.82	0.22	5	4	3	3
CBP3P	YG	19.01	45.83	125	9	0.72	0.07	5	5	3	3
CBP3Q	YG	19.25	45.61	94	5	1.05	0.16	5	3	1	1
CBP3R	YG	19.46	45.40	106	4	0.83	0.04	5	4	2	2
CBP4B	YG	15.02	48.55	101	4	0.93	0.05	7	3	6	4
CBP4C	YG	15.27	48.35	96	-	0.90	-	3	1	1	1
CBP4D	YG	15.47	48.12	109	6	1.04	0.34	6	5	3	3
CBP4F	YG	15.98	47.72	102	6	1.30	0.40	4	3	3	1
CBP4G	YG	16.29	47.61	138	7	1.45	0.07	5	2	3	2
CBP4G				50	-	0.80	-		1		
CBP4H	YG	16.67	47.37	120	4	0.60	0.09	3	3	0	0
CBP4I	YG	16.94	47.08	137	-	0.80	-	2	1	0	0
CBP4J	YG	17.22	46.89	138	21	1.35	0.48	3	2	11	9
CBP4J				56	-	1.20	-		1		
CBP4K	YG	17.38	46.65	102	-	1.00	-	3	1	2	1
CBP4K				60	-	0.90	-		1		
CBP4L	YG	17.65	46.44	116	5	0.85	0.37	7	4	7	4
CBP4L				69	-	1.60	-		1		
CBP4M	YG	17.92	46.25	116	6	0.70	0.23	4	4	4	3
CBP4N	YG	18.13	45.98	120	2	0.72	0.13	5	5	6	6
CBP4O	YG	18.35	45.79	119	10	0.90	0.09	5	3	0	0
FGSL	YG	19.81	45.16	109	7	1.02	0.31	7	5	3	3



---

PRDL	YG	18.27	45.37	120	5	1.15	0.05	4	4	4	2
SZAL	YG	18.18	45.90	133	7	0.57	0.11	3	3	4	3
SZEL	YG	20.27	46.15	132	9	0.60	0.00	5	2	2	2
TARL	YG	22.54	48.13	122	2	1.65	0.17	14	10	0	0
ZSAL	YG	21.53	46.95	106	10	1.16	0.18	9	8	2	1

---

---

Submitted paper:

JOURNAL OF GEOPHYSICAL RESEARCH, VOL. ???, XXXX, DOI:10.1029/,

## DEEP DEFORMATION PATTERN FOR THE CARPATHIAN-PANNONIAN REGION

Ehsan Qorbani,<sup>1</sup> Götz Bokelmann,<sup>1</sup> Istvan Kovács<sup>2</sup>, Frank Horváth<sup>3</sup>, and György Falus<sup>2</sup>

**Abstract.** To better understand the evolution and present-day tectonics of the Carpathian-Pannonian region (CPR), we characterize upper mantle anisotropic structures and map deep deformation patterns for this region. SKS splitting parameters measured from teleseismic events recorded by the Carpathian Basin Project (CBP) stations are presented. We investigate these measurements together with petrologic indicator of deformation in basalt-hosted upper mantle xenoliths from the Pannonian basin with regard to anisotropy, deformation geometry, and responsible mechanisms. The results show NW-SE fast orientation under the whole CPR. We contribute this anisotropy to an asthenospheric origin and interpret it as flow induced alignments within the upper mantle that is remarkably inconsistent with the lateral extrusion of the Alcapa block. Several models and scenarios have been suggested so far to explain the evolution and current stage tectonics of the Pannonian basin. These are compared with the deformation pattern observed in the SKS splitting results. We discuss the (in)consistency between these models and our results. We present here the most plausible model responsible for the deformation within the asthenospheric mantle in relation with overlying and surrounding lithosphere. In this model NW-SE deformation is mainly generated in a NE-ward compressional tectonic regime acting in a region between the Adriatic plate and the East European platform.

### 1. Introduction

Understanding the mechanisms linking surface deformation with dynamics of the Earth's interior requires constraining upper mantle processes [e.g. *Long and Silver*, 2009]. Even though the upper mantle has been extensively studied in terms of seismic velocity discontinuities, thermal conditions, and chemical and physical compositions, interaction between the upper mantle flow and lithosphere requires to be fully elucidated in terms of deformation and strain distribution in the upper mantle.

Seismic anisotropy is manifested by a directional dependence of seismic velocity. Within the upper mantle it is generated mostly by development of the crystallographic orientation of minerals in response to deformation [*Long and Becker*, 2010; *Mainprice et al.*, 2000]. Observing seismic anisotropy therefore can be used to describe the strain distribution in the upper mantle, in turn, reflecting the deformation mechanisms, active flow geometry, and also the conditions in which the rock is deformed [*Karato et al.*, 2008]. These observations allow us to address what happens at depth where stress and strain cannot be measured directly.

The Carpathian-Pannonian region (CPR) is at the north-eastern end of the Alpine mountain belt. It consists of a variety of geological structures and tectonic units resulting from subduction, plate collision, basin evolution, and thrust faulting. This region provides a unique opportunity to study mechanisms which govern deep and surface deformation, over a wide range of timescale from the past tectonic episodes until the present-day situation. A large part

of the CPR is occupied by the Pannonian basin, which is surrounded by the Alps, Dinarides, and Carpathians (Fig. 1). In order to get insight into the origin of the extensional basins within the CPR, the Carpathian Basin Project (CBP) had been established. It was aimed to provide high 3-D resolution seismic images and numerical modeling using data from seismic instruments deployed mainly in the Pannonian basin. Alongside number of seismological studies including velocity tomography and receiver functions analyses which have been done so far using the CBP data, the upper mantle anisotropy has also been studied through SKS splitting measurements [*Stuart et al.*, 2007]. While some of the results of that study agree with other recently published anisotropy analysis of the Eastern Alps [*Bokelmann et al.*, 2013; *Qorbani et al.*, 2015a], some do not. The present study is planned attempting to address this inconsistency.

In this study, we characterize upper mantle anisotropic structure and deep deformation pattern for the Carpathian-Pannonian region. We reprocess the SKS splitting parameters from the teleseismic events recorded by the CBP stations and reinvestigate them in terms of deformation geometry and its responsible tectonics. The observed anisotropy is referred to an asthenospheric origin and is interpreted as the active flow/alignments within the upper mantle. We consider the models which have been suggested so far to explain the evolution and current stage tectonics of the Pannonian basin according to the deformation pattern observed from the SKS splitting results. This is followed by discussion about the (in)consistency between these models and our results. We present here the most plausible model which may possibly explain the deep deformation pattern in relation with the present-day tectonics of the CPR and its surrounding area.

### 2. Tectonic Background

The Carpathian-Pannonian region (CPR) was formed in several major steps during the Cenozoic. The "hard collision" between Adria and the stable European platform in

<sup>1</sup>Department of Meteorology and Geophysics, University of Vienna, Austria.

<sup>2</sup>Geological and Geophysical Institute of Hungary.

<sup>3</sup>Geomega Ltd., Budapest, Hungary.

# Chapter 7

## Summary and Conclusion

The deep deformation pattern and mechanisms within the upper mantle for the Eastern Alps and Carpathian-Pannonian region constitute the focus of this work. The study has also sought to provide insight into the upper mantle structure under this region as there are number of open questions on the nature and origin of the geodynamic activities for the Alpine-Carpathian system. In particular, the Eastern Alps and its connection to the adjacent mountain belts; Carpathians, and Dinarides, and also to the evolutional basins, most importantly the Pannonian basin. Upper mantle structure under the Alps was previously studied by seismic velocity tomography. Although their results and interpretations of the downgoing European slab under Adria in the Western Alps agree with each other, they have left debates and ambiguities especially regarding the subduction geometry beneath the Eastern Alps.

To accomplish that goal we primarily utilized anisotropy analysis by measuring splitting parameters of the core shear-waves (SKS). These are the azimuth of fast axis polarization, and splitting delay time. Records of teleseismic events occurred in the epicentral distance of  $90^\circ$  to  $130^\circ$  with magnitude greater than 6 Mw have been used in the measuring process. This data had been recorded by 39 permanent broadband and 53 temporary broadband stations located in Austria, northern Italy, Slovenia, Hungary, Serbia, and Croatia. We used kinematic data of the lower crust deformation, and also petrofabric indicators from naturally deformed upper mantle rock samples as complementary information to infer the lithospheric-asthenospheric anisotropy and deformation pattern. We also benefited from the results of several geophysical studies such as tomographic velocity models, crustal depth (compiled from several geophysical studies), and lithosphere-asthenosphere boundary (LAB) depth from receiver function analyses.

## 7.1 Large-scale chain-parallel anisotropy along the Alps

As first topic, we characterized the large-scale upper mantle anisotropy, in turn, the deformation pattern all along the Alpine chain. We used the data from 12 permanent stations of the Austrian seismological network (OE) to measure the anisotropy. In Chapter 3, we showed the average values of the splitting parameters at each station. Our anisotropy measurements at the central and western part of the Eastern Alps agreed well with the previous SKS split results. The measures showed a change in the pattern of anisotropy with a jump by about  $45^\circ$  in the Eastern Alps. Including all measurements to date from previous studies for the western and central Alps, we observed a mountain-chain parallel anisotropy along the Alpine belt. It depicted a clear rotation that mimics the trend of the chain including two regions with nearly constant fast axes within the progressive rotation.

However at the Eastern Alps this relatively good agreement between anisotropy and mountain trend becomes less notably; here anisotropy pattern follows neither the Carpathians nor the Dinarides, both adjacent chains.

## 7.2 Slab detachment under the Eastern Alps

In order to get insight into the origin the upper mantle anisotropy under the Eastern Alps, in addition to the data from OE network, SKS splitting parameters were measured using the records of seismic stations in Slovenia (SL network) and in northern Italy (IV, NI, and SI networks). In Chapter 4 we showed the results of these data (average values) and explained them in terms of the large-scale anisotropy below the Alps. New measurements covering the Southern Alps and northwestern part of the Dinarides, are in good agreement with the progressive rotation of anisotropy along the Alps. We showed these results together with the former SKS splitting data (in the western and central Alps, and northern Italy). An abrupt change of anisotropy occurs across the Tauern Window area where the NE-SW fast orientation changes to NW-SE.

Beside the average values, we focused on the individual measurements achieved at each station. These results depicted a local lateral variation which varies clearly between the western and the eastern part of the Eastern Alps. While in the west the measures

show an anisotropy pattern that is uniformly NE-SW oriented, those in the east show two distinctive patterns, NE-SW, and NW-SE. We could draw a separation line between the western and the eastern part crossing the Tauern Window area. We also observed that the measurements can be divided into two categories; fast axis azimuth smaller than  $90^\circ\text{N}$ , and larger than  $90^\circ\text{N}$ , where the latter shows up only in those measured in the eastern part. Backazimuthal variation of the splitting parameters was observed significantly for the stations located in the eastern part. We recognized  $\pi/2$  periodicity of the fast azimuth with respect to the events backazimuth, which can be an indicator of vertical change in anisotropy. Therefore, we performed modeling to assess the presence of two layers of anisotropy, individually for each station. We derived a two-layer anisotropy model under the Eastern Alps. Almost all of the stations included in the modeling process showed NW-SE fast orientation for their upper layer and NE-SW as the lower layer. Comparison with the tomographic velocity models, we found very similar geometry between the upper layer of anisotropy and a low-velocity zone under the Eastern Alps. The low-velocity zone has already been observed in depth range of 100 to 400 km, above a steep high velocity body (e.g. *Koulakov et al.*, 2009; *Mitterbauer et al.*, 2011). According to the LAB depth beneath the Eastern Alps ( $< 100$  km), the amount of splitting delay time and its corresponding anisotropic path (layer thickness), and the similarity of the low-velocity zone and our upper anisotropic layer, we could rule out a lithospheric source of anisotropy for the upper layer, and concluded that this layer has an asthenospheric origin, as NW-SE oriented flow.

The lower anisotropic layer depicts a NE-SW anisotropy pattern; a similar anisotropy has been detected for the central and western Alps, where subduction of the European slab under Adria is generally agreed. We interpreted this layer as a detached part of the downgoing European slab, which might be still connected to the subducting slab under the central Alps, and reaches the depth of mantle transition zone (MTZ) under the Carpathian-Pannonian region. This detached slab may have created a slap gap (wedge shape) above, which the asthenospheric material flows through. Velocity tomographic models (e.g. *Dando et al.*, 2011) also evidence the presence of a steeply eastward dipping high velocity body from the Eastern Alps down to the Pannonian basin at MTZ depth.

The measurements obtained from the stations in the western part of the Eastern Alps mostly showed NE-SW pattern of anisotropy. They might be due to the fossil deformation within the lithosphere, or trench-parallel asthenospheric flow that turns around the slab keel. The latter has been suggested for the origin of anisotropy observed in the Western Alps (*Barruol et al.*, 2011). Here, we suggested that under the central Alps,

the deformation pattern in the lower lithosphere is aligned in the same orientation with the alignments within the asthenosphere. However we could not distinguish between lithospheric and asthenospheric origin of anisotropy for this area.

The new two-layer anisotropy model, proposed for the lithospheric-asthenospheric structures under the Eastern Alps, provides important clues and may help addressing the open questions related to the geodynamics and the subduction systems under the Eastern Alps.

### 7.3 Tauern Window, indentation depth, crustal-mantle coupling

In Chapter 5 we described coupling between crustal and mantle deformation. We implemented an analogy between the anisotropic measurements and lower crustal deformation (kinematic) indicators in the Tauern Window (TW) of the Alps. Individual measures of fast axis orientations, which are signatures of upper mantle deformation, depicted a change of orientation in the middle of the Tauern Window. D2, 3-related crustal kinematic data showing deformation pattern at the lower crustal depth, also exposed similar change in the Tauern Window. Comparison of these two independent indicators of deformation revealed that deformation in crust and mantle in the Tauern Window is coherent. Our finding confirmed the earlier suggestion of Selverstone (1988) and Royden (1996) that mantle and crust in the Eastern Alps are mechanically coupled.

In particular, correlation between NE-SW anisotropic orientation with the kinematic data in the "western part" of TW suggested crust-upper mantle coupling in this area. We also applied a comparison between the rheological layering model proposed for the Tauern Window (*Rosenberg et al.*, 2007) and our data. This indicated that a ductile lower crust and a ductile lithosphere over a viscous asthenosphere could be suggested for the western part of the Tauern Window. In the eastern part, this suggestion is valid particularly for the lower crust and asthenosphere.

We also demonstrated that the effect of indentation (of Adria) is not restricted in the crust, but it extends down to the lithospheric depth and also to the sub-lithospheric material. Mechanical coupling of crust and upper mantle in the Tauern Window most probably has happened more-or-less at the same time as the indentation started and it depends on the lifetime of the indenter.



## 7.4 Adria-East European compressional (AEC) deformation model

Finally, in Chapter 6 we investigated the upper mantle structures and deep deformation pattern under the Carpathian-Pannonian region (CPR). This region which is located to the (north) east of the Alps, provides a great opportunity to get insight into the geometry and origin of deformation pattern at depth as it has undergone a variety of tectonic episodes. To achieve this goal we analyzed the upper mantle anisotropy using the data from the Carpathian Basin Project. We considered the measurements of anisotropy (SKS splitting) together with petrofabric data from basalt-hosted upper mantle xenoliths samples taken in the Pannonian basin.

SKS splitting results showed a large-scale NW-SE uniform anisotropy pattern under the whole Carpathian-Pannonian region. Remarkably this pattern is not correlated with surface deformation and geology, topography, and mountain belts. Results of the naturally deformed upper mantle xenolith rock samples (from the Pannonian basin) mostly inferred A-type fabrics. In this type, the fast axis is parallel to the shear orientation.

A-type olivine fabric, anisotropy magnitude (e.g. 3.74%, NGVF), and thickness of anisotropic path (194 km) deduced from xenolith samples in one hand, crustal (25-30 km) and lithospheric (60-70 km) depth, and NW-SE large-scale anisotropy derived from seismic observations on the other hand, suggested that the observed anisotropy can not be created by crust/lithosphere and they can be considered as the signatures of deep deformations in the upper mantle. We therefore attributed this anisotropy to flow/alignments within the asthenospheric mantle.

In addition, according to several pieces of evidence proposing that the extrusion of the Alcoba unit occurred at the scale of the entire lithosphere, we demonstrated that NW-SE fast orientation under the whole CPR is inconsistent with the lateral (eastward) extrusion of the Alcoba. Hence, lithospheric-asthenospheric decoupling was suggested under this unit.

We also discussed the models that have been proposed to date to explain the evolution and current stage tectonics of the Carpathian-Pannonian region: mantle upwelling, subduction rollback, gravitational instability, asthenospheric flow, and tectonic inversion phase. By implementing a comparison to our results, the (in)consistencies of these models with respect to the anisotropy and deformation pattern interfered from seismic and petrofabric data were explained. We benefited the current tectonic inversion phase of the Pannonian basin (*Horváth et al.*, 2015) and applied it to introduce a (oblique)

compressional regime acting in the CPR. The compression is exerted by the Adriatic plate (Adria-push). As the Adriatic plate pushes NE-ward, the asthenospheric material between Adria and East European platform (EEP) are squeezed and aligned perpendicular to the compression direction. EEP has an important role in this regime. It plays as a backstop of the convergence. Therefore, we presented Adria-East European compressional (AEC) model as the most plausible model to explain the deep deformation pattern under the Carpathian-Pannonian region.

The subduction system beneath the Dinarides and Hellenides may also have a significant effect on the NW-SE deformation pattern. NE-ward subducted Adriatic plate (as Dinaric slab) can induced trench-parallel (NW-SE) anisotropy, especially for the region in the vicinity and under the subduction trench and forearc.

# Appendix A

## Null measurements

In the process of attempting to optimize the splitting parameters by minimizing the amplitudes on the transverse component, we sometimes observe no significant energy on it. In this case, a “null” orientation is defined, and shear-wave does not split to quasi phases as fast and slow polarizations (*Savage, 1999*). We can extract useful information by the employment of null measures, in order to determine which fast orientations cause the absence of energy in the transverse component. Null orientations can be retrieved in two cases: first, the SKS ray sampled an isotropic structure while traveling through upper mantle; second, the backazimuth of the SKS ray is nearly coincident with the fast or with the slow anisotropy orientation, meaning that the initial polarization of the ray is parallel (or almost parallel) to one of the anisotropy axes.

### A.1 Eastern Alps

In the Eastern Alps recorded 642 null measurements of which 372 showed a total polarization on their radial plan (no energy on transverse components). In order to explore the null orientation variations (green lines in Figure A.1) in more detail, we use group-averages of individual measures, which are calculated over a group of measurements showing resembling fast azimuth for each station (as in the two categories mentioned in Chapter 4).

Figure A.1 shows the group-averages together with the null orientations. In a similar fashion as in Figure 4.3 (Chapter 4), the null azimuth displaying (clockwise) an angle smaller and greater than  $90^\circ$  with respect to the North, are plotted in blue and red respectively. Indeed for the western stations one average is displayed, while for the eastern

stations two average orientations are shown. As for the fast azimuths we highlighted duplex orientations in most stations placed in the east of longitude  $12^\circ\text{E}$ , null measurements in this area show four small ranges of backazimuths for some stations (e.g. MOA in Figure A.1) where they are represented by filled and non-filled arrows respectively). This can be related to two fast and two slow anisotropy orientations at these stations. Some stations (i.e. KBA, ARSA, OBKA) give nulls in two groups of backazimuthal ranges, which can be related to either two fast orientations or single fast and single slow orientations. On the other hand, the stations positioned to the west of  $12^\circ\text{E}$ , mainly give one single fast orientation pattern. This group of stations displays null measurements mostly in agreement with the derived fast azimuths (e.g. DAVA, Figure A.1). For some stations (e.g. DOBS, ROSI) we could measure only few good nulls.

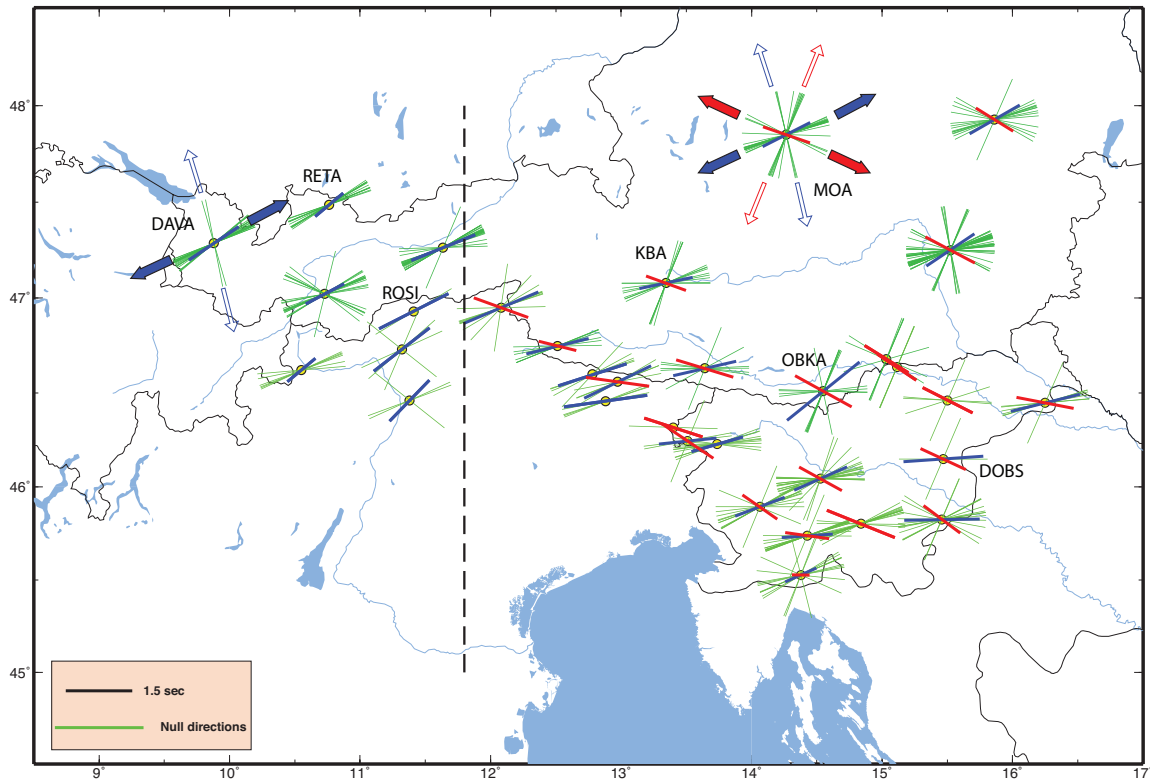


**Figure A.1:** Red and blue lines at each station represent the group-averages of individual measures. Green lines show null orientations. At each station, null orientations can be separated into few groups of backazimuth, which refer to either fast or slow orientations. For station MOA, the two groups of nulls have been outlined by filled and empty arrows; null measures are displayed parallel to fast axes and support their definition. Dashed line as in Figure 4.3.

## A.2 Carpathian-Pannonian region

Most of the null orientations measured in the Carpathian-Pannonian region are nearly perpendicular to the fast axis azimuth which can be considered as anisotropic "slow" orientations. Figure A.2 represents the nulls together with the average fast azimuth. Note that nulls depict (sub)parallelism to the faults trend in the middle Hungarian shear zone.

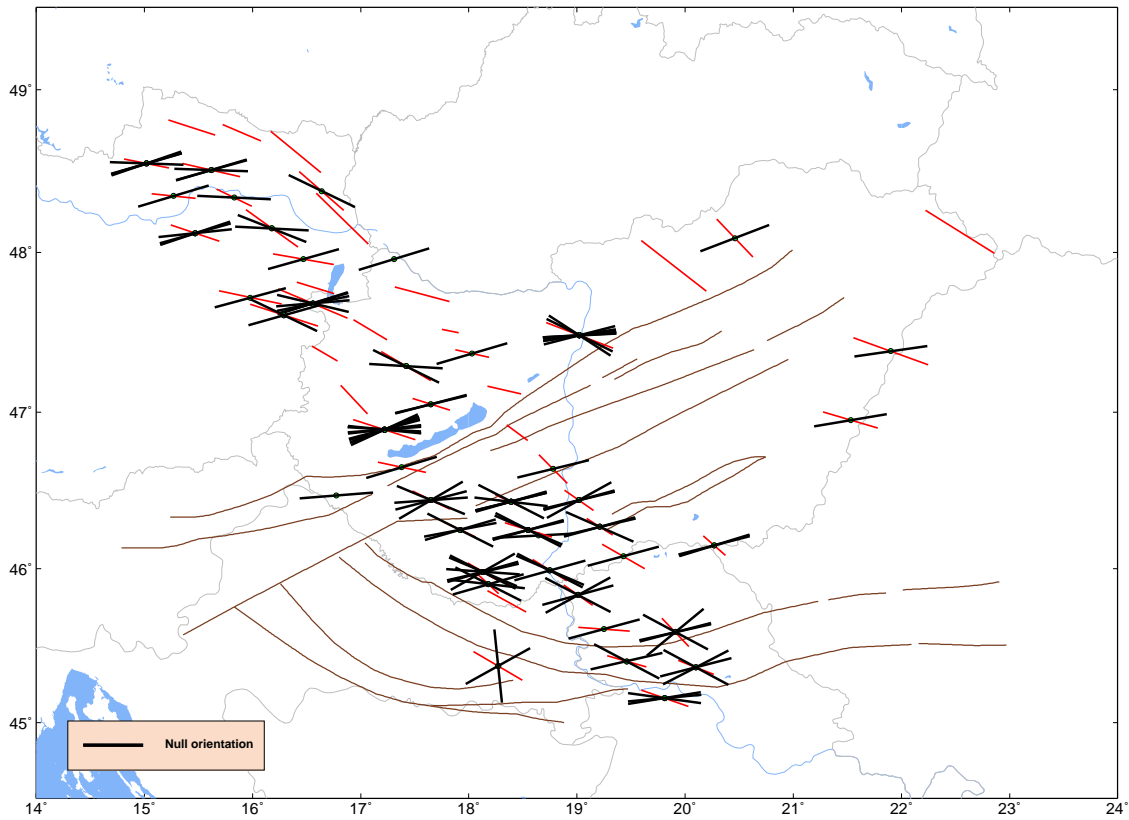


**Figure A.2:** Map of null orientation measured in the Carpathian-Pannonian region. Black bars represent azimuth of the nulls. They are shown together with the fast axis azimuth (red bars).





# Appendix B

## Chi-square and R-square

Chi-square calculation is utilized to evaluate the goodness of fit between observational and theoretical measurements. It is the sum of the squares of residuals (vertical distance between the observations and calculations) for each parameter. Modeling the presence of two anisotropic layers is a non-linear regression to find the best-fit model that explains the observational measurements. All possible values for two splitting parameters of each layer (4 in total) are tested. The most likely best-fit values are found by minimizing the Chi-square, which is the summation of the Chi-squares of  $\phi, \delta t$ , each weighted by the error of the observations (*Margheriti et al.*, 2003; *Walker et al.*, 2005a; *Fontaine et al.*, 2007; *Salimbeni et al.*, 2013).

$$X^2 = X_{\phi}^2 + X_{\delta t}^2$$

where,  $X_{\phi}^2 = \sum \frac{(\phi_o - \phi_p)^2}{\sigma_{\phi}^2}$ , and  $X_{\delta t}^2 = \sum \frac{(\delta t_o - \delta t_p)^2}{\sigma_{\delta t}^2}$

To address the question "How do we know the best-fit two layers model explain better the observations than one layer model?", the coefficient of determination (R-square) is a convenient measure that quantifies the quality of the results (*Walker et al.*, 2004).

$$R^2 = 1 - \frac{SSd}{SSo}$$
$$SSd = X^2 = \sum \left[ \frac{(\phi_o - \phi_{2layer})^2}{\sigma_{\phi}^2} + \frac{(\delta t_o - \delta t_{2layer})^2}{\sigma_{\delta t}^2} \right],$$
$$SSo = \sum \left[ \frac{(\phi_o - \phi_{1layer})^2}{\sigma_{\phi}^2} + \frac{(\delta t_o - \delta t_{1layer})^2}{\sigma_{\delta t}^2} \right]$$

SSd and SSo are the sum of the squares of residuals for two-layer and one-layer model respectively. We measured the "adjusted R-square" values (*Walker et al.*, 2005a; *Fontaine et al.*, 2007) for the best-fit model of each station, which are also listed in Table 2.

$$R_{adjusted}^2 = 1 - \frac{(N-1)(1-R^2)}{(N-k-1)}$$

Where  $N$  is the number of data (i.e. two times of number of good measurements at each station), and  $K$  is the number of parameters (i.e. 4 parameters). The adjusted R-square value is in a range of  $-\infty$  to 1. The value closer to 1 indicates that the observational measurements at a given station are a better representative of two-layer model beneath this station than a single layer model.

# Appendix C

## Table of individual splitting measurements

### C.1 Eastern Alps

List of individual SKS splitting parameters measured from the teleseismic events recorded at the permanent broadband seismic stations (OE, SL, IV, NI, and SI network) located in Austria, Slovenia, and northern Italy. Table consists the station name, events date, backazimuth of the events, incidence angles. This list also includes the fast axis azimuths (with respect to the north) and its error, splitting delay time and the corresponding error, and the relevant core shear-wave which was used to measure the splitting parameters.

Station	Event	BackAz	Incidence(°)	$\phi(^{\circ}\text{N})$	$\phi\text{-err}$	$\delta t(\text{s})$	$\delta t\text{-err}$	Phase
ABTA	2010.139	266.57	9.54	61	12	1.9	0.35	SKS
ABTA	2010.202	68.65	7.82	-85	5	1.3	0.35	SKS
ABTA	2010.210	70.15	8.50	88	1	1.3	0.15	SKS
ABTA	2011.065	201.78	7.38	80	14	1.5	0.5	SKS
ABTA	2011.152	240.03	6.68	84	5	1.7	0.35	SKS
ABTA	2011.164	70.40	7.94	86	1	1.2	0.15	SKS
ABTA	2011.192	69.07	9.16	-61	19	1.0	0.4	SKS
ABTA	2011.196	198.07	11.99	58	6	1.1	0.2	SKKS
ABTA	2011.326	250.59	9.51	-83	17	0.3	0.15	SKS
ARSA	2003.206	55.47	6.06	-61	7	1.3	0.25	SKS
ARSA	2003.322	67.24	9.50	-65	9.5	0.9	0.35	SKS
ARSA	2006.260	242.58	7.40	-57	9	1.5	0.35	SKS

ARSA	2010.079	54.21	11.29	-62	6	1.5	0.35	SKKS
ARSA	2003.073	69.41	7.36	-61	7	1.9	0.3	SKS
ARSA	2003.291	74.29	8.04	-64	18	1.0	0.35	SKS
ARSA	2004.077	249.18	8.55	-43	15.5	1.0	0.55	SKS
ARSA	2005.166	54.05	5.57	-84	17	0.7	0.25	SKS
ARSA	2006.237	247.84	8.14	-36	18.5	1.2	0.3	SKS
ARSA	2007.030	46.78	8.87	-67	8	1.8	0.45	SKS
ARSA	2011.345	300.63	9.72	69	11	1.5	0.3	SKS
ARSA	2013.237	146.43	10.42	-82	12	1.1	0.4	SKS
ARSA	2013.254	290.10	6.76	42	7.5	1.1	0.2	SKS
CONA	2010.003	52.70	5.05	-83	10	1.6	0.35	SKS
CONA	2010.079	54.20	11.35	-62	4	1.3	0.2	SKKS
CONA	2010.095	75.66	8.17	-38	13.5	1.2	0.45	SKS
CONA	2010.123	241.99	6.36	-68	12	1.1	0.3	SKS
CONA	2010.126	255.15	8.41	-47	10.5	1.0	0.25	SKS
CONA	2010.144	262.66	9.27	-43	19.5	0.5	0.15	SKS
CONA	2010.193	250.56	8.18	-55	7	0.8	0.1	SKS
CONA	2010.195	241.87	6.40	-54	14	1.2	0.55	SKS
CONA	2011.065	254.28	8.50	-44	18	1.0	0.35	SKS
CONA	2011.245	242.82	7.82	-59	12	0.7	0.2	SKS
CONA	2011.326	253.08	9.07	-61	8	0.6	0.1	SKS
CONA	2012.065	243.01	7.85	-63	11	0.8	0.2	SKS
CONA	2012.320	301.57	12.79	60	10	1.3	0.4	SKKS
CONA	2013.111	46.67	10.61	-67	3	1.0	0.1	SKS
CONA	2013.134	47.86	8.45	-72	5	1.1	0.1	SKS
DAVA	2002.285	258.24	9.90	58	9	1.3	0.45	SKS
DAVA	2002.346	48.21	11.11	88	8	1.4	0.3	SKKS
DAVA	2004.207	88.64	9.22	47	5.5	1.6	0.25	SKS
DAVA	2004.250	201.98	7.47	60	17.5	1.0	0.4	SKS
DAVA	2004.300	198.95	7.40	53	15	0.7	0.55	SKS
DAVA	2005.036	68.83	8.18	51	5	1.6	0.3	SKS
DAVA	2005.100	91.31	10.03	51	8.5	1.3	0.2	SKS
DAVA	2005.141	268.41	9.70	60	14.5	1.3	0.4	SKS
DAVA	2005.178	302.48	9.65	76	6	1.1	0.15	SKS
DAVA	2006.146	87.83	8.15	52	5	1.3	0.15	SKS
DAVA	2006.200	90.36	8.79	40	10.5	1.1	0.2	SKS

DAVA	2007.193	260.40	9.81	54	10	1.3	0.4	SKS
DAVA	2007.220	88.35	8.53	38	13.5	1.4	0.4	SKS
DAVA	2010.139	264.68	9.82	67	7	1.8	0.5	SKS
DAVA	2010.144	258.24	9.95	60	4	1.6	0.3	SKS
DAVA	2010.202	66.39	7.62	44	6.5	1.1	0.25	SKS
DAVA	2010.210	68.02	8.29	48	4	1.6	0.3	SKS
DAVA	2011.236	260.71	9.84	65	3	1.6	0.25	SKS
DAVA	2011.242	73.97	6.78	48	6.5	1.5	0.3	SKS
DAVA	2011.246	200.41	7.38	54	8	1.3	0.3	SKS
FETA	2010.125	92.51	9.66	59	17.5	0.9	0.3	SKS
FETA	2011.242	74.76	6.81	43	12.5	0.6	0.1	SKS
FETA	2010.356	41.02	9.37	85	16	0.9	0.3	SKS
FETA	2011.164	68.91	7.80	13	15	0.6	0.25	SKS
FETA	2012.001	42.69	10.37	73	10	1.0	0.3	SKS
FETA	2012.147	43.59	9.49	76	13	0.9	0.3	SKS
FETA	2012.157	38.66	10.83	71	16	1.2	0.55	SKS
FETA	2012.320	297.72	12.95	66	9	1.4	0.3	SKKS
FETA	2013.134	43.73	8.00	66	5	1.1	0.25	SKS
FETA	2013.167	296.71	10.32	71	15	1.1	0.3	SKS
KBA	2010.202	69.23	7.91	-77	10.5	0.4	0.4	SKS
KBA	2010.294	310.05	9.99	88	14	1.1	0.35	SKS
KBA	2011.245	240.98	8.09	87	9	0.8	0.3	SKS
KBA	2011.326	251.20	9.39	-35	8.5	0.8	0.3	SKS
KBA	2010.064	241.18	6.75	-67	11	1.5	0.3	SKS
KBA	2010.073	72.54	7.45	-73	19	1.3	0.5	SKS
KBA	2012.021	292.08	12.96	62	13	1.3	0.3	SKS
KBA	2012.086	297.35	8.51	63	9	1.5	0.35	SKS
KBA	2012.093	296.89	9.89	87	9	1.2	0.3	SKS
KBA	2012.149	241.18	8.15	-85	10	0.8	0.2	SKS
KBA	2012.159	240.20	6.96	-62	16	0.8	0.3	SKS
KBA	2012.269	310.78	9.88	-87	10	1.1	0.2	SKS
KBA	2013.111	44.83	10.28	83	4	1.5	0.15	SKS
KBA	2013.132	289.87	10.25	84	7	1.1	0.3	SKS
KBA	2013.134	45.91	8.18	80	4	1.4	0.15	SKS
KBA	2013.167	298.62	10.03	71	11	1.2	0.3	SKS
MOA	2002.285	261.47	9.40	-69	3	0.8	0.05	SKS

MOA	2002.304	56.22	11.42	-60	10	1.9	0.5	SKKS
MOA	2002.346	52.50	11.21	-87	8	1.1	0.25	SKKS
MOA	2003.131	73.45	7.74	-73	19	0.8	0.35	SKS
MOA	2003.146	70.91	8.73	-57	11	0.5	0.2	SKS
MOA	2003.171	261.92	9.49	-70	3	0.8	0.1	SKS
MOA	2003.206	53.99	11.48	-84	9	1.3	0.3	SKKS
MOA	2004.124	241.23	11.73	-61	11	1.6	0.45	SKKS
MOA	2004.124	241.23	6.51	-55	11	1.5	0.45	SKS
MOA	2004.251	243.42	7.88	-77	8	0.8	0.15	SKS
MOA	2005.038	52.42	11.22	-70	12	1.2	0.35	SKKS
MOA	2005.164	251.70	8.47	-54	17	1.0	0.2	SKS
MOA	2005.321	249.18	8.34	-69	14	0.9	0.15	SKS
MOA	2006.120	247.84	7.62	-68	12	1.0	0.2	SKS
MOA	2006.197	247.67	7.35	-50	11.5	1.3	0.4	SKS
MOA	2006.237	247.11	8.19	-59	12	1.0	0.25	SKS
MOA	2006.317	243.44	8.20	-85	6	1.1	0.2	SKS
MOA	2006.323	289.34	11.90	63	10	1.2	0.25	SKKS
MOA	2007.030	45.71	8.83	-80	6	1.4	0.2	SKS
MOA	2007.193	263.65	9.30	-68	5	0.7	0.1	SKS
MOA	2007.202	261.24	9.46	-71	4	0.8	0.1	SKS
MOA	2007.202	247.73	8.49	-68	9	1.0	0.15	SKS
MOA	2007.271	46.97	9.07	-79	8	1.5	0.25	SKS
MOA	2007.273	50.70	7.50	-79	16	0.9	0.3	SKS
MOA	2010.063	249.49	8.31	-69	8	1.0	0.15	SKS
MOA	2010.079	52.65	11.25	-81	6	1.0	0.1	SKKS
MOA	2011.065	253.13	8.65	-77	15	0.9	0.4	SKS
MOA	2011.171	249.76	8.35	-50	10.5	1.0	0.25	SKS
MOA	2011.206	53.63	11.42	-76	8	2.2	0.35	SKKS
MOA	2011.236	263.96	9.32	-58	17.5	0.5	0.15	SKS
MOA	2011.245	241.74	7.96	-80	7	1.3	0.2	SKS
MOA	2011.326	251.92	9.26	-68	5	0.7	0.05	SKS
MOA	2012.269	311.49	9.89	-83	11	1.2	0.3	SKS
MOA	2013.106	61.77	6.33	-76	10	1.9	0.4	SKS
MOA	2013.134	46.56	8.35	-89	3.5	1.5	0.15	SKS
MYKA	2010.032	52.24	5.23	-64	9	2.6	0.35	SKS
MYKA	2010.063	243.23	7.08	-79	5	2.4	0.35	SKS

MYKA	2010.063	248.83	8.41	-67	11	1.0	0.2	SKS
MYKA	2010.079	52.66	11.18	-75	7	2.1	0.3	SKKS
MYKA	2010.113	240.31	6.68	-84	7	1.4	0.3	SKS
MYKA	2010.123	240.16	6.57	-80	12	1.2	0.3	SKS
MYKA	2010.126	253.37	12.59	-63	12	1.2	0.3	SKKS
MYKA	2010.144	260.97	9.54	-53	14	0.5	0.15	SKS
MYKA	2010.193	248.79	8.44	-73	7	1.0	0.15	SKS
MYKA	2010.195	240.04	6.60	-88	9	1.2	0.35	SKS
MYKA	2010.202	69.57	7.92	-78	7	1.6	0.3	SKS
MYKA	2010.210	71.02	8.61	-81	7	1.3	0.3	SKS
MYKA	2010.252	240.91	6.68	-71	14	1.3	0.5	SKS
MYKA	2010.355	43.14	9.54	-87	5	2.1	0.35	SKS
MYKA	2011.065	252.51	8.79	-79	10	1.0	0.25	SKS
MYKA	2011.065	202.35	7.35	88	4	1.8	0.3	SKS
MYKA	2011.164	71.31	8.04	-65	11	0.6	0.15	SKS
MYKA	2011.171	249.11	8.47	-75	12	1.1	0.2	SKS
MYKA	2011.192	69.93	9.27	-72	15	1.4	0.5	SKS
MYKA	2011.242	77.23	7.03	-55	8	0.8	0.2	SKS
MYKA	2011.245	241.09	8.10	-87	3	1.4	0.15	SKS
MYKA	2011.246	202.28	7.35	84	9	1.5	0.45	SKS
MYKA	2011.326	251.39	9.38	-75	9	0.9	0.2	SKS
MYKA	2012.015	212.31	11.41	66	8	2.1	0.4	SKKS
MYKA	2012.093	297.10	9.80	85	9	1.1	0.35	SKS
MYKA	2012.269	310.98	9.79	89	7	0.9	0.3	SKS
MYKA	2013.112	300.97	9.65	81	5	1.5	0.15	SKS
MYKA	2013.167	298.84	3.11	71	10	1.6	0.4	SKiKS
MYKA	2013.207	200.12	7.32	72	17	1.2	0.55	SKS
MYKA	2013.229	147.86	10.36	-60	5	1.5	0.2	SKS
MYKA	2013.250	291.37	12.96	61	10	1.4	0.35	SKKS
OBKA	2002.259	62.58	6.25	-65	18	1.3	0.5	SKS
OBKA	2002.260	62.47	6.25	-52	15.5	1.4	0.35	SKS
OBKA	2002.283	68.68	7.01	-61	19	1.1	0.45	SKS
OBKA	2002.285	261.60	9.40	-40	9.5	1.2	0.25	SKS
OBKA	2003.125	72.89	7.77	-51	16.5	1.1	0.4	SKS
OBKA	2003.146	70.27	7.88	-66	15	0.8	0.2	SKS
OBKA	2003.146	71.30	8.68	-57	15	0.8	0.25	SKS



OBKA	2003.322	66.57	9.32	-57	5	1.7	0.2	SKS
OBKA	2004.124	240.84	6.56	-63	7	2.0	0.35	SKS
OBKA	2004.282	68.93	10.09	-75	15	1.3	0.5	SKS
OBKA	2005.038	53.44	5.50	-75	5	1.8	0.2	SKS
OBKA	2005.080	244.28	8.36	-66	8	1.5	0.25	SKS
OBKA	2005.164	251.67	8.50	-42	16.5	1.2	0.55	SKS
OBKA	2005.321	249.13	8.36	-63	10	1.6	0.3	SKS
OBKA	2006.120	247.67	7.67	-64	5	1.5	0.2	SKS
OBKA	2006.120	247.67	7.63	-64	7	1.6	0.25	SKS
OBKA	2006.197	247.44	7.38	-67	12	1.5	0.35	SKS
OBKA	2006.237	247.03	8.25	-67	6	1.6	0.25	SKS
OBKA	2006.260	241.76	7.54	-76	10	2.3	0.4	SKS
OBKA	2006.317	243.39	8.27	-75	5	1.6	0.2	SKS
OBKA	2007.030	46.08	8.73	-76	6	2.3	0.35	SKS
OBKA	2007.149	73.77	7.65	-54	15.5	0.9	0.3	SKS
OBKA	2007.202	247.71	8.54	-70	7	1.6	0.3	SKS
OBKA	2007.232	68.86	8.43	-53	5	1.7	0.2	SKS
OBKA	2007.271	47.30	8.94	-67	5	2.5	0.4	SKS
OBKA	2010.063	249.42	8.35	-73	16	1.5	0.55	SKS
OBKA	2010.075	242.00	6.71	-66	17	1.6	0.45	SKS
OBKA	2010.139	268.03	9.29	-28	10	1.3	0.4	SKS
OBKA	2010.193	249.38	8.36	-67	9	1.5	0.25	SKS
OBKA	2010.202	70.31	7.99	-52	11.5	1.1	0.3	SKS
OBKA	2010.204	71.51	8.68	-52	7	1.2	0.1	SKS
OBKA	2010.210	71.73	8.67	-58	9	0.9	0.15	SKS
OBKA	2010.294	310.93	9.78	-85	5	2.6	0.3	SKS
OBKA	2011.065	253.12	8.68	-61	15.5	1.1	0.4	SKS
OBKA	2011.164	72.04	8.14	-52	6	1.1	0.2	SKS
OBKA	2011.171	249.70	8.38	-62	9	1.4	0.25	SKS
OBKA	2011.192	70.62	9.35	-55	12	1.1	0.3	SKS
OBKA	2011.236	264.05	9.32	-28	8	1.2	0.35	SKS
OBKA	2011.245	241.66	8.02	-72	6	1.8	0.25	SKS
OBKA	2011.326	252.03	9.28	-58	5	1.5	0.15	SKS
OBKA	2012.112	68.59	7.03	-67	11	1.3	0.3	SKS
OBKA	2012.135	253.58	8.68	-50	6	1.6	0.2	SKS
OBKA	2012.149	241.87	8.06	-66	5	1.7	0.2	SKS

OBKA	2012.239	71.95	8.03	-46	9.5	1.1	0.3	SKS
OBKA	2012.252	68.99	6.82	-69	12	1.0	0.2	SKS
OBKA	2013.096	66.41	6.53	-60	12	1.5	0.45	SKS
OBKA	2013.164	94.99	8.71	51	10.5	2.1	0.45	SKS
RETA	2010.202	67.06	7.71	41	11.5	0.7	0.25	SKS
RETA	2010.205	68.73	8.35	41	12.5	0.7	0.2	SKS
RETA	2010.210	68.68	8.37	39	9.5	0.6	0.1	SKS
RETA	2011.065	200.96	7.36	51	26	0.9	0.2	SKS
RETA	2011.093	91.55	8.29	56	21	0.7	0.35	SKS
RETA	2011.164	68.82	7.83	45	7.5	0.7	0.15	SKS
RETA	2011.234	91.97	9.05	42	6.5	1.0	0.1	SKS
RETA	2011.236	261.36	9.74	57	10	0.8	0.25	SKS
RETA	2011.242	74.61	6.83	49	4	0.9	0.1	SKS
RETA	2011.246	200.90	12.10	79	7	1.3	0.25	SKKS
RETA	2011.318	70.78	7.43	51	9.5	0.9	0.3	SKS
RETA	2010.144	258.89	9.83	59	11	0.9	0.4	SKS
RETA	2010.204	68.46	8.37	38	11.5	0.6	0.15	SKS
SOKA	2010.063	249.78	8.29	-56	8	1.2	0.25	SKS
SOKA	2010.075	242.34	6.66	-58	20.5	1.9	0.4	SKS
SOKA	2010.113	241.12	6.58	-63	10	1.5	0.45	SKS
SOKA	2010.191	50.93	7.50	-75	6	1.4	0.2	SKS
SOKA	2010.193	249.74	8.32	-50	4	1.3	0.1	SKS
SOKA	2010.195	240.85	6.50	-57	10	0.9	0.25	SKS
SOKA	2010.202	70.65	8.04	-49	6	0.9	0.15	SKS
SOKA	2010.205	72.14	8.70	-72	19	0.8	0.35	SKS
SOKA	2010.210	72.07	8.75	-56	9	0.8	0.15	SKS
SOKA	2011.065	253.49	8.62	-39	9.5	1.3	0.45	SKS
SOKA	2011.152	241.45	6.52	-81	14	1.6	0.55	SKS
SOKA	2011.164	72.38	8.18	-54	5	0.8	0.1	SKS
SOKA	2011.171	250.06	8.34	-52	6	1.1	0.15	SKS
SOKA	2011.242	78.29	7.17	-40	26.5	0.7	0.55	SKS
SOKA	2011.245	242.01	7.96	-54	5	1.5	0.25	SKS
SOKA	2011.326	252.38	9.24	-40	3.5	1.4	0.2	SKS
SOKA	2012.135	253.94	8.62	-48	8.5	1.3	0.2	SKS
SOKA	2012.149	242.22	8.01	-56	5	1.3	0.25	SKS
SOKA	2012.108	244.10	7.06	-66	12	1.2	0.3	SKS

SOKA	2012.252	69.32	6.86	-63	8	0.8	0.1	SKS
SOKA	2013.030	247.14	12.17	-71	10	1.2	0.2	SKKS
SOKA	2013.134	47.35	8.28	-77	5	1.7	0.15	SKS
SOKA	2013.224	76.43	6.93	-52	5	0.8	0.1	SKS
WTTA	2004.207	89.93	9.40	52	5	1.1	0.1	SKS
WTTA	2005.016	52.47	7.65	66	3	2.2	0.3	SKS
WTTA	2005.163	201.47	7.35	79	5	1.2	0.15	SKS
WTTA	2006.146	89.13	8.32	47	3	1.3	0.1	SKS
WTTA	2007.020	203.24	7.43	73	6	1.8	0.25	SKS
WTTA	2007.067	42.61	10.18	67	6	2.5	0.45	SKS
WTTA	2007.220	89.65	8.72	54	7	1.1	0.15	SKS
WTTA	2010.139	265.97	9.62	68	8	1.0	0.35	SKS
WTTA	2011.246	201.33	12.10	79	5	1.7	0.25	SKKS
WTTA	2011.305	305.94	12.76	76	11	1.6	0.35	SKKS
WTTA	2005.038	50.01	11.11	88	7	1.6	0.25	SKKS
CADS	2011.012	45.99	9.63	74	6	1.2	0.15	SKS
CEY	2010.079	53.93	11.17	90	10	1.3	0.4	SKKS
CEY	2010.225	53.74	7.85	86	16	1.3	0.55	SKS
CEY	2010.226	53.81	12.29	86	9	0.9	0.25	SKKS
CEY	2010.230	53.84	7.83	-86	14	1.1	0.35	SKS
CEY	2010.294	310.81	9.73	-77	10	0.9	0.3	SKS
CEY	2011.167	56.87	11.15	83	8	1.1	0.35	SKKS
CRES	2010.062	241.93	11.80	-72	12	1.7	0.3	SKKS
CRES	2010.079	54.90	11.22	-71	11	1.7	0.5	SKKS
CRES	2010.107	62.04	11.33	-62	8	1.7	0.3	SKKS
CRES	2010.126	254.49	12.51	-44	7.5	1.2	0.2	SKKS
CRES	2010.139	268.62	12.67	-33	25.5	0.5	0.35	SKKS
CRES	2010.143	260.07	3.26	-38	18.5	0.5	0.35	SKiKS
CRES	2010.144	262.22	9.34	-28	6	0.7	0.2	SKS
CRES	2010.191	51.51	7.46	-72	9	1.3	0.35	SKS
CRES	2010.193	249.86	8.32	-44	6.5	1.0	0.2	SKS
CRES	2010.195	240.74	6.53	-57	15	1.4	0.55	SKS
CRES	2010.201	58.19	3.52	-66	26	0.7	0.45	SKiKS
CRES	2010.202	71.17	8.04	-45	6.5	0.8	0.15	SKS
CRES	2010.204	72.28	8.76	-42	13.5	0.7	0.3	SKS
CRES	2010.210	72.50	8.75	-44	7.5	0.7	0.15	SKS

CRES	2010.230	54.67	7.92	-88	3	1.7	0.35	SKS
CRES	2010.294	311.58	9.64	-82	8	1.4	0.4	SKS
CRES	2010.356	44.68	9.59	-77	8	2.4	0.4	SKS
CRES	2011.002	240.43	6.50	-78	19	0.8	0.25	SKS
CRES	2011.065	253.64	8.61	-36	14.5	0.7	0.35	SKS
CRES	2011.164	72.89	8.17	-45	7.5	0.6	0.1	SKS
CRES	2011.171	250.19	8.34	-38	5.5	1.0	0.25	SKS
CRES	2011.192	71.34	9.42	-55	17	0.8	0.35	SKS
CRES	2011.245	242.11	7.99	-50	7	1.0	0.25	SKS
CRES	2011.326	252.62	9.24	-45	8.5	0.7	0.2	SKS
CRES	2012.037	70.27	9.36	-52	16.5	0.9	0.35	SKS
CRES	2012.135	254.10	8.61	-54	10	0.8	0.15	SKS
DOBS	2010.143	260.13	3.26	-46	10.5	0.9	0.15	SKiKS
DOBS	2010.181	298.07	3.15	86	4	2.2	0.35	SKiKS
DOBS	2010.193	249.93	8.30	-70	7	1.3	0.15	SKS
DOBS	2010.199	58.31	5.53	-88	5	1.6	0.25	SKS
DOBS	2010.202	71.11	8.06	-67	17	0.8	0.25	SKS
DOBS	2010.210	72.47	8.77	-80	8	1.1	0.25	SKS
DOBS	2010.272	72.22	11.88	-44	10.5	1.4	0.45	SKKS
DOBS	2011.041	74.36	8.52	-74	10	1.0	0.25	SKS
DOBS	2011.097	295.89	12.92	90	4	1.7	0.25	SKKS
DOBS	2011.164	72.83	8.19	-67	7	0.9	0.1	SKS
DOBS	2011.171	250.26	8.33	-66	8	1.1	0.15	SKS
DOBS	2011.192	71.33	9.43	-65	16	1.4	0.4	SKS
DOBS	2011.236	264.68	9.24	-43	18	0.5	0.25	SKS
DOBS	2011.242	78.81	7.17	-77	10	1.0	0.35	SKS
DOBS	2011.245	242.18	7.96	-64	8	1.3	0.25	SKS
DOBS	2011.301	260.87	8.36	-55	17.5	0.7	0.15	SKS
DOBS	2011.318	74.88	7.79	-71	21	0.9	0.45	SKS
DOBS	2011.326	252.65	9.22	-61	9	1.2	0.2	SKS
DOBS	2011.348	62.87	11.30	-71	14	1.7	0.5	SKKS
DOBS	2012.021	293.62	12.84	84	10	1.5	0.4	SKKS
DOBS	2012.030	260.85	8.41	-39	11.5	1.0	0.25	SKS
DOBS	2012.037	70.25	9.38	-78	11	1.1	0.35	SKS
DOBS	2012.085	242.37	3.43	-72	16	1.6	0.55	SKiKS
DOBS	2012.093	298.43	9.58	82	2	1.8	0.1	SKS

GORS	2012.037	69.14	9.25	-61	18	1.0	0.4	SKS
GORS	2012.085	241.57	6.95	-74	16.5	0.9	0.3	SKS
GORS	2012.093	297.35	9.75	-83	4	2.4	0.4	SKS
GORS	2012.149	241.47	8.15	-85	8	0.9	0.2	SKS
GORS	2013.096	66.02	6.48	-56	19.5	1.7	0.4	SKS
GROS	2006.237	247.66	8.18	-74	5	1.2	0.1	SKS
GROS	2007.207	71.79	8.16	-48	3	1.1	0.1	SKS
GROS	2007.271	48.05	9.02	-70	4	2.1	0.3	SKS
GROS	2010.070	243.32	6.87	-75	15	1.1	0.35	SKS
GROS	2010.075	242.53	6.64	-69	14	1.4	0.4	SKS
GROS	2010.210	72.45	8.79	-52	8	1.0	0.2	SKS
GROS	2011.001	243.41	8.14	-65	7	1.2	0.2	SKS
GROS	2011.242	78.73	12.01	-59	13	1.0	0.2	SKKS
GROS	2011.245	242.27	7.94	-68	6	1.3	0.2	SKS
GROS	2012.037	70.25	9.41	-54	8	1.2	0.2	SKS
JAVS	2010.191	50.29	7.36	-82	7	1.1	0.15	SKS
JAVS	2010.216	60.24	5.69	-62	11	0.8	0.25	SKS
JAVS	2010.226	53.47	7.83	85	10.5	0.6	0.35	SKS
JAVS	2010.272	71.18	11.82	-45	19.5	0.9	0.5	SKKS
JAVS	2010.294	310.55	9.77	73	12	1.0	0.3	SKS
JAVS	2011.246	202.40	7.40	68	20	1.0	0.4	SKS
JAVS	2011.345	299.49	9.74	77	15	1.0	0.25	SKS
JAVS	2011.348	61.70	5.57	-50	18.5	0.9	0.4	sSKS
JAVS	2012.037	69.23	9.23	-35	8.5	1.1	0.5	SKS
JAVS	2012.086	297.71	8.37	56	9	1.5	0.4	SKS
JAVS	2012.093	297.38	9.73	67	9	0.8	0.1	SKS
JAVS	2012.108	196.03	7.44	56	7	2.4	0.3	SKS
KNDS	2007.271	47.27	8.82	87	17	0.6	0.25	SKS
KNDS	2013.111	45.55	10.18	80	15.5	0.4	0.35	SKS
KNDS	2013.134	46.98	8.13	-89	4	0.4	0.1	SKS
KNDS	2013.250	291.90	10.08	46	6.5	1.4	0.3	SKS
KNDS	2013.264	83.93	7.55	56	7	0.7	0.1	SKS
KOGS	2010.063	244.75	3.42	-73	8	1.7	0.3	SKiKS
KOGS	2010.063	250.56	8.17	-83	4	1.5	0.2	SKS
KOGS	2010.070	243.76	6.82	-80	6	1.4	0.2	SKS
KOGS	2010.123	241.56	6.42	-68	17	1.5	0.5	SKS

KOGS	2010.126	255.14	8.43	-75	9	1.3	0.25	SKS
KOGS	2010.144	262.83	9.26	-79	8	0.8	0.25	SKS
KOGS	2010.193	250.52	8.20	-83	4	1.5	0.2	SKS
KOGS	2010.195	241.44	6.43	-73	15	1.1	0.3	SKS
KOGS	2010.199	58.90	5.59	-73	14	0.8	0.3	SKS
KOGS	2011.001	243.90	8.05	-72	7	1.3	0.15	SKS
KOGS	2011.065	254.29	8.51	-88	4	1.5	0.3	SKS
KOGS	2011.097	296.46	10.05	74	13	1.3	0.3	SKS
KOGS	2011.171	250.84	8.21	-81	4	1.4	0.15	SKS
KOGS	2011.245	242.75	7.88	-83	3	1.4	0.1	SKS
KOGS	2011.326	253.23	9.11	-83	3	1.2	0.1	SKS
KOGS	2012.021	294.20	9.86	72	8	1.8	0.3	SKS
KOGS	2012.093	299.03	9.54	81	8	1.7	0.4	SKS
KOGS	2012.135	254.75	8.51	-81	6	1.5	0.25	SKS
KOGS	2012.149	242.97	7.92	-81	3	1.3	0.1	SKS
KOGS	2012.159	258.02	8.44	-78	14	1.0	0.4	SKS
KOGS	2012.210	55.33	5.55	-85	5	1.0	0.15	SKS
KOGS	2013.030	247.86	7.41	-76	8	1.6	0.3	SKS
LJU	2006.054	187.42	8.36	-51	18.5	1.4	0.5	SKS
LJU	2006.120	247.53	7.66	-52	11	1.1	0.25	SKS
LJU	2006.200	93.88	9.29	-24	11	0.6	0.15	SKS
LJU	2006.237	246.93	8.29	-45	15.5	0.6	0.25	SKS
LJU	2006.260	241.63	7.55	-72	17	0.6	0.2	SKS
LJU	2006.290	56.82	5.47	-63	5	1.3	0.2	SKS
LJU	2006.317	243.30	8.31	-73	12	0.6	0.1	SKS
LJU	2007.179	54.67	10.96	-73	11	1.3	0.35	SKKS
LJU	2010.079	53.86	11.19	-62	13	1.2	0.5	SKKS
LJU	2010.181	297.37	9.74	-83	3	1.3	0.15	SKS
LJU	2010.191	50.66	7.40	-71	3	2.0	0.15	SKS
LJU	2010.230	53.86	7.86	-58	7	1.2	0.35	SKS
LJU	2010.294	310.90	9.74	85	3	1.5	0.15	SKS
LJU	2011.347	76.45	12.37	46	5.5	1.1	0.15	SKKS
PERS	2010.063	249.83	8.29	-52	7	1.3	0.2	SKS
PERS	2010.113	241.15	6.57	-71	17	1.0	0.35	SKS
PERS	2010.126	254.39	8.55	-38	12.5	1.1	0.45	SKS
PERS	2010.193	249.79	8.32	-56	6	1.2	0.15	SKS

PERS	2010.195	240.88	6.50	-75	17	1.1	0.35	SKS
PERS	2010.202	70.73	8.05	-51	6	1.0	0.15	SKS
PERS	2010.204	71.92	8.76	-54	7	1.0	0.15	SKS
PERS	2010.210	72.14	8.76	-56	8	0.9	0.15	SKS
PERS	2011.065	253.54	8.61	-42	9.5	1.0	0.25	SKS
PERS	2011.245	242.05	7.96	-64	7	1.3	0.2	SKS
PERS	2011.326	252.44	9.24	-44	3.5	1.1	0.15	SKS
PERS	2012.085	242.34	3.43	-62	9	1.2	0.2	SKiKS
PERS	2012.135	253.99	8.61	-58	9.5	0.7	0.25	SKS
PERS	2012.149	242.26	8.01	-62	10	1.2	0.3	SKS
PERS	2012.239	72.36	8.10	-50	11.5	0.9	0.25	SKS
PERS	2012.252	69.41	6.86	-61	9	1.1	0.3	SKS
PERS	2012.135	253.99	12.55	-42	7.5	1.4	0.35	SKKS
ROBS	2011.228	73.35	7.38	-45	5.5	1.9	0.35	SKS
ROBS	2011.242	77.26	7.01	-37	6.5	1.1	0.25	SKS
ROBS	2011.245	240.93	8.15	89	3	0.8	0.15	SKS
ROBS	2011.318	73.34	7.61	-41	6.5	1.4	0.25	SKS
ROBS	2011.326	251.27	9.41	-39	7.5	0.6	0.2	SKS
ROBS	2012.021	292.20	10.17	-90	7	1.9	0.15	SKS
ROBS	2012.037	68.78	9.19	-53	17.5	1.2	0.45	SKKS
ROBS	2012.086	297.34	8.45	79	8	1.8	0.3	SKS
ROBS	2012.093	296.99	9.79	-89	5	1.6	0.15	SKS
VISS	2007.169	55.71	5.68	-54	10	2.2	0.45	SKS
VISS	2007.271	47.60	8.88	-68	6	1.5	0.3	SKS
VISS	2010.123	44.54	10.23	-85	6	1.6	0.25	sSKS
VISS	2012.210	54.29	11.15	-66	16	1.3	0.55	SKKS
FVI	2010.181	296.10	9.99	72	3	1.6	0.15	SKS
FVI	2010.204	70.15	8.51	88	10	1.2	0.45	SKS
FVI	2010.204	70.26	8.50	80	6	1.8	0.5	SKS
FVI	2010.210	70.37	8.51	88	8	1.6	0.65	SKS
FVI	2010.224	269.20	9.99	73	10	1.7	0.4	SKS
FVI	2011.065	201.90	7.39	78	19	1.7	0.4	SKS
FVI	2011.236	262.78	9.54	69	5	1.6	0.45	SKS
FVI	2012.080	296.50	12.84	51	12.5	1.5	0.55	SKKS
FVI	2012.086	296.83	8.54	57	11	2.0	0.55	SKS
FVI	2012.093	296.46	9.90	68	5	1.6	0.15	SKS



FVI	2012.102	300.88	12.79	67	13	1.5	0.4	SKKS
CLUD	2011.065	201.94	7.40	82	9	1.9	0.5	SKS
ZOU2	2010.181	296.25	12.84	56	17.5	1.5	0.45	SKKS
ZOU2	2010.202	69.06	7.85	-85	3	1.6	0.15	SKS
ZOU2	2010.204	70.31	8.54	-82	4	1.4	0.1	SKS
ZOU2	2010.204	70.41	8.51	-82	3	1.4	0.15	SKS
ZOU2	2010.210	70.53	8.53	-83	5	1.3	0.2	SKS
ZOU2	2010.224	269.34	9.96	71	5	2.0	0.35	SKS
ZOU2	2010.272	70.00	6.65	-78	3	1.8	0.15	SKS
ZOU2	2011.065	202.00	7.39	54	17	1.7	0.45	SKS
ZOU2	2011.164	70.80	7.97	-85	3	1.5	0.15	SKS
ZOU2	2011.242	76.73	6.97	-77	11	1.1	0.35	SKS
ZOU2	2011.246	201.93	7.36	74	9	1.5	0.25	SKS
ABSI	2007.030	43.44	8.51	57	2	2.1	0.25	SKS
ABSI	2007.051	71.37	7.41	45	9.5	1.6	0.3	SKS
ABSI	2007.220	89.50	8.67	41	14.5	1.7	0.3	SKS
ABSI	2010.005	194.12	7.55	60	10	1.5	0.3	SKS
ABSI	2010.204	69.12	8.36	45	4.5	1.4	0.2	SKS
ABSI	2010.215	70.44	7.71	46	5.5	1.5	0.2	SKS
ABSI	2010.356	41.49	9.38	71	7	1.3	0.2	SKS
RISI	2007.030	44.04	8.61	72	5	1.9	0.25	SKS
RISI	2007.059	203.31	7.45	71	4	2.2	0.25	SKS
RISI	2007.193	261.99	9.57	66	9	1.9	0.4	SKS
RISI	2007.202	246.08	8.76	-42	11.5	1.1	0.4	SKS
RISI	2007.220	90.02	8.77	58	8	2.1	0.45	SKS
RISI	2007.257	93.44	12.81	63	13	1.7	0.45	SKKS
RISI	2007.271	45.31	8.81	79	7	1.4	0.25	SKS
RISI	2010.092	240.43	6.87	18	10	2.3	0.45	SKS
RISI	2010.113	239.53	6.79	-84	12	0.8	0.25	SKS
RISI	2010.226	51.58	12.30	66	6	2.6	0.4	SKKS
RISI	2010.230	51.61	7.76	-80	7	2.4	0.4	SKS
RISI	2010.236	304.21	9.41	64	7	1.3	0.25	SKS
RISI	2010.294	309.11	10.07	87	21	1.2	0.5	SKS
RISI	2010.355	41.94	9.48	78	6	1.7	0.25	SKS
RISI	2011.326	250.29	9.54	-74	10	0.9	0.2	SKS
RISI	2011.348	59.17	11.16	81	10	1.7	0.5	SKKS

---

ROSI	2007.030	43.49	8.54	59	3	2.2	0.3	SKS
ROSI	2007.051	71.38	7.45	45	9.5	1.7	0.55	pSKS
ROSI	2007.220	89.53	8.68	54	7	1.7	0.25	SKS
ROSI	2007.271	44.78	8.76	63	5	1.8	0.25	SKS
ROSI	2010.113	239.13	6.82	83	6	1.2	0.25	SKS
ROSI	2010.224	268.20	10.15	74	1	1.9	0.2	SKS
MOSI	2007.030	42.83	8.45	63	5	0.8	0.15	SKS
MOSI	2007.220	88.95	8.61	55	8	1.1	0.1	SKS
MOSI	2007.232	65.71	8.06	30	9	0.7	0.15	SKS
MOSI	2010.181	294.48	10.23	60	21.5	0.7	0.3	SKS
MOSI	2010.202	67.11	7.65	47	10.5	0.9	0.35	SKS
MOSI	2010.204	68.54	8.31	43	12.5	0.7	0.25	SKS
KOSI	2006.346	70.15	8.06	36	4	1.4	0.1	SKS
KOSI	2007.021	70.57	7.70	39	7.5	1.2	0.15	SKS
KOSI	2007.193	261.46	9.68	61	5	1.5	0.4	SKS
KOSI	2007.207	68.56	7.75	47	7.5	1.2	0.25	SKS
KOSI	2007.220	89.58	8.68	44	7.5	1.4	0.2	SKS
KOSI	2007.232	66.40	8.16	40	5.5	1.2	0.2	SKS
KOSI	2007.256	68.75	7.96	41	4.5	1.5	0.15	SKS
KOSI	2007.263	92.26	10.09	36	7.5	1.1	0.2	SKS
KOSI	2010.144	259.33	9.78	55	6	1.1	0.25	SKS
KOSI	2010.202	67.82	7.71	46	9.5	1.3	0.35	SKS
KOSI	2010.204	69.21	8.36	39	3	1.3	0.05	SKS
KOSI	2010.205	69.39	8.35	39	4	1.1	0.1	SKS
KOSI	2010.210	69.32	8.37	43	4.5	1.2	0.1	SKS
KOSI	2011.318	71.59	7.44	50	6.5	1.6	0.25	SKS

---

## C.2 Carpathian-Pannonian region

List of individual SKS splitting parameters measured from the teleseismic events recorded at the temporary stations of the Carpathian Basin Project (CBP) were located in Austria, Hungary, Croatia, and Serbia, deployed on three parallel NW-SE oriented profiles. Also data from permanent broadband seismic stations of the HU network in Hungary. Table consists the station name, events date, backazimuth of the events, incidence angles. This list also includes the fast axis azimuths (with respect to the north) and its error, splitting delay time and the corresponding error, and the relevant core shear-wave which was used to measure the splitting parameters.

Station	Event	BackAz	Incidence(°)	$\phi(^{\circ}\text{N})$	$\phi\text{-err}$	$\delta t(\text{s})$	$\delta t\text{-err}$	Phase
BEHE	2007.187	295.99	9.99	82	6	1.3	0.2	SKS
BUD	2006.333	73.86	8.40	-46	14.5	1.6	0.55	SKS
BUD	2007.030	49.53	9.19	18	2	1.6	0.1	SKS
BUD	2007.076	76.32	8.46	12	5	2.3	0.4	SKS
BUD	2007.202	250.95	8.06	-87	1	2.1	0.15	SKS
BUD	2013.178	75.73	8.35	16	13	0.5	0.1	SKS
BUD	2014.134	57.91	12.13	-64	8	1.0	0.15	SKKS
BUD	2014.325	74.98	8.50	-77	8	1.1	0.3	SKS
BUD	2014.330	75.57	8.51	8	5	1.4	0.25	SKS
BUD	2005.252	57.06	3.50	-79	10	1.6	0.35	SKiKS
BUD	2005.101	270.13	12.51	-64	19.5	1.2	0.55	SKKS
BUD	2005.153	250.41	7.79	-64	14	1.6	0.55	SKS
LTVH	2012.345	81.11	7.55	-73	8	1.8	0.45	SKS
LTVH	2013.329	221.61	11.46	-78	7	1.9	0.35	SKKS
LTVH	2014.091	258.31	7.68	-58	16.5	1.4	0.5	SKS
LTVH	2014.141	301.24	12.75	11	3	1.7	0.2	SKKS
LTVH	2014.215	62.84	3.41	-65	9	1.6	0.35	SKiKS
LTVH	2014.267	252.29	7.62	14	9	1.6	0.35	SKS
LTVH	2014.274	64.54	3.49	-75	6	1.4	0.2	SKiKS
MORH	2012.149	244.46	7.75	6	3	1.4	0.1	SKS
MORH	2014.236	261.35	8.24	13	13	0.8	0.3	SKS
PSZ	2005.207	261.63	8.06	-42	8.5	1.1	0.2	SKS
PSZ	2005.207	261.63	12.35	-52	10	1.0	0.15	SKKS
PSZ	2007.055	272.90	8.27	47	10.5	1.8	0.4	SKS
PSZ	2007.202	251.65	7.96	-82	4	2.8	0.3	SKS

PSZ	2014.188	296.34	9.63	-16	10	1.4	0.25	SKS
PSZ	2014.341	58.07	5.63	-66	5	2.1	0.25	SKS
SOP	2004.287	75.94	7.12	-68	8	2.4	0.35	SKS
SOP	2006.241	76.36	8.18	-64	8	1.2	0.25	SKS
SOP	2007.030	47.56	9.02	-70	4	1.0	0.1	SKS
SOP	2007.179	55.71	3.53	12	73	1.3	0.5	SKiKS
BUKL	2005.321	253.52	7.76	-44	9.5	1.0	0.25	SKS
BUKL	2005.357	275.03	9.06	-37	8.5	1.0	0.15	SKS
BUKL	2006.237	251.39	7.64	-43	5.5	1.2	0.15	SKS
BUKL	2007.193	268.25	8.65	-48	4	1.0	0.05	SKS
BUKL	2007.202	252.08	7.91	-40	4.5	1.3	0.2	SKS
BUKL	2007.229	79.14	7.62	-45	28.5	0.7	0.5	SKS
BUKL	2007.253	278.32	9.60	-48	8.5	1.3	0.2	SKS
CBP2C	2006.120	249.20	7.45	-59	16	0.9	0.25	SKS
CBP2C	2006.237	248.42	8.00	-68	9	0.8	0.1	SKS
CBP2C	2006.317	244.73	8.01	-71	2	0.9	0.05	SKS
CBP2C	2007.202	249.03	8.30	-69	16	0.8	0.25	SKS
CBP2D	2006.120	249.52	7.38	-58	10	1.2	0.25	SKS
CBP2D	2006.198	94.91	8.82	-21	10	1.1	0.3	SKS
CBP2D	2006.237	248.74	7.96	-47	5	1.4	0.2	SKS
CBP2D	2006.252	84.44	7.76	-46	7.5	1.0	0.15	SKS
CBP2D	2007.030	47.36	9.09	-61	4	1.6	0.3	SKS
CBP2D	2007.111	235.71	5.85	-66	6	2.1	0.25	SKS
CBP2D	2007.193	265.30	9.05	-43	16.5	1.3	0.5	SKS
CBP2D	2007.202	249.36	8.25	-51	5	1.3	0.2	SKS
CBP2D	2007.232	69.96	8.73	-60	13	0.9	0.25	SKS
CBP2E	2006.146	92.63	8.81	-31	8	0.9	0.15	SKS
CBP2E	2006.237	248.85	7.96	-53	6	1.4	0.25	SKS
CBP2E	2006.290	57.57	5.72	-56	5	1.5	0.25	SKS
CBP2E	2007.051	75.14	7.94	-65	8	1.2	0.25	SKS
CBP2E	2007.220	93.21	9.25	-39	10.5	1.0	0.2	SKS
CBP2F	2006.146	92.80	8.82	-33	11.5	1.2	0.3	SKS
CBP2F	2006.237	248.94	7.95	-45	6.5	1.7	0.35	SKS
CBP2F	2007.193	265.58	9.05	-52	13.5	1.2	0.3	SKS
CBP2F	2007.202	249.58	8.23	-52	5	1.8	0.25	SKS
CBP2H	2006.139	77.25	3.29	29	6	1.6	0.25	SKiKS

---

CBP2H	2007.030	48.36	9.08	-68	5	1.6	0.25	SKS
CBP2H	2007.202	250.00	8.18	-82	14	0.7	0.25	SKS
CBP2I	2006.237	249.46	7.90	-77	28.5	0.4	0.3	SKS
CBP2I	2006.317	245.78	7.92	-80	13	0.3	0.1	SKS
CBP2J	2006.237	249.56	7.89	-82	7	0.7	0.15	SKS
CBP2J	2006.317	245.88	7.91	-70	9	0.6	0.1	SKS
CBP2J	2007.202	250.24	8.18	-80	9	0.8	0.2	SKS
CBP2K	2006.237	249.71	7.87	-78	10	0.7	0.15	SKS
CBP2K	2006.317	246.03	7.90	-76	10	0.7	0.15	SKS
CBP2L	2006.237	249.72	7.87	-52	14.5	0.5	0.1	SKS
CBP2L	2006.252	86.41	7.93	-46	23.5	0.4	0.2	SKS
CBP2L	2006.290	60.13	5.75	-62	18	0.7	0.35	SKS
CBP2M	2006.237	249.89	7.86	-40	7.5	0.9	0.25	SKS
CBP2M	2006.317	246.22	7.89	-42	4.5	0.7	0.1	SKS
CBP2M	2007.030	49.41	9.06	-59	3	1.3	0.2	SKS
CBP2M	2007.193	266.80	8.83	-37	12.5	0.5	0.15	SKS
CBP2M	2007.202	250.60	8.15	-45	17.5	0.7	0.3	SKS
CBP2N	2006.237	250.00	7.84	-52	5	0.7	0.1	SKS
CBP2N	2006.317	246.34	7.88	-60	4	0.7	0.1	SKS
CBP2N	2007.193	266.95	8.81	-57	6	0.6	0.1	SKS
CBP2N	2007.202	264.59	8.97	-51	9.5	0.8	0.2	SKS
CBP2N	2007.202	250.72	8.14	-55	4	0.8	0.05	SKS
CBP2O	2006.237	250.08	7.83	-58	6	0.7	0.05	SKS
CBP2O	2006.317	246.42	7.87	-58	8	0.8	0.15	SKS
CBP2O	2007.030	49.77	9.06	-70	13	0.5	0.1	SKS
CBP2O	2007.193	267.06	8.81	-47	9.5	0.6	0.1	SKS
CBP2O	2007.202	264.71	8.96	-53	24.5	0.5	0.2	SKS
CBP2O	2007.202	250.82	8.12	-59	8	0.7	0.1	SKS
CBP2P	2006.237	250.18	7.83	-54	7	1.1	0.2	SKS
CBP2P	2006.317	246.52	7.87	-65	6	0.8	0.1	SKS
CBP2P	2007.030	49.96	9.06	-58	2	1.3	0.1	SKS
CBP2P	2007.193	267.19	8.79	-65	8	0.8	0.2	SKS
CBP2P	2007.202	264.85	8.94	-57	5	1.0	0.15	SKS
CBP2P	2007.202	250.92	8.11	-61	8	1.0	0.15	SKS
CBP2R	2007.193	267.46	8.74	-35	9.5	0.7	0.15	SKS
CBP2R	2007.145	250.48	7.82	-52	11.5	0.9	0.25	SKS

CBP2S	2006.237	250.43	7.80	-66	13	0.8	0.15	SKS
CBP2S	2006.317	246.80	7.84	-75	13	0.7	0.2	SKS
CBP2S	2007.030	50.54	9.07	-63	6	1.0	0.2	SKS
CBP2S	2007.145	250.54	7.81	-73	11	0.6	0.15	SKS
CBP2S	2007.202	251.22	8.06	-65	19	0.8	0.25	SKS
CBP3B	2006.237	248.11	8.04	-72	15	1.0	0.3	SKS
CBP3C	2007.030	46.74	9.04	-77	10	1.2	0.3	SKS
CBP3D	2006.120	249.03	7.47	-67	16	1.0	0.35	SKS
CBP3D	2006.175	77.16	8.31	-63	15	0.4	0.1	SKS
CBP3D	2006.237	248.28	8.03	-62	9	0.9	0.15	SKS
CBP3D	2006.259	73.98	7.46	-54	14.5	0.7	0.2	SKS
CBP3D	2006.290	56.80	5.67	-73	8	0.8	0.15	SKS
CBP3D	2007.021	73.63	8.18	-60	14	0.5	0.15	SKS
CBP3D	2007.030	46.92	9.03	-69	5	1.7	0.25	SKS
CBP3D	2007.051	74.51	7.87	-59	8	0.6	0.1	SKS
CBP3D	2007.193	264.85	9.13	-61	11	0.7	0.2	SKS
CBP3D	2007.202	248.91	8.33	-69	8	0.8	0.1	SKS
CBP3D	2007.207	71.65	8.25	-66	12	0.7	0.15	SKS
CBP3E	2006.120	249.21	7.46	-43	8.5	1.4	0.4	SKS
CBP3E	2007.030	47.22	9.04	-65	3	1.9	0.25	SKS
CBP3E	2007.202	262.67	9.26	-49	18.5	0.9	0.35	SKS
CBP3E	2007.207	71.96	8.29	-54	19.5	0.6	0.2	SKS
CBP3E	2007.228	262.01	8.26	-60	9	1.7	0.4	SKS
CBP3E	2007.229	75.74	7.26	22	21.5	1.1	0.5	SKS
CBP3F	2007.030	47.47	9.05	-73	6	1.5	0.2	SKS
CBP3F	2007.202	249.28	8.29	-87	7	1.0	0.3	SKS
CBP3G	2006.139	76.47	8.20	26	8	1.6	0.3	SKS
CBP3G	2006.237	248.67	7.99	-75	6	0.7	0.1	SKS
CBP3G	2007.030	47.57	3.21	-70	9	1.2	0.3	SKiKS
CBP3G	2007.202	249.32	8.29	-71	26.5	0.5	0.3	SKS
CBP3H	2006.237	248.96	7.95	-59	13	0.8	0.2	SKS
CBP3I	2006.142	78.67	7.63	-57	5	1.6	0.2	SKS
CBP3I	2006.175	78.59	3.28	-53	12.5	1.5	0.4	SKiKS
CBP3I	2007.030	48.28	9.05	-62	2	1.1	0.1	SKS
CBP3I	2007.202	249.81	8.22	-66	19	0.5	0.15	SKS
CBP3J	2007.030	48.49	9.04	-70	11	1.2	0.4	SKS

CBP3J	2006.237	249.23	7.94	-75	20	0.4	0.2	SKS
CBP3M	2006.237	249.58	7.90	-64	7	0.7	0.05	SKS
CBP3M	2006.317	245.92	7.93	-58	12	0.6	0.15	SKS
CBP3M	2007.193	266.49	8.88	-72	9	0.8	0.25	SKS
CBP3M	2007.202	250.30	8.17	-66	7	0.7	0.1	SKS
CBP3N	2006.311	60.88	11.34	-75	16	1.2	0.4	SKKS
CBP3N	2007.030	49.26	9.03	-71	11	0.9	0.3	SKS
CBP3N	2007.076	76.20	8.36	-72	8	1.3	0.25	SKS
CBP3N	2007.202	250.37	8.18	-74	35.5	0.6	0.6	SKS
CBP3O	2006.198	96.96	9.11	-63	9	1.2	0.45	SKS
CBP3O	2007.021	76.36	8.38	-62	30.5	0.8	0.45	SKS
CBP3O	2007.193	266.69	8.84	-43	14.5	0.7	0.2	SKS
CBP3O	2007.202	250.45	8.18	-64	14	0.6	0.15	SKS
CBP3P	2006.237	249.84	7.87	-50	6	0.8	0.15	SKS
CBP3P	2006.317	246.20	7.91	-62	6	0.7	0.1	SKS
CBP3P	2007.030	49.66	9.02	-64	6	0.8	0.2	SKS
CBP3P	2007.193	266.85	8.82	-37	17.5	0.7	0.25	SKS
CBP3P	2007.202	250.59	8.17	-61	6	0.6	0.05	SKS
CBP3Q	2006.237	249.94	7.86	-84	2	1.2	0.15	SKS
CBP3Q	2006.317	246.30	7.91	-84	5	1.0	0.15	SKS
CBP3Q	2007.202	250.71	8.16	-81	5	1.2	0.2	SKS
CBP3R	2006.237	250.03	7.86	-76	7	0.9	0.1	SKS
CBP3R	2006.317	246.39	7.90	-80	5	0.8	0.15	SKS
CBP3R	2007.193	267.11	8.79	-69	10	0.8	0.3	SKS
CBP3R	2007.202	250.80	8.15	-71	5	0.8	0.05	SKS
CBP4B	2006.237	247.77	8.10	-80	18	0.9	0.4	SKS
CBP4B	2006.317	244.08	8.11	-74	9	1.0	0.15	SKS
CBP4B	2007.030	46.25	8.98	-82	6	0.9	0.1	SKS
CBP4C	2006.237	247.90	8.08	-84	12	0.9	0.35	SKS
CBP4D	2006.290	56.56	11.30	-61	18	1.6	0.7	SKKS
CBP4D	2006.311	56.84	11.24	-67	12	1.4	0.4	SKKS
CBP4D	2006.317	244.31	8.09	-76	6	0.6	0.05	SKS
CBP4D	2007.202	248.61	8.36	-71	18	0.8	0.25	SKS
CBP4D	2006.237	247.99	8.08	-82	26	0.8	0.6	SKS
CBP4F	2006.237	248.25	8.05	-82	13	0.8	0.3	SKS
CBP4F	2006.290	57.28	11.31	-81	10	1.5	0.3	SKKS



CBP4F	2007.030	47.10	8.96	-71	7	1.6	0.35	SKS
CBP4G	2006.139	76.29	8.18	50	19.5	0.8	0.45	SKS
CBP4G	2007.030	47.36	8.97	-67	6	1.5	0.3	SKS
CBP4G	2007.111	235.15	5.90	-77	12	1.4	0.4	SKS
CBP4H	2006.237	248.64	8.00	-63	16	0.7	0.2	SKS
CBP4H	2006.317	244.97	8.02	-55	15	0.5	0.25	SKS
CBP4H	2007.202	249.31	8.30	-61	13	0.6	0.1	SKS
CBP4I	2006.237	248.76	8.00	-43	10.5	0.8	0.25	SKS
CBP4J	2006.148	58.71	11.34	-57	7	1.7	0.35	SKKS
CBP4J	2007.030	48.16	8.97	-88	12	1.0	0.3	SKS
CBP4J	2007.187	296.32	12.84	56	13	1.2	0.45	SKKS
CBP4K	2007.030	48.31	8.96	102	8	1.0	0.2	SKS
CBP4K	2007.187	296.44	9.92	60	7	0.9	0.15	SKS
CBP4L	2006.237	249.09	7.96	-65	11	0.6	0.1	SKS
CBP4L	2006.317	245.43	7.99	-57	9	0.7	0.2	SKS
CBP4L	2007.111	235.25	5.88	-71	8	1.5	0.3	SKS
CBP4L	2007.187	296.63	10.03	69	5	1.6	0.2	pSKS
CBP4L	2007.202	249.80	8.25	-62	8	0.6	0.1	SKS
CBP4M	2006.237	249.22	7.95	-71	7	0.6	0.05	SKS
CBP4M	2007.030	48.77	8.96	-63	3	1.1	0.15	SKS
CBP4M	2007.193	266.13	8.94	-56	25.5	0.5	0.25	SKS
CBP4M	2007.202	249.95	8.22	-68	18	0.6	0.2	SKS
CBP4N	2006.237	249.30	7.94	-63	14	0.7	0.15	SKS
CBP4N	2006.317	245.65	7.98	-58	14	0.6	0.2	SKS
CBP4N	2007.030	48.96	8.95	-59	4	1.0	0.2	SKS
CBP4N	2007.193	266.25	8.92	-56	24.5	0.6	0.25	SKS
CBP4N	2007.202	250.03	8.21	-62	15	0.7	0.2	SKS
CBP4O	2006.237	249.40	7.93	-49	9.5	0.9	0.25	SKS
CBP4O	2006.317	245.76	7.97	-68	7	1.0	0.15	SKS
CBP4O	2007.202	250.14	8.21	-66	7	0.8	0.15	SKS
FGSL	2006.004	318.78	9.41	-75	46	1.4	0.3	SKS
FGSL	2006.146	95.33	9.19	-59	53	0.5	0.2	SKS
FGSL	2006.237	250.20	7.83	-78	47	1.3	0.2	SKS
FGSL	2006.311	62.67	11.36	-63	48	0.7	0.25	SKKS
FGSL	2006.317	246.57	7.88	-79	45	1.2	0.2	SKS
PRDL	2005.321	251.38	8.06	-55	54	1.1	0.35	SKS

---

PRDL	2006.120	249.72	7.40	-54	50	1.2	0.5	SKS
PRDL	2006.237	249.25	7.96	-63	50	1.2	0.35	SKS
PRDL	2006.317	245.62	8.00	-66	51	1.1	0.2	SKS
SZAL	2007.193	266.27	8.91	-52	59	0.5	0.1	SKS
SZAL	2007.220	94.53	9.43	-51	56	0.5	0.2	SKS
SZAL	2007.232	71.73	8.78	-38	66	0.7	0.15	SKS
SZEL	2007.193	267.80	8.68	-42	59	0.6	0.15	SKS
SZEL	2007.202	265.45	8.83	-55	56	0.6	0.1	SKS
TARL	2005.321	254.97	7.57	-55	4	2.0	0.2	SKS
TARL	2006.120	253.45	6.97	-57	4	1.7	0.15	SKS
TARL	2006.120	253.46	6.94	-61	13	1.3	0.3	SKS
TARL	2006.146	97.03	9.43	-57	10	1.1	0.3	SKS
TARL	2006.237	252.83	7.47	-59	4	1.8	0.15	SKS
TARL	2006.293	267.59	7.69	-58	7	1.6	0.2	SKS
TARL	2006.317	249.10	7.50	-63	6	1.5	0.25	SKS
TARL	2007.030	52.22	9.55	-58	3	2.0	0.2	SKS
TARL	2007.202	267.37	8.61	-55	6	1.7	0.2	SKS
TARL	2007.202	253.53	7.74	-56	3	1.8	0.1	SKS
ZSAL	2005.269	271.90	8.61	-56	53	1.4	0.65	SKS
ZSAL	2005.272	61.87	11.44	-72	47	1.6	0.3	SKKS
ZSAL	2005.321	253.95	7.70	-50	56	1.1	0.35	SKS
ZSAL	2006.237	251.80	7.60	-84	44	1.0	0.25	SKS
ZSAL	2007.187	299.54	9.53	84	30	0.7	0.25	SKS
ZSAL	2007.193	268.84	8.56	-75	49	1.3	0.2	SKS
ZSAL	2007.202	252.54	7.87	-85	45	1.1	0.25	SKS
ZSAL	2007.207	76.30	8.76	-70	45	1.1	0.55	SKS

---



# Bibliography

- Ádám, A., and V. Wetztergom (2001), An attempt to map the depth of the electrical asthenosphere by deep magnetotelluric measurements in the Pannonian Basin (Hungary), *Acta Geologica Hungarica*, *44*(2-3), 167–192.
- Anderson, M. L., G. Zandt, E. Triep, M. Fouch, and S. Beck (2004), Anisotropy and mantle flow in the Chile-Argentina subduction zone from shear wave splitting analysis, *Geophys. Res. Lett.*, *31*(23), doi:10.1029/2004GL020906.
- Apoloner, M.-T., and G. Bokelmann (2015), Modeling and detection of regional depth phases at the GERES array, *Advances in Geosciences*, *41*, 5–10, doi:10.5194/adgeo-41-5-2015.
- Apoloner, M.-T., G. Bokelmann, I. Bianchi, E. Brückl, H. Hausmann, S. Mertl, and R. Meurers (2014), The 2013 Earthquake Series in the Southern Vienna Basin: location, *Advances in Geosciences*, *36*, 77–80, doi:10.5194/adgeo-36-77-2014.
- Aric, K., R. Gutdeutsch, B. Leichter, W. Lenhardt, J. Plomerova, V. Babuska, P. Pajdusak, and U. Nixdorf (1989), Structure of the lithosphere in the eastern alps derived from P-residual analysis, *Arbeiten der Zentralanstalt für Meteorologie und Geodynamik, Vienna*, *73*(137), 1–26.
- Artemieva, I. M., H. Thybo, and M. K. Kaban (2006), Deep Europe today: Geophysical synthesis of the upper mantle structure and lithospheric processes over 3.5 Ga, *Geological Society Memoir*, *32*, 11–41.
- Babuška, V., J. Plomerová, and M. Granet (1990), The deep lithosphere in the Alps: a model inferred from P residuals, *Tectonophysics*, *176*(1–2), 137 – 165, doi:http://dx.doi.org/10.1016/0040-1951(90)90263-8.
- Babuška, V., and M. Cara (1991), *Seismic anisotropy in the Earth / by V. Babuska and M. Cara*, viii, 217 p. : pp., Kluwer Academic Publishers Dordrecht, The Netherlands ; Boston.

- Baccheschi, P., L. Margheriti, and M. Steckler (2007), Seismic anisotropy reveals focused mantle flow around the Calabrian slab (southern Italy), *Geophys. Res. Lett.*, *34*(5), L05,302, doi:10.1029/2006gl028899.
- Bada, G., S. Cloetingh, P. Gerner, and F. Horváth (1998), Sources of recent tectonic stress in the Pannonian region: inferences from finite element modelling, *Geophysical Journal International*, *134*(1), 87–101.
- Bada, G., F. Horváth, S. Cloetingh, D. D. Coblenz, and T. Tóth (2001), Role of topography-induced gravitational stresses in basin inversion: The case study of the Pannonian basin, *Tectonics*, *20*(3), 343–363, doi:10.1029/2001TC900001.
- Bada, G., F. Horváth, P. Dövényi, P. Szafián, G. Windhoffer, and S. Cloetingh (2007), Present-day stress field and tectonic inversion in the Pannonian basin, *Global and Planetary Change*, *58*(1–4), 165 – 180, doi:http://dx.doi.org/10.1016/j.gloplacha.2007.01.007, tOPO-EUROPE: the Geoscience of Coupled Deep Earth-Surface Processes.
- Bali, E., G. Falus, C. Szabó, D. Peate, K. Hidas, K. Török, and T. Ntaflou (2007), Remnants of boninitic melts in the upper mantle beneath the central Pannonian Basin?, *Mineralogy and Petrology*, *90*(1-2), 51–72.
- Balla, Z. (1984), The Carpathian loop and the Pannonian basin: kinematic analysis, *Geophysical Transactions*, *30*, 313–353.
- Baran, R., A. M. Friedrich, and F. Schlunegger (2014), The late Miocene to Holocene erosion pattern of the Alpine foreland basin reflects Eurasian slab unloading beneath the western Alps rather than global climate change, *Lithos.*, *6*(2), 124–131, doi:10.1130/L307.1.
- Barruol, G., and H. Kern (1996), Seismic anisotropy and shear-wave splitting in lower-crustal and upper-mantle rocks from the Ivrea Zone—experimental and calculated data, *Physics of the Earth and Planetary Interiors*, *95*(3–4), 175 – 194, doi:http://dx.doi.org/10.1016/0031-9201(95)03124-3.
- Barruol, G., and D. Mainprice (1993), A quantitative evaluation of the contribution of crustal rocks to the shear-wave splitting of teleseismic SKS waves, *Physics of the Earth and Planetary Interiors*, *78*(3–4), 281 – 300, doi:http://dx.doi.org/10.1016/0031-9201(93)90161-2.
- Barruol, G., and A. Souriau (1995), Anisotropy beneath the Pyrenees range from teleseismic shear wave splitting, *Geophys. Res. Lett.*, *22*(4), 493–496, doi:10.1029/94GL03225.

- Barruol, G., P. Silver, and A. Vauchez (1997), Seismic anisotropy in the eastern United States: Deep structure of a complex continental plate, *J. Geophys. Res.*, *102*(B4), 8329–8348.
- Barruol, G., M. Bonnin, H. Pedersen, G. Bokelmann, and C. Tiberi (2011), Belt-parallel mantle flow beneath a halted continental collision: The western Alps, *Earth Planet. Sci. Lett.*, *302*, 429–438, doi:10.1016/j.epsl.2010.12.040.
- Behrmann, J. H. (1988), Crustal scale extension in a convergent orogen: The Sterzing-Steinach mylonite zone in the eastern Alps, *Geodinamica Acta*, *2*, 63–73.
- Behrmann, J. H. (1990), Zur Kinematik der Kontinent-kollision in den Ostlpen, *Geotektonische Forschung*, *76*, 1–180.
- Behrmann, J. H., and W. Frisch (1990), Sinistral ductile shearing associated with metamorphic decompression in the Tauern Window, Eastern Alps, *Jahrb.Geol.B.-A*, *133*(2), 135–146.
- Ben Ismail, W., and D. Mainprice (1998), An olivine fabric database: an overview of upper mantle fabrics and seismic anisotropy, *Tectonophysics*, *296*(1–2), 145 – 157, doi:http://dx.doi.org/10.1016/S0040-1951(98)00141-3.
- Berger, A., and R. Bousquet (2008), Subduction-related metamorphism in the Alps: review of isotopic ages based on petrology and their geodynamic consequences, *Geological Society of London Special Publications*, *298*, 117–144, doi:10.1144/SP298.7.
- Bianchi, I., and G. Bokelmann (2014), Seismic signature of the Alpine indentation, evidence from the Eastern Alps, *Journal of Geodynamics*, doi:http://dx.doi.org/10.1016/j.jog.2014.07.005.
- Bianchi, I., M. S. Miller, and G. Bokelmann (2014), Insights on the upper mantle beneath the Eastern Alps, *Earth Planet. Sci. Lett.*, *403*(0), 199 – 209, doi:http://dx.doi.org/10.1016/j.epsl.2014.06.051.
- Bijwaard, H., and W. Spakman (2000), Non-linear global P-wave tomography by iterated linearized inversion, *Geophysical Journal International*, *141*(1), 71–82.
- Bijwaard, H., W. Spakman, and E. R. Engdahl (1998), Closing the gap between regional and global travel time tomography, *J. Geophys. Res.*, *103*(B12), 30,055–30,078, doi:10.1029/98JB02467.

- Bokelmann, G., and A. Wüstefeld (2009), Comparing crustal and mantle fabric from the North American craton using magnetics and seismic anisotropy, *Earth and Planetary Science Letters*, 277(3–4), 355 – 364, doi:http://dx.doi.org/10.1016/j.epsl.2008.10.032.
- Bokelmann, G., E. Qorbani, and I. Bianchi (2013), Seismic anisotropy and large-scale deformation of the Eastern Alps, *Earth Planet. Sci. Lett.*, 383, 1 – 6, doi:http://dx.doi.org/10.1016/j.epsl.2013.09.019.
- Bokelmann, G. H. (1995), P-wave array polarization analysis and effective anisotropy of the brittle crust, *Geophysical Journal International*, 120(1), 145–162.
- Bormann, P., P. Burghardt, T. Makeyeva, and L. Vinnik (1993), Teleseismic shear-wave splitting and deformation in central Europe, *Phys. Earth Planet. Inter.*, 78, 157–166.
- Bowman, J. R., and M. Ando (1987), Shear-wave splitting in the upper-mantle wedge above the Tonga subduction zone, *Geophysical Journal of the Royal Astronomical Society*, 88(1), 25–41, doi:10.1111/j.1365-246X.1987.tb01367.x.
- Brückl, E. (2011), Lithospheric Structure and Tectonics of the Eastern Alps – Evidence from New Seismic Data, in *Tectonics*, edited by D. Closson, ISBN: 978-953-307-545-7, DOI: 10.5772/14364.
- Brückl, E., F. Bleibinhaus, A. Gosar, M. Grad, A. Guterch, P. P. Hrubcová, G. Keller, M. Majdański, F. Sumanovac, T. Tiira, J. Yliniemi, E. Hegedűs, and H. Thybo (2007), Crustal structure due to collisional and escape tectonics in the Eastern Alps region based on profiles Alp01 and Alp02 from the ALP 2002 seismic experiment, *J. Geophys. Res.*, 112(B6), doi:10.1029/2006JB004687.
- Brückl, E., M. Behm, K. Decker, M. Grad, A. Guterch, G. Keller, and H. Thybo (2010), Crustal structure and active tectonics in the eastern Alps, *Tectonics*, 29(TC2011), doi:10.1029/2009TC002491.
- Brun, J.-P., and D. Sokoutis (2010), 45 m.y. of Aegean crust and mantle flow driven by trench retreat, *Geology*, 38(9), 815–818, doi:10.1130/G30950.1.
- Buontempo, B., G. Bokelmann, G. Barruol, and J. Moralest (2008), Seismic anisotropy beneath southern Iberia from SKS splitting, *Earth Planet. Sci. Lett.*, 273, 237–250.
- Bus, Z., G. Grenerczy, I. Tóth, and P. Mónus (2009), Active crustal deformation in two seismogenic zones of the Pannonian region – GPS versus seismological observations, *Tectonophysics*, 474, 343–352, doi:10.1016/j.tecto.2009.02.045.



- Buttles, J., and P. Olson (1998), A laboratory model of subduction zone anisotropy, *Earth and Planetary Science Letters*, *164*(1–2), 245 – 262, doi:http://dx.doi.org/10.1016/S0012-821X(98)00211-8.
- Calais, E., J.-M. Nocquet, F. Jouanne, and M. Tardy (2002), Current strain regime in the Western Alps from continuous Global Positioning System measurements, 1996–2001, *Geology*, *30*(7), 651–654, doi:10.1130/0091-7613(2002)030-0651:CSRITW-2.0.CO;2.
- Channell, J., and H. Kozur (1997), How many oceans? Meliata, Vardar and Pindos oceans in Mesozoic Alpine paleogeography, *Geology*, *25*(2), 183–186.
- Csontos, L. (1995), Tertiary tectonic evolution of the Intra-Carpathian area, *Acta Vulcanologica*, *7*, 1–14.
- Csontos, L., E. Marton, G. Worum, and L. Benkovics (2002), Geodynamics of SW-Pannonian inselbergs (Mecsek and Villány Mts, SW Hungary): Inferences from a complex structural analysis, *EGU Stephan Mueller Special Publication Series*, *3*, 227–245.
- Dando, B. D. E., G. W. Stuart, G. A. Houseman, E. Hegedüs, E. Brückl, and S. Radovanovic (2011), Teleseismic tomography of the mantle in the Carpathian–Pannonian region of central Europe, *Geophys. J. Int.*, *186*(1), 11–31, doi:10.1111/j.1365-246X.2011.04998.x.
- Davis, P. (2003), Azimuthal variation in seismic anisotropy of the southern California uppermost mantle, *Journal of Geophysical Research: Solid Earth (1978–2012)*, *108*(B1).
- Dégi, J., R. Abart, K. Török, E. Bali, R. Wirth, and D. Rhede (2010), Symplectite formation during decompression induced garnet breakdown in lower crustal mafic granulite xenoliths: mechanisms and rates, *Contributions to Mineralogy and Petrology*, *159*(3), 293–314, doi:10.1007/s00410-009-0428-z.
- Diaz, J., J. Gallart, A. Villasenor, F. Mancilla, A. Pazos, D. Cordoba, J. Pulgar, P. Ibarra, and M. Harnafi (2010), Mantle dynamics beneath the Gibraltar arc (western Mediterranean) from shear-wave splitting measurements on a dense seismic array, *Geophys. Res. Lett.*, *37*(L18304), doi:10.1029/2010GL044201.
- Dobosi, G., G. Jenner, A. Embey-Isztin, and H. Downes (2010), Cryptic metasomatism in clino- and orthopyroxene in the upper mantle beneath the Pannonian region, *Geological Society, London, Special Publications*, *337*(1), 177–194.

- Doglioni, C., A. Ismail-Zadeh, G. Panza, and F. Riguzzi (2011), Lithosphere–asthenosphere viscosity contrast and decoupling, *Physics of the Earth and Planetary Interiors*, 189(1–2), 1 – 8, doi:http://dx.doi.org/10.1016/j.pepi.2011.09.006.
- Dombrádi, E., D. Sokoutis, G. Bada, S. Cloetingh, and F. Horváth (2010), Modelling recent deformation of the Pannonian lithosphere: lithospheric folding and tectonic topography, *Tectonophysics*, 484(1), 103–118.
- Embey-Isztin, A., G. Dobosi, J.-L. Bodinier, D. Bosch, G. Jenner, S. Pourtales, and O. Bruguier (2014), Origin and significance of poikilitic and mosaic peridotite xenoliths in the western Pannonian Basin: geochemical and petrological evidences, *Contributions to Mineralogy and Petrology*, 168(3), 1–16.
- Engi, M., N. Scherrer, and T. Burri (2001), Metamorphic evolution of pelitic rocks of the Monte Rosa nappe: Constraints from petrology and single grain monazite age data, *Schweiz. mineral. petrogr. Mitt.*, 81(3), 305–328.
- Evangelidis, C., W.-T. Liang, N. Melis, and K. Konstantinou (2011), Shear wave anisotropy beneath the Aegean inferred from SKS splitting observations, *Journal of Geophysical Research: Solid Earth (1978–2012)*, 116(B4).
- Faccenda, M., L. Burlini, T. V. Gerya, and D. Mainprice (2008), Fault-induced seismic anisotropy by hydration in subducting oceanic plates, *Nature*, 455, 1097–1100, doi:10.1038/nature07376.
- Faccenna, C., T. W. Becker, L. Auer, A. Billi, L. Boschi, J. P. Brun, F. A. Capitano, F. Funiciello, F. Horváth, L. Jolivet, C. Piromallo, L. Royden, F. Rossetti, and E. Serpelloni (2014), Mantle dynamics in the Mediterranean, *Rev. Geophys.*, 52(3), 283–332, doi:10.1002/2013RG000444.
- Falus, G., C. Szabó, and O. Vaselli (2000), Mantle upwelling within the Pannonian Basin: evidence from xenolith lithology and mineral chemistry, *Terra nova*, 12(6), 295–302.
- Falus, G., A. Tommasi, J. Ingrin, and C. Szabó (2008), Deformation and seismic anisotropy of the lithospheric mantle in the southeastern Carpathians inferred from the study of mantle xenoliths, *Earth and Planetary Science Letters*, 272(1–2), 50 – 64, doi:http://dx.doi.org/10.1016/j.epsl.2008.04.035.
- Fischer, K. M., E. M. Parmentier, A. R. Stine, and E. R. Wolf (2000), Modeling anisotropy and plate-driven flow in the Tonga subduction zone back arc, *J. Geophys. Res.*, 105(B7), 16,181–16,191, doi:10.1029/1999JB900441.

- Flesch, L. M., W. E. Holt, P. G. Silver, M. Stephenson, C.-Y. Wang, and W. W. Chan (2005), Constraining the Extent of Crust-Mantle Coupling in Central Asia Using GPS, Geologic, and Shear-Wave Splitting Data, *Earth Planet. Sci. Lett.*, *238*, 248–268, doi: 10.1016/j.epsl.2005.06.023.
- Fodor, L., A. Magyari, M. Kázmér, and A. Fogarasi (1992), Gravity-flow dominated sedimentation on the Buda paleoslope (Hungary): Record of Late Eocene continental escape of the Bakony unit, *Geologische Rundschau*, *81*(3), 695–716, doi: 10.1007/BF01791386.
- Fodor, L., L. Csontos, G. Bada, I. Györfi, and L. Benkovics (1999), Tertiary tectonic evolution of the Pannonian Basin system and neighbouring orogens: a new synthesis of palaeostress data, *Geological Society, London, Special Publications*, *156*(1), 295–334.
- Fontaine, F. R., G. Barruol, A. Tommasi, and G. H. R. Bokelmann (2007), Upper-mantle flow beneath French Polynesia from shear wave splitting, *Geophys. J. Int.*, *170*(3), 1262–1288, doi:10.1111/j.1365-246X.2007.03475.x.
- Fontaine, F. R., G. Barruol, B. L. Kennett, G. H. Bokelmann, and D. Reymond (2009), Upper mantle anisotropy beneath Australia and Tahiti from P wave polarization: Implications for real-time earthquake location, *Journal of Geophysical Research: Solid Earth (1978–2012)*, *114*(B3).
- Fouch, M., and S. Rondenay (2006), Seismic anisotropy beneath stable continental interiors, *Phys. Earth Planet. Inter.*, *158*, 292–320.
- Frank, W. (1969), Geologie der Glocknergruppe, *Wissensch. Alpenvereinsh.*, *21*, 95–111.
- Frisch, W. (1979), Tectonic progradation and plate tectonic evolution of the Alps, *Tectonophysics*, *60*(3–4), 121 – 139, doi:http://dx.doi.org/10.1016/0040-1951(79)90155-0.
- Frisch, W., J. Kuhleman, I. Dunkl, and A. Brügel (1998), Palinspastic reconstruction and topographic evolution of the Eastern Alps during late Tertiary tectonic extrusion, *Tectonophysics*, *279*, 1–15.
- Froitzheim, N., and G. Manatschal (1996), Kinematics of jurassic rifting, mantle exhumation, and passive-margin formation in the Austroalpine and Penninic nappes (Eastern Switzerland), *Geological Society of America Bulletin*, *108*(9), 1120–1133, doi: 10.1130/0016-7606(1996)108<1120:KOJRME>2.3.CO;2.

- Froitzheim, N., S. M. Schmid, and M. Frey (1996), Mesozoic paleogeography and the timing of eclogite facies metamorphism in the Alps: A working hypothesis, *Eclogae geol. Helv.*, *89*, 81–110.
- Froitzheim, N., D. Plasienka, and R. Schuster (2008), Alpine tectonics of the Alps and Western Carpathians, in *The geology of Central Europe: Mesozoic and Cenozoic*, edited by T. McCann, pp. 1141–1232, Geol. Soc. London.
- Fry, B., F. Deschamps, E. Kissling, L. Stehly, and D. Giardini (2010), Layered azimuthal anisotropy of Rayleigh wave phase velocities in the European Alpine lithosphere inferred from ambient noise, *Earth Planet. Sci. Lett.*, *297*(1–2), 95 – 102, doi: <http://dx.doi.org/10.1016/j.epsl.2010.06.008>.
- Fukao, Y. (1984), Evidence from core-reflected shear waves for anisotropy in the Earth's mantle, *Nature*, *309*(5970), 695–698.
- Funiciello, F., M. Moroni, C. Piromallo, C. Faccenna, A. Cenedese, and H. A. Bui (2006), Mapping mantle flow during retreating subduction: Laboratory models analyzed by feature tracking, *J. Geophys. Res.*, *111*(B3), doi:10.1029/2005JB003792.
- Gaherty, J. B. (2004), A surface wave analysis of seismic anisotropy beneath eastern North America, *Geophysical Journal International*, *158*(3), 1053–1066, doi:10.1111/j.1365-246X.2004.02371.x.
- Gebrande, H., E. Lüschen, M. Bopp, F. Bleibinhaus, B. Lammerer, O. Oncken, M. Stiller, J. Kummerow, R. Kind, K. Millahn, H. Grassl, F. Neubauer, L. Bertelli, D. Borrini, R. Fantoni, C. Pessina, M. Sella, A. Castellarin, R. Nicolich, A. Mazzotti, and M. Bernabini (2002), First deep seismic reflection images of the eastern Alps reveal giant crustal wedges and transcrustal ramps, *Geophys. Res. Lett.*, *29*(10), 92.1–92.4, doi:10.1029/2002GL014911.
- Genser, J., and F. Neubauer (1989), Low angle normal faults at the Eastern margin of the Tauern window (Eastern Alps), *Mitt. Österr. Geol. Ges.*, *81*, 233–243.
- Genser, J., J. D. van Wees, S. Cloetingh, and F. Neubauer (1996), Eastern Alpine tectono-metamorphic evolution: Constraints from two-dimensional P-T-t modeling, *Tectonics*, *15*(3), 584–604, doi:10.1029/95TC03289.
- Glodny, J., U. Ring, and A. Kühn (2008), Coeval high-pressure metamorphism, thrusting, strike-slip, and extensional shearing in the Tauern Window, Eastern Alps, *Tectonics*, *27*(4), doi:10.1029/2007TC002193.

- Grad, M., A. Guterch, G. R. Keller, T. Janik, E. Hegedűs, J. Vozár, A. Ślaczka, T. Tira, and J. Yliniemi (2006), Lithospheric structure beneath trans-Carpathian transect from Precambrian platform to Pannonian basin: CELEBRATION 2000 seismic profile CEL05, *Journal of Geophysical Research: Solid Earth* (1978–2012), 111(B3).
- Gripp, A. E., and R. G. Gordon (2002), Young tracks of hotspots and current plate velocities, *Geophys. J. Int.*, 150(2), 321–361, doi:10.1046/j.1365-246X.2002.01627.x.
- Gutdeutsch, R., and K. Aric (1987), Tectonic block models based on the seismicity in the east Alpine-Carpathians and Pannonian area, in *Geodynamics of the Eastern Alps*, edited by H. W. Flügl and P. F. (Ed.), pp. 309–324, F. Deuticke, Vienna.
- Haas, J., P. Mioč, J. Pamić, B. Tomljenović, P. Árkai, A. Bérczi-Makk, B. Koroknai, S. Kovács, and E. Rálich-Felgenhauer (2000), Complex structural pattern of the Alpine–Dinaridic–Pannonian triple junction, *International Journal of Earth Sciences*, 89(2), 377–389.
- Handy, M. R., S. M. Schmid, R. Bousquet, E. Kissling, and D. Bernoulli (2010), Reconciling plate-tectonic reconstructions of Alpine Tethys with the geological–geophysical record of spreading and subduction in the Alps, *Earth-Science Rev.*, 102(3–4), 121 – 158, doi:10.1016/j.earscirev.2010.06.002.
- Harangi, S., A. Novák, B. Kiss, I. Seghedi, R. Lukács, L. Szarka, V. Wesztergom, M. Metwaly, and K. Gribovszki (2015), Combined magnetotelluric and petrologic constrains for the nature of the magma storage system beneath the Late Pleistocene Ciomadul volcano (SE Carpathians), *Journal of Volcanology and Geothermal Research*, 290, 82–96.
- Hausegger, S., W. Kurz, R. Rabitsch, E. Kiechl, and F.-J. Brosch (2010), Analysis of the internal structure of a carbonate damage zone: Implications for the mechanisms of fault breccia formation and fluid flow, *Journal of Structural Geology*, 32, 1349–1362, doi:10.1016/j.jsg.2009.04.014.
- Hess, H. (1964), Seismic anisotropy of the uppermost mantle under oceans, *Nature*, 203, 629–631, doi:10.1038/203629a0.
- Hetényi, G., G. W. Stuart, G. A. Houseman, F. Horváth, E. Hegedűs, and E. Brückl (2009), Anomalous deep mantle transition zone below Central Europe: Evidence of lithospheric instability, *Geophysical Research Letters*, 36(21), doi:10.1029/2009GL040171, 121307.

- Hetényi, G., Y. Ren, B. Dando, G. W. Stuart, E. Hegedűs, A. C. Kovács, and G. A. Houseman (2015), Crustal structure of the Pannonian Basin: The AlCaPa and Tisza Terrains and the Mid-Hungarian Zone, *Tectonophysics*, *646*, 106–116.
- Hoernle, K., D. L. Abt, K. M. Fischer, H. Nichols, F. Hauff, G. A. Abers, P. van den Bogaard, K. Heydolph, G. Alvarado, M. Protti, and W. Strauch (2008), Arc-parallel flow in the mantle wedge beneath Costa Rica and Nicaragua, *Nature*, *451*(7182), 1094–1097, doi:10.1038/nature06550.
- Horváth, F., G. Bada, P. Szafián, G. Tari, A. Ádám, and S. Cloetingh (2006), Formation and deformation of the Pannonian Basin: constraints from observational data, *Geological Society, London, Memoirs*, *32*(1), 191–206, doi:10.1144/GSL.MEM.2006.032.01.11.
- Horváth, F., B. Musitz, A. Balázs, A. Végh, A. Uhrin, A. Nádor, B. Koroknai, N. Pap, T. Tóth, and G. Wórum (2015), Evolution of the Pannonian basin and its geothermal resources, *Geothermics*, *53*(0), 328 – 352, doi:http://dx.doi.org/10.1016/j.geothermics.2014.07.009.
- Horváth, F. (1988), Neotectonic behavior of the Alpine-Mediterranean Region, in *The Pannonian Basin: A Study in Basin Evolution/Book and Maps*, edited by L. Royden and F. Horváth, 394, pp. 49–55, American Association of Petroleum Geologists; Hungarian Geological Society.
- Horváth, F. (1993), Towards a mechanical model for the formation of the Pannonian basin, *Tectonophysics*, *226*(1), 333–357.
- Horváth, F., and C. Faccenna (2011), Understanding extension within a convergent orogen: initial results on seismic structure from the Carpathian Basins Project, in *EGU General Assembly*, EGU2011-8894-2, Vienna, Austria.
- Hoschek, G. (2001), Thermobarometry of metasediments and metabasites from the Eclogite zone of the Hohe Tauern, Eastern Alps, Austria, *Lithos*, *59*(3), 127–150, doi:doi:10.1016/S0024-4937(01)00063-9.
- Houseman, G., and G. Stuart (2011), Understanding Extension within a Convergent Orogen: Lithospheric Structure of the Pannonian Basin, *Scientific Report SEIS-UK loan: 795*, NERC Geophysical Equipment Facility.
- Houseman, G. A., and L. Gemmer (2007), Intra-orogenic extension driven by gravitational instability: Carpathian-Pannonian orogeny, *Geology*, *35*(12), 1135–1138, doi:10.1130/G23993A.1.

- Huisman, R. S., Y. Y. Podladchikov, and S. Cloetingh (2001), Dynamic modeling of the transition from passive to active rifting, application to the Pannonian Basin, *Tectonics*, *20*(6), 1021–1039, doi:10.1029/2001TC900010.
- Inger, S., and R. Cliff (1994), Timing of metamorphism in the Tauern Window, Eastern alps: Rb-Sr ages and fabric formation, *Journal of Metamorphic Geology*, *12*(5), 695–707, doi:10.1111/j.1525-1314.1994.tb00052.x.
- Ito, G., R. Dunn, A. Li, C. J. Wolfe, A. Gallego, and Y. Fu (2014), Seismic anisotropy and shear wave splitting associated with mantle plume-plate interaction, *Journal of Geophysical Research: Solid Earth*, *119*(6), 4923–4937.
- Ivan, M., M. Popa, and D. Ghica (2008), SKS splitting observed at Romanian broad-band seismic network, *Tectonophysics*, *462*, 89–98, doi:10.1016/j.tecto.2007.12.015.
- Jadamec, M. A., and M. I. Billen (2010), Reconciling surface plate motions with rapid three-dimensional mantle flow around a slab edge, *Nature*, *465*(7296), 338–341.
- Jones, A. G., J. Plomerova, T. Korja, F. Sodoudi, and W. Spakman (2010), Europe from the bottom up: A statistical examination of the central and northern European lithosphere–asthenosphere boundary from comparing seismological and electromagnetic observations, *Lithos*, *120*(1–2), 14 – 29, doi:http://dx.doi.org/10.1016/j.lithos.2010.07.013.
- Jung, H., I. Katayama, Z. Jiang, T. Hiraga, and S. Karato (2006), Effect of water and stress on the lattice-preferred orientation of olivine, *Tectonophysics*, *421*(1–2), 1 – 22, doi:http://dx.doi.org/10.1016/j.tecto.2006.02.011.
- Karato, S., H. Jung, I. Katayama, and P. Skemer (2008), Geodynamic Significance of Seismic Anisotropy of the Upper Mantle: New Insights from Laboratory Studies, *Annu. Rev. Earth Planet. Sci.*, *36*, 59–95, doi:10.1146/annurev.earth.36.031207.124120.
- Karato, S.-i. (1995), Effects of Water on Seismic Wave Velocities in the Upper Mantle, *Proceedings of the Japan Academy, Series B*, *71*(2), 61–66.
- Kázmér, M., and S. Kovács (1985), Permian-Paleogene paleogeography along the eastern part of the Insubric-Periadriatic lineament system: evidence for continental escape of the Bakony-Drauzug unit, *Acta Geologica Hungarica*, *28*(1-2), 71–84.



- Kissling, E., S. M. Schmid, R. Lippitsch, J. Ansorge, and B. Fugenschuh (2006), Lithosphere structure and tectonic evolution of the Alpine arc: new evidence from high-resolution teleseismic tomography, *Geol. Soc. London. Memoirs*, 32, 129–145, doi:10.1144/GSL.MEM.2006.032.01.08.
- Klébesz, R., Z. Grácz, G. Szanyi, N. Liptai, I. Kovács, L. Patkó, Z. Pintér, G. Falus, V. Wessztergom, and C. Szabó (2015), Constraints on the thickness and seismic properties of the lithosphere in an extensional setting (Nógrád-Gömör Volcanic Field, Northern Pannonian Basin), *Acta Geodaetica et Geophysica*, pp. 1–17, doi:10.1007/s40328-014-0094-0.
- Kneller, E. A., and P. E. van Keken (2007), Trench-parallel flow and seismic anisotropy in the Mariana and Andean subduction systems, *Nature*, 450(7173), 1222–1225, doi:10.1038/nature06429.
- Koulakov, I., M. K. Kaban, M. Tesauro, and S. Cloetingh (2009), P- and S-velocity anomalies in the upper mantle beneath Europe from tomographic inversion of ISC data, *Geophys. J. Int.*, 179(1), 345–366, doi:10.1111/j.1365-246X.2009.04279.x.
- Kovács, I., G. Falus, G. Stuart, K. Hidas, C. Szabó, M. Flower, E. Hegedűs, K. Posgay, and L. Zilahi-Sebess (2012a), Seismic anisotropy and deformation patterns in upper mantle xenoliths from the central Carpathian-Pannonian region: Asthenospheric flow as a driving force for Cenozoic extension and extrusion?, *Tectonophysics*, 514–517, 168–179, doi:10.1016/j.tecto.2011.10.022.
- Kovács, I., A. Rosenthal, H. S. C. O'Neill, W. O. Hibberson, and B. Udvardi (2012b), An Experimental Study of Water in Nominally Anhydrous Minerals in the Upper Mantle near the Water-saturated Solidus, *J. Petrol.*, 53(10), 2067–2093, doi:10.1093/petrology/egs044.
- Kovács, I., and C. Szabó (2008), Middle Miocene volcanism in the vicinity of the Middle Hungarian zone: evidence for an inherited enriched mantle source, *Journal of Geodynamics*, 45(1), 1–17.
- Kovács, I., L. Csontos, C. Szabó, E. Bali, G. Falus, K. Benedek, and Z. Zajacz (2007), Paleogene–early Miocene igneous rocks and geodynamics of the Alpine-Carpathian-Pannonian-Dinaric region: An integrated approach, *Geological Society of America Special Papers*, 418, 93–112.

- Kovács, S., T. Szederkényi, J. Haas, G. Buda, G. Császár, and A. Nagymarosy (2000), In the pre-Neogene basement of the Hungarian part of the Pannonian area, *Acta Geologica Hungarica*, 43(3), 225–328.
- Kozur, H. (1991), The evolution of the Meliata-Hallstatt ocean and its significance for the early evolution of the Eastern Alps and Western Carpathians, *Palaeogeogr. Palaeoclimatol. Palaeoecol.*, 87(1–4), 109 – 135, doi:[http://dx.doi.org/10.1016/0031-0182\(91\)90132-B](http://dx.doi.org/10.1016/0031-0182(91)90132-B).
- Krézsek, C., and A. W. Bally (2006), The Transylvanian Basin (Romania) and its relation to the Carpathian fold and thrust belt: Insights in gravitational salt tectonics, *Marine and Petroleum Geology*, 23(4), 405–442.
- Kummerow, J., and R. Kind (2006), Shear wave splitting in the Eastern Alps observed at the TRANSALP network, *Tectonophysics*, 414(1–4), 117–125, doi:10.1016/j.tecto.2005.10.023.
- Kummerow, J., R. Kind, O. Oncken, P. Giese, T. Ryberg, K. Wylegalla, and F. Scherbaum (2004), A natural and controlled source seismic profile through the Eastern Alps: TRANSALP, *Earth and Planetary Science Letters*, 225(1–2), 115 – 129, doi:<http://dx.doi.org/10.1016/j.epsl.2004.05.040>.
- Kurz, W. (2005), Tectonic map and overall architecture of the Alpine orogen: Comment., *Eclogae geol. Helv.*, 98, 97–98.
- Kurz, W. (2006), Penninic Paleogeography from the Western toward the Eastern Alps - Still Open Questions?, *International Geology Review*, 48, 996–1022.
- Kurz, W., and N. Froitzheim (2002), The Exhumation of Eclogite-Facies Metamorphic Rocks-a Review of Models Confronted with Examples from the Alps, *International Geology Review*, 44(12), 1163–1164, doi:10.2747/0020-6814.44.12.1163.
- Kurz, W., and F. Neubauer (1996), Deformation partitioning and shear localization during the updoming of the Sonnblick area in the Tauern Window (Eastern Alps, Austria), *J. Struct. Geol.*, 18, 1327–1343.
- Kurz, W., F. Neubauer, H. Genser, and H. Horner (1994), Sequence of Tertiary brittle deformations in the eastern Tauern Window (Eastern Alps), *Mitt. Österr. Geol. Ges.*, 86(1993), 153–164.

- Kurz, W., F. Neubauer, and J. Genser (1996), Kinematics of Penninic nappes (Glockner Nappe and basement-cover nappes) in the Tauern Window (Eastern Alps, Austria), during subduction and Penninic-Austroalpine collision, *Eclogae geol. Helv.*, *89*, 573–605.
- Kurz, W., F. Neubauer, J. Genser, and E. Dachs (1998), Alpine geodynamic evolution of passive and active continental margin sequences in the Tauern Window (eastern Alps, Austria, Italy): a review, *Geologische Rundschau*, *87*(2), 225–242, doi:10.1007/s005310050204.
- Kurz, W., F. Neubauer, J. Genser, W. Unzog, and E. Dachs (2001), Tectonic evolution of Penninic Units in the Tauern Window during the Paleogene: Constraints from structural and metamorphic geology, in *Paleogene of the Eastern Alps*, vol. 14, edited by W. E. Piller and M. W. Rasser, pp. 347–375, Österr. Akad. Wiss., Schriftenr. Erdwiss. Komm.
- Kurz, W., E. Jansen, R. Hundenborn, J. Pleuger, W. Schäfer, and W. Unzog (2004), Microstructures and crystallographic preferred orientations of omphacite in Alpine eclogites: implications for the exhumation of (ultra-) high-pressure units, *Journal of Geodynamics*, *37*(1), 1–55, doi:http://dx.doi.org/10.1016/j.jog.2003.10.001.
- Kurz, W., R. Handler, and C. Bertoldi (2008), Tracing the exhumation of the Eclogite Zone (Tauern Window, Eastern Alps) by  $^{40}\text{Ar}/^{39}\text{Ar}$  dating of white mica in eclogites, *Swiss Journal of Geosciences*, *101*(1), 191–206, doi:10.1007/s00015-008-1281-1.
- Lammerer, B., and M. Weger (1998), Footwall uplift in an orogenic wedge: the Tauern Window in the Eastern Alps of Europe, *Tectonophysics*, *285*(3–4), 213 – 230, doi: http://dx.doi.org/10.1016/S0040-1951(97)00272-2.
- Lave, J., J. Avouac, R. Lacassin, P. Tapponnier, and J. Montagner (1996), Seismic anisotropy beneath Tibet: Evidence for eastward extrusion of the Tibetan lithosphere?, *Earth Planet. Sci. Lett.*, *140*(1), 83–96.
- Legendre, C. P., T. Meier, S. Lebedev, W. Friederich, and L. Viereck-Götte (2012), A shear wave velocity model of the European upper mantle from automated inversion of seismic shear and surface waveforms, *Geophys. J. Int.*, *191*(1), 282–304, doi:10.1111/j.1365-246X.2012.05613.x.
- Lev, E., M. Long, and R. V. der Hilst (2006), Seismic anisotropy in eastern Tibet from shear-wave splitting reveals changes in lithosphere deformation, *Earth Planet. Sci. Lett.*, *251*, 293–304, doi:10.1016/j.epsl.2006.09.018.

- Levin, V., W. Menke, and J. Park (1999), Shear wave splitting in the appalachians and the Urals: A case for multilayered anisotropy, *J. Geophys. Res.*, *104*(B8), 17,975–17,993.
- Lippitsch, R., E. Kissling, and J. Ansorge (2003), Upper mantle structure beneath the Alpine orogen from high-resolution tomography, *J. Geophys. Res.*, *108*(B8), 2376, doi:10.1029/2002JB002016.
- Long, M., and T. Becker (2010), Mantle dynamics and seismic anisotropy, *Earth Planet. Sci. Lett.*, *297*, 341–354, doi:10.1016/j.epsl.2010.06.036.
- Long, M., and P. Silver (2009), Shear wave splitting and mantle anisotropy: Measurements, interpretations, *Surv Geophys*, *30*, 407–461, doi:10.1007/s10712-009-9075-1.
- Long, M., and R. van der Hilst (2005), Shear wave splitting from local events beneath the Ryukyu arc: Trench-parallel anisotropy in the mantle wedge, *Phys. Earth Planet. Inter.*, *155*, 300–312, doi:10.1016/j.pepi.2006.01.003.
- Lüschen, E., D. Borrini, H. Gebrande, B. Lammerer, K. Millahn, F. Neubauer, and R. Nicolich (2006), TRANSALP—deep crustal Vibroseis and explosive seismic profiling in the Eastern Alps, *Tectonophysics*, *414*(1–4), 9 – 38, doi:http://dx.doi.org/10.1016/j.tecto.2005.10.014.
- Mainprice, D. (1990), A FORTRAN program to calculate seismic anisotropy from the lattice preferred orientation of minerals, *Computers & Geosciences*, *16*(3), 385–393.
- Mainprice, D., G. Barruol, and W. Ben Ismail (2000), The seismic anisotropy of the Earth's mantle: From single crystal to polycrystal, in *Composition, Structure and Dynamics of the Lithosphere–Asthenosphere System*, *Geophys. Monogr. Ser.*, vol. 117, edited by S. Karato, A. Forte, R. Liebermann, G. Masters, and L. Stixrude, p. 237, AGU.
- Margheriti, L., C. Nostro, M. Cocco, and A. Amato (1996), Seismic anisotropy beneath the northern Apennines (Italy) and its tectonic implications, *Geophys. Res. Lett.*, *23*, 2721–2724.
- Margheriti, L., F. Lucente, and S. Pondrelli (2003), SKS splitting measurements in the Apenninic-Tyrrhenian domain (Italy) and their relation with lithospheric subduction and mantle convection, *J. Geophys. Res.*, *108*(B4), 2218, doi:10.1029/2002JB001793.

- Marone, F., S. van der Lee, and D. Giardini (2004), Shallow anisotropy in the Mediterranean mantle from surface waves, *Geophys. Res. Lett.*, *31*(6), L06,624, doi:10.1029/2003GL018948.
- Márton, E. (1987), Palaeomagnetism and tectonics in the Mediterranean region, *Journal of Geodynamics*, *7*(1), 33–57.
- Márton, E. (2001), Tectonic implications of Tertiary paleomagnetic results from the PANCARDI area (Hungarian contribution), *Acta Geologica Hungarica*, *44*(2), 135–144.
- Matenco, L., and D. Radivojević (2012), On the formation and evolution of the Pannonian Basin: Constraints derived from the structure of the junction area between the Carpathians and Dinarides, *Tectonics*, *31*(6), n/a–n/a, doi:10.1029/2012TC003206, tC6007.
- Maupin, V., and J. Park (2007), Theory and Observations - Wave Propagation in Anisotropic Media, in *Treatise on Geophysics*, edited by G. Schubert, chap. 1.09, pp. 289–321, Elsevier, Amsterdam.
- Mauritsch, H. J., and W. Frisch (1980), Palaeomagnetic results from the eastern Alps and their comparison with data from the southern Alps and the Carpathians, *Mitt. Österr. Geol. Ges.*, *73*, 5–13.
- Meulenkamp, J., M. Kováč, and I. Cicha (1996), On Late Oligocene to Pliocene depocentre migrations and the evolution of the Carpathian-Pannonian system, *Tectonophysics*, *266*(1), 301–317.
- Mitterbauer, U., M. Behm, E. Brückl, R. Lippitsch, A. Guterch, G. Keller, E. Koslovskaya, E. Rumpfhuber, and F. Sumanovac. (2011), Shape and origin of the East-Alpine slab constrained by the ALPASS teleseismic model, *Tectonophysics*, *510*(1), 195–206, doi:10.1016/j.tecto.2011.07.001.
- Nagel, T., D. Herwartz, S. Rexroth, C. Münker, N. Froitzheim, and W. Kurz (2013), Lu–Hf dating, petrography, and tectonic implications of the youngest Alpine eclogites (Tauern Window, Austria), *Lithos*, *170–171*, 179 – 190, doi:http://dx.doi.org/10.1016/j.lithos.2013.02.008.
- Nakajima, J., and A. Hasegawa (2004), Shear-wave polarization anisotropy and subduction-induced flow in the mantle wedge of northern Japan, *Earth Planet. Sci. Lett.*, *225*, 365–377, doi:10.1016/j.epsl.2004.06.011.

- Németh, B., K. Török, I. Kovács, C. Szabó, R. Abart, J. Dégi, J. Mihály, and C. Németh (2015), Melting, fluid migration and fluid-rock interactions in the lower crust beneath the Bakony-Balaton Highland volcanic field: a silicate melt and fluid inclusion study, *Mineralogy and Petrology*, 109(2), 217–234, doi:10.1007/s00710-015-0366-6.
- Neubauer, F., J. Genser, W. Kurz, and X. Wang (1999), Exhumation of the Tauern window, Eastern Alps, *Physics and Chemistry of the Earth, Part A: Solid Earth and Geodesy*, 24(8), 675 – 680, doi:http://dx.doi.org/10.1016/S1464-1895(99)00098-8.
- Nicolas, A. (1993), Why fast polarization directions of SKS seismic waves are parallel to mountain belts, *Phys. Earth Planet. Inter.*, 78(3-4), 337–342.
- Nicolas, A., and N. Christensen (1987), Formation of anisotropy in upper mantle peridotites: A review, in *Composition, Structure and Dynamics of the Lithosphere–Asthenosphere System, Geodynamics series.*, vol. 16, edited by K. Fuchs and C. Froidevaux, p. 111, AGU, Washington, D.C.
- Nocquet, J.-M., and E. Calais (2003), Crustal velocity field of western Europe from permanent GPS array solutions, 1996–2001, *Geophys. J. Int.*, 154(1), 72–88, doi:10.1046/j.1365-246X.2003.01935.x.
- Nocquet, J.-M., and E. Calais (2004), Geodetic Measurements of Crustal Deformation in the Western Mediterranean and Europe, *Pure Appl. Geophys.*, 161(3), 661–681, doi:10.1007/s00024-003-2468-z.
- Norris, R. J., E. R. Oxburgh, R. A. Cliff, and R. C. Wright (1971), Structure (the Eastern Alps), in *Structural, Metamorphic and Geochronological Studies in the Rieseck and Southern Ankogel Groups, the Eastern Alps*, vol. 114, edited by E. R. Oxburgh, Jahrb. Geol. B.-A., Wien.
- Okay, N., T. Zack, A. I. Okay, and M. Barth (2011), Sinistral transport along the Trans-European Suture Zone: detrital zircon–rutile geochronology and sandstone petrography from the Carboniferous flysch of the Pontides, *Geological Magazine*, 148(03), 380–403.
- Okaya, N., S. Cloetingh, and S. Mueller (1996), A lithospheric cross-section through the Swiss Alps—II. Constraints on the mechanical structure of a continent-continent collision zone, *Geophysical Journal International*, 127(2), 399–414, doi:10.1111/j.1365-246X.1996.tb04729.x.

- Park, J., and V. Levin (2002), Seismic anisotropy: Tracing plate dynamics in the mantle, *Science*, *296*, 485–489.
- Pécskay, Z., O. Edelstein, I. Seghedi, A. Szakacs, M. Kovacs, M. Crihan, and A. Bernad (1995), K-Ar datings of Neogene-Quaternary calc-alkaline volcanic rocks in Romania, *Acta Vulcanologica*, *7*, 53–62.
- PecsKay, Z., J. Lexa, A. Szakacs, I. Seghedi, K. Balogh, V. Konecny, T. Zelenka, M. Kovacs, T. Poka, A. Fulop, et al. (2006), Geochronology of Neogene magmatism in the Carpathian arc and intra-Carpathian area, *GEOLOGICA CARPATHICA-BRATISLAVA*-, *57*(6), 511.
- Piomallo, C., and C. Faccenna (2004), How deep can we find the traces of Alpine subduction?, *Geophys. Res. Lett.*, *31*(6), doi:10.1029/2003GL019288.
- Piomallo, C., and C. Morelli (2003), P wave tomography of the mantle under the Alpine-Mediterranean area, *J. Geophys. Res.*, *108*(B2), 2065, doi:10.1029/2002JB001757.
- Plomerová, J., and V. Babuška (2010), Long memory of mantle lithosphere fabric—European LAB constrained from seismic anisotropy, *Lithos*, *120*(1), 131–143.
- Plomerová, J., M. Granet, S. Judenherc, U. Achauer, V. Babuška, P. Jedlička, D. Kouba, and L. Vecsey (2000), Temporary Array Data for Studying Seismic Anisotropy of Variscan Massifs – The Armorican Massif, French Massif Central And Bohemian Massif, *Studia Geophysica et Geodaetica*, *44*(2), 195–209, doi:10.1023/A:1022110809240.
- Plomerova, J., L. Margheriti, J. Park, V. Babuska, S. Pondrelli, L. Vecsey, D. Piccinini, V. Levin, P. Baccheschi, and S. Salimbeni (2006), Seismic anisotropy beneath the Northern Apennines (Italy): mantle flow or lithosphere fabric?, *Earth Planet. Sci. Lett.*, *247*, 157–170, doi:10.1016/j.epsl.2006.04.023.
- Plomerova, J., L. Vecsey, and V. Babuska (2012), Mapping seismic anisotropy of the lithospheric mantle beneath the Northern and Eastern Bohemian Massif (Central Europe), *Tectonophysics*, *564-565*, 38–53, doi:10.1016/j.tecto.2011.08.011.
- Posgay, K., T. Bodoky, E. Hegedüs, S. Kovácsvölgyi, L. Lenkey, P. Szafián, E. Takács, Z. Tímár, and G. Varga (1995), Asthenospheric structure beneath a Neogene basin in southeast Hungary, *Tectonophysics*, *252*(1–4), 467 – 484, doi:http://dx.doi.org/10.1016/0040-1951(95)00098-4.



- Prosser, G. (1998), Strike-slip movements and thrusting along a transpressive fault zone: The North Giudicarie line (Insubric line, northern Italy), *Tectonics*, *17*(6), 921–937, doi:10.1029/1998TC900010.
- Qorbani, E., G. Bokelmann, I. Kovács, and G. Falus (2014), Anisotropic structure of the upper mantle in the Carpathian-Pannonian region: From SKS splitting data and xenolith constraints, in *AGU fall Meeting 2014*, San Francisco, USA, dI33A-4295.
- Qorbani, E., I. Bianchi, and G. Bokelmann (2015a), Slab detachment under the Eastern Alps seen by seismic anisotropy, *Earth Planet. Sci. Lett.*, *409*(0), 96 – 108, doi:http://dx.doi.org/10.1016/j.epsl.2014.10.049.
- Qorbani, E., W. Kurz, I. Bianchi, and G. Bokelmann (2015b), Correlated crustal and mantle deformation in the Tauern Window, Eastern Alps, *Austrian Journal of Earth Science*, *108*(2).
- Ranalli, G. (1995), *Rheology of the Earth*, Springer Science & Business Media.
- Ratschbacher, L., W. Frisch, H.-G. Linzer, and O. Merle (1991), Lateral extrusion in the eastern Alps, part II: Structural analysis, *Tectonics*, *10*(2), 257–271, doi:10.1029/90TC02623.
- Ratschbacher, L., O. Merle, P. Davy, and P. Cobbold (1991a), Lateral extrusion in the eastern Alps, part I: Boundary conditions and experiments scaled for gravity, *Tectonics*, *10*, 245–256, doi:10.1029/90TC02622.
- Reddy, S., R. Cliff, and R. East (1993), Thermal history of the Sonnblick Dome, south-east Tauern Window, Austria: Implications for heterogeneous uplift within the Pennine basement, *Geologische Rundschau*, *82*(4), 667–675, doi:10.1007/BF00191494.
- Ren, Y., G. Stuart, G. Houseman, B. Dando, C. Ionescu, E. Hegedüs, S. Radovanović, and Y. Shen (2012), Upper mantle structures beneath the Carpathian–Pannonian region: Implications for the geodynamics of continental collision, *Earth and Planetary Science Letters*, *349–350*, 139 – 152, doi:http://dx.doi.org/10.1016/j.epsl.2012.06.037.
- Robl, J., and K. Stüwe (2005), Continental collision with finite indenter strength: 1. Concept and model formulation, *Tectonics*, *24*(4), TC4005, doi:10.1029/2004TC001727.
- Rosenberg, C., J.-P. Brun, and D. Gapais (2004), Indentation model of the Eastern Alps and the origin of the Tauern Window, *Geology*, *32*(11), 997–1000, doi:10.1130/G20793.1.

- Rosenberg, C. L., J.-P. Brun, F. Cagnard, and D. Gapais (2007), Oblique indentation in the Eastern Alps: Insights from laboratory experiments, *Tectonics*, *26*(2), doi:10.1029/2006TC001960.
- Royden, L. (1996), Coupling and decoupling of crust and mantle in convergent orogens: Implications for strain partitioning in the crust, *Journal of Geophysical Research: Solid Earth*, *101*(B8), 17,679–17,705, doi:10.1029/96JB00951.
- Royden, L., and T. Baldi (1988), Early Cenozoic tectonics and paleogeography of the Pannonian and surrounding regions, in *The Pannonian Basin: A Study in Basin Evolution*, vol. 45, edited by L. Royden and F. Horvath, pp. 1–16, AAPG Memoir.
- Rümpker, G., A. Tommasi, and J.-M. Kendall (1999), Numerical simulations of depth-dependent anisotropy and frequency-dependent wave propagation effects, *J. Geophys. Res.*, *104*(B10), 23,141–23,153, doi:10.1029/1999JB900203.
- Salimbeni, S., S. Pondrelli, L. Margheriti, J. Park, and V. Levin (2008), SKS splitting measurements beneath Northern Apennines region: a case of oblique trench retreat, *Tectonophysics*, *462*, 68–82, doi:10.1016/j.tecto.2007.11.075.
- Salimbeni, S., S. Pondrelli, and L. Margheriti (2013), Hints on the deformation penetration induced by subductions and collision processes: Seismic anisotropy beneath the Adria region (Central Mediterranean), *J. Geophys. Res.*, *118*(11), 5814–5826, doi:10.1002/2013JB010253.
- Savage, M. (1999), Seismic anisotropy and mantle deformation: What have we learned from shear wave splitting?, *Rev. Geophys.*, *37*, 65–106.
- Scharf, A., M. Handy, S. Favaro, S. Schmid, and A. Bertrand (2013), Modes of orogen-parallel stretching and extensional exhumation in response to microplate indentation and roll-back subduction (Tauern Window, Eastern Alps), *International Journal of Earth Sciences*, *102*(6), 1627–1654, doi:10.1007/s00531-013-0894-4.
- Schmid, S., B. Fugenschuh, E. Kissling, and R. Schuster (2004), Tectonic map and overall architecture of the Alpine orogen, *Eclogae Geol. Helv.*, *97*, 93–117, doi:10.1007/s00015-004-1113-x.
- Schmid, S., D. Bernoulli, B. Fugenschuh, L. Matenco, S. Schefer, R. Schuster, M. Tischer, and K. Ustaszewski (2008), The Alpine-Carpathian-Dinaridic orogenic system: correlation and evolution of tectonic units, *Swiss Journal of Geosciences*, *101*(1), 139–183, doi:10.1007/s00015-008-1247-3.

- Schmid, S., A. Scharf, M. Handy, and C. Rosenberg (2013), The Tauern Window (Eastern Alps, Austria): a new tectonic map, with cross-sections and a tectonometamorphic synthesis, *Swiss Journal of Geosciences*, *106*(1), 1–32, doi:10.1007/s00015-013-0123-y.
- Schmid, S. M., and E. Kissling (2000), The arc of the western Alps in the light of geophysical data on deep crustal structure, *Tectonics*, *19*(1), 62–85, doi:10.1029/1999TC900057.
- Selverstone, J. (1988), Evidence for east-west crustal extension in the Eastern Alps: Implications for the unroofing history of the Tauern window, *Tectonics*, *7*(1), 87–105, doi:10.1029/TC007i001p00087.
- Serpelloni, E., C. Faccenna, G. Spada, D. Dong, and S. D. P. Williams (2013), Vertical GPS ground motion rates in the Euro-Mediterranean region: New evidence of velocity gradients at different spatial scales along the Nubia-Eurasia plate boundary, *J. Geophys. Res.*, *118*(11), 6003–6024, doi:10.1002/2013JB010102.
- Silver, P. (1996), Seismic anisotropy beneath the continents: probing the depths of geology, *Annu. Rev. Earth Planet. Sci.*, *24*, 385–432.
- Silver, P. G., and W. Chan (1988), Implications for Continental Structure and Evolution from Seismic Anisotropy, *Nature*, *335*(6185), 34–39, doi:{10.1038/335034a0}.
- Silver, P. G., and W. W. Chan (1991), Shear wave splitting and subcontinental mantle deformation, *J. Geophys. Res.*, *96*(B10), 16,429–16,454.
- Silver, P. G., and M. K. Savage (1994), The interpretation of shear-wave splitting parameters in the presence of two anisotropic layers, *Geophysical Journal International*, *119*(3), 949–963, doi:10.1111/j.1365-246X.1994.tb04027.x.
- Smith, G. P., and G. Ekström (1999), A global study of pn anisotropy beneath continents, *Journal of Geophysical Research: Solid Earth*, *104*(B1), 963–980, doi:10.1029/1998JB900021.
- Stampfli, G. (1994), Exotic terrains in the Alps: A solution for a single Jurassic ocean, *Schweiz. mineral. petrogr. Mitt.*, *74*, 449–452.
- Stegena, L., B. Geczy, and F. Horváth (1975), Late Cenozoic evolution of the Pannonian basin, *Tectonophysics*, *26*(1), 71–90.
- Stuart, G., G. Houseman, B. Dando, E. Hegedüs, E. Brückl, S. Radovanovic, G. Falus, A. Kovács, H. Hausmann, and A. Brisbane (2007), Understanding extension within

- a convergent orogen: initial results on seismic structure from the Carpathian Basins Project, in *AGU Fall Meeting 2007*, S41A-0235, San Francisco, CA, USA.
- Szabó, C., S. Harangi, and L. Csontos (1992), Review of Neogene and Quaternary volcanism of the Carpathian-Pannonian region, *Tectonophysics*, *208*(1), 243–256.
- Szafián, P., and F. Horváth (2006), Crustal structure in the Carpatho-Pannonian region: insights from three-dimensional gravity modelling and their geodynamic significance, *International Journal of Earth Sciences*, *95*(1), 50–67.
- Tari, G., T. Báldi, and M. Báldi-Beke (1993), Paleogene retroarc flexural basin beneath the Neogene Pannonian Basin: a geodynamic model, *Tectonophysics*, *226*(1), 433–455.
- Tari, G., P. Dövényi, I. Dunkl, F. Horváth, L. Lenkey, M. Stefanescu, P. Szafián, and T. Tóth (1999), Lithospheric structure of the Pannonian basin derived from seismic, gravity and geothermal data, *Geological Society, London, Special Publications*, *156*(1), 215–250.
- Tommasi, A., B. Tikoff, and A. Vauchez (1999), Upper mantle tectonics: three-dimensional deformation, olivine crystallographic fabrics and seismic properties, *Earth and Planetary Science Letters*, *168*(1–2), 173 – 186, doi:[http://dx.doi.org/10.1016/S0012-821X\(99\)00046-1](http://dx.doi.org/10.1016/S0012-821X(99)00046-1).
- Tommasi, A., D. Mainprice, G. Canova, and Y. Chastel (2000), Viscoplastic self-consistent and equilibrium-based modeling of olivine lattice preferred orientations: Implications for the upper mantle seismic anisotropy, *Journal of Geophysical Research: Solid Earth*, *105*(B4), 7893–7908, doi:10.1029/1999JB900411.
- Török, K. (1995), Garnet breakdown reaction and fluid inclusions in a garnet-clinopyroxenite xenolith from Szentbékállya (Balaton-Highland, Western Hungary), *Acta Vulcanologica*, *7*, 285–290.
- Török, K., B. Németh, F. Koller, J. Dégi, E. Badenszki, C. Szabó, and A. Mogessie (2014), Evolution of the middle crust beneath the western Pannonian Basin: a xenolith study, *Mineralogy and Petrology*, *108*(1), 33–47, doi:10.1007/s00710-013-0287-1.
- Ustaszewski, K., S. Schmid, B. Fügenschuh, M. Tischler, E. Kissling, and W. Spakman (2008), A map-view restoration of the Alpine-Carpathian-Dinaridic system for the Early Miocene, *Swiss Journal of Geosciences*, *101*(1), 273–294, doi:10.1007/s00015-008-1288-7.

- Van Bemmelen, R. (1973), Geodynamic models for the Alpine type of orogeny (Test-case II: The Alps in Central Europe), *Tectonophysics*, 18(1), 33–79.
- Vauchez, A., A. Tommasi, and E.-S. Marcos (1994), Self-indentation of a heterogeneous continental lithosphere, *Geology*, 22(11), 967–970, doi:10.1130/0091-7613(1994)022<0967:SIOAHC>2.3.CO;2.
- Vecsey, L., J. Plomerová, and V. Babuška (2008), Shear-wave splitting measurements — Problems and solutions, *Tectonophysics*, 462(1–4), 178 – 196, doi:http://dx.doi.org/10.1016/j.tecto.2008.01.021.
- Vinnik, L., V. Krishna, R. Kind, P. Bormann, and K. Stammer (1994), Shear wave splitting in the records of the German Regional Seismic Network, *Geophys. Res. Lett.*, 21(6), 457–460.
- Vinnik, L., G. Kosarev, and L. Makeeva (1984), Lithosphere Anisotropy from the Observation of SKS and SKKS Waves, *Doklady Akademii Nauk SSSR*, 278(6), 1335–1339.
- Vinnik, L. P., L. I. Makeyevaand, A. Milev, and A. Y. Usenko (1992), Global patterns of azimuthal anisotropy and deformations in the continental mantle, *Geophysical Journal International*, 111(3), 433–447, doi:10.1111/j.1365-246X.1992.tb02102.x.
- von Blanckenburg, F., and J. H. Davies (1995), Slab breakoff: A model for syn-collisional magmatism and tectonics in the Alps, *Tectonics*, 14(1), 120–131, doi:10.1029/94TC02051.
- Walker, K. T., A. A. Nyblade, S. L. Klemperer, G. H. R. Bokelmann, and T. J. Owens (2004), On the relationship between extension and anisotropy: Constraints from shear wave splitting across the East African Plateau, *J. Geophys. Res.*, 109(B8), doi:10.1029/2003JB002866.
- Walker, K. T., G. H. R. Bokelmann, S. L. Klemperer, and G. Bock (2005a), Shear-wave splitting around the Eifel hotspot: evidence for a mantle upwelling, *Geophys. J. Int.*, 163(3), 962–980, doi:10.1111/j.1365-246X.2005.02636.x.
- Wessel, P., and W. H. F. Smith (1998), New improved version of the Generic Mapping Tools released, *Trans. Am. Geophys. Union*, 79, 579.
- Wiejacz, P. (2001), Shear wave splitting across Tornquist-Teisseyre zone in Poland, *Journal of the Balkan Geophysical Society*, 4(4), 91–100.

- Willingshofer, E., and S. Cloetingh (2003), Present-day lithospheric strength of the Eastern Alps and its relationship to neotectonics, *Tectonics*, *22*(6), doi:10.1029/2002TC001463.
- Willingshofer, E., D. Sokoutis, S. Luth, F. Beekman, and S. Cloetingh (2013), Subduction and deformation of the continental lithosphere in response to plate and crust-mantle coupling, *Geology*, *41*(12), 1239–1242.
- Wilson, M., and H. Downes (1992), Mafic alkaline magmatism associated with the European Cenozoic rift system, *Tectonophysics*, *208*(1), 173–182.
- Wortel, M. J. R., and W. Spakman (2000), Subduction and Slab Detachment in the Mediterranean-Carpathian Region, *Science*, *290*(5498), 1910–1917, doi:10.1126/science.290.5498.1910.
- Wüstefeld, A. (2007), Methods and applications of shear wave splitting: The East European Craton, Ph.D. thesis, Universite Montpellier 2 Sciences et Techniques du Languedoc.
- Wüstefeld, A., and G. Bokelmann (2007), Null detection in shear-wave splitting measurements, *Bull. Seismol. Soc. Am.*, *97*(4), 1204–1211, doi:10.1785/0120060190.
- Wüstefeld, A., G. Bokelmann, C. Zaroli, and G. Barruol (2008), SplitLab: A shear-wave splitting environment in Matlab, *Comput. Geosci.*, *34*, 515–528.
- Wüstefeld, A., G. Bokelmann, G. Barruol, and J.-P. Montagner (2009), Identifying global seismic anisotropy patterns by correlating shear-wave splitting and surface-wave data, *Physics of the Earth and Planetary Interiors*, *176*(3–4), 198 – 212, doi:http://dx.doi.org/10.1016/j.pepi.2009.05.006.
- Zhang, S., and S.-i. Karato (1995), Lattice preferred orientation of olivine aggregates deformed in simple shear, *Nature*, *375*(6534), 774–777.
- Ziegler, P. A., and P. Dèzes (2006), Crustal evolution of Western and Central Europe, *Geological Society, London, Memoirs*, *32*(1), 43–56, doi:10.1144/GSL.MEM.2006.032.01.03.

# Curriculum Vitae

### Personal Information

Full name Ehsan Qorbani Chegeni  
Date of birth 23 August 1979, in Iran  
Address Department of Meteorology and Geophysics (IMGW), University of Vienna  
Althanstrasse 14, UZA II, 2D506, 1090 Vienna, Austria  
Phone +43-699-110-69102; +43-1-4277-53727  
Email ehsan.qorbani@univie.ac.at; eqorbani@gmail.com

### Education

2012–2015 **Ph.D. in Geophysics-Seismology**, *University of Vienna*, Vienna, Austria.  
2005–2007 **MSc. in Geophysics-Seismology**, *Institute for Advanced Studies in Basic Sciences (IASBS)*, Zanzan, Iran.  
1998–2004 **Bachelor of Science**, *Material Engineering*, Isfahan, Iran.

### Research

**Key words:** Seismology, Tectonics and deformation mechanisms, Seismic anisotropy, Shear-wave splitting, Velocity tomography, Inverse problems, Seismicity.

- PhD, 2015: University of Vienna - Geological and Geophysical Institute of Hungary.  
Research study on deep deformation pattern and anisotropic structure beneath the Pannonian basin by utilizing the shear-wave (SKS) splitting method. Using the anisotropy measurements together with the petrological indicators of deformation in basalt-hosted upper mantle xenoliths from the Pannonian basin.  
Adviser: Götz Bokelmann
- PhD, 2014: IMGW, University of Vienna.  
Anisotropy analysis on the upper mantle structure under the Eastern Alps by means of seismic anisotropy. Modeling of the vertical variations of the splitting parameters in terms of two layers of anisotropy.  
Adviser: Götz Bokelmann
- PhD, 2014: University of Vienna - Karl-Franzens-University of Graz.  
Study of coupling between crust and mantle in the Tauern Window area of the Eastern Alps. Measurements of the upper mantle anisotropy (deformation signatures) were compared with the kinematic data as the indicators of crustal deformation.  
Advisers: Götz Bokelmann, Walter Kurz
- M.Sc., 2007 Institute for Advanced Studies in Basic Sciences  
Seismic velocity tomography of the Tehran region, Iran. Relocating the local events by re-picking the crustal phases. Performing a joint inversion approach of the travel times and event locations simultaneously. Analyzing the local seismicity.  
Advisers: Abdolreza Ghods, Farhad Sobouti



---

## Publication

- **Qorbani, E.**, I. Bianchi, G. Bokelmann, 2015a Slab detachment under the Eastern Alps seen by seismic anisotropy, Earth and Planetary Science Letters, doi: 10.1016/j.epsl.2014.10.049.
- **Qorbani, E.**, W. Kurz, I. Bianchi, G. Bokelmann, 2015b, Correlated crustal and mantle deformation in the Tauern Window, Eastern Alps, Austrian Journal of Earth Science, 108/1.
- Bokelmann, G., **E. Qorbani**, I. Bianchi, 2013, Seismic anisotropy and large-scale deformation of the Eastern Alps, Earth and Planetary Science Letters, doi:10.1016/j.epsl.2013.09.019.
- **Qorbani, E.**, G. Bokelmann, I. Kovács, F. Horávth, G. Falus, Deep deformation pattern for the Carpathian-Pannonian region, submitted to Journal of Geophysical Research.
- Fuchs, F., P. Kolinsky, G. Gröschl, M.T. Apoloner, **E. Qorbani**, F. Schneider, G. Bokelmann, 2015, Site selection for a countrywide temporary network in Austria: Noise analysis and preliminary performance, Adv. Geosci, 41, 25-33, doi:10.5194/adgeo-41-25-2015.
- Bianchi, I., M. Anselmi, M.T. Apoloner, **E. Qorbani**, K. Gribovski, G. Bokelmann, 2015, The installation campaign of 9 seismic stations around the KTB site to test anisotropy detection by the Receiver Function Technique, Adv. Geosci, 41, 11-23, doi:10.5194/adgeo-41-11-2015.

---

## Experience

### Field work

- SEISMIC STATION DEPLOYMENT, EASI (Eastern Alpine Seismic Investigation) project, Austria.
- SEISMIC STATION DEPLOYMENT, Ground Truth and Application for the Anisotropic Receiver Functions Technique - Test site KTB, Germany.
- SEISMIC STATION DEPLOYMENT, Aftershock recording of the Ebreichsdorf Earthquakes, Austria.
- MAGNETIC SURVEY, Iron Ore Exploration, joint project of Geological Survey of Iran and Institute for Advanced Studies in Basic Sciences(IASBS), Sirjan, Iran.

### Teaching

- Seismotectonics, Teacher Assistant (TA), Course, Institute for Advanced Studies in Basic Sciences (IASBS), Zanjan, Iran, 2006
- Generic Mapping Tools (GMT), Training course, Institute for Advanced Studies in Basic Sciences (IASBS), Zanjan, Iran, 2006
- SEISAN, Training course, Institute for Advanced Studies in Basic Sciences (IASBS), Zanjan, Iran, 2006
- Seismology(I), Teacher Assistant (TA), Course, Institute for Advanced Studies in Basic Sciences (IASBS), Zanjan, Iran, 2007
- Earthquake and hazard assessments, BSc program in civil engineering, Course, SAMA College, Khorramabad, Iran, 2010

### Employments

- Sr. Manager of tunnel excavation, (Geo-section), Kakareza Tunnel project, Khorramabad, Iran.
- Sr. Manager of shaft/tunnel excavation and rock movement monitoring, B-Tunnel project, Tehran, Iran.
- Research assistant, (seismic travel time tomography, local seismicity, and event location), Metafan Co., Tehran, Iran.

---

## Award and scholarship

- 2015 Dissertation completion fellowship, awarded by center of doctoral studies, University of Vienna, Prepared and submitted by E. Qorbani.
- 2014 Conference travel grant, awarded by Austrian Research Foundation, to attend the AGU fall meeting 2014, project No. 06/14204.
- 2012 Research grant of young scientists, awarded by center of doctoral studies, University of Vienna, Prepared and submitted by E. Qorbani.
- 2003 Ranked 64th among more than 10,000 participants in the Iranian nationwide university entrance graduate exam.

2004 Excellent final project of Bachelor program (First Grade)

## Computer skill

Platform	LINUX, MAC, WINDOWS
Programming	LINUX SHELL SCRIPTING, MATLAB, FORTRAN
Geoscience software	SEISAN, SplitLab, SAC, VELEST, Generic Mapping Tools (GMT), Computer Programs in Seismology (Herrmann)
General	L <sup>A</sup> T <sub>E</sub> X, Adobe Illustrator, OpenOffice, Tecplot, ArcGIS, MS-Project, Computer Hardware and Support

## Language

English	<b>Fluent</b>
Persian	<b>Native</b>
German	<b>Intermediate</b>
Arabic	<b>Basic</b>

## Membership

2012-Present	European Geosciences Union (EGU)
2012-Present	American Geophysical Union (AGU)
2013	European Association of Geoscientists and Engineers (EAGE)
2015	Seismological Society of America (SSA)

## Recent conference contribution

### Invited talk:

- 2015 **Qorbani E.**, Bokelmann G., Seismic anisotropy under the Alps, invited talk, Departmental colloquium, University of Salzburg.
- 2015 **Qorbani E.**, Bokelmann G., Upper mantle structure beneath the Eastern Alps, invited talk, Eötvös Lorand University, Budapest, Hungary.
- 2014 Bianchi, I., Apoloner, M.-T., **Qorbani, E.**, Lloyd, S., Gribovszki, K., Gerner, A., Arneitz, P., Jordakiev, P., Bokelmann, G., The ground truth of crustal anisotropy from receiver functions, Invited talk, AGU fall Meeting 2014, San Francisco, USA. (presented by E. Qorbani)

### Oral presentation:

- 2014 **Qorbani, E.**, Bokelmann, G., Bianchi, I., 2014, Upper mantle anisotropic structure of the Eastern Alps, PANGEO 2014 in Graz.
- 2014 **Qorbani, E.**, Bokelmann, G., Bianchi, I., Upper mantle anisotropic structure of the Eastern Alps, presentation at the LABPAX workshop, Hainburg.

### Poster presentation:

- 2015 **Qorbani, E.**, Bianchi, I., Bokelmann, G., Slab detachment under the Eastern Alps seen by seismic anisotropy, EGU 2015, Vienna, Austria.
- 2015 **Qorbani, E.**, Bokelmann, G., Kovacs, I., Falus, F., Anisotropic Structure of the Upper Mantle in the Pannonian Basin: From SKS Splitting data and Xenolith Constraints, EGU 2015, Vienna, Austria.
- 2015 **Qorbani, E.**, Kurz, W., Bianchi, I., Bokelmann, G., Correlated lower crust and mantle deformation in the Tauern Window, Eastern Alps, EGU 2015, Vienna, Austria.
- 2014 **Qorbani E.**, Bianchi I., Bokelmann G., Slab detachment under the Eastern Alps seen by seismic anisotropy, AGU fall Meeting 2014, San Francisco, USA.
- 2014 **Qorbani, E.**, Bokelmann, G., Kovacs, I., Falus, F., Anisotropic structure of the upper mantle in the Carpathian-Pannonian region: From SKS splitting data and xenolith constraints, AGU fall Meeting 2014, San Francisco, USA.